The Effect of Land Cover on the Air and Surface Urban Heat Island of a Desert Oasis

ABDULRAHMAN MUBARAK H AL-ALI

The Effect of Land Cover on the Air and Surface Urban Heat Island of a Desert Oasis

Submitted for the degree of

Doctor of Philosophy

Submitted by

Abdulrahman Mubarak H. Al Ali

Department of Geography

Durham University

United Kingdom

June 2015

The Effect of Land Cover on the Air and Surface Urban Heat Island of a Desert Oasis

Abdulrahman Mubarak H. Al Ali

Abstract

Cities often experience a distinct climate compared to the surrounding area characterized by differences in air temperature, humidity, wind speed and direction, and amount of precipitation. Thus far, research on the urban heat island (UHI) effect has focused on cool temperate, Mediterranean and tropical climatic regions, whereas less attention has been given to the study of arid regions where the daytime surface temperature can be extremely high. This study concerns the Al Ahsa oasis, Saudi Arabia, which is a rapidly developing urban centre in an arid region. The aim of this study is to analyze the effect of land cover on the urban and sub-urban environment using ground data and multi-scale and multi-temporal satellite thermal imagery.

Land surface temperatures derived from satellite thermal imagery are compared with observations from ground-based fixed and mobile temperature and relative humidity logging stations for periods in February and July. Thermal radiometers from different sensors, Landsat 7 ETM+ and MODIS, were used to measure the outgoing radiation budget at specific locations within the urban landscape. Fieldwork was undertaken contemporary with satellite overpasses to measure the diurnal air temperatures and relative humidity across different land cover types including agriculture, urban, water, exposed rock surfaces, sabkha and sand dunes. These data provide the most complete experiment so far conducted to test and refine models of the thermal radiation budget of the arid zone at the sub-city scale.

The findings of this study have emphasized the effectiveness of combining the two methods, ground and satellite data, to investigate the relationship between land cover and UHI intensity. Results reveal a significant relationship between UHI spatial distribution and land cover using the two methods: mobile traverses and remote sensing. The UHI intensity is higher during the summer than the winter and at night-time than in the day. The highest UHI intensity, (10.5 °C), is located over the two major cities in the oasis (Al Hufuf and Al Mubarraz) while the lowest temperatures (-6.4 °C below UHI), are recorded in the small villages and vegetated areas during summer at night. The outcome of this thesis will help future urban development and planning projects and provide a framework for implementing rules and regulations by local government agencies for a sustainable urban development approach.

Table of Contents

LIST OF ILLUSTRATIONS

List of Figures

List of Tables

Declaration

This thesis is the result of my own work and has not been submitted for consideration in any other examination. Material from the work of other authors, which is referred to in the thesis, is acknowledged in the text.

Statement of Copyright

ACKNOWLEDGEMENTS

First and foremost, praise is to ALLAH the lord of the worlds, for his generous blessings, guidance and aid to complete this work. Second, I would like to express my sincere thanks to my parents who encouraged me to complete my higher education and kept supporting me with their prayers. I am most grateful to my wife and my children for their encouragement. Without their support it would have been impossible to complete this thesis.

My deepest gratitude is for my supervisors, Professor Danny Donoghue and Professor Tim Burt, for their valuable guidance throughout the PhD process. Without their scientific zeal, ever willing and determined assistance, and amiable appreciation of my limitations, it would have never been possible for me to complete such an arduous task.

Thanks are due to my parent institution, Al-Imam Muhammad Ibn Saud Islamic University, Geography Department for providing me a full scholarship to study at the Department of Geography, Durham University. Thanks also due for Durham University, Geography Department and to Al Ahsa Municipality for providing the different tools and instruments and research data to complete the fieldwork.

I am grateful to the airport weather station in Al Ahsa oasis, for providing the metrological data and for their guidance during the fieldwork. Also, thanks for King Abdulaziz City for Science and Technology in Saudi Arabia and to United States Geological Survey for providing the satellite images which used in this research.

Chapter 1: Introduction

1.1 Applied Climatology and Urban Climate

The development of applied climatology goes back more than sixty years. It focuses on three interactive functional areas. The first area is the inner core of applied climatology, including the development of instrumentation and keeping of climate records. The second area is the interpretation and generation of climate data, generally based on interactions with users. The third area consists of the use and application of climatology products. In addition, the application of climate information fall into four classes: 1) the design of structures and planning activities; 2) evaluations of current and past conditions including the assessment of extreme events; 3) review of the relationships between weather and climate conditions; and 4) operation of weather-sensitive systems that involve climatic data to make policy and other decisions (Changnon, 1995).

The field of urban climate studies has been growing in association with an increase in the number of urban inhabitants globally, and the profound effects of cities and their inhabitants on the atmosphere and vice versa. The topics covered in urban climate studies vary and include the need to know more about the fundamental physics, biology and chemistry of the urban atmosphere, and integrate this understanding into operational weather forecasting and air quality models; increase awareness of environmental sustainability and the desire to plan settlements and build houses that are more friendly to the environment; address concerns about environmental health, whether related to air quality, heat stress, 'homeland security'; understand the consequences of the dispersion of toxic substances in cities.

Example of papers that have been published in urban climatology during the last ten years cover varies topics, for example, analysing methodologies (Kanda, 2006), scale models (Grimmond, 2006), measurements (Masson, 2006), numerical models (Best, 2006), forecasting and numerical models, and (Voogt and Oke, 2003) thermal remote sensing. The spatial patterns

of urban climate (e.g., urban heat islands), energetics and dynamics (e.g., surface energy balance), and modelling (e.g., simulating the surface energy balance model (SEB)) have been important topics in the urban climatology field in recent years (Souch and Grimmond, 2006).

1.2 Urban Heat Islands

1.2.1 Definition and Background

Most urban and suburban areas record elevated temperatures compared with their rural surroundings and this difference in air and surface temperature is what establishes the heat island phenomenon (Gartland, 2008). The annual mean air temperature of a city with one million or more people can be 1 to 3 °C warmer than its surroundings (Oke, 1997) and on a clear, calm night, this temperature difference can be as much as 12 °C (Oke, 1987).

Even smaller cities and towns will produce heat islands, though the effect decreases as city size decreases (Oke, 1982). In another words, the urban heat island (UHI) is the name given to describe the characteristic warmth of both the atmosphere and surfaces in urban areas compared with their non-urbanised surrounding areas (Voogt, 2004). Figure 1-1 shows the variation in surface and atmospheric temperatures over different land use areas during the day- and night-time. Surface temperature differs more than air temperatures during the day, but they both are fairly similar at night.

Figure 1-1 Sketch of an urban heat island temperature profile

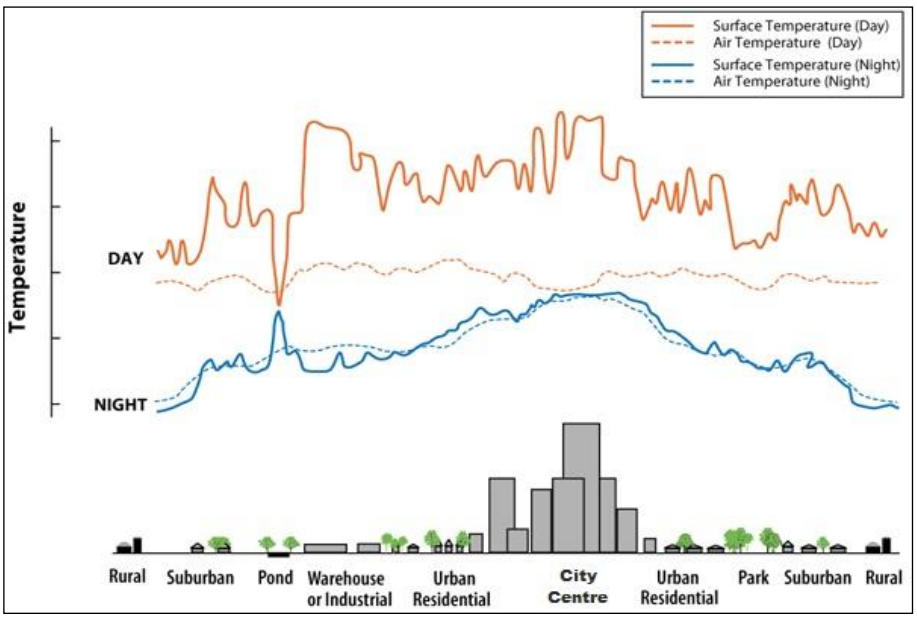

Source: (EPA, 2013).

The climatic differences between urban and rural environments have been recognised for almost 200 years, of which the variation in temperature is the most obvious (Taha, 1997, Unger et al., 2001). The differences in temperatures between urban centres and their surrounding country sides were first documented by Luke Howard in 1818 in his book 'The Climate of London'. Over a nine-year period, he showed that for London, the night-time temperature was 3.70 ºC warmer and day time 0.34 ºC cooler in the city than in the countryside (Mills, 2008).

UHIs develop when a large fraction of the natural land cover in an area is replaced by built surfaces that trap incoming solar radiation during the day and then re-radiate it at night (Clarke, 1972, Oke, 1982, Quattrochi, 2000). The change of land use types from natural land covers to build structures results in changes to the natural surface of the Earth. Man-made structures affect the airflow, reducing the heat transfer away from the urban environment (Ojima, 1990). The microclimate caused by the UHI results in increasing the demand for cooling energy in both commercial and residential buildings (Crutzen, 2004).

UHIs occur when changes to surface features modify the urban thermal climate, usually leading to warmer temperatures than in surrounding rural areas (Voogt and Oke, 2003). The intensity of temperature differences is dependent on the turbulent exchange of heat and modified radiant flux budgets (Landsberg, 1981). Energy exchanges and surface conditions in

the urban environment do not have fully predictable variables, meaning that UHI characteristics may differ between occurrences and may be caused under different microclimatic energy flux processes (Arnfield, 2003). Even a change as small as a new building may affect the microclimate and could contribute to the UHI effect (Landsberg, 1981).

There are some commonalities in UHI research that are well accepted. In general, UHI will exhibit higher temperatures in a city centre, which gradually decrease towards suburbs, before falling dramatically in rural areas (Critchfield, 1983). Under UHI conditions, temperature differences are greatest at night because of a decrease in the diurnal range in urban areas, as compared to rural areas (Critchfield, 1983). UHI conditions are maximised during calm, clear weather conditions and may exhibit seasonal fluctuations (Landsberg, 1981). The size of the UHI will often coincide with the extent of urban development, though the location and intensity of landscape features also affect UHI conditions (Critchfield, 1983). Modifying the heat budget and increasing warmth in an urban area will cause energy exchange by the mixing of overlying atmospheric layers (Arnfield, 2003). Recognising the interchange of energy between these two levels introduces the concept of scale to the UHI study.

1.2.2 Types of Urban Heat Islands

1.2.2.1 *Surface Urban Heat Islands*

Surface Urban Heat Island SUHI, Figure 1-2, refers to the relative warmth of urban surfaces. During the summer season, urban surfaces such as roads, roofs, and pavements can be heated by the sun to 27 °C to 50 °C hotter than the air (Berdahl and Bretz, 1997), while the shaded or moist surfaces, often in more rural surroundings, remain close to air temperatures. Surface urban heat islands are classically present day and night, but tend to be strongest during the day when the sun is radiating. On average, the difference in daytime surface temperatures between urban and countryside areas is about 10 °C to 15 °C; while it ranges from 5 °C to 10 °C in the night-time (Roth et al., 1989, Voogt and Oke, 2003). The size and intensity of surface urban heat islands vary with season, due to changes in the sun's intensity as well as differences in ground cover types and weather. As a result of such variation, surface urban heat islands are typically largest in the summer (Oke, 1982).

1.2.2.2 *Atmospheric Urban Heat Islands*

The atmospheric urban heat island effect can be defined as warmer air in urban areas compared to cooler air in nearby rural surrounding areas. Atmospheric urban heat islands can be divided into two different types. The first one is canopy layer heat island CLHI, which extends from the ground to below the tops of trees and roofs. The second type of atmospheric urban heat islands is boundary layer heat island (BLHI), which starts from the rooftop and treetop level and extends up to the point where urban landscapes no longer influence the atmosphere (Figure 1-2). This region typically extends no more than one mile (1.5 km) above the surface. Atmospheric urban heat islands are often weak during the late morning and throughout the day and become more pronounced after sunset due to the slow release of heat from urban infrastructure. The timing of this peak, however, depends on the properties of the urban and rural surfaces, season, and prevailing weather conditions (Oke, 1982).

Figure 1-2 Urban heat islands types: Urban boundary layer, canopy layer heat island, and surface heat island

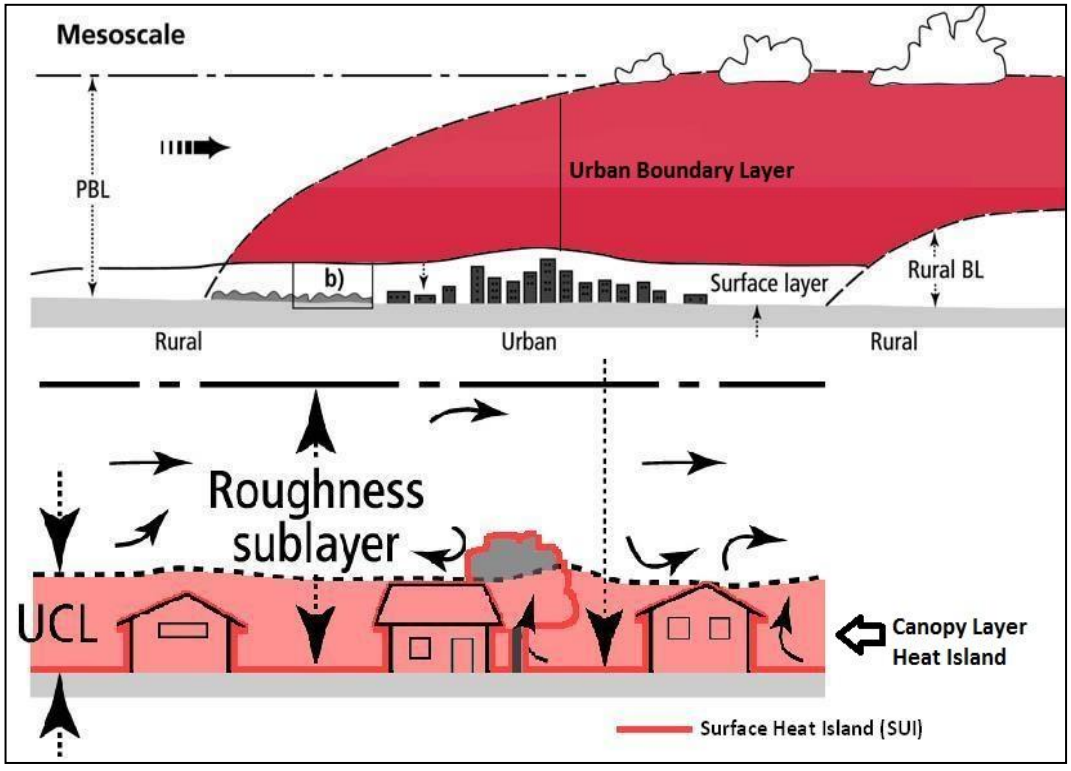

Source: (Oke, 1997).

1.3 **Microclimates and the Urban Heat Island**

The urban climate is considered to be composed of three variables: the large mesoscale climate, proximity to surface features and modifications caused by urbanisation. The effect of urbanisation is the summed responses of the various microscale urban surface features. According to Critchfield (1983): "Any change in albedo, water capacity and retention, evaporation, transpiration, or surface roughness may produce a change in climate, but the results are complex, difficult to measure, and not easily predicted." Figure 1-3 shows the urban heat islands processes in scale of mesoscale and microscale.

Lo and Quattrochi (2003) cities land use change, vegetation cover change, low urban albedo and increased pollution as factors that create the UHI. Taha (1997) estimated that a modest increase in urban albedo could reduce air temperature by as much as 2ºC. Cotton (1995) also noted the importance of albedo as well as the amount of latent heat as variables in urban climate modification. Other authors have linked deforestation and the introduction of impervious surfaces to the causes of UHI (LO et al., 1997). The intensity of the UHI may vary seasonally due to plant phenology, fuel use, solar angle (Roth et al., 1989) and topography (Landsberg, 1981). Together, these variables can cause urban modifications in climate that may lead to the formation of a UHI.

Figure 1-3 Urban heat islands processes in scale of mesoscale and microscale: Urban Boundary Layer (UBL), Rural Boundary Layer (RBL), and Urban Canopy layer (UCL)

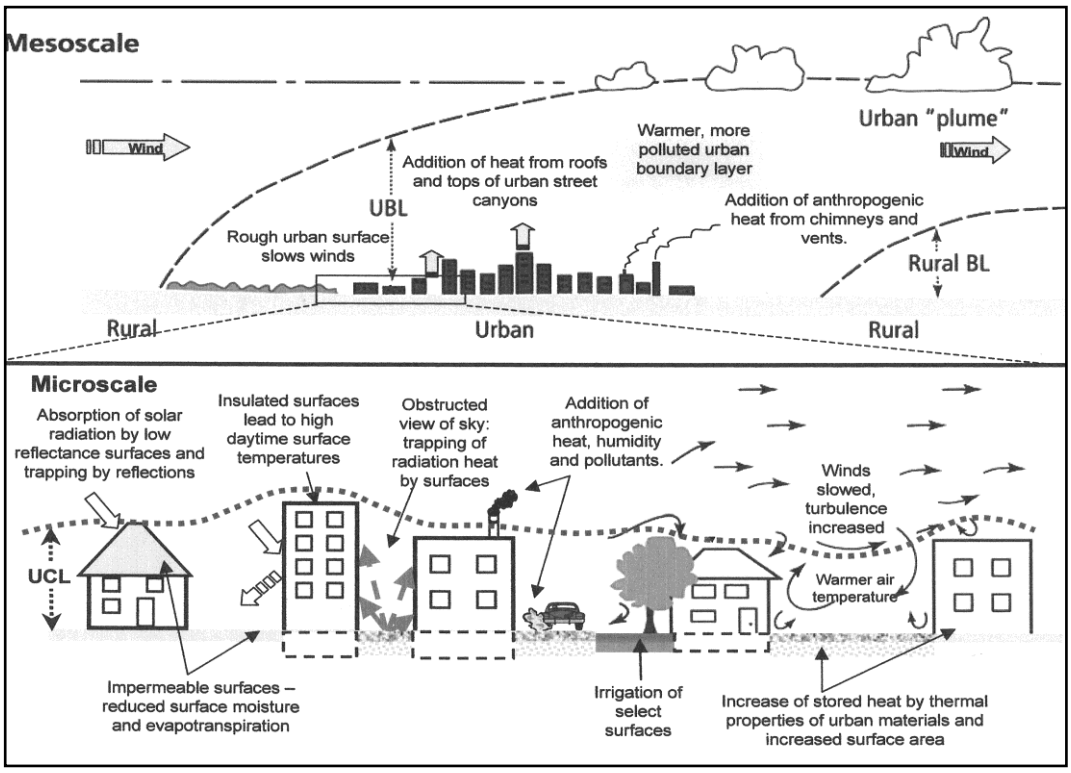

Source: (Voogt, 2000).

Topographical features are considered to constitute the relative surface roughness. Cities create extremely rough surface elements and can affect certain aerodynamic processes including surface drag, shearing stress, wind profile forms and turbulence characteristics (Arnfield, 2003). The surface roughness of cities as a whole can alter mesoscale winds, slowing them and causing them to flow around the city (Cotton, 1995). At the microscale, tall features on the urban surface create disturbances in the energy fluxes and create a roughness sub layer (Arnfield, 2003).

The absorption of energy will raise the temperature, meaning that the amount of energy reflected significantly affects UHI intensity. Urban surfaces reflect in a different manner than rural, vegetated surfaces. This makes albedo a primary factor in the urban energy flux (Small, 2006). Albedo is the hemispherically and wavelength-integrated reflectivity with typical urban ranges from 0.10 to 0.20 (Taha, 1997). Dark materials with low albedo absorb more energy and can enhance the UHI (Gluch et al., 2006).

During urbanisation, vegetated areas are replaced with impervious surfaces. These surfaces, such as asphalt, store heat and cause an increase in surface temperature. Impervious surfaces also do not allow the infiltration of rainwater into the soil profile. Instead, impervious surfaces collect water, quickly and efficiently removing it from urban features. The reduced presence of water in urban areas reduces evaporation, or latent heat transfer, from the heat budget and increases the amount of energy absorbed by urban features (Landsberg, 1981). Similarly, the removal of vegetation in urban areas will lower the capacity for precipitation interception (Critchfield, 1983) and increase the sensible heat. An increase in urban vegetation, on the other hand, will increase the latent heat required for evapotranspiration and lower sensible heat in the heat budget.

1.3.1 The formation of urban heat islands

There are several factors contributing to the formation of urban heat islands. These factors are reduced vegetation cover, urban material properties, urban geometry, anthropogenic heat emissions, weather conditions and geographical location (Wong et al., 2011). Below is a brief discussion of these factors and how they contribute to the urban energy balance to create urban heat islands.

1.3.1.1 *Reduced vegetation cover in urban areas*

Vegetation and open land typically dominate the landscape in rural areas, and trees and vegetation provide shade, which helps to lower the surface temperature. In addition, trees and vegetation also help to reduce the air temperature by evapotranspiration when releasing water to the surrounding air, dissipating ambient heat (Goggins, 2009). However, urban areas are characterized by dry, impervious surfaces, such as roofs, sidewalks, roads, and parking lots. Changes in ground cover will cause less shading and moisture to keep the urban areas cool (Wong et al., 2011). Therefore, the built-up area will elevated the air temperature, as there is less evaporation (Figure 1-4).

Figure 1-4 Impervious surface and reduced evapotranspiration

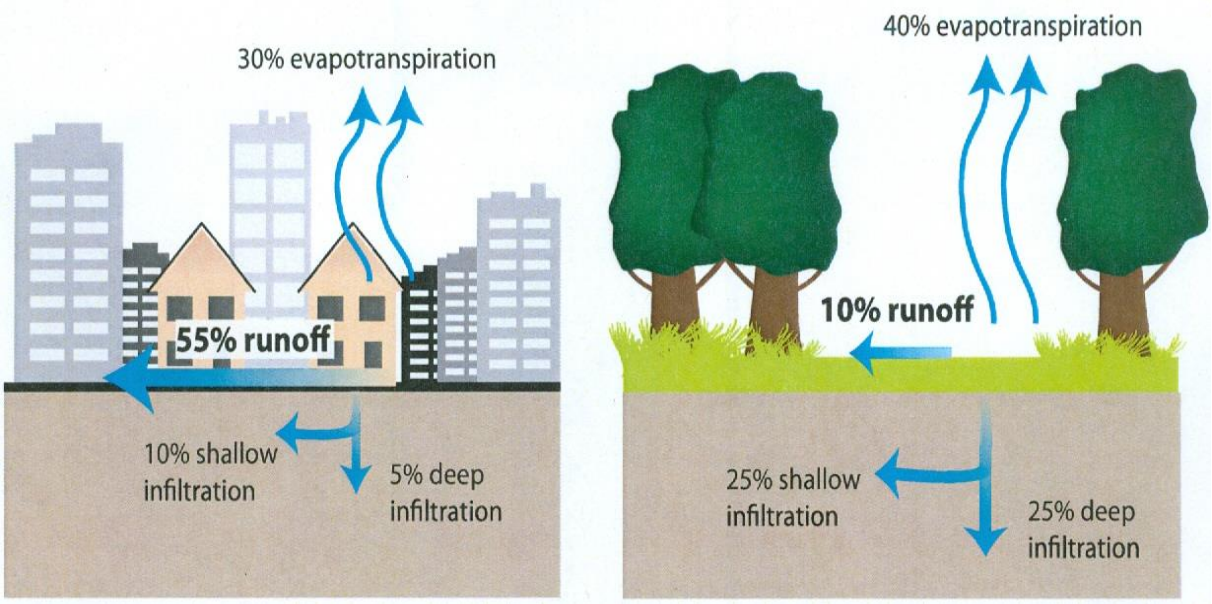

Note: Highly developed urban areas (right), which are characterized by 75%-100% impervious surfaces, have less surface moisture available for evapotranspiration than natural ground cover, which has less than 10% impervious cover (left). This characteristic contributes to higher surface and air temperatures in urban areas. Source: (Wong et al., 2011).

1.3.1.2 *Properties of urban materials*

Properties of urban materials, particularly solar reflectance, thermal emissivity, and heat capacity, also affect urban heat island formation, as they determine how the sun's energy is reflected, emitted, and absorbed. When looking at the solar energy that reaches the Earth's surface on a clear summer day, we see three types of short-wave radiation (Figure 1-5), in different percentages: ultraviolet 5%, visible light 43% and infrared 52% Energy in all of these wavelengths contributes to the creation and formation of urban heat islands. In addition, the albedo, which is the percentage of the solar energy reflected by the surface, is another important factor that influences the development of urban heat islands. Dark surfaces usually have lower solar reflectance values than light surfaces (Wong et al., 2011).

Figure 1-5 Solar energy versus wavelength reaching earth's surface

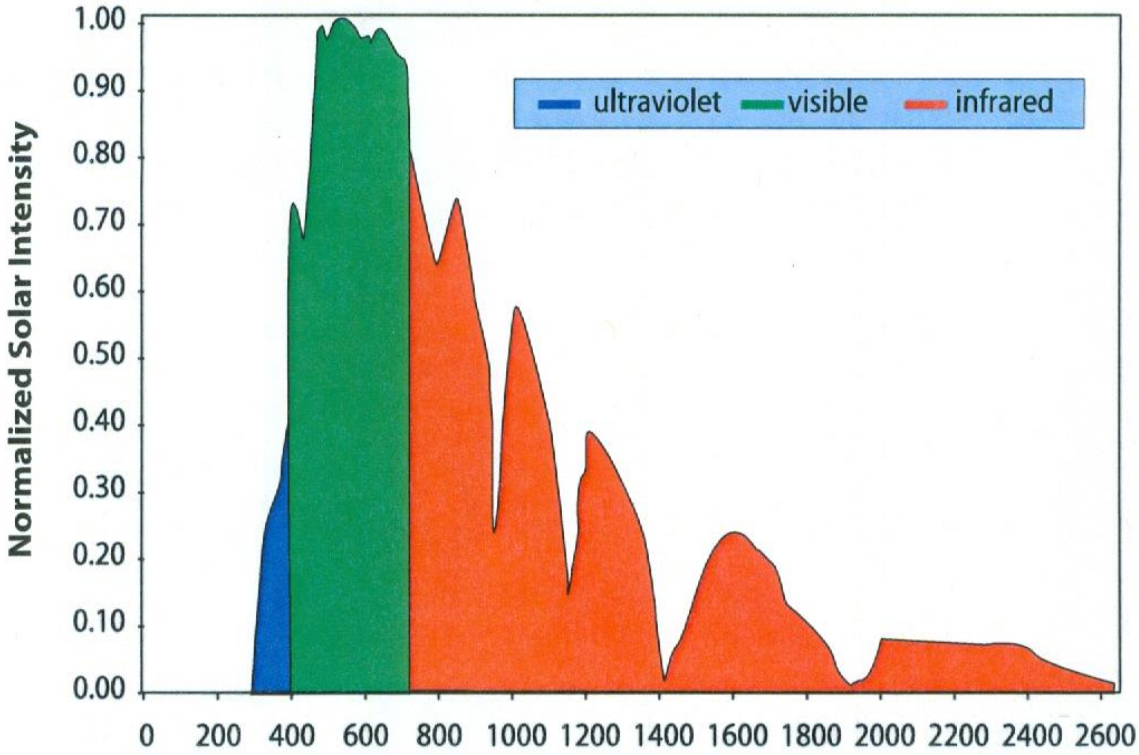

Note: Solar energy intensity varies over wavelengths from about 250 to 2500 nanometres. Source: (Wong et al., 2011).

1.3.1.3 *Urban geometry*

Another factor that influences the development of an urban heat island is urban geometry, particularly at night. Urban geometry is defined as the dimensions of and spacing between buildings, which influences the wind flow, energy absorption, and the ability of building surfaces to emit long-wave radiation to the space. It can be summarised as narrow streets lined by tall buildings. Moreover, urban geometry, or the 'sky view factor' (SVF), has an effect on urban heat islands (Wong et al., 2011, Zhu et al., 2013). For example, an open parking lot has fewer obstructions and a large SVF value close to 1, while an urban canyon in a city centre area where tall buildings are densely packed has a low SVF value close to zero. Tall buildings can create shade, reducing surface and air temperatures. On the other hand, when the sunlight reaches the surfaces, the sun's energy is reflected and absorbed by the building walls, which further lowers the city's albedo and then increase the temperature (Zhu et al., 2013).

1.3.1.4 *Radiation and energy budget*

Solar radiation is defined as the energy radiation receives from the sun in electromagnetic waves including visible and ultraviolet light and infrared radiation (Oke, 1987, Santamouris, 2013). The radiation balance can be expressed in a budget equation, composed of different terms that each represents a radiation transport or conversion process, as presented in the following equation (Oke, 1987):

$$Q^* = (K\downarrow - K\uparrow) + (L\downarrow - L\uparrow)$$

$$= K^* + L^*$$

where is:

Q^*: net all-wave radiation
K^* : net shortwave radiation
$K\downarrow$: incoming shortwave radiation
$K\uparrow$: outgoing shortwave radiation
L^*: net longwave radiation
$L\downarrow$: incoming longwave radiation
$L\uparrow$: outgoing longwave radiation

The balance of incoming and outgoing energy flows, or fluxes, provides an equation that quantifies the energy budget (Figure 1-6). The surface energy budgets of urban areas and their rural surroundings will differ based on the differences in land cover, surface characteristics, and human activity levels. These differences will affect the generation and transfer of heat, which can lead to different surface and air temperatures in urban and rural urban areas (Wong et al., 2011). Different elements of the budget include the following:

1.3.1.4.1 Short-wave radiation

Short-wave radiation can be defined as ultraviolet, visible light and near-infrared radiation coming from the sun that reaches the Earth. This energy is the main factor that drives urban heat islands (Oke, 1982). Urban surfaces such as concrete and asphalt reflect less radiation back to the atmosphere than natural ground cover such as vegetation or sand. On other words,

man-made ground surfaces absorb and store more energy from radiation, thus raising the area's temperature and helping to create an urban heat island.

1.3.1.4.2 Thermal storage

Thermal storage increases in urban areas due to less solar reflectance and is influenced by the thermal properties of different materials and urban geometry. Urban geometry can also cause some short-wave radiation within the canyon level to then be reflected on to nearby surfaces such as building walls and other surfaces, where it is absorbed rather than escaping into the atmosphere (Oke, 1982, Wong et al., 2011) (Figure 1-6).

Figure 1-6 Urban surface energy budge

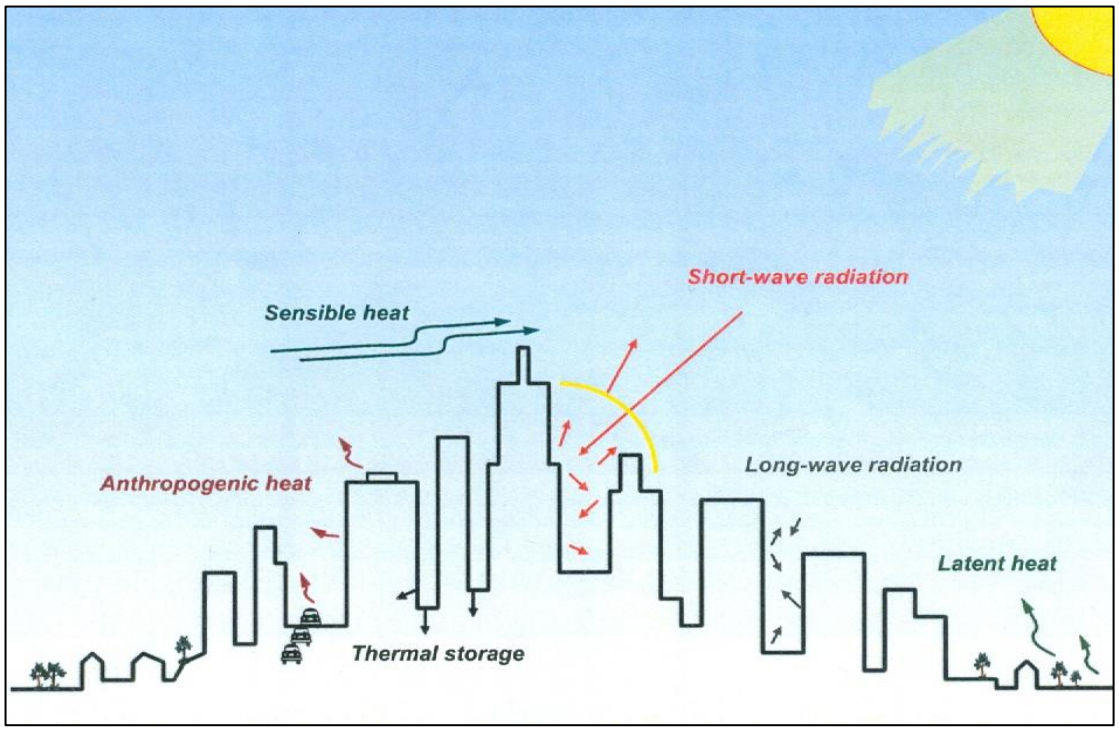

Source: (David, 2007).

Similarly, urban geometry can block the release of long-wave, or thermal infrared, radiation into the atmosphere. The buildings or other objects in urban areas absorb incoming short-wave radiation; then they can radiate that energy as long-wave energy or heat. However, during the night, due to the dense infrastructure in some urbanized areas that have low sky view factors, which prevents long-wave radiation to the cooler, open sky, this trapped heat contributes to the

creation of urban heat islands (Zhu et al., 2013). Another factor that affects the urban energy balance is evapotranspiration, which can be described as the transformation of latent heat and felt as the humidity that emits from the Earth's surface to the air via evaporating water. Due to the nature of urban surfaces, the level of evapotranspiration is lower in such areas, which makes built-up areas dry and impervious urban infrastructure can reach very high surface temperatures, contributing to higher air temperatures (Wong et al., 2011).

1.3.1.5 *Anthropogenic heat*

Anthropogenic heat is produced by human activities and contributes to the air in urban heat islands. There are several sources of anthropogenic heat: running appliances, transportation and industrial processes. Therefore, more activities mean more heat, especially in urban areas where heat can significantly contribute to heat island formation (Voogt, 2002, Shahmohamadi et al., 2011). A recent study by Shahmohamadi et al. (2011) investigated the impact of anthropogenic heat on formation of urban heat island (UHI) and also determined which factors could directly affect energy use in the city. The study found that there is strong evidence that the average temperature of the Earth's surface is rising because of increased energy consumption helping to form the urban heat islands (Shahmohamadi et al., 2011).

1.3.1.6 *Weather conditions and geographical location*

Other factors that influence the formation of urban heat islands are the weather and geographical location, which communities have little control over, but residents can benefit from understanding the role they play. Wind (speed and direction) and cloud cover are the two important factors affecting urban heat island development. Urban heat islands form and become stronger when winds are calm and on clear days due to the maximum amount of solar energy reaching the surface and the minimum amount of heat that can be convected away, while strong winds and cloud cover supress urban heat islands (Oke, 1973). In addition, the geographical location including topography and climate can affect the formation of urban heat islands. For example, large bodies of water moderate the local temperature and help to generate wind, convecting the heat away from urban areas. Mountains also have an effect on urban island areas, as they can either block wind from reaching such areas or create wind patterns that pass through cities (Wong et al., 2011).

All climatic variables such air temperature, humidity, air pressure, wind speed, and precipitation are affected by each other (Givoni, 1976). The air temperature variation affects the evaporation and air capacity, leading to the change in air humidity. Furthermore, the air temperature differences between different locations will also create different air masses that will lead to different air pressures systems, which in turn would produce air movement, thereby wind and gusts. This variation in humidity and wind speed and direction affects rainfall (Valsson and Bharat, 2011). Air temperature and humidity are important properties of the UHI, and have effects on health and thermal comfort. Thermal comfort depends on both factors: air temperature and humidity (Escobedo, 2014). Relative humidity is used to measure the amount of the water vapour in the air. It is defined as the amount of water in the air relative to saturation amount the air can hold at given temperature multiplied by 100. The relationship between temperature and relative humidity is that when the temperature decreases the relative humidity goes up, while when the temperature increases the relative humidity goes down (Valsson and Bharat, 2011).

1.4 **Measuring Urban Heat Islands**

1.4.1 Ground Data Applications

It has been reported that UHI can be examined using a fixed weather station at the city scale or on a small university campus such as National University of Singapore (Wong and Jusuf, 2007). With different numbers of fixed weather stations, urban heat island intensity can be investigated and modelled. This number of fixed weather station can be two stations, such Kim and Baik (2002), or six like Hoffmann et al. (2012), or up to 31 weather stations (Kim and Baik, 2005). The comparison between the urban site and rural site is the most common method to calculate the UHI intensity and its magnitude based on ground data (Oke, 1987). Urban heat island was investigated in Hamburg, Germany using several weather stations to predict the future relationship between different meteorological variables (wind speed, cloud cover, relative humidity, pressure, and water vapour pressure) and UHI. The study found that there is no significant changes based on the regional model while there is moderate increase and strong UHI days can be predicted based on climate local model (Hoffmann et al., 2012).

Similar study from Seoul using two meteorological observatories, urban and rural sites, for period of 23 years found that there is an effect of the wind speed, relative humidity, and cloud cover on the UHI intensity. The study indicated that the UHI is weakest in the summer and strong during the autumn and winter and also higher during the night-time than the daytime (Kim and Baik, 2002). Also, another study from Seoul, using 31 automatic weather stations for one year from March 2001 to February 2002, found the similar (Kim and Baik, 2005) results. The study found that the spatial distribution of UHI intensity varies according to the location and the topography of the local region. The UHI intensity during the night-time is stronger than the day time and when the wind speed is increased and cloud cover is decreased. Also, the study found that the UHI intensity is stronger during the weekdays than the weekends, while might refer to the intensities of the human activities and traffic (Kim and Baik, 2005).

A study by Sofer and Potchter (2006) using ground-based data showed the development of a moderate UHI located around the most intensive area of human activity: the city business centre and dense hotel belt. The UHI is more significant at midday during the summer period, while early morning inversions in winter have a weakening effect on the UHI intensity. Eilat is located in an extremely hot and arid zone on the northern coast of the Red Sea. The study used diurnal predawn and early afternoon measurements from the winter and summer seasons for two consecutive years. The data demonstrated that UHI is more significant at midday during the summer period, while early morning inversions in winter have a weakening effect on its intensity. Also, it was found that the topography and wind regime have a dominant effect on the location and intensity of the UHI, while the sea appeared to have a very marginal effect. This study suggests that information to better define the spatial patterns of UHIs, particularly in the summer months, is needed to understand heat stress in arid cities (Sofer and Potchter, 2006).

The spatial and temporal aspects of the urban heat island in the small, arid city of Casa Grande, Arizona were studied by Hedquist (2005). Meteorological data such as temperature, dew point, and wind speed were collected through a combination of fixed station and two mobile routes over a short period, on four separate clear and calm nights. The results of this study showed that a maximum heat difference of 4.7 °C was recorded along an east to west route across the city and increased in the far eastern areas where the commercial corridor was located. However, the far southern and western areas of the city were cooler than other regions due to

the higher density of rural agricultural fields. The main finding of this study determined that wind speed has a significant effect on the urban heat island intensity of the study area. Due to very light wind speeds during the study period, surface thermal properties and land cover may have played the main role in determining heat islands. In addition to this conclusion, thermal imagery of Landsat taken of the study area at night-time, similar to transect time, confirmed the same results that surface thermal material properties may play a large role in determining heat island characteristics near the ground in the absence of strong winds (Hedquist, 2005).

In a recent study by Charabi and Bakhit (2011), the impact of the rapid growth of Muscat city from 1970 to 2003 was observed in relation to the regional climate and air quality. The study investigated the effects of topography, mesoscale circulation, urban form, and landscape variability on urban heat islands that exist in an extreme hot and tropical arid area and complex topography located on the coast of the Sea of Oman. Spatio-temporal variability of air temperature at the meso- and microscale were recorded using mobile traverses for one year. In addition, fixed meteorological stations were installed to record air temperature in rural, suburban, and urban areas. The results of this study indicate that the peak of the urban heat island occurs about 6 to 7 hours after sunset and it is best established during the summer season. The highlighted portion of the study area represents the warmer core of the urban heat island, which may reflect the nature topography of this area, along a narrow valley characterised by low ventilation, high business activities, multi-storied buildings, and heavy road traffic. Moreover, these mountainous areas play a main role in increasing the regional temperature by absorbing the short radiation waves through dark-coloured rocks and isolating the area from the cooling effect of the land–sea breeze circulation during the day time. In the lowlands of the study area, the urban density and land breeze circulation affect the thermal pattern among urban and suburban areas.

Alghannam and Al-Qahtnai (2012) investigated the relationship between the urban micro-climate and density of the vegetation to estimate the cooling effect imposed by the rural environment in Al Ahsa oasis. The heat flux behaviour was observed in four surrounding locations with different densities of trees using hourly data recorded for three months. The outcome of this study indicated that the urban areas such as Al Hofuf city were the warmest compared with Al Qurain village, whose surroundings have a high density of palm trees. The

study also found that the north and north-west of the oasis, which has a high density of vegetation, were colder than the south region, which is mostly urban area.

Other examples of heat islands in arid environments include studies on Phoenix and Tucson, Arizona (Balling, 1986, Hsu, 1984, Jr and Brazel, 1987, Tarleton and Katz, 1995), Kuwait City (Nasrallah et al., 1990); Eilat City (Sofer and Potchter, 2006); and Dammam City, in the east province of Saudi Arabia (Habib, 2007). The Arizona studies, mainly based on ground-based observations, show that the UHI intensity was highest during summer nights. However, the UHI for Kuwait City was poorly developed. Explanations suggested include the proximity of the city to the coast and the effect of the Arabian Gulf sea breeze; low average building height in both the commercial and residential areas; and the extensive use of local building materials that have thermal characteristics similar to those of the surrounding uninhabited area. Moreover, UHI distributions in Dammam City were analysed using two Landsat images of the study area in July and November 2001. The study estimated the surface and atmosphere heat islands using ground data and remote sensing techniques in relation with different land cover and use within the city. The outcome of the study suggests that there is a need to establish more green areas such as local parks and add more trees on the streets to help reduce the temperatures in the centre and industrial areas of the study area (Habib, 2007).

Wong and Yu (2005) used a mobile survey to explore both the intensity of the UHI effect and cooling impact of green areas at the macro-level in Singapore. The temperature distribution was mapped relying on data derived from the mobile survey. The outcome of this study suggested that there is a strong correlation between the decrease in temperature and the appearance of large green areas in the city. Summarily, mobile traverses were used in Tokyo, Japan by Yokobori and Ohta (2009) and in Utrecht, the Netherlands by Brandsma and Wolters (2012) to conduct air temperature to clarify the effect of different land cover on the UHI intensity. The air temperature measurement took place using a bicycle at different times of the day before sunrise and after noon. In general, the results suggest that there are seasonal variations in UHI intensity among different land cover. The maximum UHI intensity was recorded under the calm and cloudless conditions during all seasons of the years examined.

The ground-data method (weather stations) represents one of the most popular methods to investigate the temperature and temperature changes around the world. In a recent study by

Rohde et al. (2013), a new mathematical framework is presented for mapping temperature changes in large-scale averages obtained from weather station thermometers data. The study uses the Kriging statistical method to interpolate the data from stations to arbitrary locations on the Earth. The new framework applies to the Global Historical Climatology Network (GHCN) monthly land temperature dataset and derives a new global land temperature record from 1800 to the present. The outcomes of this study were in close agreement with earlier estimates made by the groups at NOAA, NASA and at the Hadley Centre/Climate Research Unit in the UK. The study found that the global land mean temperature had increased by 0.89 ^{o}C ± 0.06 ^{o}C in the difference of the Jan 2000-December 2009 average from the January 1950-December 1959 average (95% confidence for statistical and spatial uncertainties) (Rohde et al., 2013).

1.4.2 Remote Sensing Applications

Thermal remote sensing approach is the most common detection tool to estimate the surface temperatures (Voogt and Oke, 2003). Different satellites images with different temporal and spatial resolutions have been utilized including Landsat, the Advanced Spaceborne Thermal Emission and Reflection Radiometer (ASTER), Advanced Thermal and Land Applications Sensor (ATLAS), and the Advanced Very High Resolution Radiometer (AVHRR).

In 1978, the satellite sensor for the Heat Capacity Mapping Mission (HCMM) was first used to map Earth surface temperature. The HCMM sensor, Table 1-1, gathered thermal infrared (10.5–12.5μm) radiance data in support of studies to determine the feasibility of using remote sensing to compute the thermal inertia of the Earth's surface (Chen and Allen Jr, 1987, Vukovich, 1984). Also, Landsat/Thematic Mapper data sets collected over the metropolitan area of Washington, DC were used to investigate the urban heat island. Surface energy composites of five surface categories were analysed by combining the derived spectral albedos and temperatures. The results indicate that urban heating is attributable to a large excess of heat from the rapidly heating urban surfaces consisting of buildings, asphalt, bare-soil and short grasses. In summer, the symptoms of diurnal heating begin to appear by mid-morning and can be about 10 °C warmer than nearby woodlands (Kim, 1992)**.**

In 1989, NOAA AVHRR (Table 1-1) infrared satellite data were used to display the surface radiant temperature heat islands of Vancouver, British Columbia, Seattle, Washington, and Los

Angeles, California. Despite the low spatial resolution of the satellite imagery, the study found that the heat island intensities were largest in the day-time and in the warm season, while might be because of the location of these cities and the effect of sea breeze systems which are very common in such cities. In addition, the results showed that daytime intra-urban thermal patterns were strongly correlated with land use; e.g. industrial areas were warmer than vegetated, riverine, or coastal areas (Roth et al., 1989). Similar results in a study by Pinho and Orgaz (2000), on the city of Aveiro in Portugal, showed that building density, weather and coastal proximity influence the UHI effect. Therefore, good urban planning is important to help mitigate this effect.

Table 1-1 Satellites launch date, thermal bands, wavelength, and spatial resolution

Sensor	Launch Date	Thermal Band	Wavelength Range	Spatial Resolution	Revisit
HCMM	1978	1,2, and 3	10.5-12.5µm	500m	16 days
NOAA- AVHRR	1978	4 and 5	11-12µm	1.1km	1-2 days
MODIS	1999	20-23	0.4 -14.4µm	250-1000m	1-2 days
AATSR	1991	2 and 3	10.8-12µm	1000m	16 days
NASA-Landsat5 TM	1984	6	10.4-12.5µm	30m	16 days
NASA-Landsat7 ETM+	1999	6	10.4-12.5µm	15m	16 days
NASA-Landsat8 LDCM	2013	10 and 11	10.60-11.19 µm 11.50-12.51 µm	15m	16days

Source: Adapted from (WDC-RSA, 2010) and the USGS website.

The energy balance of urban areas used to be measured *in situ* using traditional processes to quantify the heat flux, but these represent only a small local scale within the heterogeneous urban environment. For this reason, remote sensing approaches are very useful tools to explain and collect more spatially widespread information. Xu et al. (2008) used hyperspectral imagery from a new airborne sensor, the Operative Modular Imaging Spectrometer, along with a survey map and meteorological data, to derive the land cover information and surface parameters required to map spatial variations in the turbulent sensible heat flux of the centre of Shanghai, China. Two spatially explicit flux retrieval methods were applied to the study area: (1) the Local-scale Urban Meteorological Parameterization Scheme; and (2) an Aerodynamic Resistance Method. Based on the two different methods, sensible heat fluxes were determined at 6 m spatial resolution, and then the results were applied to 30 and 90 m spatial resolutions. The study suggested that the use of much lower spatial resolution space borne imagery data, for example from Advanced Space Borne Thermal Emission and Reflection Radiometer (ASTER), is likely to be a practical solution for heat flux determination in urban areas.

Multiple sets of UHI measurements spanning several years (for example satellite measurements of Houston, USA, by (Streutker, 2003) can be used to measure the relative increase in surface temperature of urban areas. Such studies have measured a mean temperature increase in magnitude of 0.8 K, with an increase in the mean UHI area of up to 650 km^2 depending on the method of analysis. It is will be helpful if ASTER thermal data are combined with ground data such as mobile traverses to examine models of UHI and identify its main cause (Nichol et al., 2009).

Thermal infrared satellite data provide better spatial coverage than ground-based observations and are widely used for estimating surface albedo and evapotranspiration estimates required in studies related to surface energy balance. A recent study by Badarinath et al. (2005) describes the analysis of day and night AATSR sensor data for urban heat island and surface thermal inertia. Field campaigns were conducted simultaneously with the AATSR data to validate the remote surface temperature estimation, and it was found that satellite derived surface temperature values were within ±1 °C of ground measured values. Heat island formations in urban regions of Hyderabad and environs can be clearly seen in the night-time AATSR data with core urban regions showing high temperatures (Badarinath et al., 2005). A study using NASA's Moderate Resolution Imaging Spectroradiometer (MODIS) satellite data over Southern Africa led to the conclusion that the reflectance, emissivity and surface temperature were derived within ±0.015, ±0.01 and ±1 K, respectively. A direct application of the MODIS mid-infrared surface reflectances can be applied to the fire detection problem and the results compare well with higher spatial resolution Landsat 7 data (Petitcolin and Vermote, 2002).

The thermal channels of the MODIS satellite have been used to investigate the UHI intensity during extreme weather events and heatwaves. It has been determined that ASTER and MODIS thermal bands provide similar results if the atmospheric correction and calculation of emissivity calculated with high accuracy (Akhoondzadeh and Saradjian, 2008). Cheval et al. (2009) explored the characteristics of the air and land surface temperature in Bucharest, Romania during the extreme high temperatures that affected the region in July 2007. The study integrates thermal data supplied by MODIS sensors and meteorological data ground-based weather stations. The main finding of this study is that the correlations between the air temperature measured at the weather stations and the corresponding surface temperature show significant values either under "normal" conditions or under "extreme" temperature. That

suggests that MODIS sensor is a useful instrument for air and surface temperature validation and investigate the UHI intensity during the extreme weather conditions. Combination of MODIS and ground measurements of air temperature was studied in Birmingham, United Kingdom between 2003 and 2009 including the heatwave period event in 2006. The outcomes of this study quantify the local UHI intensity as well as the impact of atmospheric stability on UHI development. During the high atmospheric stability, the UHI intensity reached a peak value of 5 °C in the central business district of the city. The lowest value of the urban heat island was recorded at the park site of up to 7 °C lower than the city centre (Tomlinson et al., 2012).

The Pearl River Delta (PRD) in southern China is experiencing rapid urbanisation resulting in a remarkable UHI effect, which may impact the regional climate, environment, and socio-economic development (Chen et al., 2006). In this study, Landsat TM and ETM+ images from 1990 to 2000 in the PRD were selected to retrieve information on brightness, temperatures and land use. The analysis showed that the highest temperatures in the UHI are located in a scattered pattern, related to certain land-cover types. Kardinal et al. (2007) identified land use types that have the most influence on ambient temperature in Singapore. Remote sensing data and geographical information systems (GIS) were used to obtain a large-scale view of Singapore and carry out both qualitative and quantitative analysis showing that the land management practice had a clear influence on urban temperature.

MODIS, ASTER, and Landsat 7 ETM+ have been used to estimate the surface temperature in the desert city area of Abu Dhabi. MODIS with high revisiting time was used to analysis the daily variation, medium resolution data from ASTER and Landsat 7 ETM+ has been used to evaluate the local urban heat island in more details in district level. The results of these studies show cold urban heat island over the downtown during the daytime and high or positive UHI intensity during the night-time in general and during the summer season in particular (Nichol et al., 2009, Lazzarini et al., 2013).

In a recent study, the upward long-wave radiation flux density from urban surfaces was analysed using a high-resolution thermal-infrared (TIR) camera and meteorological measurements in the city of Berlin, Germany (Meier, 2010). Spatial-temporal patterns of the difference between upward long-wave radiation flux density from courtyard surfaces and the

roof were reported. For temporal analysis, the TIR camera recorded one TIR image per minute over a period of two days from 3rd to 5th May 2007. Three hourly averaged thermal patterns showed persistence effects due to shadow, sky-view factor (SVF) distribution in the courtyard, thermal properties of the surface materials, human activities and turbulence characteristics of the surface–atmosphere interface. Shadow caused by temporarily parked cars results in a lower upward long-wave radiation flux density compared to the non-shadowed surface close to it. Immediately after car departure, this difference decreases. As a result of this study, a method to derive the thermal admittance of a concrete surface based on TIR data from this attenuation process was proposed. This study found that ground-based high-resolution TIR imagery is highly suitable to investigate surface thermal properties and the dynamic processes controlling thermal patterns within a complex three-dimensional (3D) urban structure (Meier, 2010)**.**

The US National Research Council Decadal Survey (2008) indicated a need for a TIR sensor that has adequate revisit times or multiple thermal spectral bands to provide the information needed to model UHI dynamics and its impact on humans and the adjacent environment (NASA, 2008). As a response to this need, NASA plans to launch the Hyperspectral Infrared Imager (HyspIRI) before 2020 (Weng, 2009). This multispectral thermal infrared imaging instrument will have a return time, spectral characteristics, and nighttime viewing capabilities that will greatly enhance our knowledge of UHI's form, spatial extent, and temporal characteristics for urban areas across the globe. Additionally, HyspIRI will provide a high spatial resolution that is currently not available from previous Earth-observation satellites for assessing how urbanization affects adjacent ecosystems. HyspIRI is well suited for deriving land cover and other biophysical attributes for urban climate and environmental studies. However, it will not be launched soon enough to influence the study proposed here.

This review demonstrates that, while some progress has been made, the thermal remote sensing of urban areas has been slow to advance beyond qualitative description of thermal patterns and simple correlations. Advances in the application of thermal remote sensing of natural surfaces suggest insights into possible methods to advance techniques over urban areas. Improvements in satellite resolution provide more detailed measurements of urban surfaces and the availability of low-cost, high-resolution portable thermal scanners will allow progress in the study of the climate of urban areas (Voogt and Oke, 2003). In a recent study by Good (2015), a method for estimating daily Tmin and Tmax at the pixel scale using geostationary satellite data

has been tested. This study has developed a model based on the dynamic multiple linear regression between geostationary satellite data and co-located station observations using daily minimum and maximum land surface temperature, fraction of vegetation, distance from the coast, latitude, urban fraction, and elevation as predictors. The method is applied over Europe for 2 years 2012-2013; estimation with station observations indicates a mean satellite-minus-station bias of 0.0 °C to 0.5 °C with a root-mean-square difference of 2.3 °C to 2.7 °C. The study also found that the satellite surface temperature data have larger uncertainties comparing with *in situ* data sets; however, the satellite surface data can cover more spatial details than the ground station can provide (Good, 2015).

There are some points can be summarized from the above literature review of urban climatology in general and urban heat islands studies in particular. Although more information on the form and dynamics of the UHI is available for climatic zones that are located in temperate regions, it is also now available for climate zones outside these regions but there is still a need for more understanding of the UHI in different regions such arid regions (Arnfield, 2003). The majority of the studies required to measure and investigate the energy balance are focused in suburban areas ; however, sampling and measurement of height and other observation are needed for the city centre which is more difficult to meet compared to the suburban area because the high-rise buildings. Urban heat islands are "well described but rather poorly understood" (Oke, 1982). Nevertheless, simple methods that used to investigate UHI intensity are still needed within the urban areas as a function of time, weather conditions and structural attributes, for applied applications such as road climatology, phenology, energy conservation, and weather forecasting. There is a strong recommendation to use methods that link both small scale and mesoscale to study and examine the UHI intensity (Arnfield, 2003). For example, Voogt and Grimmond (2000) used remote sensing estimation of the surface temperature and sensible heat flux and (Masson, 2000) employed concepts of canyon geometry to estimate the surface energy budgets in mesoscale of the urban area.

In summary, the majority of the urban heat islands studies using remote sensing have been applied in Temperate, Mediterranean, and humid and cool regions. Examples of these studies investigating the relationship between meteorological features and green distribution area Saito et al. (1990) in Kumamoto city in Japan, Kawashima (1990) in the Tokyo Metropolis, Jauregui (1990) in Mexico city, Jeffrey K. Sonne (2000) in Melbourne and Florida, Avissar (1996) in

Colorado, and in Singapore by Tso (1996) and Wong and Yu (2005). Moreover, urban heat islands have been reported in many other countries, states, and cities around the world. A recent review study of urban heat islands and its relation to death rate around the world, Wong et al. (2013) listed about 50 cities; these cities are located in different climate zones, polar, temperate, arid, tropical, and Mediterranean. However; the majority of these cities are not located in arid regions where the temperature is extremely high and the urbanization growth is at the high levels. Combining fixed weather stations, mobile traverses, and remote sensing methods will allow more understanding in order to model and examine the UHI from the large to the small scale. Therefore, this study investigates the effect of different land cover types on urban heat islands in arid zones using ground and different temporal and spatial scales of the satellite images.

1.5 **Significance of this Research**

The Urban Heat Island is an important phenomenon to be studied in general and in urban climate studies in particular. Urban Heat Islands are related to many problems around the world, for example, global warming, energy use, air quality, human health and comfort, and water quality.

1.5.1 Global Warming

Global warming has achieved much attention because the global mean surface temperature has increased since the late 19th century. Figure 1-7 indicates a time series of global land and marine surface temperature from 1850 to 2011. It shows that the 2011 was the twelfth warmest year. Since more than 50% of the human population lives in cities, urbanization has become an important contributor to global warming (Chen et al., 2006). Global warming can occur from a variety of causes, both natural and human induced. In common usage, "global warming" often refers to the warming that can occur as a result of increased emissions of greenhouse gases from human activities. The impacts from urban heat islands and global climate change (or global warming) are often similar. For example, some communities may experience longer growing seasons due to either or both phenomena. Urban heat islands and global climate change can both also increase energy demand, particularly summertime air conditioning

demand, and associated air pollution and greenhouse gas emissions, depending on the electric power system fuel mix (Grimmond, 2007).

Figure 1-7 Combined of global land and marine surface temperature record from 1850 to 2011

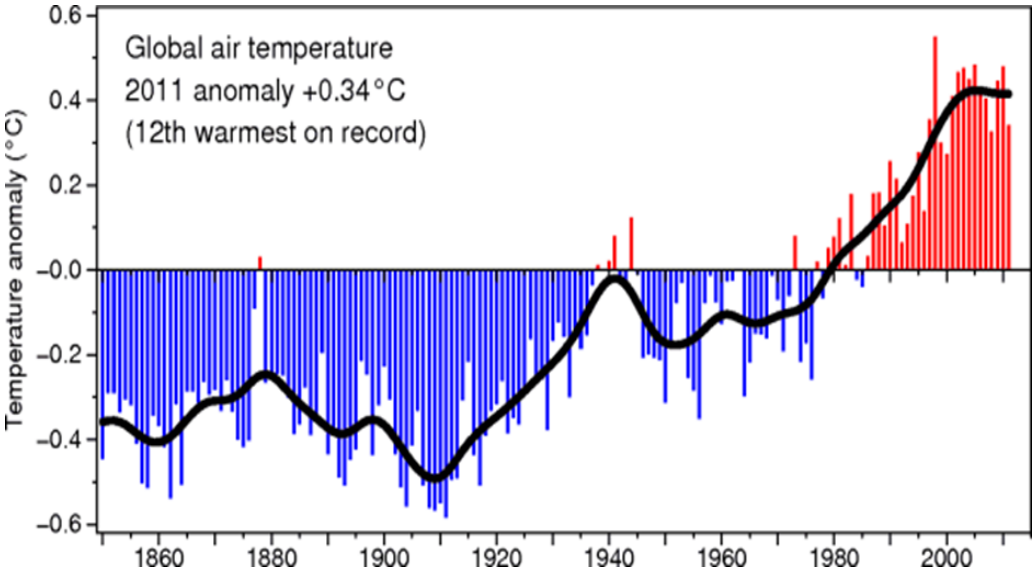

Source: The key reference for this time series is (Morice et al., 2012) available online: http://www.cru.uea.ac.uk/

1.5.2 Land Cover Change

Land cover change, especially from green areas to urban areas, may increase land surface temperature (LST) in semi-arid regions such as the study area that is represented here. The land cover of Al Ahsa has changed continually during the last 30 years, especially with the development of the oil industry since the 1970s (Ait Belaid, 2002, Mufareh, 2002). A study by Mufareh (2002) compared the land cover of Al Ahsa between 1987 and 2001 and found that the urban land area has increased by 5,326 ha in 2001, from which 2,746 ha were converted from sabkha[1], 1,500 ha from open space (urban planning), 972 ha from sand dunes and 513 ha from agricultural lands in 1987 (Figure 1-8). The urban heat island is a climatic pattern that occurs in which "surface and atmospheric modifications due to urbanization will generally lead to a modified thermal climate that is warmer than the surrounding non-urbanized area" (Voogt

[1] The area which is characterised by a crusty surface consisting of evaporated deposits (including salt, gypsum and calcium carbonate), windblown sediments and tidal deposits. (Fryberger et al.,1983).

and Oke, 2003). Therefore, it is important to map and quantify changes in land cover and identify its impacts on the surface temperature regime in the Al Ahsa oasis study area.

Figure 1-8 Land cover change of Al Ahsa oasis between 1987 (left) and 2001 (right)

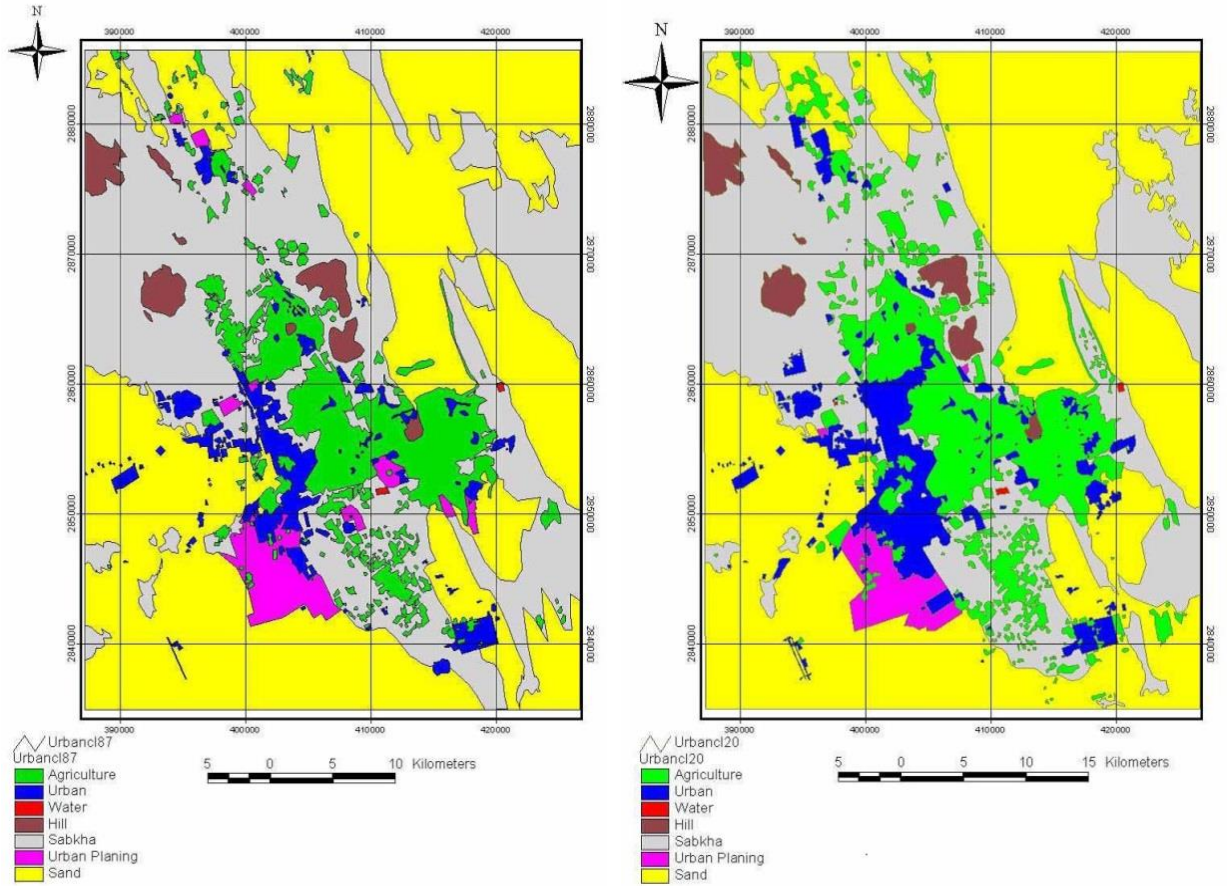

Source: (Ait Belaid, 2002).

1.5.3 Energy Use

Due to the high temperature during the summertime, the energy demand for cooling will increase in the cities. Studies indicate that electricity needs for cooling increase 1.5% to 2.0% for every 0.6 °C increase in air temperature, starting from 20 °C to 25 °C, suggesting that around 5% to 10% of the community demand for electricity is used to compensate for the heat island effect (Akbari, 2005) Figure 1-9 shows the relation between the electricity load and the temperature increase in New Orleans.

Figure 1-9 Increase of electrical load when temperatures exceed about 20 °C to 25 °C in New Orleans

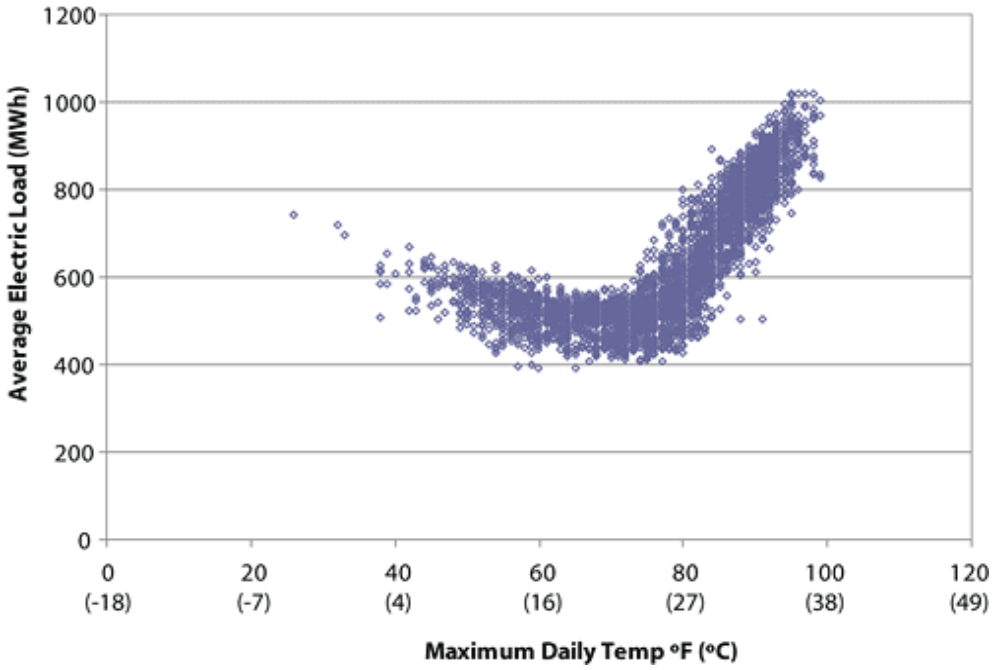

Source: (Sailor, 2002).

In hot arid regions such Al Ahsa oasis, especially in the summer season when air temperature can reach around 50 °C in July and August months, the demand on electricity is very high for cooling systems, lights, and appliances. In addition, during extreme heat events, which are exacerbated by urban heat islands, the resulting demand for cooling can overload systems and require that a utility institute controlled, rolling brownouts or blackouts to avoid power outages.

1.5.4 Air Quality

As a result of the high demand on electricity during the summer season, companies that produce electricity typically rely on fossil fuel power plants to meet that demand, which means an increase in air pollution and greenhouse gas emissions. An example of some pollutant gases are sulphur dioxide (SO_2), nitrogen oxides (NOx), particulate matter (PM), and carbon monoxide (CO). These pollutants can be very harmful to human health. Also, these gases can play a major role in contributing to air quality problems such as the formation of ground level ozone (smog), fine particulate matter, and acid rain. Moreover, an increase in fossil fuel

powered plant use can lead to an increase in the emissions of greenhouse gases, such as carbon dioxide (CO_2), which contribute to global climate change (EPA, 2013).

1.5.5 Human Health and Comfort

UHIs have the potential to directly influence the health and welfare of urban residents. Within the United States alone, an average of 1,000 people die each year due to extreme heat (Changnon et al., 1996). As UHIs are characterised by increases in temperature, they have the potential to increase the magnitude and duration of heat waves within cities. Research has found that the mortality rate during a heat wave increases exponentially with the maximum temperature, an effect that is exacerbated by the UHI (Buechley et al., 1972, Zaitchik, 2006). If the temperature in day time increases, the night time cooling will decrease. A high level of pollution is linked with urban heat islands and can affect human health by causing general discomfort, respiratory difficulties, heat cramps and exhaustion, non-fatal heat stroke, and heat-related mortality (EPA, 2013).

Heat islands can also aggravate the impact of the heat waves, which are defined as abnormally hot weather. Children, older adults, and people with existing health conditions are at risk from such events. A previous study done in Toronto found that there is a relationship between death rates of different age groups and hot waves in the summer season (Smoyer-Tomic and Rainham, 2001). Similar results were found in different countries such as the United States, Canada, the People's Republic of China and Egypt. The results of the studies suggest that heat-related mortality is estimated to rise significantly in all four countries if the earth warms, with the greatest impacts in China and Egypt (Kalkstein and Smoyer, 1993). Moreover, increases in air temperatures and heat wave events can result in the urban heat islands effect, which can have severe human health impacts and create more severe droughts and related environmental problems (Zaitchik, 2006). Table 1-2 shows the impact of heat waves and droughts experienced in selected cities.

Table 1-2 Some of the heat waves events and droughts around the world

Event	Year	Location	Impact
Heat wave	1987	Athens	Estimated 900 deaths
Heat wave	1995	Chicago	Estimated 700 deaths
Heat wave and drought	2002	Australia	Poor crop yield
Drought	2002	SW, USA	Poor crop yield
Heat wave and drought	2003	France	Estimated 15,000 deaths Poor crop yield, Down 4-10% by yield
Drought	2005	Illinois, USA	Poor crop yield

Modified after: Committee on Earth Science and Applications from Space, 2007; (Zaitchik et al., 2006).

1.5.6 Water Quality

Storm water can be heated when the surface of pavements and rooftops is high. One study has shown that pavements that are 38 °C can raise initial rainwater temperature from roughly 21 ºC to over 35 ºC (James, 2002). Another study in Arlington, Virginia, showed the same results; increases in surface temperature can increase water temperature as high as 4 °C in 40 minutes after heavy summer rains (Roa-Espinosa et al., 2003). This heated storm water generally becomes runoff, which drains into storm sewers and raises water temperatures as it is released into streams, rivers, ponds, and lakes. When the water temperature rises above normal, it will affect all aspects of aquatic life, especially the metabolism and reproduction of many aquatic species (EPA, 2013).

1.6 Research Questions, Aims and Objectives

1.6.1 Research Questions

1) Is there a direct relationship between the urban expansion and spatial and temporal pattern of radiative energy flux in the study area?
2) Do urban heat islands develop in arid zone cities?
3) Do local land cover classes have a direct influence on determining local UHIs and their dynamics?
4) Will combining thermal data obtained from satellite images and ground measurements help to scale up models of UHIs over arid regions, such as Al Ahsa oasis, from the local to the city-scale?

1.6.2 The Aim

The aim of this study is to analyse the variations in the thermal environment that exists throughout Al Ahsa oasis due to different land cover conditions. Satellite remote sensing data and statistical study of ground-based observations will provide quantitative baseline data and recommendations to local governmental agencies for the planning of sustainable urban development.

1.6.3 The Research Objectives

1) To investigate the influence of various land cover types on the air and surface temperatures and UHI intensity by using a combination of ground data and remote sensing;
2) To compare field observations to a remote sensing-based model of UHI intensity in arid regions ;
3) To study the air and surface temperatures and UHI distribution across the different land cover types at different scales from small to large using ground data and satellite images.

1.7 Thesis Structure

The second chapter of this thesis provides a definition of the study area and a detailed description including its location, microclimate, demographics, and land use patterns. Also, this chapter discusses the spatial variables that affect the thermal structure of the study area. Chapter Three describes the research data and its sources including the fixed weather stations, mobile data, satellite images of Landsat and MODIS. In this chapter, data pre-processing and methodology used is given for fixed weather stations, mobile data, and satellite images. The data set and processing of satellite images of Landsat 7 ETM+ and MODIS during winter and summer seasons are described. A detailed description of images calibration, processing, classification, mapping the emissivity, and estimating surface temperature using remote sensing is also given. Chapter Four describes the seasonal distribution of the local urban heat islands in the study area. Air and surface temperatures, relative humidity, and wind and gust

speed are presented among different land covers. UHI intensity and different land cover data are statistically tested during the winter and summer seasons. Chapter Five includes the spatial and temporal distribution of the local urban heat island among different land cover. In this chapter also, UHI intensity based on mobile data is statistically tested among different land covers and the distribution of UHI intensity is mapped during both seasons and at the night-time and after sunset. Chapter Six provides a detailed estimation of the regional surface temperature using the remote sensing technique and different satellite sensors (Landsat 7 ETM+ and MODIS). The land covers classification results using different data sets and software is given. Also, comparison between the air temperature, fixed weather station and mobile data, and brightness temperature obtained from the different satellite images is examined. Finally, in this chapter the relationship between the land cover and urban heat island intensity is statistically tested and graphically described. Chapter Seven includes reviews of previous urban heat islands studies and provides a detailed approach to quantifying and mapping this phenomenon in arid regions. It compares previous results with the findings in this research and discusses any differences. The main findings, evaluation of the aim and objectives, conclusions, and recommendations and directions of the future research are highlighted.

Chapter 2: Description of the Study Area

2.1 Introduction

This chapter is concerned with two important features of the study area. The first section describes its geographical features with regard to its location, topography and climatology. The second section examines various spatial variables which might affect the thermal characteristics of the study area, i.e. land cover/use patterns, population density, housing pattern and building type. The reasons for choosing this location as the study area are included at the end of this chapter.

2.2 Geographical location and background

Saudi Arabia covers approximately 80% of the total area of the Arabian Peninsula, extending from longitude 34° east at its northernmost point (Ras Al-Sheikh Humeid) to 56° at its south-eastern border, and from latitude 16° to 32° north (MP, 1992) (Figure 2-1). There are three large deserts in Saudi Arabia; the Ad-Dahna Desert, Rub- Alkhali Desert (Empty Quarter) and An-Nafud Desert (Figure 2-2).

Figure 2-1 The location of Saudi Arabia

Source: (Union, 2009).

Al Ahsa oasis, the study area, is located in the eastern province of Saudi Arabia, forming part of the Rub-Alkhali Desert. It is located between longitudes 49°33' and 49°46' east and latitudes 25°21' and 25°42' north. Al Ahsa oasis stretches from the Arabian Gulf to the Ad-Dahna and Oman deserts, bordering Qatar, the United Arab Emirates, and the Sultanate of Oman (Al-Mass, 1999). The total arable land is approximately 20,000 hectares in size, in an L-shape that extends over an area of 10 × 17 km east–west and 6 × 24 km north–south (Hussain, 1982) (Figure 2-3).

Figure 2-2 The location of the three main deserts in Saudi Arabia

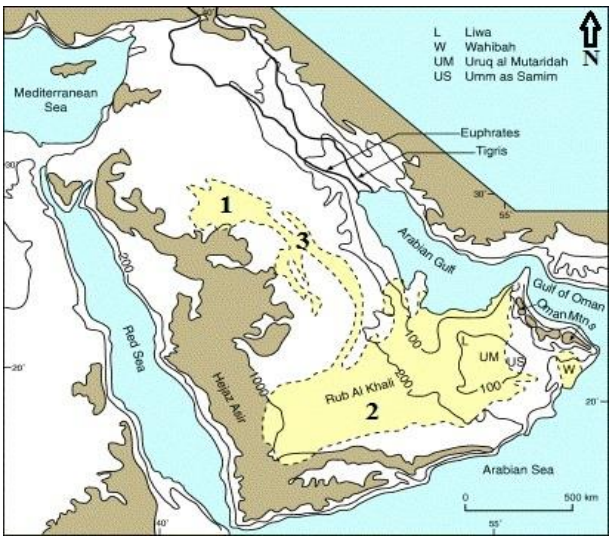

Note: (1) Ad-Dahna.(2) Rub-Alkhali. (3) An-Nafud. Modified after (Glennie and Singhvi, 2002).

The Al Ahsa oasis region is considered to be possibly one of the oldest existing agricultural areas in the world. Both Pliny, in his “Natural History”, and Strabo, in his “Geography of the Roman Empire”, referred to Al Ahsa as an agricultural production centre almost two thousand years ago. Strabo also reported the existence of a permanent river originating in Al Ahsa and flowing to Al-Uqair seaport, an ancient harbour on the Arabian (Persian) Gulf located about 75 km east of Al-Hofuf city (Humaidan, 1980). At this time, Al Ahsa was a very important stop-over for merchants travelling between India and the Mediterranean.

Over the years, many scholars from a variety of countries and backgrounds have travelled through Al Ahsa oasis and written about the area and its people. The list includes such scholarly authors as Sadlier (1823), Ibn Battutah (1854), Palgrave (1865), Khosrau (1881), Zwemer (1900), Lorimer (1908), Raunikiaer (1916), Cheesman (1926), Twitchel (1947) and Vidal (1953). All referred to the relative economic importance of Al Ahsa, both as a food-producing area and as a trading centre (Humaidan, 1980).

Figure 2-3 Map of Al Ahsa oasis location (study area), Saudi Arabia

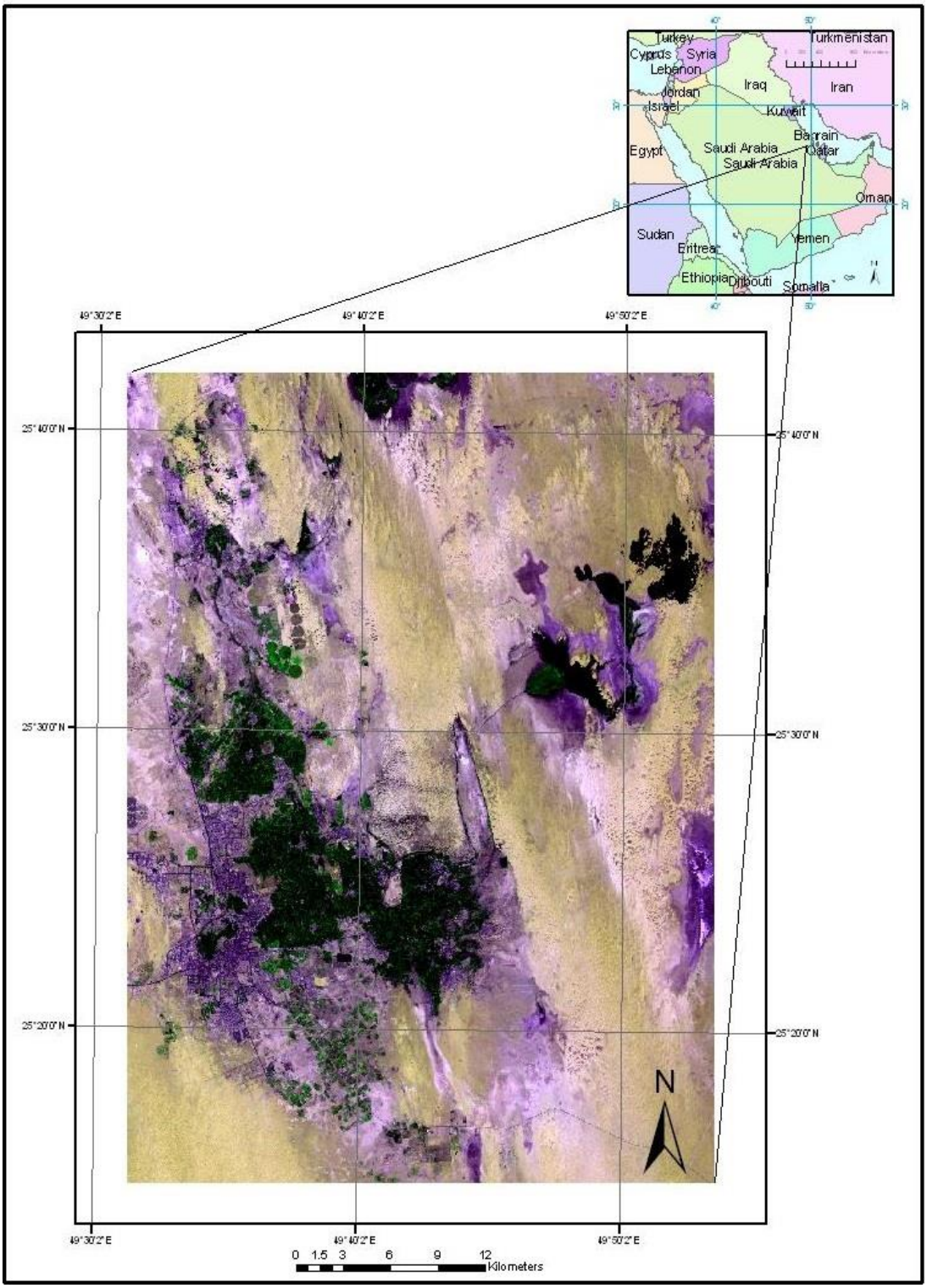

Source: (King Abdulaziz City for Science and Technology, 2010).

Al Ahsa oasis one of the largest date producing regions in Saudi Arabia It also produces wheat, rice and some vegetables, such as tomatoes, cucumbers, onions, and carrots and some fruit

(watermelons, melons). Alfalfa, pomegranates, grapes and figs are also common in Al Ahsa (Al-Omeer, 1987). Palm trees are the most common arboreal species in this oasis (Figure 2-4).

Figure 2-4 Palm trees farms in Al Ahsa oasis. View from the top of Al Qarah Mountain

2.3 **Topography**

Al Ahsa oasis located on a plain, generally sloping gently to the east and northeast. The elevation ranges from 150 m above sea level in the south to 110 m -125 m in the north. There are four main topographic features in the study area, Aeolian formations, sabkha deposits, gravel deposits and erosional hills and mesas.

2.3.1 Aeolian formations

Aeolian formations result from very fine sand and silt deposited by the wind (Binda, 1983, Fryberger *et al*., 1983) (Figure 2-5). Al Ahsa is completely surrounded by sand and sand dunes in four directions. However, the active belt of drifting sand extends from the north to the northern border of the east villages. The dunes are high in this area, reaching up to 15 m in height (Abolkhair, 1981). The main sources of the sand for these dunes are the Al Nafud

desert, in the north, Al Dahna desert to the west and Al Jafura desert, which surrounds the study area to the north.

Figure 2-5 The main topographic features in Al Ahsa oasis

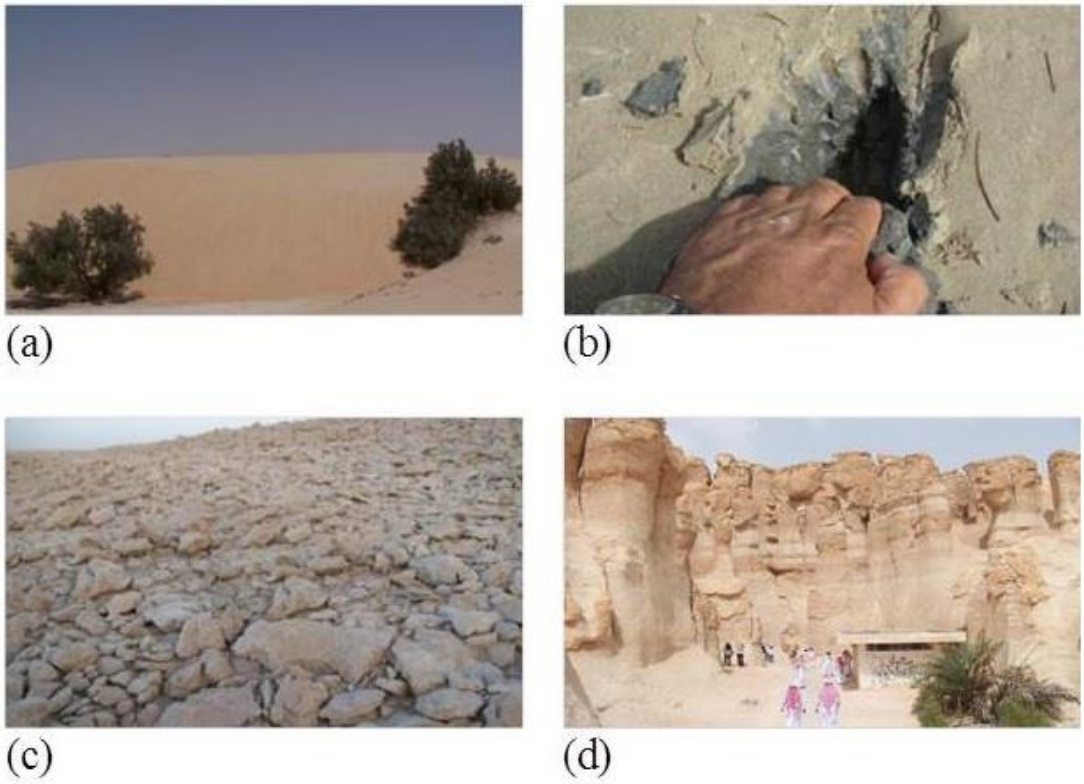

Note: (a) Aeolian formed sand dune. (b) Sabkha deposits. (c) Gravel deposits. (d) Erosional hills and mesas (Al Qarah Mountain).

2.3.2 Sabkha deposits

Sabkha is an Arabic term for a low-lying flat area, usually in arid regions, found in coastal and inland areas. It is characterised by a crusty surface consisting of evaporated deposits (including salt, gypsum and calcium carbonate), windblown sediments and tidal deposits (Fryberger et al., 1983, Sabtan and Shehata, 2003, Al-Farraj, 2005). Figure 2-5(b) shows salty and muddy wet sand in a sabkha site located east of the study area. There are a number of sabkha areas; Sabkha Umm Hishah, about 30 km northeast, Sabkha Murayqip, about 20 km east are the largest one located to the east of Al Hofuf city.

Abolkhair (1981) and Al-Taher (1999) have suggested that there are several reasons for the formation of the sabkha in the study area: (1) the flat nature of the Al Ahsa landscape so that

irrigation and rainfall water remains near the surface; (2) the movement of the sand from the north to the south of the oasis. These sand dunes prevent the drainage of water along the general slope to the east and north east; (3) the nature of the groundwater, which is found near the surface in the majority of the study area; (4) the movement of water from groundwater to the surface through capillary action and; (5) the existence of a hard pan-layer in the study area keeping the water near the surface.

2.3.3 Gravel deposits

The gravel plains, in the eastern province of Saudi Arabia, can be divided into two areas. The first is Dibdiba of Wadi al Batin, which is located in the northern part of Al Ahsa, southwest of Kuwait. The second area is Hidiba, in the southern Al Ahsa region. In both areas the gravel layers include pebbles from a crystalline basement complex or from interior limestone plateau formations (Abolkhair, 1981). The gravel sizes range between 25 mm and 125 mm in diameter and were mainly formed as a result of massive erosion effects in the central Arabian Peninsula and from the local erosion of the eastern edge of the Assumman and Shedgum plateaus (Powers *et al*., 1966) (Figure 2-5).

2.3.4 Hills and Mesas

Hills and mesas, known locally as Jabal, are one of the major topographic features in Al Ahsa oasis. The average height of these hills and mesas is about 220 m above sea level. They are characterised by sink holes, solution cavities and caves. Jabal Al Qarah, Buraiga, Shabah, Kanzan and Dukhnah are examples of these isolated erosional remnants (Abolkhair, 1981) (Figure 2-5).

2.4 Local Climate

According to the Köppen world climate classification system, Saudi Arabia, including the Al Ahsa oasis study area, is located in a BWh zone (arid desert, hot temperature) (Peel *et al*., 2007). The following sections examine the seasonal air temperature, relative humidity, sea level pressure, wind speed and rainfall in the study area over the last twenty-eight years, from 1985 to 2012.

2.4.1 Air Temperature

The air temperature in the study area over the four seasons of the year is directly related to the amount of solar irradiation. When the amount of sunlight increases and the sky is clear, the temperature increases. Conversely, when the days shorten and it is cloudy (i.e. in the winter), the temperature decreases (Al-Omeer, 1987). Between 1985 and 2012, the monthly maximum air temperature ranged from 21 °C to 29 °C in the winter and 41 °C to 45 °C in the summer. Over the same period the monthly mean for the minimum air temperature ranged from 8 °C to 15 °C in the winter and 24 °C to 29 °C in the summer. Based on the above figures, the monthly mean air temperature ranged between 14 °C and 22 °C in the winter season and 33 °C and 37 °C in the summer (Figure 2-6).

Figure 2-6 Monthly mean maximum, mean minimum and mean air temperatures in the Al Ahsa oasis region for the period 1985 to 2012

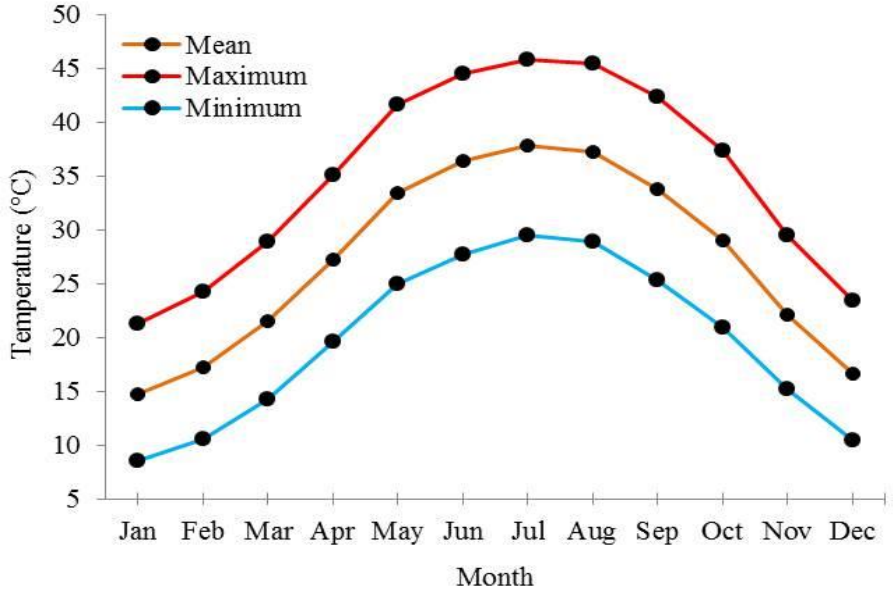

Source: (Presidency of Meteorology and Environment, 2011).

2.4.1.1 *Summer and winter temperatures*

According to the meteorological calendar, summer starts in June and finishes in August. However, the summer season of the study area extends over five months of the year, starting in May and finishing at the end of September (Al-Abdeen, 1986). Table 2-1 shows the season times in the region by month compared with the common meteorological calendar. The average of air temperature during the summer is 40 °C, with a maximum average of 45 °C during July

and August. The maximum absolute temperature may reach more than 50 °C. A temperature of 52 °C was recorded in July 1969, and 51°C in August of the same year (Leichtweiss, 1978). The minimum temperature during the summer in the region is still high, with a yearly average of 22 °C, climbing to an average of 24 °C during July and August (Al-Omeer, 1987).

Winter starts in November and continues until the end of March. It is mild, with a mean maximum temperature of 21 °C and a mean minimum of 8 °C. Sometimes, however, the absolute temperature drops to below the 0 °C. For example, on December 23, 1971, a temperature of (- 4 °C) was recorded. The region is subject to rare frosts, occurring approximately every fifteen years (Leichtweiss, 1973).

Table 2-1 Season times in the study area compared to the common meteorological calendar

Season	Meteorological calendar	Study area season
Winter	December	Winter
	January	Winter
	February	Winter
Spring	March	Winter
	April	Spring
	May	Summer
	June	Summer
Summer	July	Summer
	August	Summer
Autumn	September	Summer
	October	Autumn
	November	Winter

Adapted from (Al-Omeer, 1987).

2.4.1.2 *Spring and autumn temperatures*

Based on the climatic conditions seen in this region, spring only lasts for one transitional month (April) and autumn equates with October. Temperatures during these two seasons fluctuate between the typical summer and winter temperatures. In summary, the Al Ahsa oasis region has the highest air temperatures in Saudi Arabia, with a maximum mean air temperature of about 37 °C and minimum mean of approximately 18 °C. Generally, the average annual air temperature is 26 °C. The average spring/autumn temperature fluctuates between 12 °C in January and 19 °C in September (Al-Taher, 1999) (Figure 2-6).

2.4.1.3 *Relative humidity*

In study of geographical of Al Ahsa by Al-Taher (1999) the average relative humidity of the study area was 38% over the period 1985–2012. The monthly relative humidity level varies from month to month and from season to season. The monthly mean relative humidity ranges between 31 % and 55 % in the winter and 21 % and 29 % in the summer season (Figure 2-7). Relative humidity is at its lowest in May, June and July at an average of 23 %, with its highest levels in January and December, averaging 55 %. This might be due to the high air temperature during the summer season and the different pressure systems that affect the wind patterns in the study area from season to season (Al-Taher, 1999).

Figure 2-7 Monthly mean relative humidity from 1985 to 2012

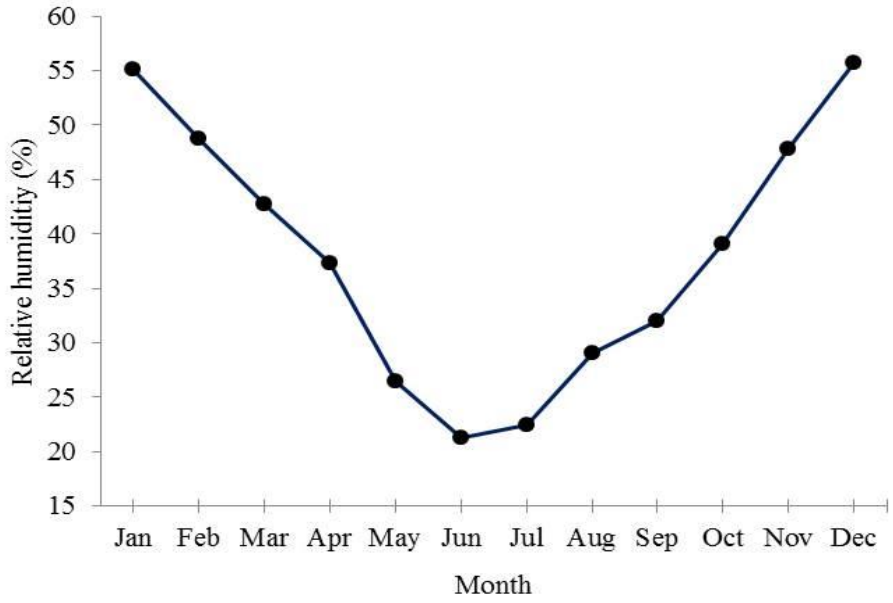

Source: (Presidency of Meteorology and Environment in Saudi Arabia)

2.4.1.4 *Synoptic systems and wind patterns in the study area*

Surface pressure is considered to be the most important factor affecting the climate in the study area. Solar radiation, temperature, relative humidity, evaporation, rain and winds are linked strongly to air pressure, especially in terms of horizontal and vertical air flow (Al-Taher, 1999). Pressure systems also play a vital role in determining the path of air masses, and thus temperature patterns, in the study area. The following is a brief summary regarding pressure and wind systems during the summer and winter periods in the study area.

2.4.1.4.1 Pressure systems and winds in the winter

High pressure systems dominate Al Ahsa oasis in November and extend through to March. Over the period 1985–2012, the monthly mean sea level pressure in November was 1016.33 mb and 1013.79 mb in March (Figure 2-8). During this period, Al Ahsa oasis falls within the extension of the Siberian high pressure region which covers south west Asia and is connected to a group of high pressure centred on Armenia, Anatolia and in the northern part of Iraq. It is also connected to the high-pressure region in the north and middle of the Arabian Peninsula. This high-pressure area affects the climate of the eastern parts of the Arabian Peninsula by acting as a barrier restricting the eastern movement of air masses (Al-Taher, 1999).

Figure 2-8 Monthly means of sea level pressure and wind speed from 1985 to 2012

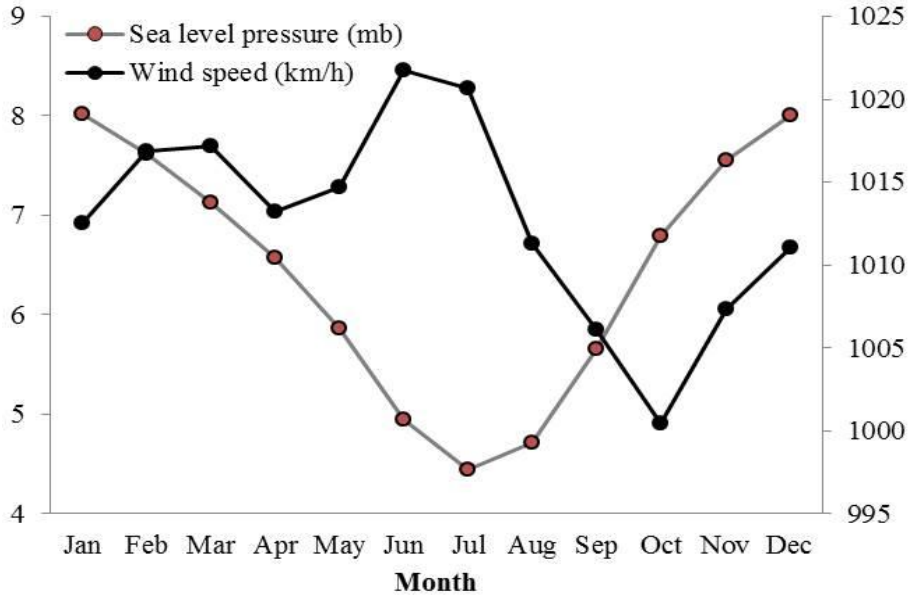

Source: (Presidency of Meteorology and Environment, 2011).

The region is also affected by the extension of the Atlantic sub-tropical high pressure systems, which extend eastward and cover the northern part of Africa and the Red Sea (Figure 2-9). It is also influenced by low pressure regions that affect the Arabian Gulf waters. Based on these pressure distributions, the Arabian Gulf region, of which the study area is a part, receives continental and relatively cold winds from the middle of Asia in the winter (Al-Taher, 1999). Figure 2-8 indicates that the monthly mean wind speed was 1.68 ms^{-1} in November and 2.13 ms^{-1} in March over the period 1985-2012. It is also important to note that the pressure regions

mentioned above result in north and northeast winds that are dry and cold during this season. These are interrupted by changes caused by storms coming from Icelandic low pressure centre via the Mediterranean (Judah, 1989). Al-Taher (1999) report that the wind direction in Saudi Arabia during the winter is changeable, but is generally north-easterly. These winds bring cool winds over Saudi Arabia, especially the eastern region, which includes the study area. The wind direction may shift to become northerly as a result of low pressure centred on the Mediterranean, the Black Sea, the Red Sea and the Arabian Gulf. The Arabian Gulf borders the study area to the east for about 70 km (Humaidan, 1980).

Figure 2-9 Sea level air pressure means in January

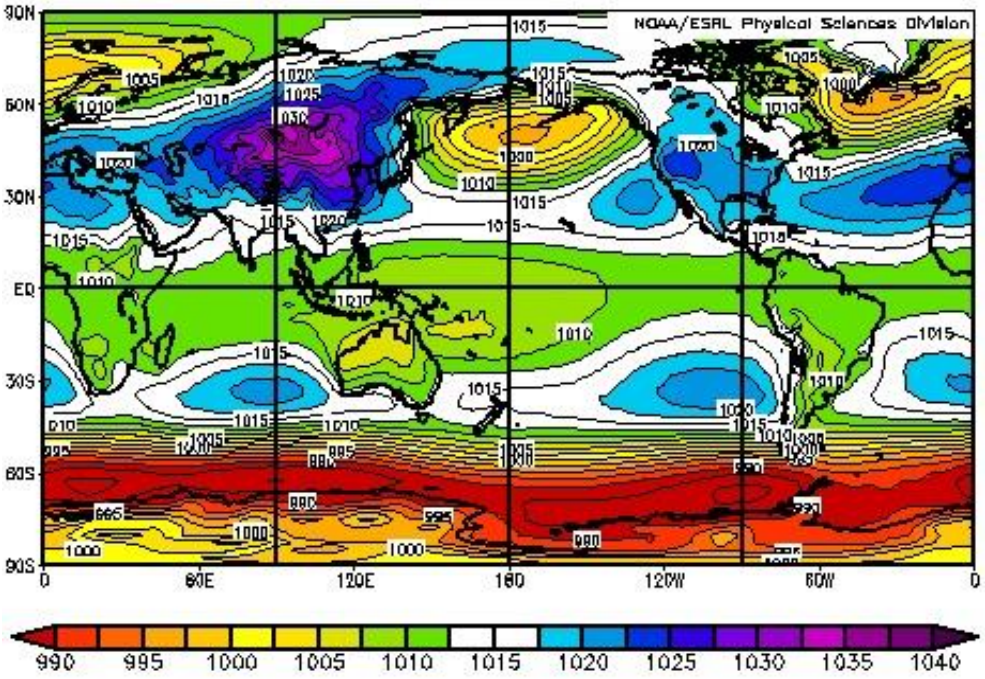

Source: (Kalnay *et al*., 1996). Image provided by the NOAA/ESRL Physical Sciences Division, Boulder Colorado from their Web site at http://www.esrl.noaa.gov/psd/

2.4.1.4.2 Pressure systems and winds in the summer

High pressure regions in the study area start to be replaced with low pressure regions by the end of March. The study area comes under the influence of low air pressure (less than 1012 mb) from April to October (Al-Taher, 1999). The pressure is lowest during July and August; the average pressure reached 996 mb during July 2012 (Figure 2-10).

One of the key low pressure zones in the region is the seasonal Indian low which appears in July. In a similar way, the region is affected by high pressure centred in the centre of the Atlantic, sometimes extending to the southeast of Europe and the east of the Mediterranean. This high pressure area causes an acceleration in the northwest winds and the occurrence of sand and dust storms (Al-Taher, 1999). The effect of the tropical low pressure system may extend to affect the study area, reaching the southern parts of the Arabian Peninsula. During this season, local low pressure increase the flow of dry air, dust, and sands from the Rub-Alkhali desert (Empty Quarter) to the south (Judah, 1989).

Figure 2-10 Sea level pressure mean in July

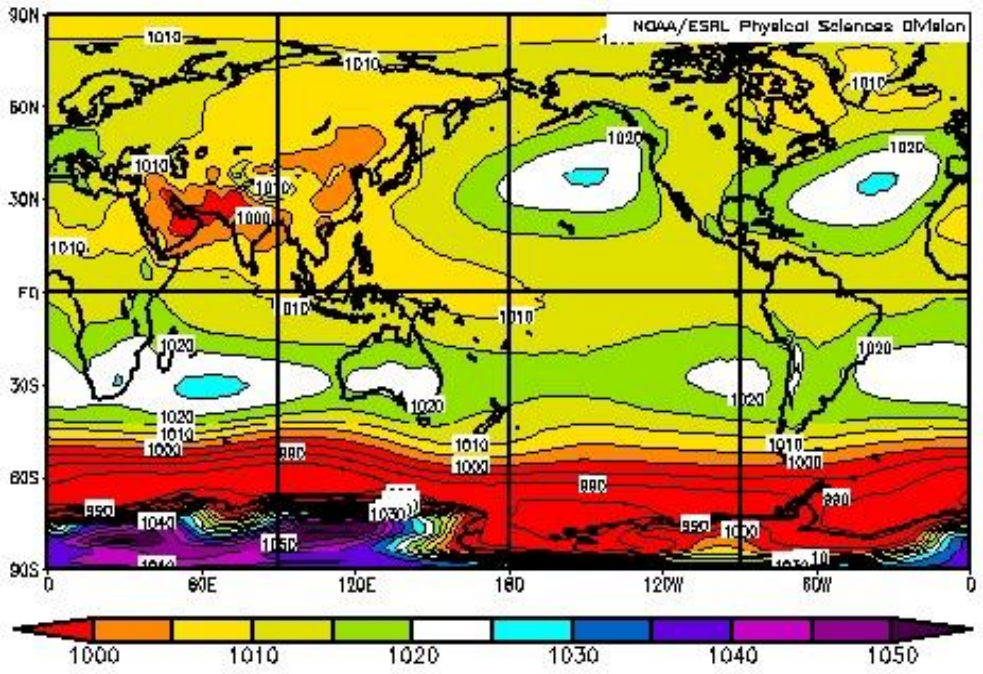

Source: (Kalnay *et al*., 1996). Image provided by the NOAA/ESRL Physical Sciences Division, Boulder Colorado from their Web site at http://www.esrl.noaa.gov/psd/

2.4.2 Rainfall

Al Ahsa oasis located in the region of lowest rainfall in Saudi Arabia. The rainfall total varies greatly from year to year. For example, the annual total rainfall in 1995 was recorded as 266 mm while in 2008 it was only 14 mm (Figure 2-11). The mean annual rainfall over the years 1985–2012 was 85 mm. Most of the rain falls in the winter and spring seasons. The monthly mean rainfall for the winter and spring seasons over the period 1985–2012 were 6.02, 20.86, 15.05, 10.92, 15.81 and 12.71 mm for November, December, January, February, March

and April, respectively (Presidency of Meteorology and Environment, 2011). The monthly mean for the summer and autumn seasons over the same period were 0.53, 3.15, 0.01, 0.05, 0.08 and 0.00 mm for October, May, June, July, August and September, respectively (Figure 2-12).

Figure 2-11 Annual total rainfall for the period from 1985 to 2012

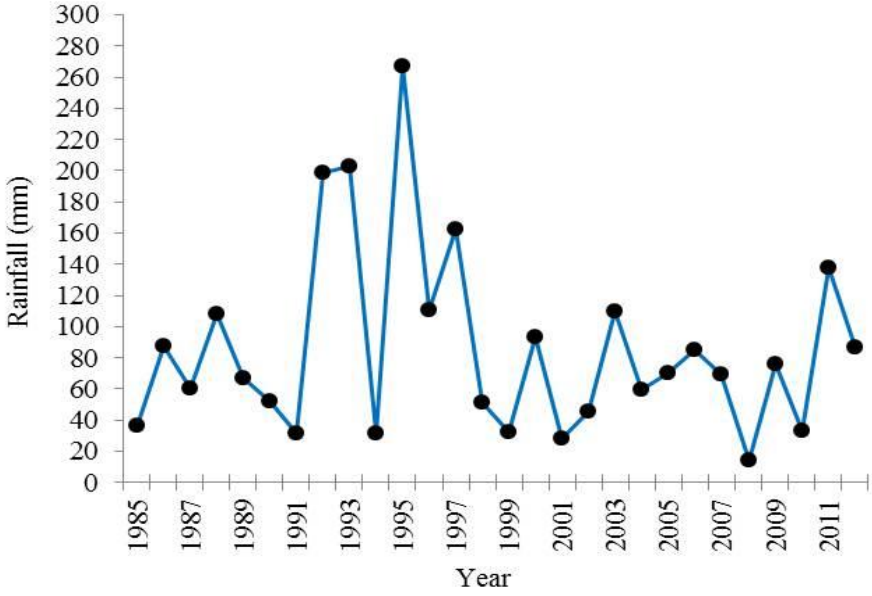

Source: (Presidency of Meteorology and Environment, 2011).

Figure 2-12 Monthly mean total rainfall from 1985 to 2012

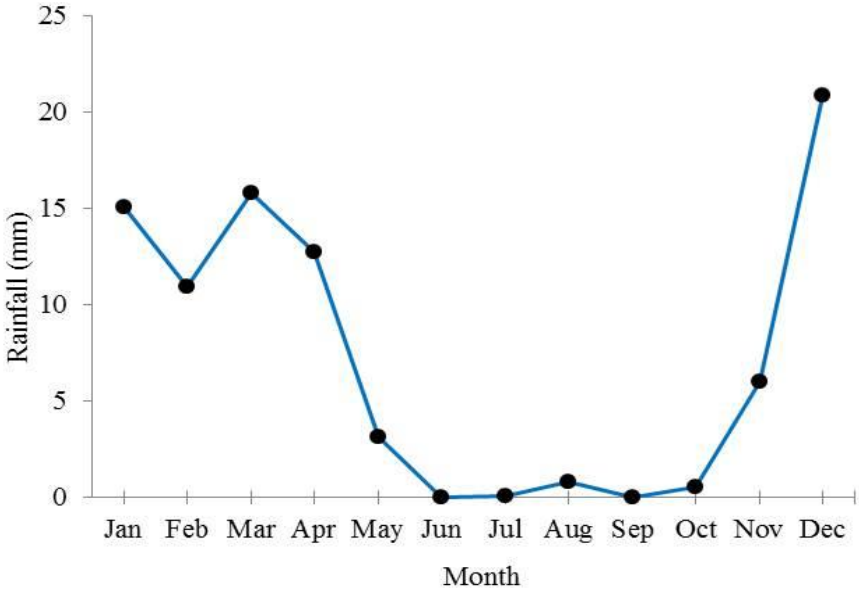

Source: (Presidency of Meteorology and Environment, 2011).

2.5 **Population**

Al Hofuf, Al Mubarraz, Al Omaran and Al Uyon are the principal large cities in the oasis area, with approximately 48 additional villages scattered throughout the 320 km^2 area (Humaidan, 1980). The population of the East province of Saudi Arabia, (where the study area is located), and the Al Ahsa oasis area has grown rapidly since 1972. According to the 1974, 1992, 2004 and 2010 population censuses, and several demographic research bulletins, the population of Saudi Arabia grew from 7 million in 1972 to 27 million in 2010. Similarly, in the eastern province of Saudi Arabia the population grew from 2 million in 1992 to 4 million in 2010. The population of the study area itself grew from 244,000 in 1974 to 937,000 in 2010 (Al-Taher, 1999, Ministry of Economy and Planning, 2010). Figure 2-13, Figure 2-14, and Figure 2-15 show the population growth in Saudi Arabia, the East province and the Al Ahsa oasis area, respectively.

Figure 2-13 Population of Saudi Arabia 1972–2010

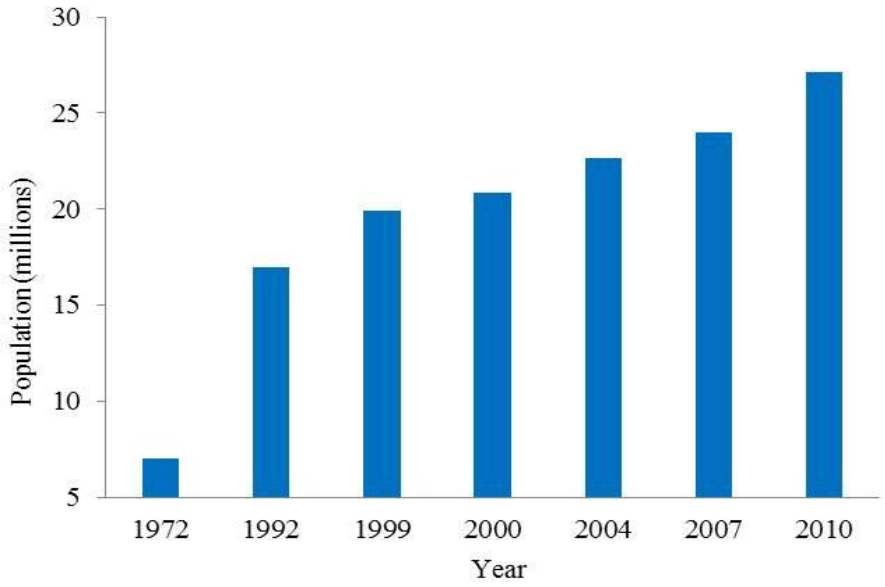

Source: (Ministry of Economy and Planning, 2010).

Figure 2-14 East Province population 1972–2010

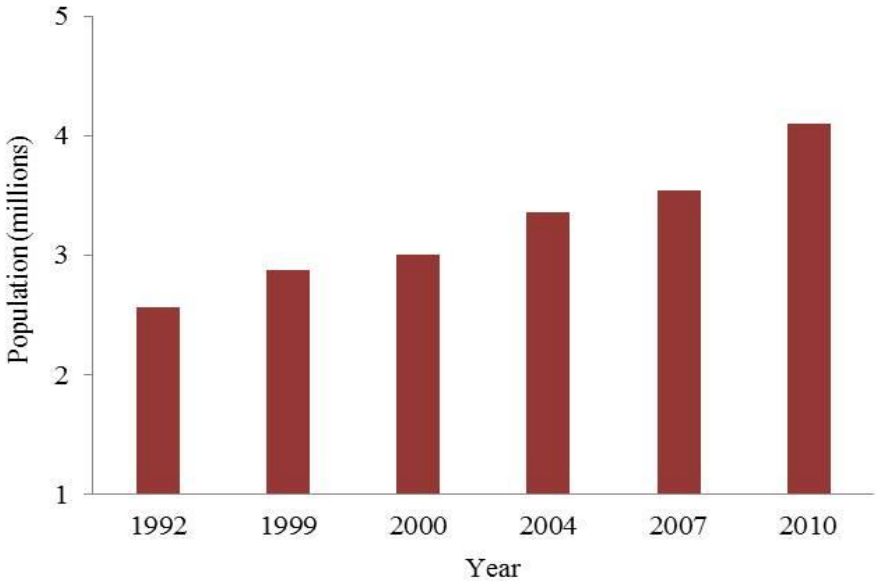

Source: (Ministry of Economy and Planning, 2010).

Figure 2-15 Al Ahsa oasis population from 1905 to 2010

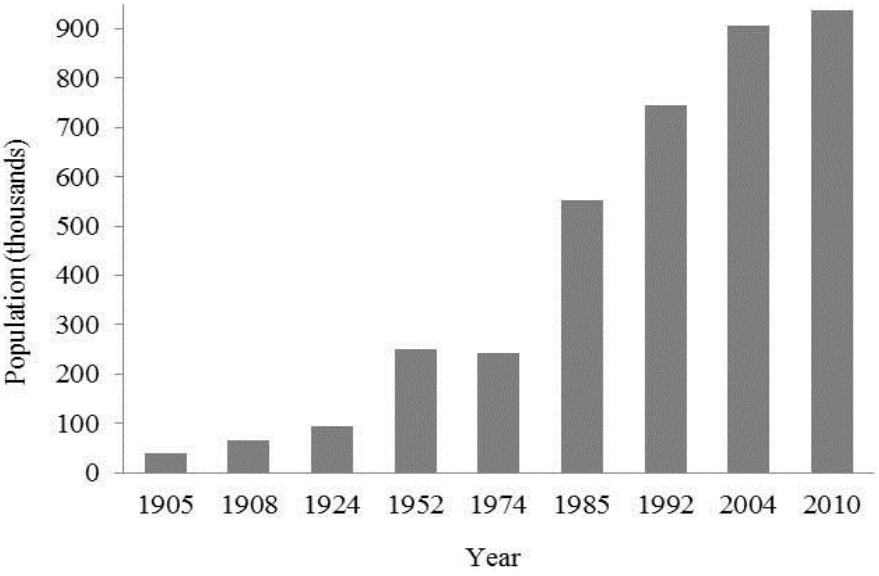

Note: 1905 to1952 figures are estimated based on demographic research bulletins and previous studies (Al-Taher, 1999). 1974–2010 are based on official population censuses and demographic research bulletins

2.6 **Variables affecting the thermal characteristics of the study area**

Over the last sixty years, urbanisation has been a common phenomenon across almost every Middle East country, including Saudi Arabia, with the rapid growth of settlements, towns and cities (Al-But'hie and Eben Saleh, 2002). Since the discovery of oil in 1938, modern

urbanisation came to Saudi Arabia and Al Ahsa, with developments in the fields of education, business, health care and politics (Al-Mubarak, 1999). Several cities in the eastern province of Saudi Arabia, such as Jubail, Yanbu and Abqaiq, grew rapidly over a short period of time, and became some of the biggest industrials cities in the world. This development has an effect on the cities and the villages within the study area, leading to changes in land use (Al-But'hie and Eben Saleh, 2002).

As has been mentioned previously (Chapter One), the recent changes in land cover and use may have a key influence on air and surface temperature in cities around the world (Hu and Jia, 2009, Kim, 2009, Laras et al., 2012). Further studies are required to examine the impact of changes in land cover and use on the thermal environment as a result of developing residential, commercial, and industrial patterns within the study area.

The land use in Al Ahsa can be classified into five main classes: (1) residential; (2) agricultural; (3) recreational; (4) industrial; and (5) commercial (Figure 2-16). Agriculture accounts for most land use in the study area. Arable land in the oasis area covered about 20,000 hectares in the early 19th century. This has changed over time, with 8000, 7070, 5907, 7096, 10,351 and 8000 hectares being used for this purpose in the years 1963, 1968, 1974, 1980, 1985 and 1990, respectively (Al-Taher, 1999). Agricultural areas have been replaced by other land use, such as residential, industrial and commercial. It can be seen by comparing data from 1987 and 2011 that the number of licences issued to open new shops (e.g. grocers, general businesses, industrial, auto-maintenance and petrol stations) has increased in the Eastern Province of Saudi Arabia (Ministry of Municipal and Rural Affairs, 2013) (Figure 2-17). This increase indicates that these activities might have a direct and indirect effect on the local thermal pattern driven by the land use changes during that period.

Figure 2-16 Main land use in the Al Ahsa oasis area

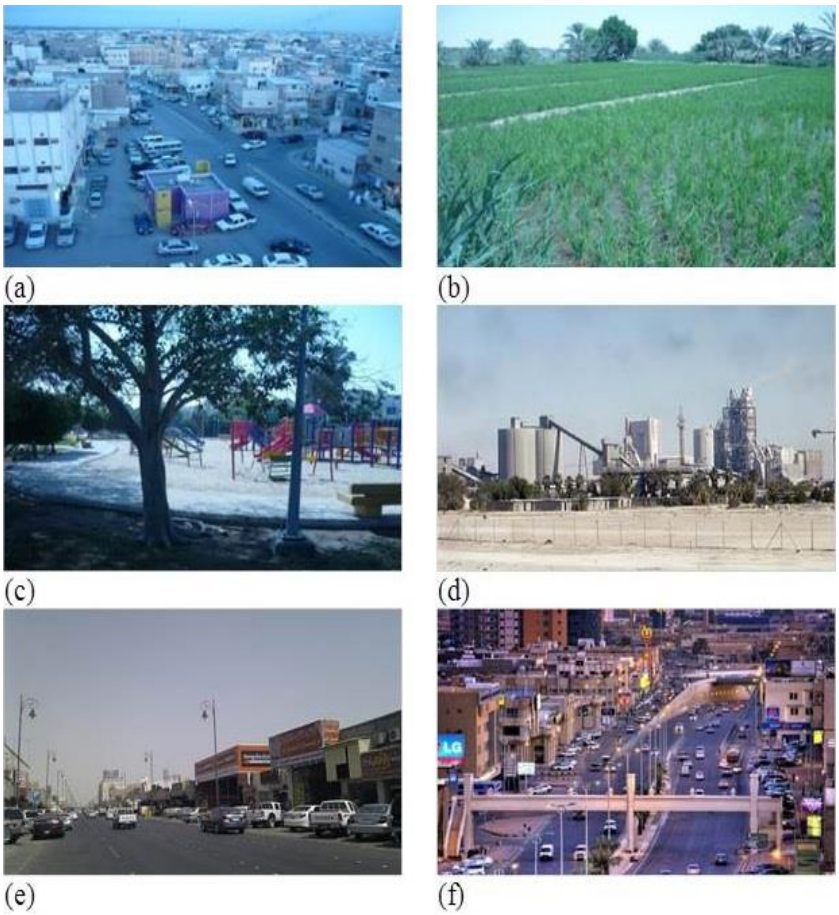

Note: (a) Al Mubarraze city centre (residential), (b) Rice field (agriculture), (c) Mahasan park (recreational), (d) Cement factory (industrial), (e) and (f) Main street (commercial).

Figure 2-17 Number of licenses issued by the Ministry of Municipal and Rural Affairs to open new shops in the Eastern Province of Saudi Arabia for the years 1987 and 2011

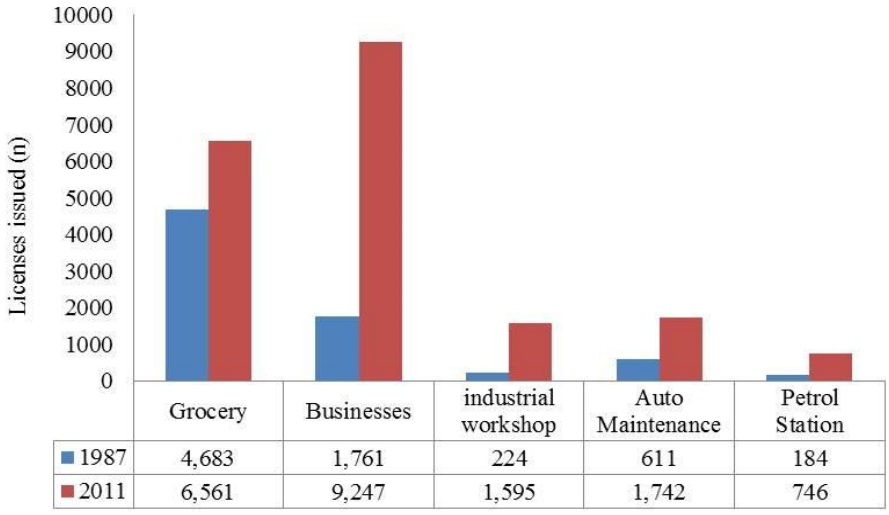

	Grocery	Businesses	industrial workshop	Auto Maintenance	Petrol Station
1987	4,683	1,761	224	611	184
2011	6,561	9,247	1,595	1,742	746

Source: (Ministry of Municipal and Rural Affairs, 2013).

In addition, population density, housing, traffic, air conditioners, power consumption and fossil fuel use have had an impact on the thermal environment in the cities (Shahmohamadi *et al.*, 2010). The general movement of the population from the suburbs and villages to the urban areas and cities has led to acceleration in urbanisation and an increase in city populations. The relationship between the intensity of urban heat islands and city size is examined by Oke (Oke, 1973, Oke, 1982). The density of population and housing in the study area is highest in the city centre of the capital Al Hufof and in the second major city Al Mubarraze.

The shape of houses, as well as their height and roof types, varies across Al Ahsa oasis. Figure 2-18 shows the different densities and heights of the housing in different parts of the study area. Figure (a1) shows the random planning with narrow streets and metal roofs that exists in the centre of the city of Al Mubarraze. In contrast, (b1) and (c1) indicate the lower housing density in the suburbs of the city, with tiled roofs, different heights and a modern planning shape.

Figure 2-18 Different types and densities of housing in the study area

Note: (a1), (b1) and (c1) represent Google views. (a2), (b2) and (c2) represent digital images for the same area.

Moreover, the sky view factor as mentioned in Chapter One is one of the most important explanatory variables for estimating the UHI intensity. There is a strong relationship between the maximum observed UHI intensity and the mean value of the sky view factor in the central part of the city (Oke, 1981). The study area has different shapes of houses and streets and different height of buildings that might influence the sky view factor and the wind regime and have an effect on the formation of the local UHI. Figure 2-19 shows the different houses and streets in the old and new city centre which affect the local climate and contribute to the local UHI.

Figure 2-19 Different types of houses and streets in the old and new city centre of the study area

(a) (b) (c) (d) (e) (f)

Note: (a) and (b), narrow streets with less sky view in the old city centre, (c) and (d) wide streets and different height of buildings in new residential area, and (e) and (f) an example of the high buildings of the study area.

Most of the buildings in the study area were built using concrete for beams and bricks for the walls. However, the building roofs varied. The four main roof types are tile; marble, metal and concrete (Figure 2-20). Different building materials will affect the heat budget of the city as they absorb the heat during the day and reemit it overnight (Shahmohamadi *et al*., 2010). The thermal conductivity of the major building materials in Saudi Arabia have been studied and compared to the results with the data reported in the handbooks. The study used seven types of clay bricks, one type of sand lime bricks, five types of concrete blocks and one type of prefabricated. The results of this study suggests that although the thermal conductivities of these materials lie within the range of the values reported in the handbook, these materials are classified in the high side range. The study recommends that as the thermal conductivity of these materials increase with the material temperature, it is more appropriate to use higher values when designing buildings and air-conditioning systems in hot countries like Saudi Arabia (Abdelrahman et al., 1990). A simulate investigation of the different buildings materials used in a typical residential house, and their effects on energy consumption and air conditioning systems, was carried out in Saudi Arabia. The study found that more than half of the total peak cooling load establishes the thermal transmission through the walls and roof in the base house. Also, the study found that houses built with gypsum blocks consumed up to 13% less energy than a basic house (Ahmad, 2004).

Figure 2-20 Different types of roofs in the study area

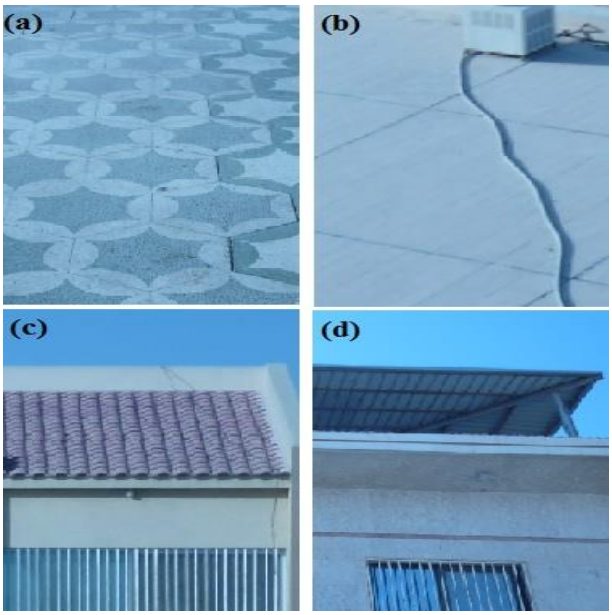

Note: (a) Marble, (b) Concrete, (c) Tile. (d) Metal.

2.7 **Summary**

The study area of Al Ahsa includes the largest oasis in Saudi Arabia; one of the largest oases in the world. The importance of Al Ahsa relates to its geography, with more than three millions palm trees and thousands of spring wells (Al-Taher, 1999). In addition, there are hundreds of oil and gas fields located in the Al Ahsa oasis area. The Al Ghawar oil field, located in the southwest of the study area, is the largest oil field in the world (Edgell, 1992).

In recent years, the study area has faced several geographical problems such as sand dune movements, increasing soil salinity, shortening of the optimal growing season for some local crops and a decrease in available ground water (Sharaf, 1997). All of these problems might be linked to the increasing air temperature and the urban heat island phenomenon in relation to global warming problem. Moreover, previous studies have determined changes in the land coverage of Al Ahsa, dating back to 2001 (Mufareh, 2002). The study area offers a unique environment for the evaluation of heat islands because of the different land uses previously mentioned. In addition, the use of differing types of roof and building materials in the region which might affect thermal patterns.

Chapter 3: Data Sources and Methodology

3.1 Introduction

The study of the urban climate requires a variety of data sets and instruments, especially with regard to the examination of urban heat islands. Based on the literature review detailed in Chapter One, the most common approaches used to measure and model SUHI intensity are remote sensing, aerial thermal imaging and fixed weather stations. Each of these methods has advantages and disadvantages. For example, airborne surveys and fixed weather stations provide accurate measurements of air and surface temperature, with a degree of spatial resolution, but can only cover a small area. On the other hand, surface temperature can be estimated over a large area through the use of remote sensing, but only with low temporal and other spatial resolutions (Voogt and Oke, 2003).

This study attempts to use methods with high temporal and spatial resolutions to measure the two types of urban heat islands intensity, SUHI and CLHI, with relation to land cover in an arid region such as Al Ahsa oasis. Surface temperature results from the higher-resolution Landsat satellite system, as well as from regional to global sensors, such as the Moderate Resolution Imaging Spectroradiometer (MODIS), were compared with surface temperature measurements obtained during fieldwork in a variety of different land cover classes. This calibration allowed accurate application of satellite and sensor results over a variety of surface types. In addition, the ground results included data for the two selected periods covering both day and night, which helped to provide an accurate temporal scale for this study. In this chapter, data sources and preparation, research procedure and methodology are discussed.

3.2 **Data sources**

Two main sources of data were used in this study; that obtained from fieldwork and that acquired from satellites. Published meteorological data, fixed and mobile weather station results, and thermal and satellite images were all used. The following instruments were used to collect the data: five HOBO data loggers, a Global Positioning System sensor (GPS Garmin Oregon 300), a laptop and a thermal camera (FLIR Systems P65), provided by Durham University, Geography Lab. What follows is a description of the data sources used and the preparation for the study.

3.2.1 Published meteorological records

The Presidency of Meteorology and Environment in Saudi Arabia was the first source for study data. The data were obtained directly from the Al Ahsa airport weather station, which is located southwest of the study area outside of the urban zone (Figure 3-1). The data are a daily record of the mean minimum, maximum and overall mean of air temperature, relative humidity and sea level atmospheric pressure, over the last twenty-eight years (1985 to 2012). Wind strength, direction and gust speed, as well as total rainfall, were also obtained from the same weather station for the same period. In addition, air temperature, relative humidity, and wind and gust speed were obtained for selected winter and summer months (21/01/2011–28/02/2011 and 26/07/2011–31/08/2011, respectively). Al Ahsa airport weather station uses a standard mixture of instruments and high accuracy sensors including those for solar radiation, wind speed and direction, air pressure, relative humidity, and dry and wet bulb air temperatures (Figure 3-1). The data were used to create historical graphs of the study area, to compare it with fixed weather station data, located in the urban area and to validate satellite data.

Figure 3-1 Al Ahsa airport weather station location

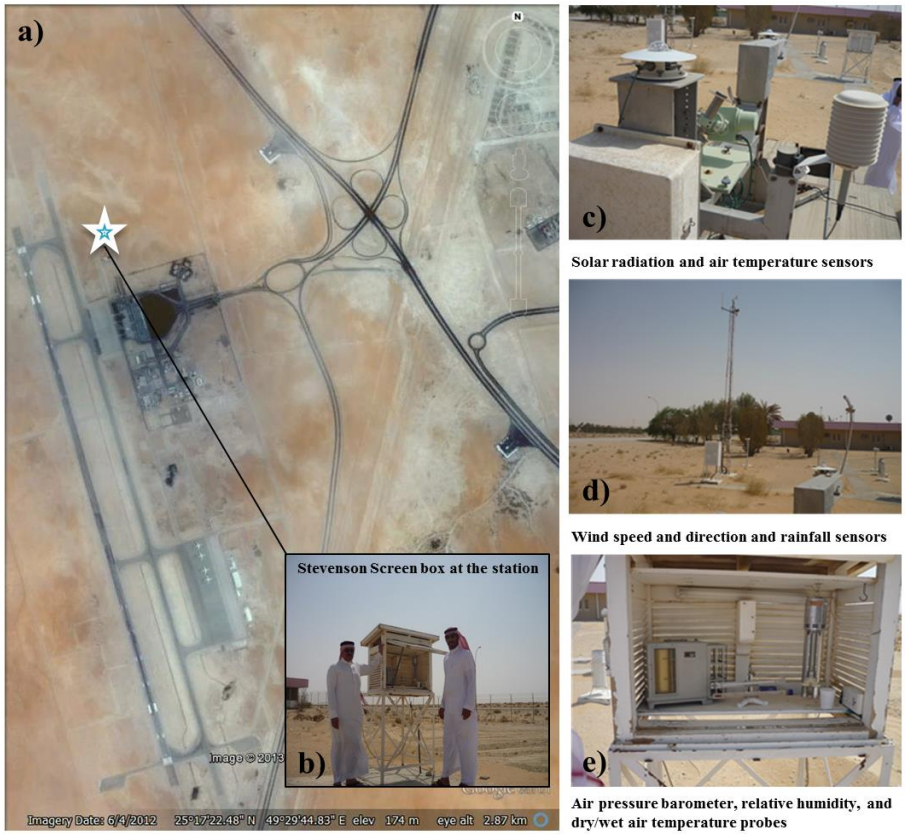

Source: (a) Google Earth and (b), (c), (d), and (e) were taken during fieldwork in August 2011.

3.2.2 Fixed weather station data

Five fixed weather stations were established in this study under standard conditions (Skye Instruments Limited, 2013). They were all built on flat open areas, with radiation shields protecting the sensors from direct sunlight. The air and relative humidity sensors were mounted at a height of 1.5 m (Oke, 1973), while the surface temperature probe was placed directly on the ground and shielded from direct sunlight with a small piece of wood. This arrangement was tested during the pilot fieldwork and found to be a satisfactory data collection method (Escobedo, 2014). The wind-speed probe was mounted level or slightly above the highest surrounding object using an 11 m extension cable. The farm wind-speed probe was placed above the level of surrounding palm trees, which were about 8 m high.

The locations of the fixed weather stations were selected according to the main land cover/use existing in the study area, at secure sites. Pilot fieldwork was therefore required to find suitable locations and arrange with local government offices for the establishment of these micro-

stations. The selected locations were designated as ‘farm’, ‘factory’, ‘city centre’, ‘sabkha’ and ‘park’ (Figure 3-2). The purpose of establishing five fixed weather stations were: (1) to collect data from the main land cover types found in the study area; (2) to compare the data with the only weather station, which is located outside the urban area and; (3) to help calibrate satellite observations and mobile measurements made during the study period.

The data were collected by five small purpose-built weather stations (HOBO Data Loggers), equipped with three sensors and one radiation shield, provided by Durham University, Geography Department Lab. Figure 3-3 and Figure 3-4 show one of the fixed-weather stations (farm site), including the data logger and sensor specifications. The thermometer was mounted at a height of 1.5 m (Oke, 1973), in common with the airport weather station sensor, and fitted inside a radiation shield. The surface temperature sensor was shielded from direct sunlight by a piece of wood. Hourly air and surface temperatures, relative humidity, wind and gust speed results were collected over a sample winter and summer period (21/01/2011–28/02/2011 and 26/07/2011–31/08/2011, respectively).

Figure 3-2 Fixed weather stations locations in the study area.

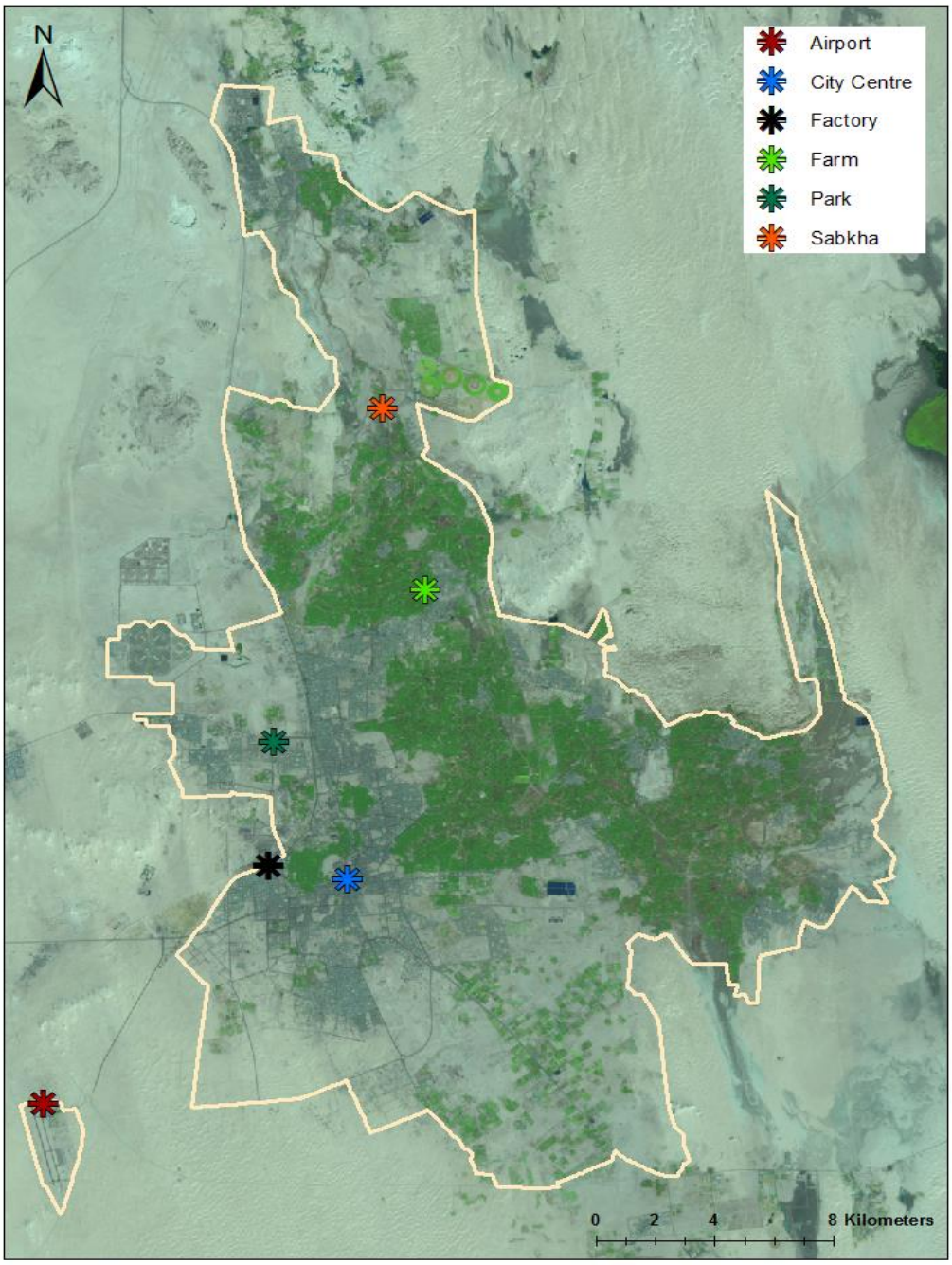

Figure 3-3 HOBO data logger with general specifications

Operating Range	-20° to 50°C with alkaline batteries -40° to 70°C with lithium batteries
Sensor Inputs	Up to four smart sensors (including multiple parameter sensors)
Memory	512K non-volatile flash data storage
Logging Interval	1 second to 18 hours, user-specified interval
Time Accuracy	0 to 2 seconds for the first data point and ±5 seconds per week
Logger Start Modes	Immediate, push-button, or delayed start options
Environmental Rating	Weatherproof, with Gore™ Vent for deployment in harsh weather conditions

Modified from (Onset Hobo Data Loggers Company, 2013).

Figure 3-4 Farm fixed micro-station and instrument specifications

ID	Sensor	Measurement Range	Accuracy	Resolution	Response Time
(b)	Air temperature and RH	Temp: - 40 °C to 75 °C RH: 0 – 100 %	Temp: +/- 0.21 °C from 0 °C to 50 °C RH: +/- 2.5 % from 10 % to 90 %	Temp: 0.02 °C at 25 °C RH: 0.1 % at 25 °C	Temp: 5 minutes in air moving 1 m/sec RH: 5 minutes in air moving 1 m/sec with protective cap
(c)	Surface temperature	- 40 °C to 100 °C	< ± 0.2 °C from 0 °C to 50 °C	< ± 0.03 °C from 0 °C to 50 °C	< 3 minutes typical to 90% in 1 m/sec air flow < 30 seconds typical to 90% in stirred water
(d)	Wind and gust speed	0 to 45 m/s	± 1.1 m/s	0.38 m/s	-

Note: (a) Data logger. (b) Surface sensor. (c) Wind speed probe. (d) Temperature and relative humidity sensor. Images (c), (d), and specifications obtained from (Onset Hobo Data Loggers Company, 2013).

The fixed weather stations were positioned to take near simultaneous measurements of surface and air temperature, relative humidity, and wind and gust speeds across weather gradients to assess the peak times for the formation of urban heat islands and the influence of land cover/use on temperature across the study area. The data were analysed to look for any statistically significant differences between the mean temperatures at the different fixed weather stations. Results from each fixed micro-station were compared both with the airport weather station records and also with the readings from the other micro-stations. The fixed weather data were used to calibrate the satellite images with regard to ground temperature.

3.2.3 Mobile temperature and relative humidity data

Temperature and relative humidity sensors were mounted on a vehicle to collect air temperature and relative humidity data. A system was designed to allow HOBO thermal and relative humidity probes to be placed inside a radiation shield linked to a data logger. The radiation shield was used to stabilise wind flow from all directions when the vehicle was moving. The speed of the vehicle was maintained in the range 15–30 km/h (4.1 to 8.3 m s^{-1}) (Oke, 1973) to further minimise the effect of the wind on the sensors. The system allowed weather and GPS data to be collected simultaneously every 30 seconds. The data logger used HOBO software, installed on a laptop (Figure 3-5).

Figure 3-5 Mobile thermometer and Garmin Oregon 300 GPS device used during the mobile experiments.

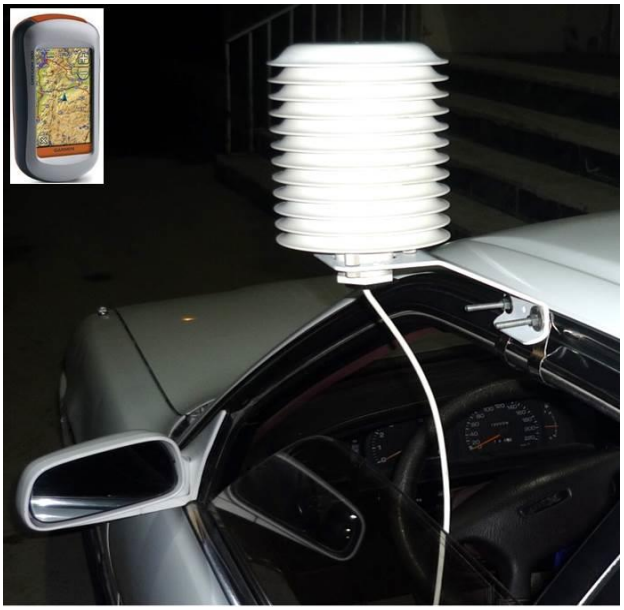

Data were collected twice daily over the winter and summer seasons of 2011 – immediately after sunset and during the night time. The reason for this method of data collection was to identify the variation and peak of CLHI occurrence during the day and night time, and to see how different land cover and use affected the results (Janet, 2005, Van Weverberg et al., 2008). The experiments were therefore repeated at the same times (after sunset and at night) and on the same routes to increase the likelihood of passing the same point each time the measurements were taken. During the fieldwork phase, twenty-six experiments (day and night time) were completed during January and February (Table 3-1) and twenty experiments during August (

Table 3-2). An example of the GPS tracking points from the mobile experiments carried out during the winter season (night and after sunset measurements) is shown in (Figure 3-6).

Table 3-1 Mobile traverses schedule during January and February 2011 (night and after sunset)

27/Jan	After sunset	17:34:15	19:43:45	02:09:30	06:27	17:22
	Night	01:50:52	03:55:52	02:05:00		
02/Feb	After sunset	17:59:50	19:12:12	01:12:22	06:24	17:26
	Night	02:57:37	04:43:07	01:45:30		
06/Feb	After sunset	18:18:43	20:23:13	02:04:30	06:22	17:29
	Night	02:28:53	04:41:53	02:13:00		
08/Feb	After sunset	18:10:38	20:04:09	01:53:31	06:21	17:31
	Night	03:25:37	05:16:35	01:50:58		
12/Feb	After sunset	18:15:52	20:04:22	01:48:30	06:19	17:33
	Night	02:15:50	04:05:50	01:50:00		
15/Feb	After sunset	18:22:38	20:39:38	02:17:00	06:17	17:35
	Night	00:10:35	02:18:05	02:07:30		
18/Feb	After sunset	18:10:27	19:50:57	01:40:30	06:14	17:37
	Night	03:47:45	05:24:15	01:36:30		
19/Feb	After sunset	17:57:32	20:23:02	02:25:30	06:14	17:38
	Night	01:16:05	03:29:35	02:13:30		
20/Feb	After sunset	18:22:15	20:13:45	01:51:30	06:13	17:38
	Night	00:04:49	01:48:49	01:44:00		
21/Feb	After sunset	18:42:38	21:04:08	02:21:30	06:12	17:39
	Night	00:00:39	02:12:09	02:11:30		
22/Feb	After sunset	18:44:14	21:09:14	02:25:00	06:11	17:39
	Night	00:16:05	02:42:35	02:26:30		
23/Feb	After sunset	18:53:53	22:44:23	03:50:30	06:10	17:40
	Night	00:01:14	03:59:14	03:58:00		
24/Feb	After sunset	20:06:04	20:57:34	00:51:30	06:10	17:41
	Night	03:24:43	04:12:43	00:48:00		

Note: Sunrise and sunset times obtained from the weather underground Inc. website: http://www.wunderground.com/

Table 3-2 Mobile traverses schedule during August 2011 (night and after sunset)

Date	Period	Starting time	Ending time	Duration	Sunrise	Sunset
02/Aug	After sunset	18:33:59	20:58:36	02:24:37	05:09	18:27
	Night	01:47:15	04:43:28	02:56:13		
07/Aug	After sunset	19:00:45	20:52:35	01:51:50	05:11	18:23
	Night	02:45:17	04:21:04	01:35:47		
09/Aug	After sunset	19:14:31	21:29:31	02:15:00	05:12	18:22
	Night	02:11:05	04:25:05	02:14:00		
12/Aug	After sunset	18:56:47	21:25:17	02:28:30	05:14	18:19
	Night	02:28:29	04:48:59	02:20:30		
16/Aug	After sunset	19:01:16	20:48:46	01:47:30	05:15	18:16
	Night	02:27:41	04:03:11	01:35:30		
18/Aug	After sunset	18:58:01	21:31:31	02:33:30	05:16	18:14
	Night	02:20:07	04:47:07	02:27:00		
20/Aug	After sunset	18:48:41	21:10:11	02:21:30	05:17	18:13
	Night	02:35:50	04:39:50	02:04:00		
23/Aug	After sunset	18:54:54	21:15:54	02:21:00	05:18	18:10
	Night	02:27:06	04:24:06	01:57:00		
25/Aug	After sunset	18:57:27	20:57:57	02:00:30	05:19	18:08
	Night	02:26:52	04:28:52	02:02:00		
28/Aug	After sunset	18:43:38	19:58:08	01:14:30	05:20	18:05
	Night	02:45:51	04:20:21	01:34:30		

Note: Sunrise and sunset times obtained from the weather underground Inc. website: http://www.wunderground.com/

Figure 3-6 Mobile experiment and GPS tracking points in the winter (night and after sunset traverses)

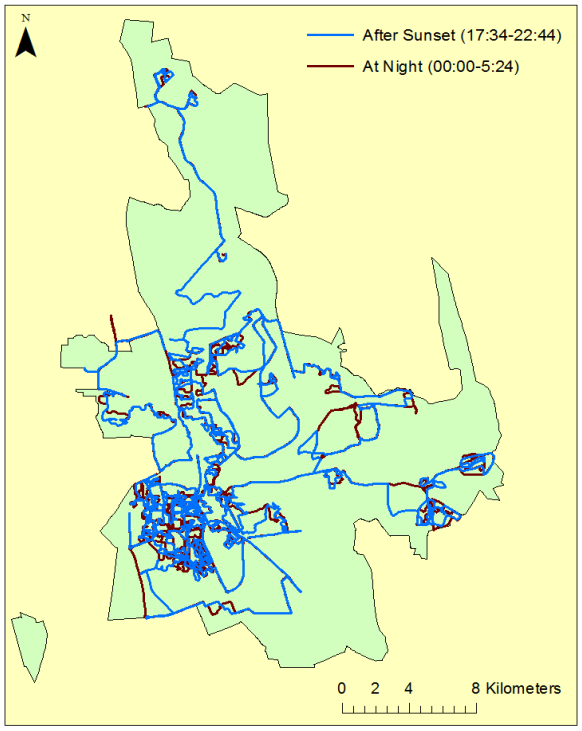

The purpose of mobile data collection was to capture the geographic and temporal patterns of air temperature and relative humidity ranges related to differing land cover/use and to try to synchronize these ground measurements with data from satellites passing over the study area. This would help validate the satellite data and test its accuracy.

3.2.4 Accuracy and uncertainty of ground-based measurements

As mentioned above, six data loggers were used to collect air and surface temperatures, relative humidity, and wind and gust speeds. There are three points which need to be considered when using these data loggers: the accuracy of the sensors, the response time of the sensors, and the influence of the prolonged time period of the mobile traverses. These sensors are not calibrated against each other; however, they are tested by the company and the accuracy of the air temperature is +/- 0.21 and < ± 0.2 from 0 °C to 50 °C for the surface temperature sensors, and +/- 2.5% from 10% to 90% for relative humidity. For more details on the accuracy and respond time of these sensors see Figure 3-4. To more accurately test this conclusion, both mobile logger and fixed weather stations data were compared with each others when they were matched closely in the time and the location. The result of this comparison is mentioned in Chapter 5 section (5.6).

Another issue here relating to the sensors measurements of mobile traverses data is the duration of each traverse and the change of the air temperature and relative humidity within the traverse time. Therefore, errors in measurements might occur because the change in the air and relative humidity within the duration of the traverses. Moreover, errors might be also due to the type of the solar radiation shield used with HOBO data loggers. A recent study by da Cunha (2015) examined the HOBO data sensors in different solar radiation shields and found that the HOBO data loggers are inaccurate when used without shelter or under shelters that do not meet the World Meteorological Organization (WMO) requirements. The study also recommended that the gill-type (multi-plate prototype plastic) shelter is the most sufficient type to be used when measurement the air and surface temperature or relative humidity with HOBO data sensors (da Cunha, 2015).

3.2.5 Remote sensing datasets

Satellites images differ in terms of spatial and temporal factors. Therefore, this study used three different satellite images: GeoEye-1 imagery, MODIS and Landsat Enhanced Thematic Mapper Plus (Landsat7 ETM+). The Landsat data were used in two main analyses to classify the land cover and to derive the surface temperature as it has a 30 m spatial and 60 m thermal resolution. MODIS data were used to provide daily surface temperature figures over the day and night during the study period. Finally, GeoEye-1 imaging was used to classify the different surfaces and roofs to calculate the emissivity values in order to estimate surface temperature.

3.2.5.1 *Landsat 7 ETM+ source and sets*

Landsat 7 was successfully launched on April 15, 1999 from the Western Test Range of Vandenberg Air Force Base, California. Landsat 7 is one of the most accurate Earth observing satellites. Its measurements are very accurate when compared to the same measurements made on the ground. For that reason this satellite sensor has been called "the most stable, best characterized Earth observation instrument ever placed in orbit". The satellite is in sun-synchronous orbit, about 705 km above the earth. It collects data across a 185 km band. It revisits each area every 16 days. The Landsat ETM+ bands 1–5 and 7 are of 30 × 30 m spatial resolution, while the thermal infrared band 6 (10.40–12.50 µm) and band 8 (panchromatic) have spatial resolutions of 60 × 60 m and 15 × 15 m, respectively. The thermal band includes two thermal imagers; low gain (6 L) and high gain (6 H) (Jensen, 2005a).

The satellite mission ran flawlessly until May 2003 when a hardware component failure left wedge-shaped data gaps. Even though the data gaps affect about 78% of the image pixels the data from this satellite are still some of the most geometrically and radiometrically accurate of all civilian satellite data in the world. A number of methods have been developed to fill these gaps and create an image that is suitable for scientific interpretation and analysis. The method that is used to fill the gaps is routinely applied in data pre-processing (NASA, 2013a). Since 2008 the Landsat 7 data has been free to the public and can be downloaded from the United State Geological Survey (USGS) website (USGS Global Visualization Viewer available at http://glovis.usgs.gov/).

Landsat 7 ETM+ images for February and August 2011, with Universal Transverse Mercator UTM projection and covering zone 39 north, were downloaded as free data from the USGS website (Figure 3-7). In addition, some images were obtained from the King Abdulaziz City for Science and Technology – Space Research Institute in Saudi Arabia (Table 3-3).

Figure 3-7 Figure 3 9 USGS global visualization viewer (GloVis)

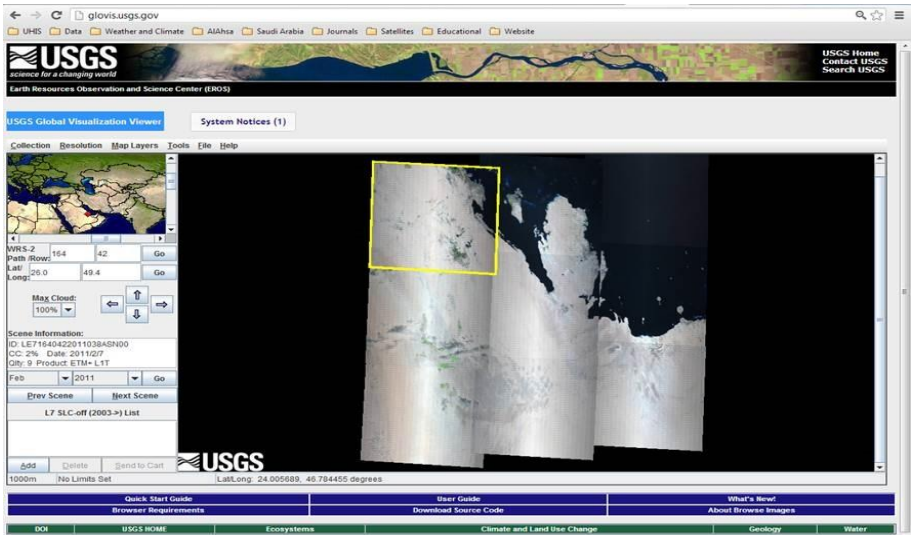

Source: (United State Geological Survey, 2011).

Table 3-3 Landsat 5 TM and Landsat 7 ETM+ information and sources

Sensor	WRS	Acquisition date	Acquisition time (GMT)	Cc	Image source	Spatial resolution
5TM	Path 164 and Row 42	07-30-1984	06:40:08		USGS	Multi-spectral (MS) – 30 m & Thermal infra-red – (TIF) 120 m for Landsat 5TM
5TM		06-15-1985	06:40:59			
5TM		08-16-1990	06:30:51			
5TM		05-31-1991	06:33:34		KACST	
5TM		07-05-1998	06:49:02			
5TM		01-29-1999	06:49:56			
7ETM+		06-30-1999	07:03:34			
7ETM+		01-24-2000	07:03:41	1%		
7ETM+		07-02-2000	07:02:32			
5TM		07-26-2000	06:47:59	10%		
7ETM+		07-05-2001	07:00:15		USGS	
7ETM+		01-13-2002	06:59:39	2%	KACST	Multi-spectral (MS) – 30 m & Thermal infra-red – (TIF) 60 m for Landsat 7 ETM+
7ETM+		06-06-2002	06:59:28			
7ETM+		01-16-2003	06:59:20	62%		
7ETM+		02-01-2003	06:59:26	1%		
7ETM+		05-24-2003	06:59:34			
7ETM+		02-07-2011	07:04:18	2%	USGS	
7ETM+		02-23-2011	07:04:23	5%		
7ETM+		08-18-2011	07:04:17			
7ETM+		05-03-2013	07:06:48			

GMT = Greenwich Mean Time. USGS = United State Geological Survey. KACST = King Abdulaziz City for Science and Technology. WRS = Worldwide Reference System. Cc = Cloud Cover.

3.2.5.2 *MODIS source and sets*

The MODIS was launched in December 1999 and is one of the best satellites in terms of temporal resolution. The MODIS instrument operates on both the Terra and Aqua spacecraft, providing continuous global coverage every 1–2 days. Its detectors measure 36 spectral bands in the range 0.405–14.385 μm. The first two bands (1–2) have a resolution of 250 m; five bands (3–7) have a resolution of 500 m. The remaining bands (8–36) have a resolution of 1000 m (Roy et al., 2002, NASA, 2012). The MODIS data are, (MYD11A1) and (MYD021KM), also available as free public data which can be downloaded from the USGS website, or directly from Reverb, GloVis, Data Pool, or the Earth Explorer search tools. Daily images from February and August 2011 were obtained from the GloVis data search website to estimate the surface temperature and calculate the UHI intensity in daily bases. (Figure 3-7). Also, the daily MODIS data were examined with the land cover types either statistically or graphically to investigate the effect of land cover in daily cycle.

3.2.5.3 *GeoEye-1 image source and sets*

The third set of satellite images used in this study is GeoEye-1 images. The satellite was launched in September 2008 from Vandenberg Air Force Base in California, and has the world's highest spatial resolution. GeoEye-1 imagery has a resolution of about 0.5 m, which enables an object on the ground of approximately 0.41 m × 0.41 m to be seen in four bands (Jablonsky, 2013). Table 3-4 shows more details and specifications for GeoEye-1 images. The image that used in this study was obtained from the Al Ahsa Municipality in Saudi Arabia. The image obtained in 2012 only included three bands; blue, green and red. The image was used to provide high resolution details of surfaces and roof covers so that emissivity could be calculated and the urban heat islands of the study area modelled.

Table 3-4 GeoEye-1 image specifications

Imaging mode	Panchromatic	Multispectral
Spatial resolution	0.41 m GSD at Nadir	1.65 m GSD at Nadir
Spectral range	450–900 nm	450–520 nm (blue); 520–600 nm (green); 625–695 nm (red); 760–900 nm (near IR)
Swath width	15.2 km	
Off-Nadir imaging	Up to 60 degrees	
Dynamic range	11 bits per pixel	
Mission life	Expectation > 10 years	
Revisit time	Less than 3 days	
Orbital altitude	681 km	
Nodal crossing	10:30 am	

Source: (LAND INFO Worldwide Mapping, 2013). GSD = *Ground sample distance.*

3.3 **Data processing packages**

Several software packages were used to process the study data. Fieldwork data was collected by HOBO data loggers using Hobo ware software and processed by GPS Utility, ArcGIS 10 software, Stata 12.1 and Excel software. The satellite images were processed in three different remote sensing packages; ERDAS Imagine 11.0, Environment for Visualization Images (ENVI) 5.0 and Definiens Professional 5.0. Finally, thermal research basic software was used to analyse the thermal images of different land cover and sites.

3.3.1 GPS utility 5.03

GPS utility software is useful for mapping, managing and manipulating GPS waypoints, routes and track information. It is also used to transfer data between GPS devices and PCs. The program can convert between many different map data and coordinate formats. In addition, the software supports a variety of import and export file formats (GPS Utility, 2013). The software was used to read the GPS points and convert them to a suitable format to be opened on ArcMap software, where it could be analysed.

3.3.2 Stata version 12.1

Stata is a statistical software package created in 1985 by the StataCorp Company. It is one of the most powerful statistical software packages with regard to the management and analysis of data. Stata version 12.1 was used in this study to analyse the distribution of the study data and run specific analyses and tests. Fixed weather station data, mobile experiment data and satellite

pixel values were analysed using the Stata software. Stata and Excel software were additionally used to create study graphs and run some statistical tests, e.g. Linear Regression and two-way ANOVA analyses.

3.3.3 ArcGIS

ArcGIS 10 software includes a set of tools designed for geographic analysis, data editing, data management, visualization and geo-processing. The software has three applications; ArcMap for map production and analysis; ArcCatalog for managing data and; ArcToolbox for data conversion and analysis. In this study, the mapping, visualization and editing aspects of fieldwork data analysis were performed using ArcGIS software 10. ArcCatalog 10 was used for data management. ArcGIS software was used to convert the GPS data collected during the fieldwork into the shapefile format. The software was also used to prepare the data for spatial analysis by combining data from both the satellite images and fieldwork.

3.3.4 ERDAS Imagine

Earth Resource Data Analysis System (ERDAS 11.0) Imagine software can be used for image mapping, visualization, enhancement, geocorrection and reprojection, including remote sensing analysis and spatial modelling. The software has two methods of data format access; direct access or import and export. In this study, Landsat images were reprojected and geocorrected using the basic image manipulation tools of the ERDAS software.

3.3.5 ENVI

The third software package that was used to process the data in this study was the Environment for Visualization Images (ENVI) software. The software allows the user to access and work with images in different formats and from a variety of sources. ENVI software was used in this study to analysis MODIS and Landsat data in estimating surface temperature. In addition, the software was used to process unsupervised and supervised classification methods for different satellites images.

3.3.6 Definiens Professional software

Definiens 5.0 is one of the best software packages for classifying different images based on an object-oriented technique using a segmentation method, instead of single pixel classification. In this study, this software was used to classify the Landsat 7 ETM+ satellite images based on the colours and textures of the images objects. This enabled the classification of different surfaces to help in developing models of surface urban heat island SUHI.

3.4 Data pre-processing and analysis

3.4.1 Micro-station data

As mentioned before, the ground data were collected from fixed micro-stations, the airport weather station and from the mobile experiments during the winter and summer months in 2011. The data that were collected at the five fixed weather stations were exported from the HOBO data logger format into Excel format, using the option available in the HOBO software. The data represent hourly measurements of the air and surface temperature and relative humidity. However, because there was only one wind speed probe available, this sensor was moved between stations every five days during the fieldwork period. The data loggers were disconnected while the wind sensor was installed or removed, but restarted again within an hour to ensure continuity of the data logger record. Every time this process was repeated the data were exported and saved in Excel format.

The downloaded fixed weather station data were organized using Microsoft Excel 2010, using the same methods that were employed for the airport weather station data. Descriptive statistics such as hourly means and standard deviations were calculated to allow comparison of the selected sites. The most commonly used technique to detect an urban climatic effect is to measure the differences in the temperature between representative urban and rural weather stations (Yagüe et al., 1991, Jauregui et al., 1992, Karaca et al., 1995). In this study, the airport weather station was used as a control because of its location outside the city boundary while the fixed weather stations (city centre, sabkha, park, farm, and factory) were used to represent different land cover types within the urban area. The hourly means of air temperature, surface temperature, relative humidity, and wind and gust speed from all the fixed weather stations,

including the one at the airport, were analysed to measure and assess the presence and intensity of any CLHI effect.

3.4.2 Statistical modelling

3.4.2.1 *Normality test of the data distribution*

It is most important to test the statistical distribution of primary data to evaluate central tendency and distribution of the data in order to select the most appropriate statistical procedures for further analysis (parametric or non-parametric). A parametric method assumes the data are normally distributed, while non-parametric statistics can be more appropriate when the data do not meet the distribution requirements of parametric methods (Altman and Bland, 2009). A good complete normality analysis should consider the use of both procedures plots and statistical tests (D'Agostino et al., 1990).

Using the Stata 12.1 package, the probability distribution plots of air temperature, surface temperature, and relative humidity during summer and winter seasons were created. Air temperature, surface temperature, and relative humidity either during the winter and summer seasons showed that these data are not normally distributed. There is some skewness seen in the tails of these data distributions. Moreover, the Stata 12.1 package was used also to test the data normality statistically. For a sample of size n; $x_1, x_2, \dots\dots\dots, x_n$ the sample estimates of skewness ($\sqrt{\beta_1}$) and kurtosis (β_2) are respectively (Pearson, 1895):

$$\sqrt{b_1} = {m_3}/{m_2^{3/2}}$$

$$\text{and } b_2 = {m_4}/{m_2^2}$$

$$\text{where } m_k = {\sum (x_i - \bar{x})^k}/{n} \text{ and } \bar{x}(sample\ mean) = {\sum x_i}/{n}$$

As descriptive statistics values of $\sqrt{b_1}$ and b_2 close to 0 and 3, respectively, indicate that the data are normally distributed. D'Agostino et al. (1990) suggest these values as 0 and $3(n-1)/(n+1)$ to more precisely estimate normality. Values different from these estimates of skewness ($\sqrt{b_2} > 0$) and kurtosis ($b_2 > 3(n-1)/(n+1)$ provide a robust indicators of non-normality.

3.4.2.2 *Non-parametric methods*

Because the study data did not meet the basic conditions of the parametric method such the normality distribution, a non-parametric method was used to compare between the medians of more than two samples to determine whether the samples have come from different populations. The Kruskal-Wallis *H* test was used as a nonparametric statistic to compare more than two populations (Vargha and Delaney, 1998). The sample values of air temperature, surface temperature, and relative humidity were tested by comparing the population group medians instead of one-way analysis of variance (ANOVA) (Davis, 2002). To test the equivalency of air temperature, surface temperature, and relative humidity in different land cover (City centre, Sabkha, Park, Farm, Factory, and Airport) has been derived by Kruskal and Wallis H-statistic (Kruskal and Wallis, 1952):

$$H = \left[\frac{12}{N(N+1)} * \sum_{j=1}^{k} \frac{R_k^2}{n_k}\right] - 3(N+1)$$

where, $R_k = \sum_{i=1}^{n_k} R(x_{ik})$; $R(x_{ik})$ represents the rank of the ith observation in the kth sample. The total number of observations is$N = \sum_{j=1}^{k} n_k$, where $n_k$is the number of observations in the kth sample. H_0 leads rejection for higher values of$H$at $df = k - 1$. If the samples comes from identical continuous populations and n_k are not too small, distribution of Hfollows$\lambda^2(C-1)$, permitting use of readily available tables of λ^2. Post-hoc median comparison between groups was tested when Kruskal-Wallis *H* test gave significant results using adjusted *P* value.

3.4.3 Mobile data

The mobile experimental data, which were collected every 30 seconds using the Garmin Oregon 300 GPS device, simultaneously with the data logger, were downloaded directly from the GPS and data logger devices to the PC in different formats. The GPS data were stored as coordinates points in a GPX format, while the logger saved the air temperature and relative humidity in the HOBO format. The GPS data were opened using the GPS Utility software and then exported as text files. These were then opened using Excel software and exported in Excel spread sheet format. The logger data files were exported directly from the logger as Excel files.

In order to create the shape file, the data logger and GPS points were linked, based on the time of recording, by adding the air temperature and relative humidity as new columns and then saved as Excel files. The Excel files were opened with ArcMap10 software and X/Y information used to incorporate the data into the study area projection. This was then saved in shape file format. Figure 3-8 shows an example of the shape file output. The Figure shows the air temperature and relative humidity at night and after sunset on 2nd February 2011. This process was repeated for all the mobile experimental data collected during the winter and summer seasons after sunset and at night traverses.

Figure 3-8 An example of mobile traverse of air temperature (left) and relative humidity (right) recorded using HOBO and Garmin GPS 300 on 2nd February 2011

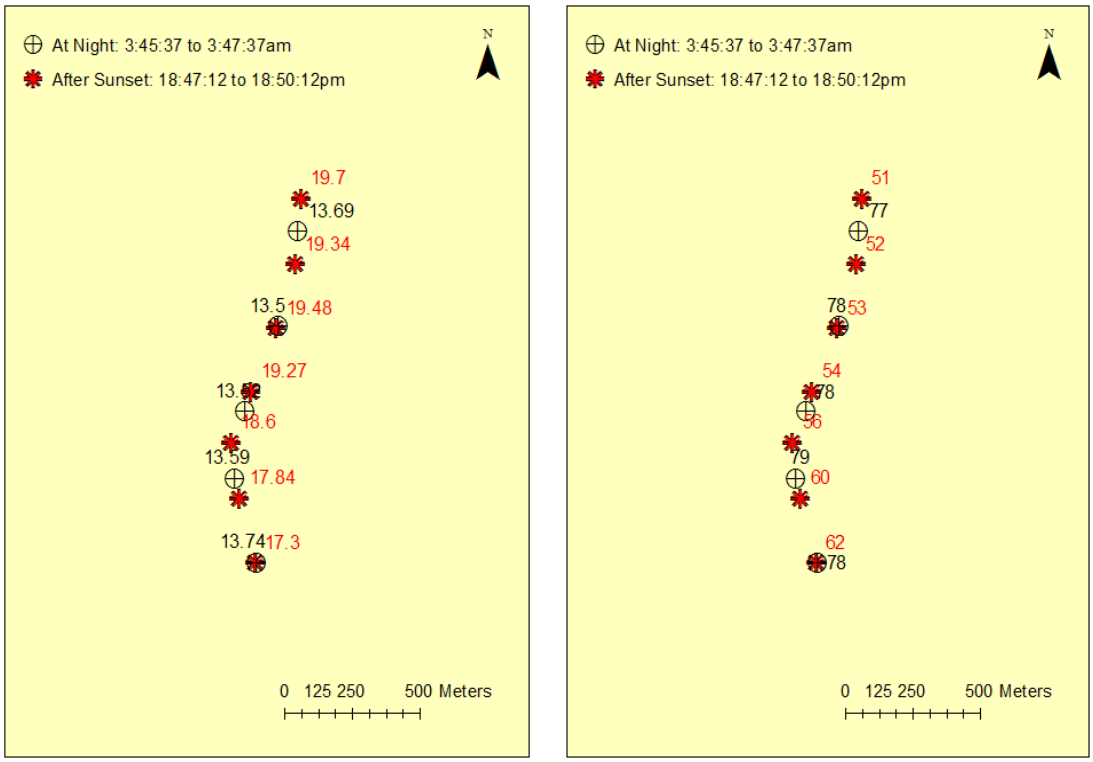

Note: air temperature in (°C) and relative humidity in (%).

The data shown in Figure 3-8 represent mobile points at different distances from each other during the night and after sunset collection runs. According to this shapefile, the distances between the night and after sunset points ranged between 2.23 and 115.43 m. Further analysis was carried out so as to include only the closest points to give more accurate results. Within the ArcMap software, the 'selection by location' option was used to select the points which fell within 35 meters of each other. The 35 meters distance was chosen after conducting several analyses and found to produce more appropriate results. Initially, the after sunset shapefile was

selected as the target layer and the night layer as the source layer for proximity analysis, then vice versa. The selected points from both layers were edited and saved in joint attribute tables. An example of this analysis is shown in Figure 3-9. The Figure illustrates the results of this analysis for part of the second experiment on 2nd February, during the winter at the night and the sunset periods.

Figure 3-9 An example of mobile points which fall within 35 meter of each other for air temperature (left) and relative humidity (right), recorded using HOBO and Garmin GPS 300 on 2nd February 2011.

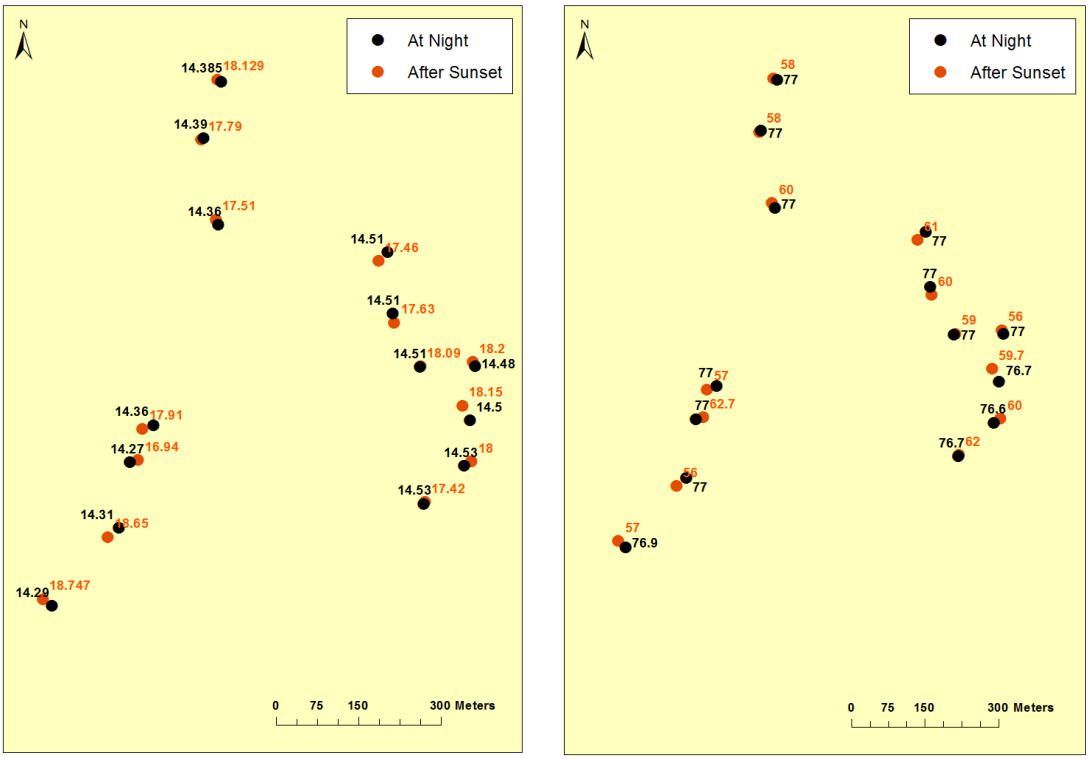

Note: air temperature in (°C) and relative humidity in (%).

The above analysis was applied to all the mobile experimental data collected during both seasons during the night and after sunset periods. Following classification of the land cover types found within the study area, these spatial databases were used to determine the relationship between CLHI and different land coverage.

3.4.3.1 *Calculation of local UHI intensity based on mobile data*

In order to calculate the UHI intensity of the study area Al Ahsa oasis the difference between representative urban and rural station is used to describe the local UHI intensity. This method (ΔT *u-r*) has been identified by (Oke, 1973) and applied in several studies e.g. (Yagüe et al.,

1991, Jauregui et al., 1992, Karaca et al., 1995, Hoffmann et al., 2012). This technique is used to detect the influence of the different land cover and urbanization on the local UHI intensity. The different between the represented mobile data (at night and after sunset) and the airport weather station identified the UHI intensity. For more accurate of measurements, the time of each mobile data is considered to match or at least fall in the same hour of the traverses. All the mobile traverses are overlaid over the classified image map of the study area and extract the value of the land cover of each pointe to investigate the relationship between the different land cover and UHI intensity graphically and statistically.

3.4.3.2 *Interpolation of mobile traverses*

The forty six mobile traverses during the summer and winter are used to calculate the CLHI intensity at the night and after sunset. The mobile data as mentioned in data sources are completed during twenty three days and the average of each traverse is about one and half hour. Therefore, inverse distance weighted interpolation method is used in this step to map the distribution of UHI intensity during these days over the different land cover. The goal of this analysis is to show the distribution of the UHI intensity over the different land cover during the night and after sunset in the study area scale. This method has been used widely by the earth scientists (Ware et al., 1991) to map the UHI distribution such as (Montávez et al., 2000, Vicente Serrano et al., 2005).

3.4.3.3 *Land cover percentage within a MODIS pixel*

The Figure 3-10 shows the major steps followed to calculate the major land cover pixels (30m) within sample spatially located MODIS pixel. Landsat 7 ETM+ 18 August 2011 imagery has classified using supervised maximum likelihood imagery under five major land cover classes; Sabkha, Sand, Urban (built-up area), Vegetation, and Water body. The classification vector of each resultant class has been converted to 30m-pixel raster format which then converted to point data. The points under each land cover classes were spatially estimated using a vector 1km-grid layer which derived from 1km-MODIS imagery to estimate the percentage of each class spatially located within each MODIS pixel size grid.

Figure 3-10 The steps followed to calculate the land cover percentage of MODIS and Landsat 7 ETM+ pixels

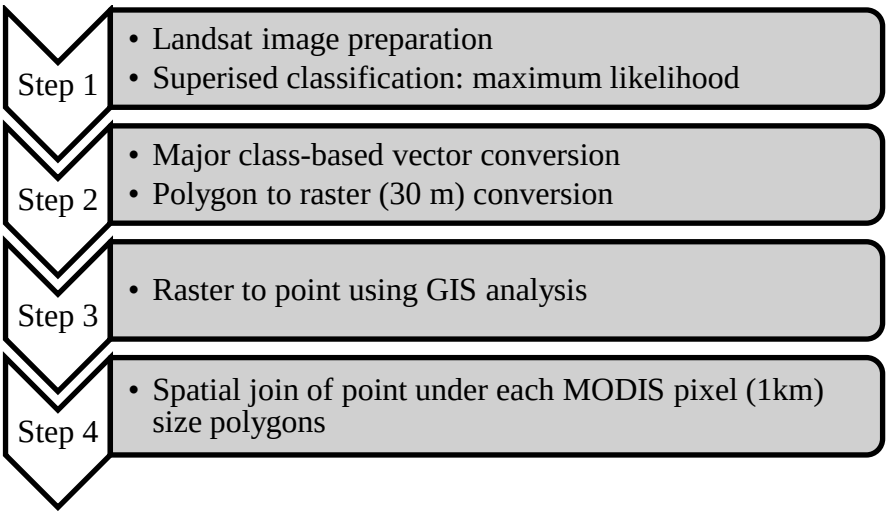

3.4.4 Remote sensing data

3.4.4.1 *Georeferencing of Landsat 7 ETM+ Data*

In order to analyse the remote sensing datasets, it was necessary to ensure that the data were correctly georeferenced, both with respect to the 'real world' and, ultimately, with the GPS datasets. Comparative analysis between ground survey data and thermal imagery data requires spatial accuracy in both datasets (Malleswara Rao *et al*., 1986) and so special emphasis was given to matching spatial locations in both Landsat 7 ETM+ imagery and mobile datasets.

As a result, geometric correction of the Landsat image was necessary, based on the GeoEye image and mobile points, in order to enhance the accuracy and match of both images. Geometric correction was performed using a first-order polynomial transformation on both Landsat 7 ETM+ satellite images in order to achieve data integrity (Figure 3-11). Geometric correction of the August Landsat image was performed using the ground control points (GCPs), which were collected during the fieldwork, as the reference data. GCPs were distributed across the Landsat image of the study area, and used in the correction stage. The February Landsat image was then compared to the corrected August Landsat scene in an image-to-image analysis. In addition, GCPs were selected from across the February Landsat image and then the corresponding reference points identified on the August Landsat image.

Figure 3-11 Geometric correction model used for image geo-correction of Landsat scenes

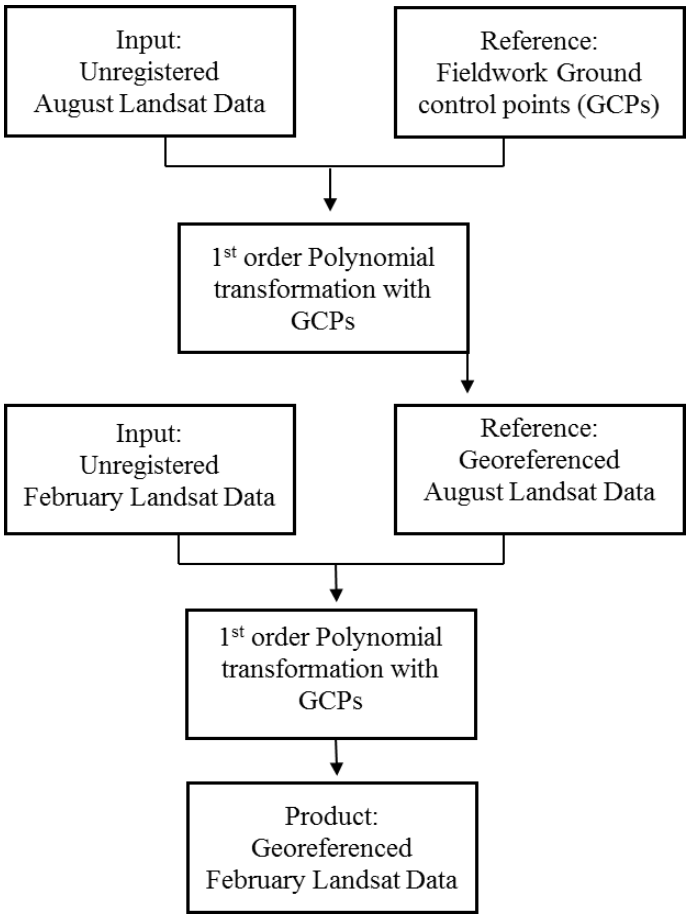

The accuracy obtained by overlaying the mobile points on the GeoEye image is acceptable, with the error falling in a range of 4–6 m. Figure 3-12 shows an example of mobile points overlaid on the GeoEye image of the study area. In addition, the mobile points were also overlaid on the Landsat 7 ETM+ to test the accuracy and match of these points with ground datasets. The accuracy was found to be lower with a shift between some points of approximately 15–20 m.

Figure 3-12 Positional accuracy of ground-based GPS tracks overlaid on the GeoEye

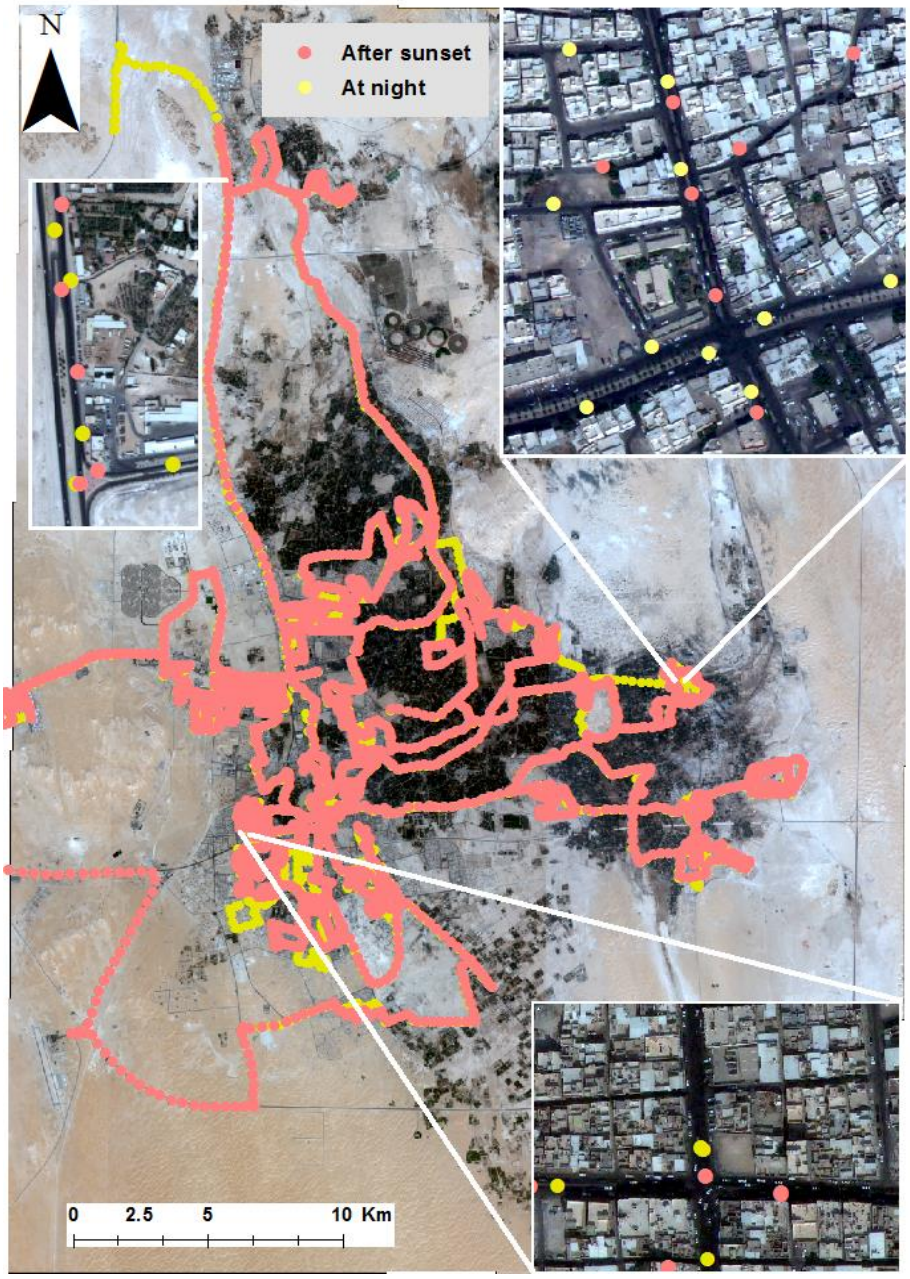

3.4.4.2 *Georeferencing of MODIS data*

MODIS data of the study area are obtained in Sinusoidal projection. In order to overlay the mobile traverses and other images of the study area e.g. GeoEye and Landsat 7 ETM+, it is important to project MODIS images to the local projection. Therefore, MODIS images including the bands 7, 4, and 3 for classification stage and 31 and 32 to estimate surface temperature, are projected to the study area projection, which is WGS 1984 UTM Zone 39N

using ArcMap 10.2 software. Figure 3-13 shows an example of MODIS images before and after the projecting process.

Figure 3-13 MODIS data before projected (left) and after projected to the study area projection (right)

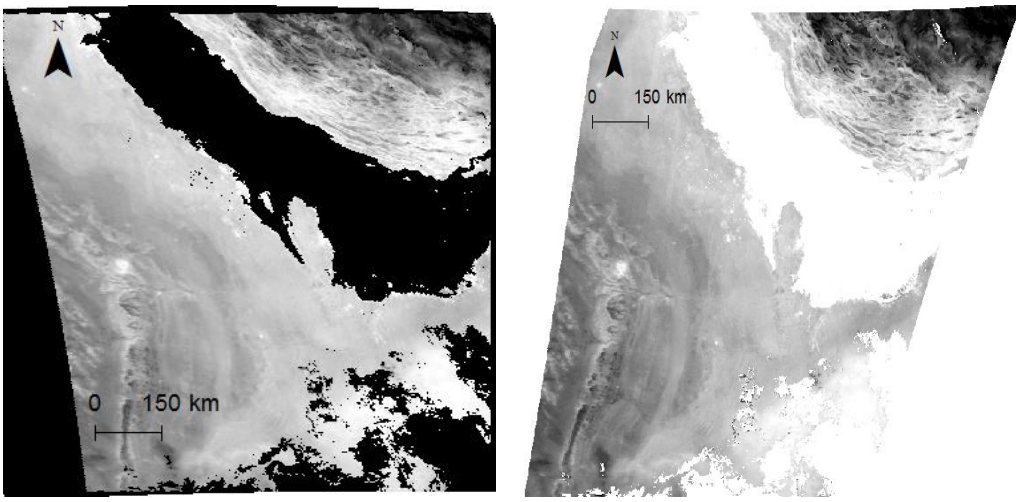

3.5 **Estimating surface temperature based on satellite data**

Satellites have been used to infer land surface temperatures in different regions across the world. Even though the satellites examine the intensity of different wavelength bands rather than directly measuring surface temperature this has proved a successful method to estimate land surface temperature and detect SUHI. Two different satellites datasets were used in this study to estimate the surface temperatures; Landsat 7 ETM+ and MODIS (Table 3-5).

Table 3-5 Satellites imageries used to estimate the surface temperature

Sensor	WRS	Resolution	Spectral bands	Date	Source	Cc
Landsat 7 ETM+	Path164/Row42	60 m	6	7/02/11 23/02/11 18/08/11	USGS	2% 5% 0%
MODIS	H/22 V/6	1000 m	20–25 27–36	21/01/11 to 28/02/11 26/07/11 to 31/08/11	USGS	Vary

Note: WRS = Worldwide Reference System. H/V = horizontal and vertical. USGS = United State Geological Survey. Cc = Cloud cover.

The investigation of land cover/use and its relationship with surface temperature has been a common theme in the study of SUHI using a remote sensing approach (Chen et al., 2006, Qian et al., 2006, Stathopoulou and Cartalis, 2007, Yokobori and Ohta, 2009). The nature and materials used in land coverage alter the surface emissivity. Therefore, a system of land cover classification is necessary to identify the different types of land cover/use when creating an emissivity map for the purpose of estimating the surface temperature. Emissivity is defined as the ratio of absorbed radiation energy to the total incoming radiation energy, compared to a perfect black body and is thus a measure of absorption.

3.5.1 Supervised classification

The multispectral bands from the Landsat 7 ETM+ imagery, taken in February 2011, of the study area were classified based on supervised classification using ERDAS and ENVI software. Different classes – e.g. vegetation areas (palm trees), urban areas, bodies of water, flat sand, sabkha and sand dunes – were considered in this study to be classified. A sample of known pixels was extracted from the texture images as regions of interest (ROI) from each class to generate the supervised classification method. As the spatial resolution of the multispectral bands of Landsat is only 30 m, different classes might fall within that pixel area, but be classified as one class. Therefore, using high resolution spatial data such as that obtained from GeoEye-1, with a resolution of 0.5 m, would provide more logical classification of land cover. GeoEye-1 images were classified using the Definiens software to create a detailed map of the study area land cover.

A maximum likelihood classifier algorithm was used in this study to apply the supervised classification, this being one of the most popular methods of classification (Bailly et al., 2007, Jensen, 2005b, Lillesand, 2000, Xiuping and Richards, 1999). The maximum likelihood classifier allocates each pixel to a class according to the highest probability of a match. This involves the calculation of the discriminant functions for each pixel in the image, using the following formula (Jensen, 2005a).

$$\mathrm{p_i.p(\omega_i)} = \log_e p(\omega_i) - {}^1/_2 \log_e |V_i| - [{}^1/_2 (X - M_i)^T V_i^{-1} (X - M_i)]$$

where:

ω_i = classes

$p(\omega_i)$ = probability function of class ω_i

X = unknown measurement vector

V_i = covatiance matrix of class i

M = mean vector of class i

p_i = probability of class i

The goal of the classification process is identifying the land cover type so as to be able to use the emissivity value of each class or objects to estimate surface temperatures in the summer and winter seasons (Janet, 2009). In addition, the images, once classified, provided spatial data of help in analysing the effect of the different land cover types and could be used for the air and surface temperatures of the study area. More details and results of classifications will be discussed in chapter five.

Landsat 7 ETM+ also is classified using Definiens Professional 5.0 which involves segmentation and object-based processing. Two stages were taken in order to classify the image. The first step involves image data segmentation, which segments the image into a network of homogeneous image objects. The second stage is object-oriented, whereby land cover classes are related to the segmented image objects.

Also, MODIS images including bands 7, 4, and 3 are classified using the same mentioned method above then the results are exported as vector. The decision of different classes and sub-classes of MODIS data is considered the urban climate zones scheme described by Oke (2006). The urban climate zone (UCZ), is not only describes each site or class as individual district but also consider the capacity to modify the local climate and the potential transitions to different urban climate zones (Oke, 2006). Table 3-4 shows the urban climate zones classification in the order of the ability to impact the local climate. Using ArcMap 10.2 software and XTools Pro option the fishnet of the study area image are created based on MODIS pixel size which is 1000 metres. From joins and relates options, both data the classified image and the fishnet are joined. New field is added for emissivity values for each land cover then exported as map in order to estimate the surface temperature for the study area. In the following section more details about how the brightness temperature is estimated from both sensors Landsat 7 ETM+ and MODIS.

Table 3-4 Simplified classification of distinct urban forms arranged in approximate decreasing order of their ability to impact local climate

Urban Climate Zone[1]	**Image**	**Rough-ness class**[2]	**Aspect ratio**[3]	**% Built** (imperm-eable)[4]
Intensely developed detached close-set high-rise building, e.g. downtown towers	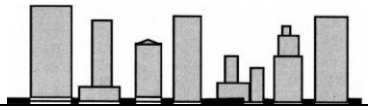	8	>2	> 90
Intensely developed high density urban with 2 – 5 storey, attached or very close-set buildings often of brick or stone, e.g. old city core	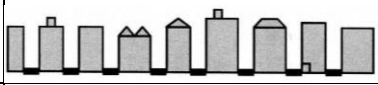	7	1.0 – 2.5	> 85
Highly developed, medium density urban with row or detached but close-set houses, stores & apartments e.g. urban housing		7	0.5 – 1.5	70 – 85
Highly developed, low or medium density urban with large low buildings & paved parking, e.g. shopping mall, warehouses		5	0.05 – 0.2	70 – 95
Medium development, low density suburban with 1 or 2 storey houses, e.g. suburban housing		6	0.1 – 0.6, up to >1 with trees	35 – 65
Mixed use with large building in open landscape, e.g. institutions such as hospital, university, airport	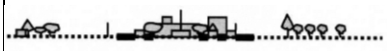	5	0.1 – 0.5, depends on trees	< 40
Semi-rural development, scattered houses in natural or agricultural area, e.g. farm, estates	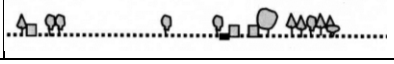	4	> 0.05, depends on trees	< 10

Key to image symbols:

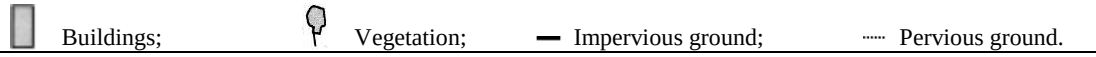

1. A simplified set of classes that includes aspects of the schemes of (Auer, 1978) and (Ellefsen, 1991) plus physical measures relating to wind, thermal and moisture controls (columns at right). Approximate correspondence between UCZ and Ellefsen's urban terrain zones is: 1(Dc1, Dc8), 2 (A1-A4, Dc2), 3 (A5, Dc3-5, Do2), 4 (Do1, Do4, Do5), 5 (Do3), 6 (Do6), 7 (none).
2. Effective terrain roughness according to the Davenport classification (Davenport et al., 2000).
3. Aspect ratio = zH/W is average height of the main roughness elements (buildings, trees) divided by their average spacing, in the city centre this is the street canyon height/width. This measure is known to be related to flow regime types (Oke, 1987) and thermal controls (solar shading and longwave screening (Oke, 1981). Tall trees increase this measure significantly.
4. Average proportion of ground plan covered by built features (buildings, roads, paved and other impervious areas) the rest of the area is occupied by pervious cover (green space, water and other natural surfaces). Permeability affects the moisture status of the ground and hence humidification and evaporative cooling potential.

The table is Modified after (Oke, 2006).

3.5.2 Mapping the emissivity (εσ)

In order to estimate the surface temperature of the study area, it is important to map the emissivity value after the classification and accuracy assessment steps. The emissivity, as defined in the literature review and methodology chapters, is the ratio of the absorbed radiation energy to the total incoming radiation energy compared to a perfect emitter (black body), and thus is a measure of absorptivity (Becker and Li, 1995). Based on the emissivity values in previous studies of arid regions (Table 3-5) and on lookup tables of emissivity values of different materials and land covers (Zhang, 2011), emissivity maps of the Al Ahsa oasis are produced by integrating the emissivity values of each land cover class after the classification step using ENVI software (Shunlin, 2001, Janet, 2009, Sobrino et al., 2012).

Table 3-5 Emissivity values of different land cover of the study area, based on previous studies of arid regions

ID	Class name	Description of the class	Emissivity Reference (1)*		Emissivity Reference (2) and (3)*
			25 °C	45 °C	
1	Vegetation (1)	Palm trees	.97	.97	.99
2	Vegetation (2)	Grass (Park)	.96	.96	.98
3	Sabkha	Wet sand	.95	.95	.90
4	Water	Water	.98	.98	.99
5	Sand1	Sand dunes	.93	.94	.89
6	Sand2	Sandstone	.92	.93	.88
7	Sand3	Red sand	.93	.94	.89
8	Built-up (1)	Houses and concrete	.95	.95	.94
9	Built-up (2)	Asphalt and pavement	.96	.96	.96

*Reference (1) (Qina et al., 2005) and reference (2) and (3) (Ogawa et al., 2008, Sobrino et al., 2012).

3.5.3 Estimating surface temperature using Landsat 7 ETM+

It is possible to map the surface temperature of the study area by capturing emitted thermal radiation from the surface of the Earth. Planck's blackbody radiation equation relates spectral radiance and wavelength with the radiant temperature of an object. The radiation values of a Landsat image are stored in images by pixel or digital number (DN) value. The thermal temperature is calculated from the DN value. The thermal band (band 6) of Landsat 7 ETM+ image pixels were converted into units of absolute radiance. The calculation can be carried out using the following three steps:

(Step 1): Conversion of the DN values of the satellite images to spectral radiance values using equation (1):

$$\text{Radiance} = \text{gain} \times \text{DN} + \text{offset} \quad (1)$$

The radiance can also be expressed as the following (Markham and Barker, 1986):

$$L_\lambda = \frac{L_{max(\lambda)} - L_{min(\lambda)}}{(Q_{calmax})} \times (Q_{cal}) + L_{min(\lambda)} \quad (2)$$

where:

L_λ = spectral radiance, (watts/m^2. sr. µm)

Q_{clamax} = maximum grey level (255)

Q_{cal} = digital number or grey level of analysed pixel

$L_{\min(\lambda)}$ = minimum detected spectral radiance (0.0 in low gain, 3.2 in high gain)

$L_{max(\lambda)}$ = maximum detected spectral radiance (17.04 in low gain, 12.65 in high gain)

For the low-gain of the band-6 data, equation (2) can be converted to

$$L_{\lambda l} = 6.682 \times 10^{-2} \times DN \quad (3a)$$

For the high-gain of the band-6 data, equation (2) can be converted to;

$$L_{\lambda h} = 3.706 \times 10^{-2} \times DN + 3.2 \quad (3b)$$

where:

$L_{\lambda \iota}$ = spectral radiance in low gain

$L_{\lambda h}$ = spectral radiance in high gain

DN = digital number of pixel

A relation can be obtained between DNs and radiance through calculation using equations (3a) and (3b) (Mishra *et al*., 2011).

(Step 2): Conversion of the spectral radiance to radiant temperatures by using the following equation (4) (Gupta, 2005):

$$T_R = \frac{K_2}{ln\left(\frac{K_1}{L_\lambda} + 1\right)} \quad (4)$$

where:

T_R = radiant temperature (Kelvin)

K_1 = alibration constant for Landsat7 ETM + sensor (666.09 watts/m^2. sr. μm)

K_2 = $c$alibration constant for Landsat 7 ETM + sensor (1282.71 degree Kelvin)

(Step 3): Changing the brightness temperature to the surface temperature based on equations (5) and (6).

$$T_k = T_R \times \varepsilon_\lambda^{-1/4} \quad (5)$$

$$T_{k'} = T_k - 273 \quad (6)$$

where:

T_k = surface temperature (Kelvin)

$T_{k'}$ = surface temperature (Celsius)

ε_λ = emissivity (0.97)

As this study attempted to map the surface temperature based on different emissivity values, the emissivity map produced was considered as providing the most accurate method of deriving surface temperature when using satellite data and remote sensing approaches. Through this analysis the thermal structure of the study area was evaluated and examined against the spatial data regarding land cover types. This method also helped to identify the intensity of the SUHI and their distribution in the region. Chapters 6 and 7 discuss in more detail the processes that followed from this approach and its outcome.

Surface temperature maps can then be created for the study area for different parts of the study period. These maps will show the location and densities of the SUHI at the different scales seen by the Landsat and MODIS sensors. Finally, the ground surface temperature data for the 60-days (January and July) can be compared to satellite imagery to test its accuracy.

3.5.4 Estimating surface temperature using MODIS data

It is possible to estimate the surface temperature using the thermal bands of MODIS and investigate the UHI intensity and its relationship to the land cover. The split-window method is one of the several methods to estimate the surface temperature and has been used by several authors in many studies such as (Wan et al., 2002, Wan et al., 2004, Coll et al., 2005, Wan,

2008). The split-window method algorithms are found as the correct for atmospheric effect including (absorption and emission) and emissivity by using 36 bands of MODIS sensor. That addresses several problems which associated with remote sensing measurements of surface temperature such as emissivity assumptions and unknown atmospheric effects (Zhengming and Dozier, 1996, Tomlinson et al., 2012).

In order to estimate the surface temperature using MODIS, the study area is projected to the local projection, land cover is identified and the emissivity is mapped. Conversion of the scaled integer (SI) values of Aqua/MODIS band 31 and 32 data refer to the observed spectral radiance (L_λ) requires both the lower and upper original rescaling factors R_{scale} and R_{offset}. In order to convert the scaled integer of the observed spectral radiance the calibration constants of the thermal bands of Aqua/MODIS data have been used (Table 3-6). The conversion is calculated using the equation (7) (Anonymous, 2006, Oguro et al., 2011):

Table 3-6 Calibration constants of Aqua/MODIS thermal bands for converting scaled integer to observed spectral radiance

Band	$R_{\text{scale}\lambda}$ (W/(m^2.sr.µm))	$R_{\text{offset}\lambda}$
31	0.0006.5080720	2035.9332
32	0.0005.7100126	2119.0845

$$L_\lambda = R_{\text{scale}\,\lambda}(SI_\lambda - R_{\text{offset}\,\lambda}) \quad (7)$$

where $R_{\text{scale}\,\lambda} = \frac{L_{\max\lambda} - L_{\min\lambda}}{32767}$ and $R_{\text{offset}\,\lambda} = \frac{32767 \times L_{\min\lambda}}{L_{\max\lambda} - L_{\min\lambda}}$

where L_λ is observed spectral radiance in W/(m^2.sr.µm),

SI_λ is scaled integer value of 16 bits unsigned integer data in dimensionless,

$L_{\min\lambda}$ is observed spectral radiance scaled to 0 in W/(m^2.sr.µm),

$L_{\max\lambda}$ is observed spectral radiance scaled to 32767 in W/(m^2.sr.µm),

$R_{\text{scale}\,\lambda}$ is radiance rescaling gain factor in W/(m^2.sr.µm),

$R_{\text{offset}\,\lambda}$ is radiance rescaling offset factor in dimensionless,

The second stage to estimate the surface temperature using MODIS data is to convert the thermal data of 31 and 32 bands from observed spectral radiance (L_λ) to observed BT applying the Planck's law of blackbody radiation. The conversion is calculated using the equation (8) (Anonymous, 2006, Oguro et al., 2011):

$$T = \frac{hc/k\lambda}{\ln(2hc^2/(L_\lambda \lambda^5 \times 10^6) + 1} \quad (8)$$

where T is observed brightness temperature (BT) in Kelvin,

h is Plank constant (6.62606896 x 10^{-34}J.s),

c is speed of light (2.99792458* 10^{+8}m/s)

k is Boltzmann constant (1.3806504*10^{-23} J/k)

λ is centre wavelength in meter, and

L_λ is observed spectral radiance in W/(m^2.sr.μm).

3.6 **Methodological framework**

The model which is followed in this study to measure and estimate the SUHI and CLHI intensity is shown in Figure 3-14. The model includes both data set that have been used in this study, the ground and remote sensing data in order for better understanding of the effect of the land cover on SUHI intensity.

Figure 3-14: The study model of urban heat island

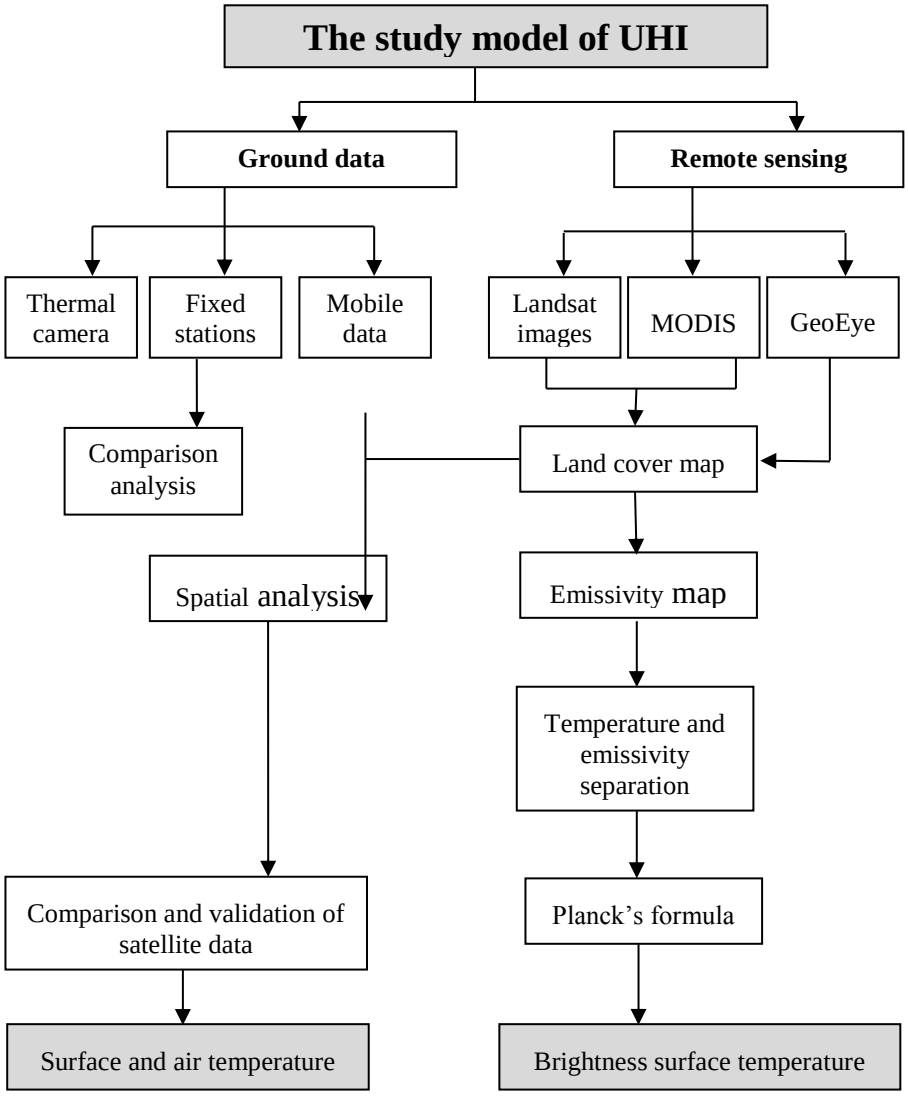

3.7 **Summary**

This chapter has described the nature of the data used in this study. Ground data, fixed weather stations and mobile data, and remote sensing, Landsat 7 ETM+ and MODIS data were the main dataset used to measure and estimate the SUHI and CLHI intensity. Data pre-processing and analysis are included in this chapter with explanations of some of the limitations encountered and the methods used to overcome them. The estimation of surface temperature using different satellite images is addressed. Finally, the methodological framework of this study is summarised. The results of data pre-processing and further data processing, along with study data evaluation, are discussed in the following chapters.

Chapter 4: Seasonal Distribution of Air and Surface UHI

4.1 Introduction

This chapter will discuss the nature of CLHI, in relation to variations in air temperature, surface temperature and relative humidity, and their variations during two seasons (summer and winter) in 2011. The aim of this chapter is to investigate the existence of CLHIs at both seasonal and diurnal scales during the selected period, using data from fixed weather stations located in different land cover types. The six weather stations are located at: 1) the city centre where the intensity of built-up area is the greatest; 2) a farm where the intensity of vegetation and palm trees is the greatest; 3) a park, which represents a green area located in the urban area; 4) sabkha, which is the most common land cover of the area studied, representing a low-lying area wet sand; 5) a factory, where industrial activities are located in the urban area; and 6) the airport weather station which is located outside the urban area, included as a control station (Figure 4-1). The fixed weather stations recorded hourly data of air and surface temperatures, relative humidity, and wind and gust speed using HOBO data loggers for two periods: winter (January and February) and summer (July and August) 2011 (see appendix 4.1 for mean and stander deviation of air and surface temperatures and relative humidity of each site). (For more details see data sources and methodology chapter section 3.4.1) The significant differences between the median groups of the fixed weather station data were investigated using non-parametric statistical methods, as the primary data showed that the distribution is not normal, especially during the summer season. Local CLHIs were addressed and defined. The average of air and surface temperatures and relative humidity were calculated and compared between the rural station (airport weather station) and the other fixed station data relating to the different urban land covers (park, sabkha, factory, city centre, and farm). (Figure 4-1)

Figure 4-1 The location of the fixed weather stations built during winter and summer season fieldwork (January, February, July, and August) in the study area Al Ahsa.

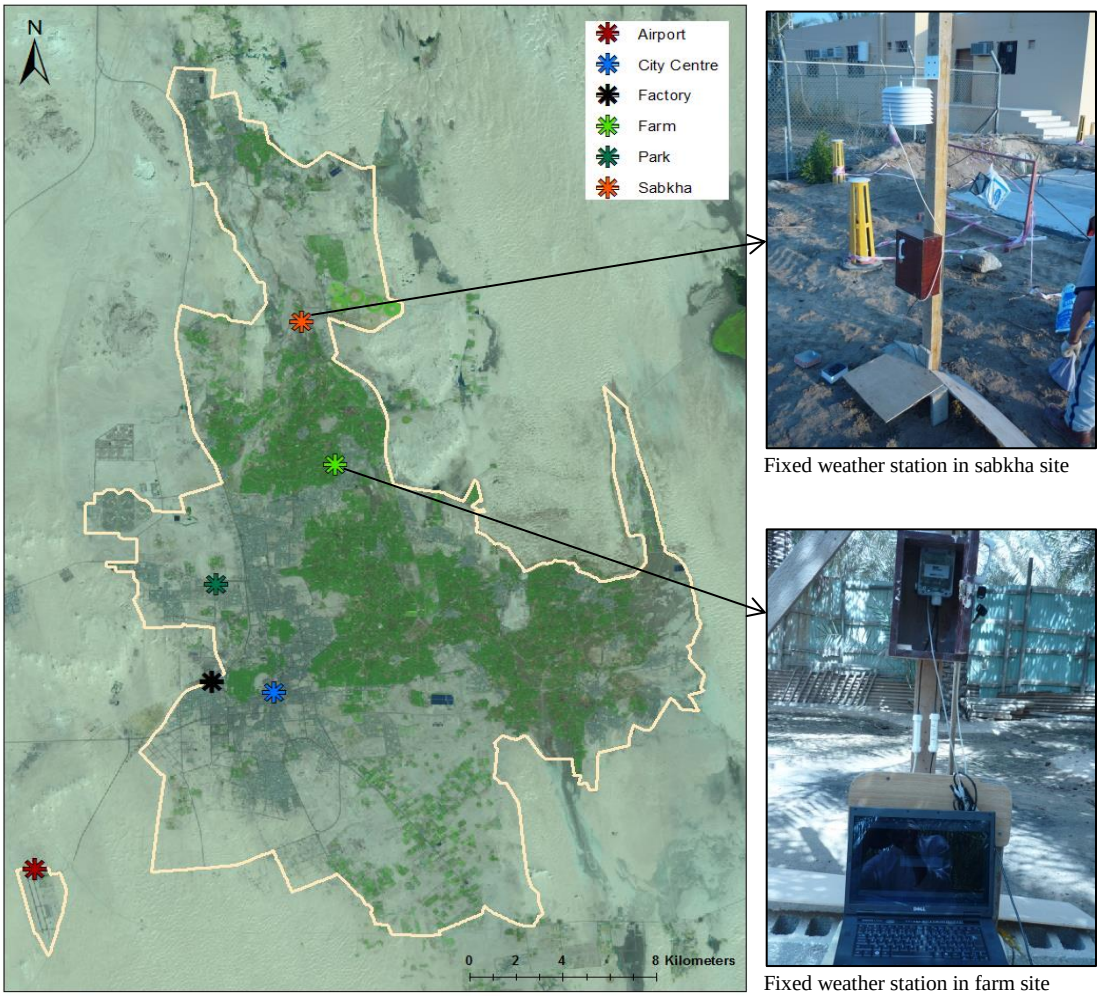

Fixed weather station in sabkha site

Fixed weather station in farm site

4.2 **Fixed weather stations data distribution**

Histograms of air temperature, surface temperature, and relative humidity of different land cover areas (City centre, Sabkha, Park, Farm, Factory, and Airport) indicated some resemblance to a normal distribution during winter, but not a normal distribution during summer (Figure 4-2, Figure 4-4, and Figure 4-6). Probability distribution plots also showed the same types of data distribution for air temperature, surface temperature, and relative humidity during both winter and summer seasons (Figure 4-3, Figure 4-5, and Figure 4-7). The probability plots showed some skewness in the tail of the data distributions for all the variables in both seasons, but especially during summer (see also appendix 4.2).

Overall, the highest air temperatures were observed in the city centre; then, in descending order: factory, park, airport, sabkha, and farm sites, both in winter and summer (Figure 4-2). The two peaks of the data distributions during the summer season for all variables (air temperature, surface temperature, and relative humidity), might indicate the CLHI effects that occur in the study area. The mean air temperature of the city centre was 18.9 °C during winter and 39.2 °C during summer. The lowest air temperature was recorded at the farm site, both in the winter (16.3 °C) and summer (33.3 °C). The differences in mean air temperature between different fixed weather station data are greater in the summer than the winter.

Figure 4-2 Frequency distribution of hourly air temperature in the different land-cover areas studied

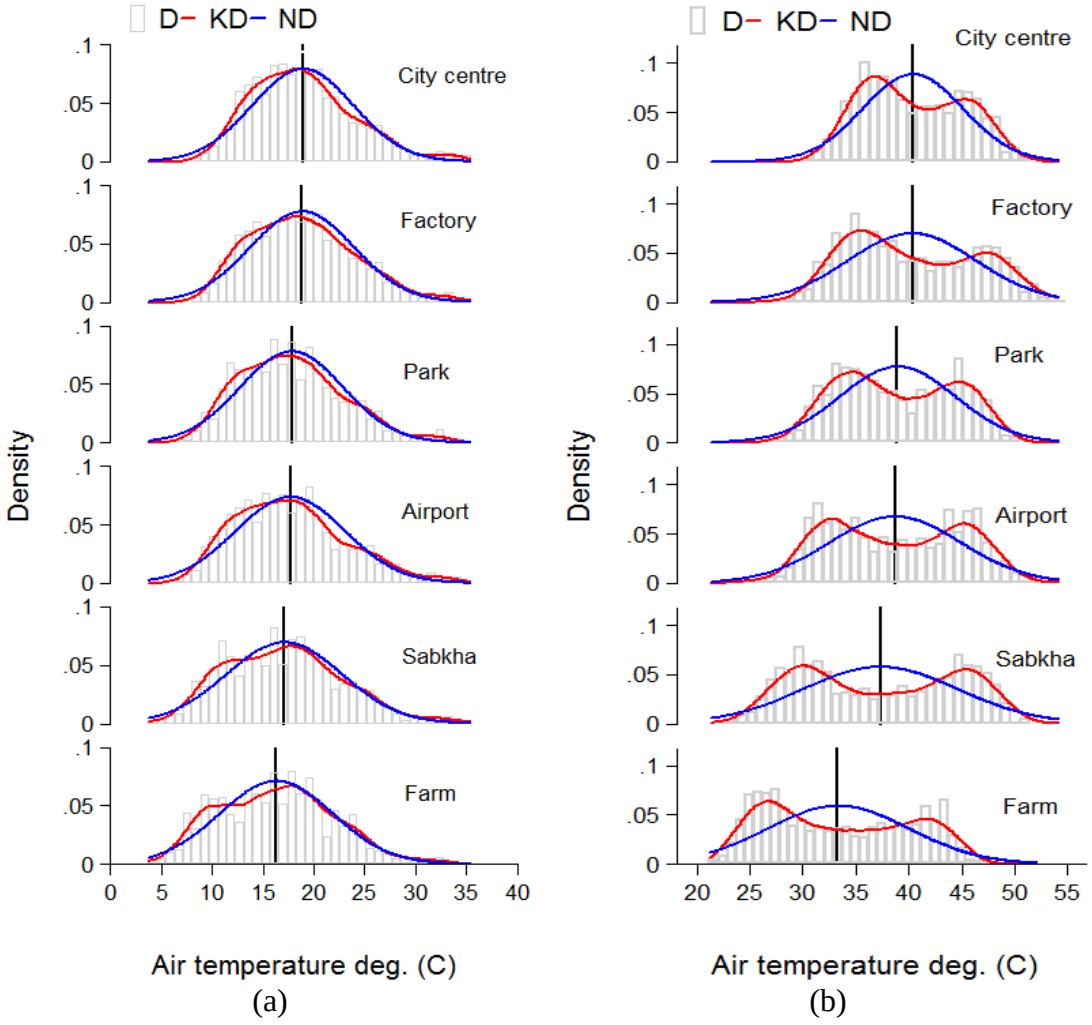

Note: (a) Winter season - January and February 2011 (b) Summer season - July and August 2011. D=density, KD= kernel density, ND=normal density. The reference line indicates the mean value.

Figure 4-3 Probability distribution plots of air temperature (°C) during summer (27July to 31August 2011) and winter (21 January to 28 February 2011) for different land cover areas

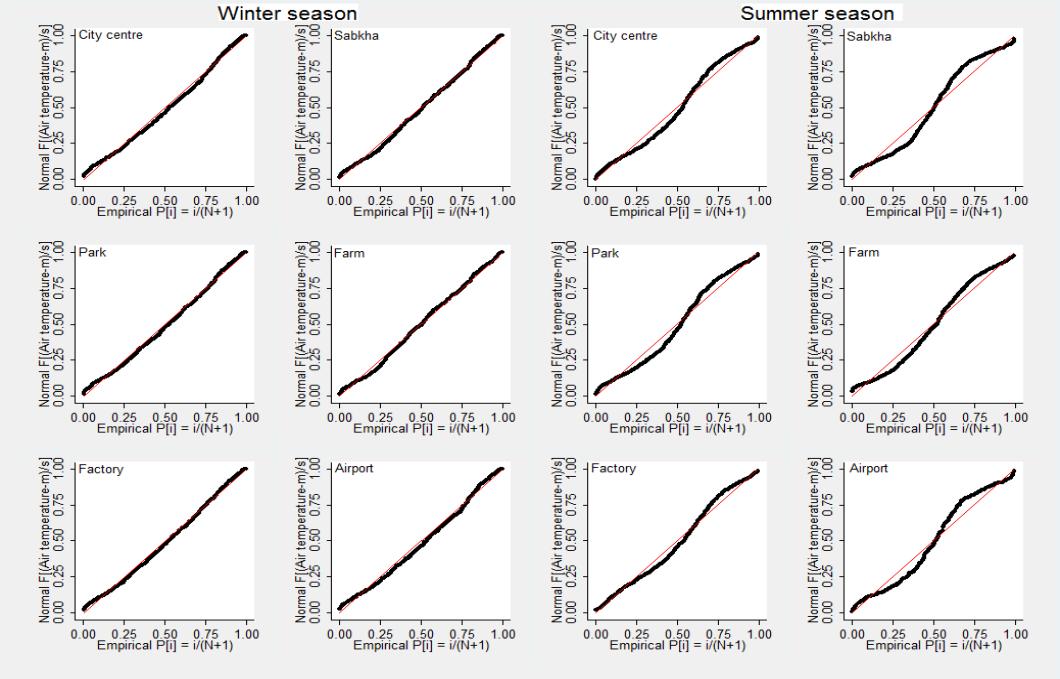

These statistics also indicate that air temperature, surface temperature, relative humidity, wind speed, and gust speed data are not normally distributed. The result of Skewness/Kurtosis tests showed a fail to accept null hypothesis which is the air temperature, surface temperature, relative humidity, wind speed, and gust speed are normally distrusted at $P<0.05$ level in different land cover areas during both winter (21/01 to 28/02/2011) and summer (26/07 to 31/08/2011). Statistically, the air temperature data in both seasons are not normally distributed (Table 4-1). Although some individual locations showed a normal distribution, such as Sabkha, Park, and Airport during the summer season, the histograms and plots showed that these are not in fact normally distributed. Deciding on normality was based on both methods (graphical and statistical) to meet the good complete normality test (D'Agostino et al., 1990).

Table 4-1 Results of Skewness/Kurtosis tests for normality (air temperature (°C) during winter (21/01 to 28/02/2011) and summer (26/07/2011 to 31/08/2011)

Season	Location	Obs	Pr (Skewness)	Pr (Kurtosis)	Chi^2 (2)	Pr>chi^2
Winter	City centre	936	0.000	0.197	50.81	0.000
	Sabkha	936	0.000	0.173	22.05	0.000
	Park	936	0.000	0.667	31.69	0.000
	Farm	936	0.003	0.002	18.50	0.000
	Factory	936	0.000	0.199	29.27	0.000
	Airport	936	0.000	0.683	40.13	0.000
Summer	City centre	888	0.031	0.000	263.04	0.000
	Sabkha	888	0.678	.	.	.
	Park	888	0.329	0.000	552.79	0.000
	Farm	888	0.020	0.000	3543.58	0.000
	Factory	888	0.002	0.000	335.31	0.000
	Airport	888	0.662	0.000	800.34	0.000

The surface temperature shows a similar data distribution to the air temperature in the different land cover areas during both winter and summer (Figure 4-4). Histograms for surface temperature show a near-normal distribution during the winter season, but not in the summer season. The surface temperature data showed a bimodal distribution during the summer season in all locations. The mean surface temperatures of the city centre and factory stations during winter and summer were 20.4 °C and 21.8 °C, while the maxima were 42.0 °C and 40.1 °C respectively. The lowest surface temperature was recorded at the farm and park sites, both in winter and summer - 15.9 °C, 16.5 °C and 31.8 °C, 36.7 °C respectively (Figure 4-4).

Figure 4-4 Frequency distribution of hourly surface temperature in different land cover areas studied

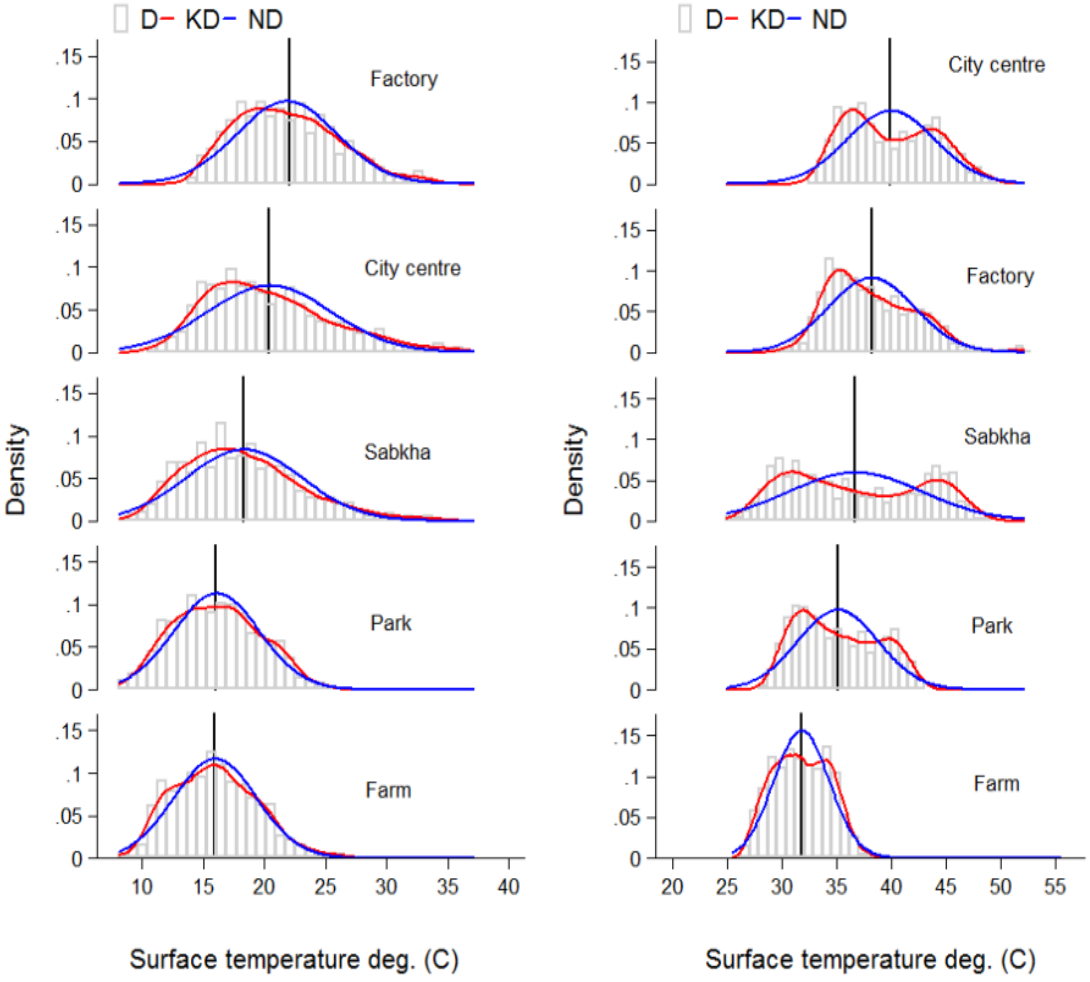

Note: Winter season - January and February 2011(left). Summer season - July and August 2011 (right). D=density, KD= kernel density, ND=normal density. The reference line indicates the mean value.

The probability distribution plots of surface temperature showed the same pattern as raw data distribution histograms (Figure 4-5). The probability plots also indicate skewness in the tail of the data distributions for all the locations in both seasons, especially during summer. Statistical tests indicate that surface temperature data are not normally distributed. The result of a Skewness/Kurtosis test showed that the null hypothesis cannot be accepted at $P<0.05$ level for surface temperature in different land cover areas during both winter (21/01 to 28/02/2011) and summer (26/07 to 31/08/2011) (Table 4-2). Although at some locations histograms appear to show normal distributions of temperature data, such as the Park in the winter and the Farm in the summer with P=0.084 and 0.408 respectively, the histograms and plots show that these are not in fact normally distributed.

Figure 4-5 Probability distribution plots of surface temperature (°C) during summer (27July to 31August 2011) and winter (21 January to 28 February 2011) at different land cover areas

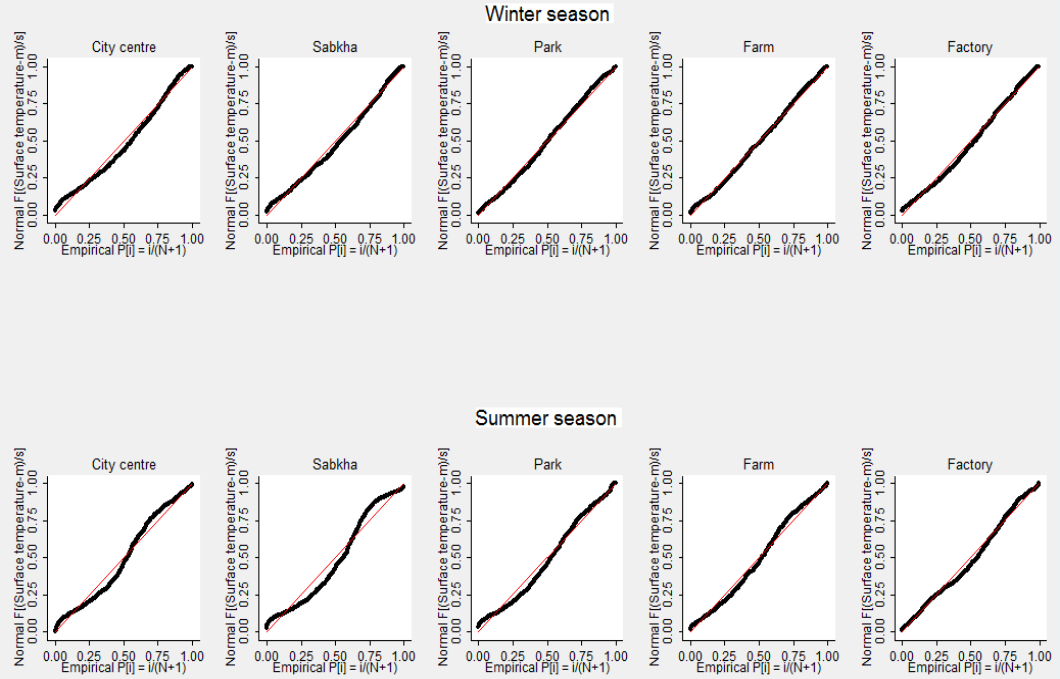

Table 4-2 Results of Skewness/Kurtosis tests for normality (Surface temperature (°C) during winter (21/01/2011 to 28/02/2011) and summer (26/07/2011 to 31/08/2011)

Season	Location	Obs	Pr (Skewness)	Pr (Kurtosis)	Chi^2 (2)	Pr>chi^2
Winter	City centre	936	0.000	0.5265	65.31	0.000
	Sabkha	936	0.000	0.0772	63.03	0.000
	Park	936	0.084	0.0000	40.92	0.000
	Farm	936	0.000	0.0225	19.58	0.000
	Factory	936	0.000	0.0216	33.19	0.000
Summer	City centre	888	0.002	0.000	268.44	0.000
	Sabkha	888	0.046	0.000	4346.91	0.000
	Park	888	0.002	0.000	397.29	0.000
	Farm	888	0.408	0.000	91.55	0.000
	Factory	888	0.000	0.469	52.03	0.000

Histograms of Relative humidity data show differences among the different land cover areas and between the winter and summer periods. Mean relative humidity was higher in winter than in summer. The mean relative humidity levels are 45%, 50%, 51%, 54%, and 63% in the city centre, airport, park, sabkha, and farm respectively. The mean relative humidity ranges between 21% and 29% during summer at all locations, except the farm which averages 44% (Figure 4-6).

Figure 4-6 Frequency distribution of hourly relative humidity in different land cover areas studied

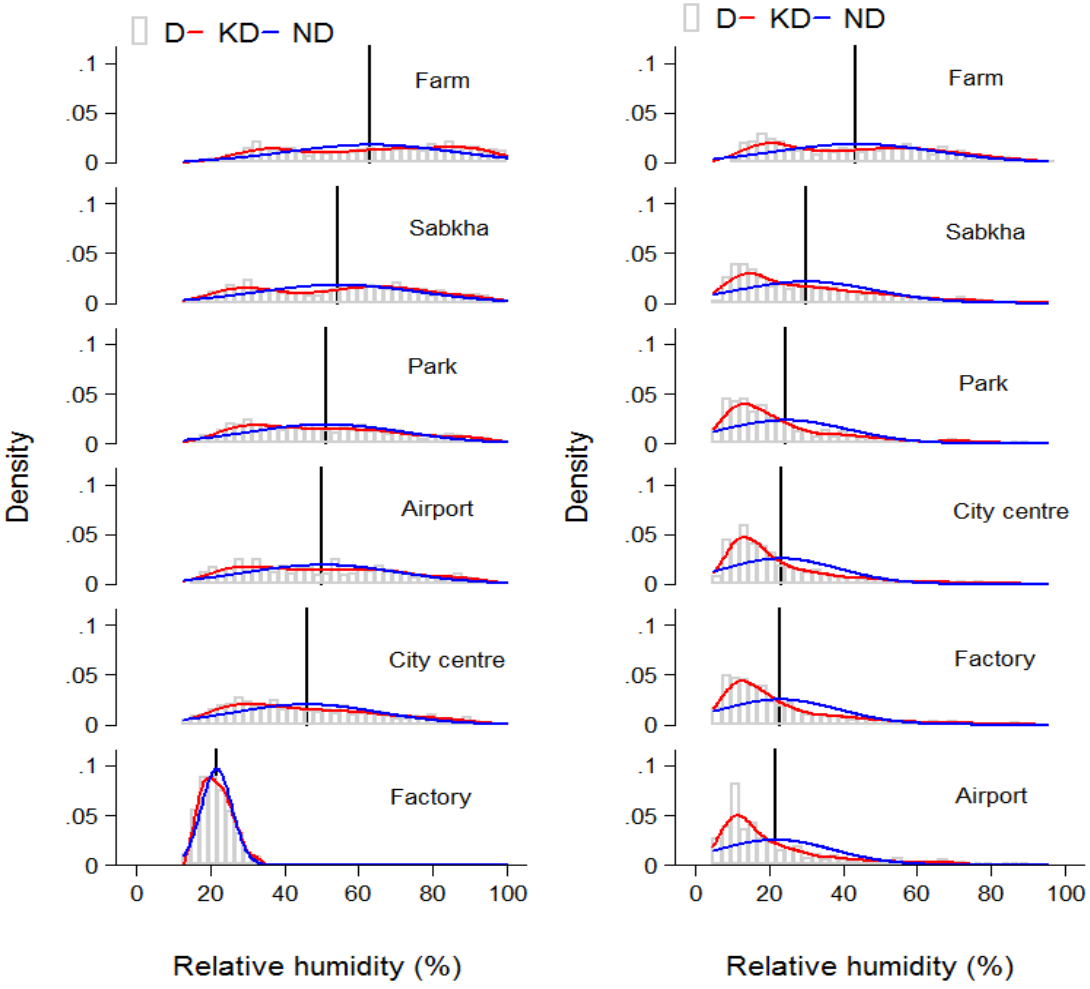

Note: Winter season-January and February 2011 (left). Summer season-July and August 2011 (right). D=density, KD= kernel density, ND=normal density. The reference line indicates the mean value.

The probability distribution plots of relative humidity show the same results as the data distribution histograms (Figure 4-7). The probability plots show skewness in the tail of the data distributions for all the locations in both summer and winter periods. Relative humidity data for all locations, except for the Sabkha and Farm sites in the winter, are not normally distributed. The result of the Skewness/Kurtosis test showed that the null hypothesis cannot be accepted at $P<0.05$ level for relative humidity in different land cover areas during both winter (21/01 to 28/02/2011) and summer (26/07 to 31/08/2011) (Table 4-3). Although some locations seem to show a normal distribution, such as the Sabkha and Farm in the winter with P=0.838 and 0.087 respectively, the histograms and plots show that these data are not normally distributed.

Figure 4-7 Probability distribution plots of relative humidity (%) during summer (27 July to 31 August 2011) and winter (21 January to 28 February 2011) at different land cover areas

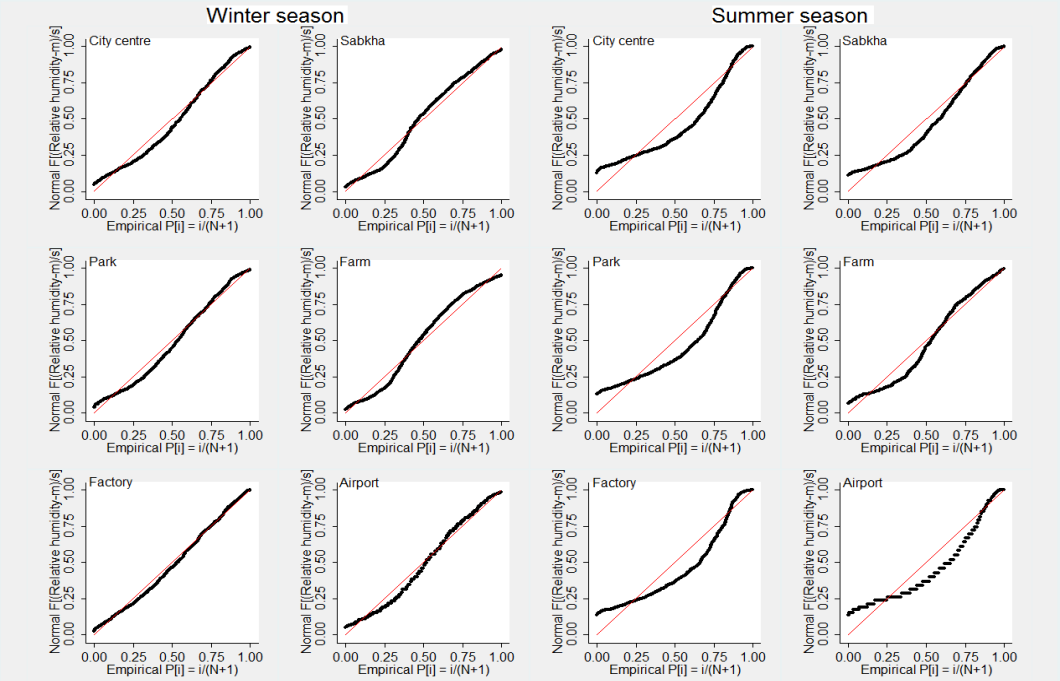

Table 4-3 Results of Skewness/Kurtosis tests for normality (relative humidity (%) during winter (21/01/2011 to 28/02/2011) and summer (26/07/2011 to 31/08/2011)

Season	Location	Obs	Pr (Skewness)	Pr (Kurtosis)	Chi^2 (2)	Pr>chi^2
Winter	City centre	936	0.000	0.000	84.86	0.000
	Sabkha	936	0.838	0.000	366.01	0.000
	Park	936	0.000	0.000	118.74	0.000
	Farm	936	0.087	0.000	946.43	0.000
	Factory	936	0.000	0.022	33.19	0.000
	Airport	936	0.001	0.000	186.13	0.000
Summer	City centre	888	0.000	0.000	278.52	0.000
	Sabkha	888	0.000	0.269	99.31	0.000
	Park	888	0.000	0.000	236.13	0.000
	Farm	888	0.001	0.000	226.07	0.000
	Factory	888	0.000	0.000	257.42	0.000
	Airport	888	0.000	0.000	276.38	0.000

Box plots (Figure 4-8 and Figure 4-9) show the distribution of the wind and gust speed among the different land cover areas during the winter (January and February) and summer (July and August) periods. The median of the wind speed ranges between 0 to 13 km/h in the summer and 0 to 9 km/h during the winter period. While the median of the gust speed ranges between 4 to 18 km/h in the summer and 7 to 18 km/h in the winter (Figure 4-9). The maximum wind speed during both seasons was recorded in the Airport weather station 39 km/h in the winter and 43 km/h in the summer. While the minimum wind speed during both seasons was observed

in the most of the fixed weather station however the farm and city centre fixed weather stations are the most locations to record low wind speed and observe the calm status of 0 km/h (Figure 4-8).

Figure 4-8 Box plot of wind speed (km/h) during winter and summer seasons

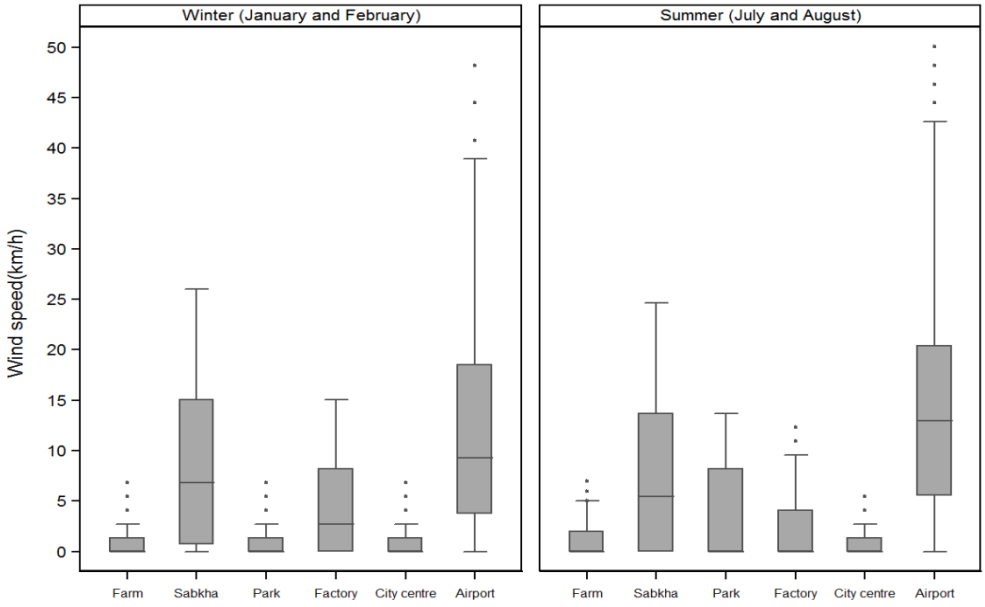

Note: The graph shows the medians (central lines) and inner quartile ranges (boxes) at land cover.

Figure 4-9 Box plot of gust speed (km/h) during winter and summer seasons

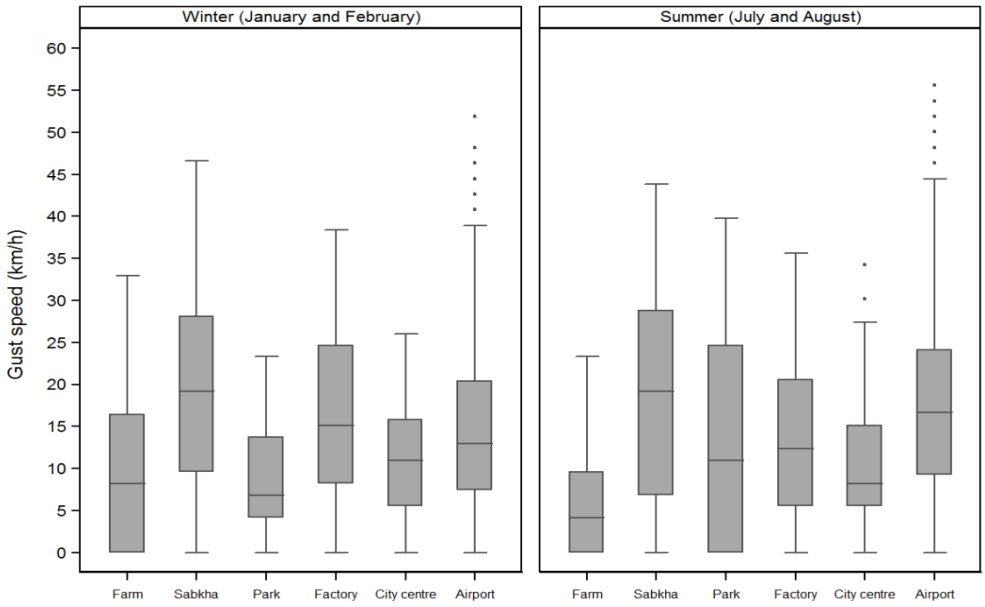

Note: The graph shows the medians (central lines) and inner quartile ranges (boxes) at land cover.

The probability distribution plots of the wind and gust speed during the summer and winter seasons show skewness in the tail of the data distributions for all the fixed weather stations

including the Airport weather station. Moreover, the quantile distribution plots also show the same results that the wind and gust speed data distribution is not normal (see the appendix figures 23 and 24).

The result of the Skewness/Kurtosis test showed that the null hypothesis, which is the wind and gust speed data distribution is normally distributed, cannot be accepted at $P<0.05$ level for wind and gust speed in different land cover areas during both seasons winter (21/01/2011 to 28/02/2011) and summer (26/07/2011 to 31/08/2011) (
Table 4-4 and Table 4-5). Although some locations seem to show a normal distribution, such as the city centre and sabkha in the winter with $P=0.353$ and 0.593 respectively, the histograms and plots show that these data are not normally distribute.

Figure 4-10 Probability distribution plots of wind and gust speed during summer (27 July to 31 August 2011) at different land cover areas

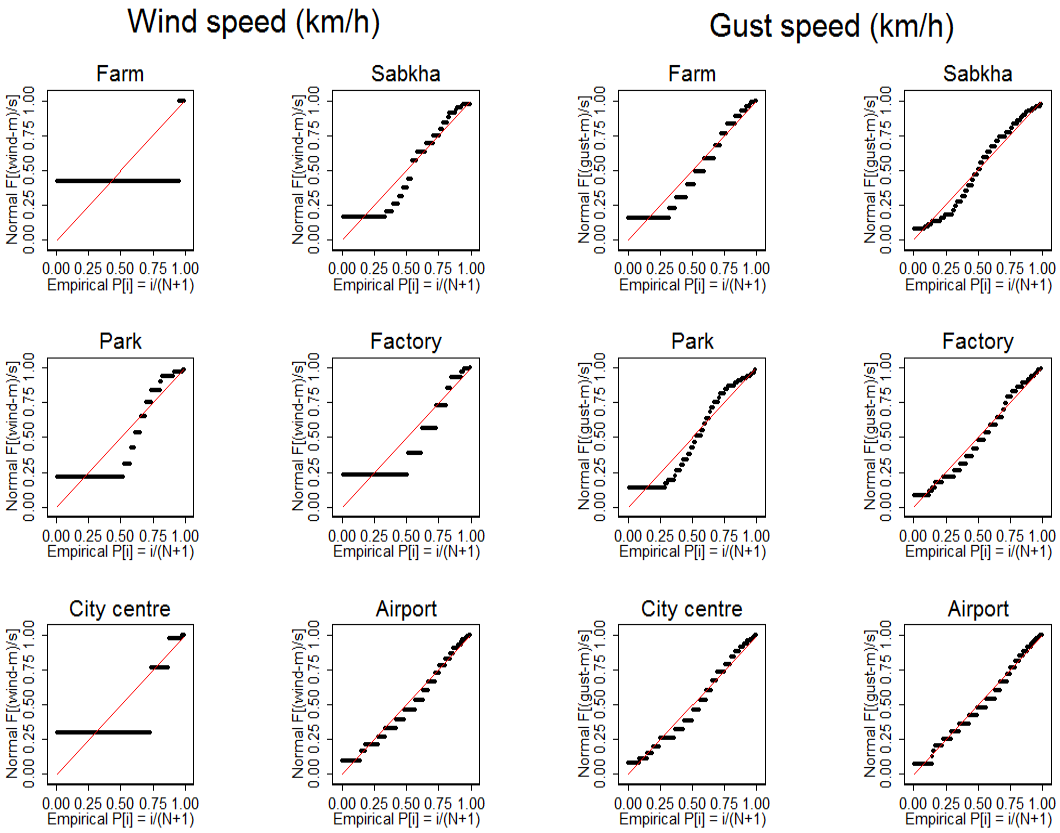

Figure 4-11 Probability distribution plots of wind and gust speed during winter (21 January to 28 February 2011) at different land cover areas

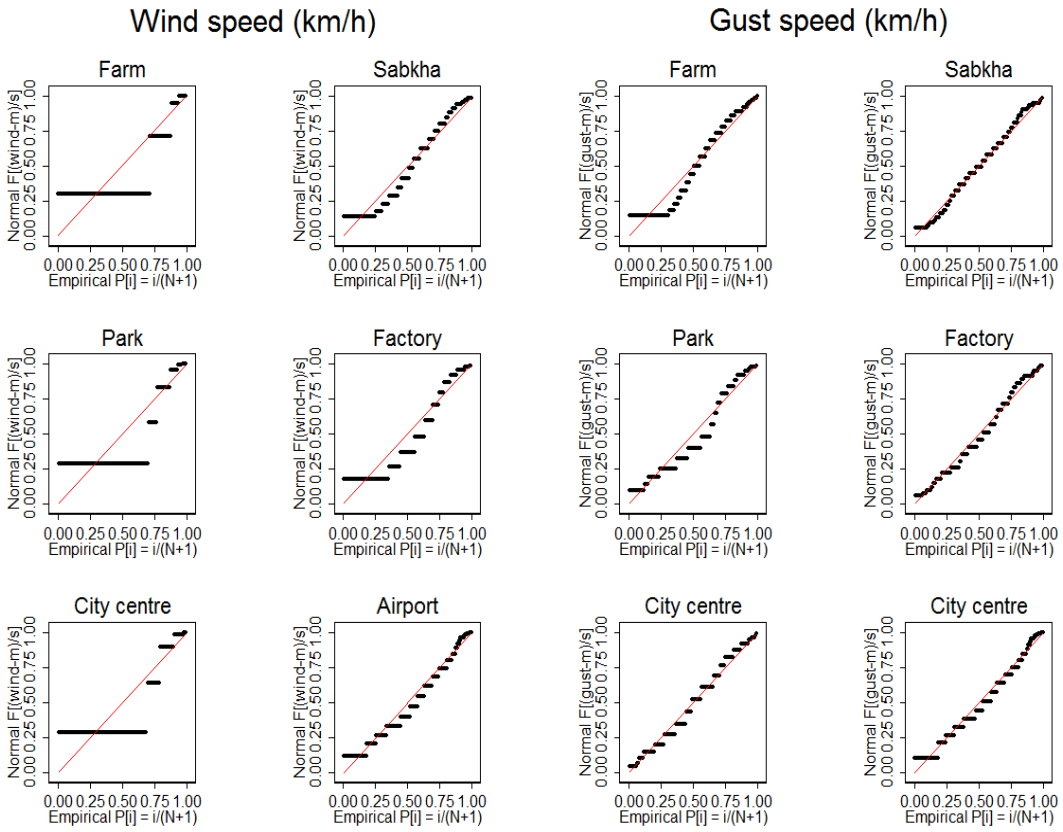

Table 4-4 Results of Skewness/Kurtosis tests for normality (Wind speed (km/h) during winter (21/01/2011 to 28/02/2011) and summer (26/07/2011 to 31/08/2011)

Season	Location	Obs	Pr (Skewness)	Pr (Kurtosis)	Chi^2 (2)	Pr>chi^2
Winter	City centre	128	0.0000	0.0023	33.82	0.0000
	Sabkha	168	0.0086	0.0000	23.66	0.0000
	Park	132	0.0000	0.0014	36.93	0.0000
	Farm	366	0.0000	0.0000	.	0.0000
	Factory	142	0.0002	0.0212	15.35	0.0005
	Airport	936	0.0000	0.0316	.	0.0000
Summer	City centre	174	0.0000	0.0000	45.19	0.0000
	Sabkha	145	0.0058	0.0000	24.94	0.0000
	Park	142	0.0002	0.0001	23.08	0.0000
	Farm	265	0.0000	0.0000	.	0.0000
	Factory	169	0.0000	0.0224	31.39	0.0000
	Airport	895	0.0000	0.5356	52.19	0.0000

Table 4-5 Results of Skewness/Kurtosis tests for normality (Gust speed (km/h) during winter (21/01/2011 to 28/02/2011) and summer (26/07/2011 to 31/08/2011)

Season	Location	Obs	Pr (Skewness)	Pr (Kurtosis)	Chi^2 (2)	$Pr>chi^2$
Winter	City centre	128	0.3530	0.0031	8.56	0.0139
	Sabkha	168	0.5931	0.0000	17.02	0.0002
	Park	132	0.0054	0.0067	12.64	0.0018
	Farm	366	0.0005	0.0000	67.20	0.0000
	Factory	142	0.1613	0.0005	11.94	0.0026
	Airport	936	0.0000	0.6037	52.87	0.0000
Summer	City centre	174	0.0024	0.3596	8.99	0.0112
	Sabkha	145	0.4621	0.0000	56.29	0.0000
	Park	142	0.0671	0.0000	.	0.0000
	Farm	265	0.0000	0.5341	19.83	0.0000
	Factory	169	0.0199	0.0021	12.64	0.0018
	Airport	895	0.0000	0.6499	31.97	0.0000

4.3 **Relationship between surface and air temperature**

There is a strong relationship between the surface and air temperature especially in the canopy layer, which is closest to the surface. The influence of the surface temperature has a significant impact on the air and near-surface temperature. For example, parks and vegetated areas, which have cooler surface temperature, lead to cooler air temperature, while the built-up areas, on the other hand, lead to warmer air temperature. Pearson correlation tests between surface and air temperature during the August and February shows a significant relationship with correlation values of (0.863) for August and (0.883) for February (Figure 4-12).

Figure 4-12 Correlation between the surface and air temperature during August and February 2011

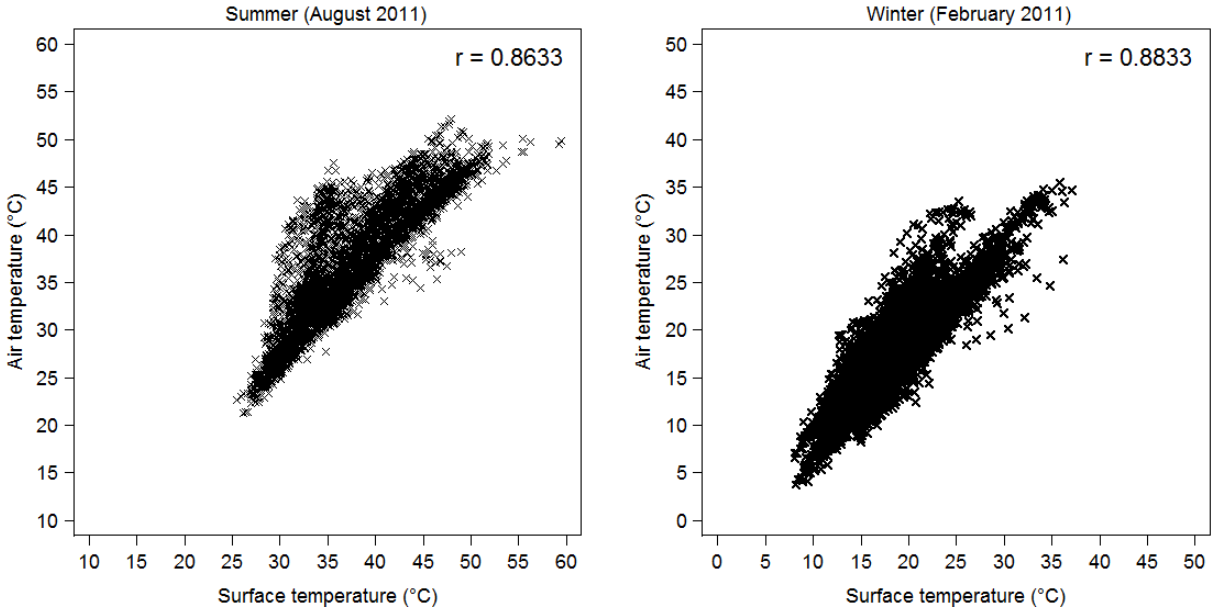

4.4 **Seasonal variations of meteorological data in different land cover**

A non-parametric test of the median values for air temperature, surface temperatures, relative humidity, wind speed, and gust speed of each land cover area (City centre, Sabkha, Park, Farm, Factory, and Airport) for both seasons (winter and summer), showed that there is a statistically significant difference among these groups. The results of a Kruskal–Wallis test for median comparison of air temperatures, surface temperatures, relative humidity, wind speed, and gust speed indicates λ2=150.16 with (5) *d.f.* *P*=0.0001, λ2=1100.003 with (4) *d.f.* *P*=0.0001, λ^2=2052.331 with (5) *d.f.* *P*=0.0001, λ^2= 686.358 with (5) *d.f.* *P*=0.0001, and λ^2=135.208 with (5) *d.f.* *P*=0.0001 respectively during the winter. While the results of a Kruskal–Wallis test for median comparison of air temperatures, surface temperatures, relative humidity, wind speed, and gust speed indicates λ2=471.726 with (5) *d.f.* *P*=0.0001, λ2=1743.199 with (4) *d.f.* *P*=0.0001, λ2=793.541 with (5) *d.f.* *P*=0.0001, λ2=775.140 with (5) *d.f.* *P*=0.0001, and λ2=259.283 with (5) *d.f.* P=0.0001 respectively during the summer (Table 4-6, Table 4-7, Table 4-8, Table 4-9, and Table 4-10).

Table 4-6 Kruskal–Wallis test for median comparison of air temperature during winter and summer seasons

Season	Location	Obs	Rank sum	Summary of the test result
Winter	City centre	936	2.94e+06	λ2 = 150.16 with (5) *d.f.* *P*=0.0001 λ2 with ties = 150.16 with (5) *d.f.* *P*=0.0001
	Sabkha	936	2.44e+06	
	Park	936	2.64e+06	
	Farm	936	2.25e+06	
	Factory	936	2.93e+06	
	Airport	936	2.58e+06	
Summer	City centre	888	2.80e+06	λ2= 471.726 with (5) *d.f.* *P*=0.0001 λ2 with ties = 471.727 with (5) *d.f.* *P*=0.0001
	Sabkha	888	2.17e+06	
	Park	888	2.48e+06	
	Farm	888	1.59e+06	
	Factory	888	2.74e+06	
	Airport	888	2.42e+06	

Table 4-7 Kruskal–Wallis test for median comparison of surface temperature during winter and summer seasons

Season	Location	Obs	Rank sum	Summary of the test result
Winter	City centre	936	2.64e+06	λ2= 1100.003 with (4) *d.f.* *P*=0.0001 λ2 with ties = 1100.008 with (4) *d.f.* *P*=0.0001
	Sabkha	936	2.13e+06	
	Park	936	1.57e+06	
	Farm	936	1.52e+06	
	Factory	936	3.10e+06	
Summer	City centre	888	2.82e+06	λ2= 1743.199 with (4) *d.f.* *P*=0.0001 λ2 with ties = 1743.204 with (4) *d.f.* *P*=0.0001
	Sabkha	888	2.05e+06	
	Park	888	1.78e+06	
	Farm	888	733627.00	
	Factory	888	2.47e+06	

Table 4-8 Kruskal–Wallis test for median comparison of relative humidity during winter and summer seasons

Season	Location	Obs	Rank sum	Summary of the test result
Winter	City centre	936	2.58e+06	λ^2= 2052.331 with (5) *d.f.* *P*=0.0001 λ^2 with ties = 2052.340 with (5) *d.f.* *P*<0.0001
	Sabkha	936	3.10e+06	
	Park	936	2.92e+06	
	Farm	936	3.62e+06	
	Factory	936	703541.00	
	Airport	936	2.85e+06	
Summer	City centre	888	2.09e+06	λ2= 793.541 with (5) *d.f.* *P*=0.0001 λ2 with ties = 793.559 with (5) *d.f.* *P*=0.0001
	Sabkha	888	2.59e+06	
	Park	888	2.15e+06	
	Farm	888	3.44e+06	
	Factory	888	2.04e+06	
	Airport	888	1.89e+06	

Table 4-9 Kruskal–Wallis test for median comparison of wind speed during winter and summer seasons

Season	Location	Obs	Rank sum	Summary of the test result
Winter	City centre	128	65250.00	λ^2= 686.358 with (5) *d.f.* *P*=0.0001 λ^2 with ties = 726.173 with (5) *d.f.* *P*<0.0001
	Sabkha	168	180625.00	
	Park	132	68090.00	
	Farm	366	178474.50	
	Factory	142	118437.00	
	Airport	936	1.14e+06	
Summer	City centre	174	82602.50	λ2= 775.140 with (5) *d.f.* *P*=0.0001 λ2 with ties = 829.803 with (5) *d.f.* *P*=0.0001
	Sabkha	145	136156.00	
	Park	142	97959.50	
	Farm	265	100015.50	
	Factory	169	106090.50	
	Airport	895	1.08e+06	

Table 4-10 Kruskal–Wallis test for median comparison of gust speed during winter and summer seasons

Season	Location	Obs	Rank sum	Summary of the test result
Winter	City centre	128	105817.00	λ^2= 135.208 with (5) *d.f.* *P*=0.0001 λ^2 with ties = 136.031 with (5) *d.f.* *P*<0.0001
	Sabkha	168	202228.50	
	Park	132	91787.00	
	Farm	366	274915.00	
	Factory	142	154795.50	
	Airport	936	923585.00	
Summer	City centre	174	130490.00	λ2= 259.283 with (5) *d.f.* *P*=0.0001 λ2 with ties = 260.680 with (5) *d.f.* *P*=0.0001
	Sabkha	145	155983.00	
	Park	142	119731.00	
	Farm	265	129357.50	
	Factory	169	145184.50	
	Airport	895	922199.00	

4.4.1 Air temperature variation

The distribution of air temperature is presented in Figure 4-13. The median, maximum, minimum, and first and third quartiles of air temperature data vary among the different land cover areas in the study area during the winter and summer. In general, the farm, park, and sabkha sites have the lowest air temperature, due to the shading and transpiration of the trees and vegetation in the farm and park and due to the evaporation effect in the sabkha site. This effect on the maximum temperature is caused by palm trees at the farm, and trees and grass at the park, channelling the solar gain into latent heat. However, the opposite distribution of air temperature was seen at the city centre and factory sites during both winter and summer. High temperatures may be explained in the city by emissions from roads and concrete buildings, which are the most common features in this location; and by industrial activities at the factory site.

There are statistically significant differences in air temperature between each pair of land cover areas during both winter and summer (Table 4-11). The Kruskal-Wallis test showed that the air temperature at all locations is significantly different, with P=0.000. That difference might be referred to the different of the nature surfaces of these locations, e.g. (between city centre and sabkha), which might affect the reflected radiation and the reflected heat balance. However, there is no statistically significant differences in air temperature between city centre and factory (P=0.852 in winter and P=0.262 in summer); sabkha and park (P=0.003), farm (P=0.007), and airport (P=0.033) in winter; and park and airport (P=0.384 in winter and P=0.281 in summer). The equal medians of the above mentioned sites might be explained by the similarity of the conditions between, for example, city centre and factory on one hand, and park and farm on the other. These results strongly indicate the presence of a heat island effect in the study area during the study periods.

Figure 4-13 Box plot of hourly air temperature (°C) during winter and summer seasons

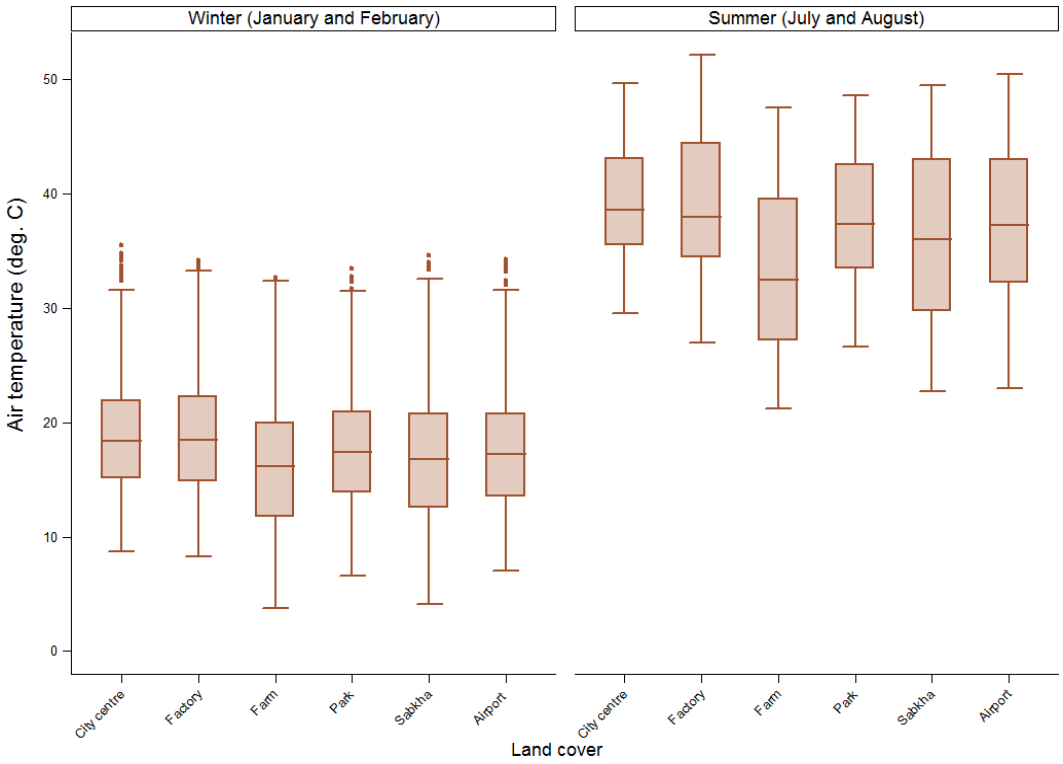

Note: The graph shows the medians (central lines) and inner quartile ranges (boxes) at land cover.

Table 4-11 A result of the Kruskal–Wallis test of air temperature during winter and summer between each pair of land cover areas

Location	Season	City centre	Sabkha	Park	Farm	Factory	Airport
City centre							
Sabkha	Winter	≠(0.000)					
	Summer	≠(0.000)					
Park	Winter	≠(0.000)	=(0.003)				
	Summer	≠(0.000)	≠(0.000)				
Farm	Winter	≠(0.000)	=(0.007)	≠(0.000)			
	Summer	≠(0.000)	≠(0.000)	≠(0.000)			
Factory	Winter	=(0.852)	≠(0.000)	≠(0.000)	≠(0.000)		
	Summer	=(0.262)	≠(0.000)	≠(0.000)	≠(0.000)		
Airport	Winter	≠(0.000)	=(0.033)	=(0.384)	≠(0.000)	≠(0.000)	
	Summer	≠(0.000)	≠(0.000)	=(0.281)	≠(0.000)	≠(0.000)	

Note: '=' indicates no difference (accept – H_0) and '≠' indicates significant difference (accept - H_1). Values in parentheses indicate calculated *P* values. Adjusted probability (P'=0.0033).

4.4.2 Surface temperature variation

There is clear variation in surface temperature distribution during both seasons at different land covers (Figure 4-14). The median, maximum, minimum, and first and third quartiles of surface

temperature data vary among the different land covers in the study area during both winter and summer. Overall, the farm and park sites had the lowest surface temperatures during both seasons, which can be explained by the irrigation water used and by the shade of trees and palms at both sites. The shade and irrigation water have an impact on the rate of cooling, and accelerate the loss of heat which was absorbed during the daytime. However, the opposite distribution of surface temperature can be found at the city centre, factory, and sabkha sites during both seasons. Factors that might increase surface temperatures here may include the extensive use of concrete in buildings, roads and in emissions from industrial activities and factories.

There are statistically significant differences in surface temperature between each land cover area during both seasons (Table 4-12). The Kruskal-Wallis test showed that the surface temperature at all locations is significantly different between each pair (P=0.000). The exception is between the park and farm sites, which indicate no significant difference (P=0.360). Equal median temperatures at the farm and park sites may be explained by the similarity of the surface land cover - irrigated shadowed land in the farm area, and wet grass land in the park.

Figure 4-14 Hourly surface temperature distributions in different land cover areas during winter and summer

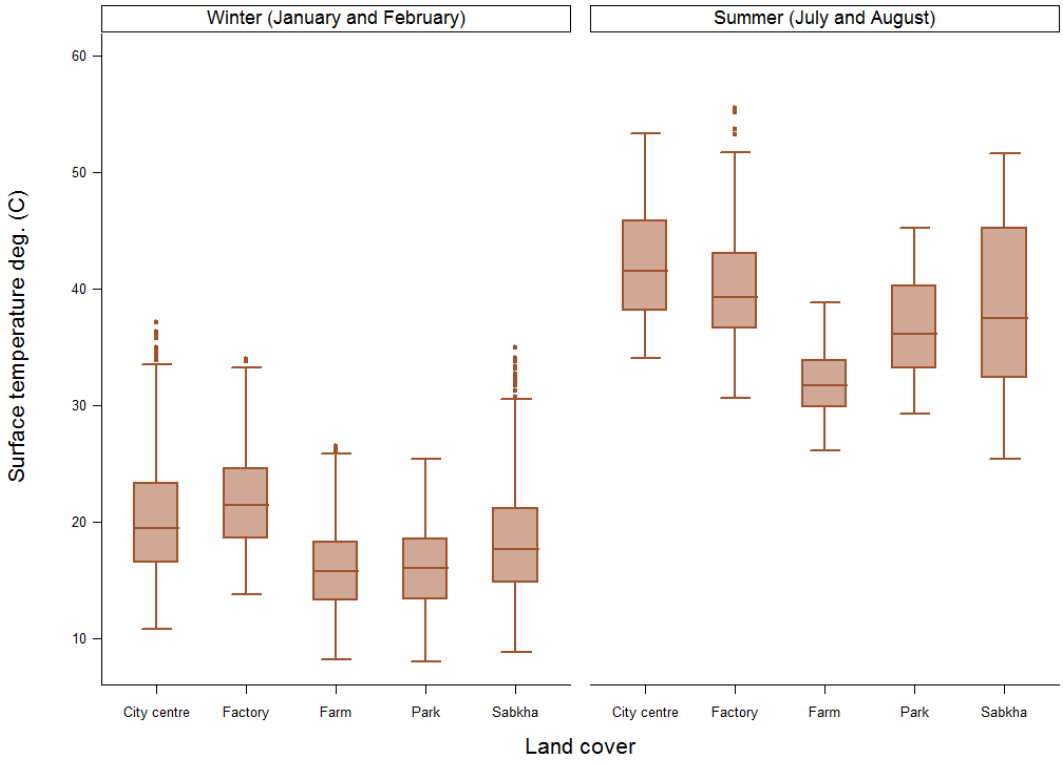

Table 4-12 Results of the Kruskal–Wallis test for surface temperature during winter and summer seasons between each pair of land cover areas

Location	Season	City centre	Sabkha	Park	Farm	Factory
City centre						
Sabkha	Winter	≠(0.000)				
	Summer	≠(0.000)				
Park	Winter	≠(0.000)	≠(0.000)			
	Summer	≠(0.000)	≠(0.000)			
Farm	Winter	≠(0.000)	≠(0.000)	=(0.360)		
	Summer	≠(0.000)	≠(0.000)	≠(0.000)		
Factory	Winter	≠(0.000)	≠(0.000)	≠(0.000)	≠(0.000)	
	Summer	≠(0.000)	≠(0.000)	≠(0.000)	≠(0.000)	

Note: '=' indicates no difference (accept – H_0) and '≠' indicates significant difference (accept - H_1). Values in parentheses indicate calculated *P* values. Adjusted probability (P'=0.005).

4.4.3 Relative humidity variation

Relative humidity data distributions for all locations during winter and summer are shown in Figure 4-15. Overall, it is clear that relative humidity measurements were lower in summer than in winter. That could be explained by the different atmospheric circulation systems that affect the study area in summer, as mentioned in Chapter Two (Study Area, section 2.4). The maximum relative humidity is observed in the farm area during the winter and summer. However, the city centre and factory show the opposite data distribution to the farm, with the lowest median of relative humidity. The park, sabkha, and airport showed different distributions during the winter and summer.

The Kruskal–Wallis test between pairs shows that there is a significant difference between each pairs of relative humidity measurements with (P=0.000) during both winter and summer seasons (Table 4-13). However, the park and city centre sites indicate no significant difference in relative humidity during summer (P=0.483). This might be explained by the close proximity of the park and city centre sites to one another.

Figure 4-15 Hourly relative humidity distributions in the different land cover areas during winter and summer

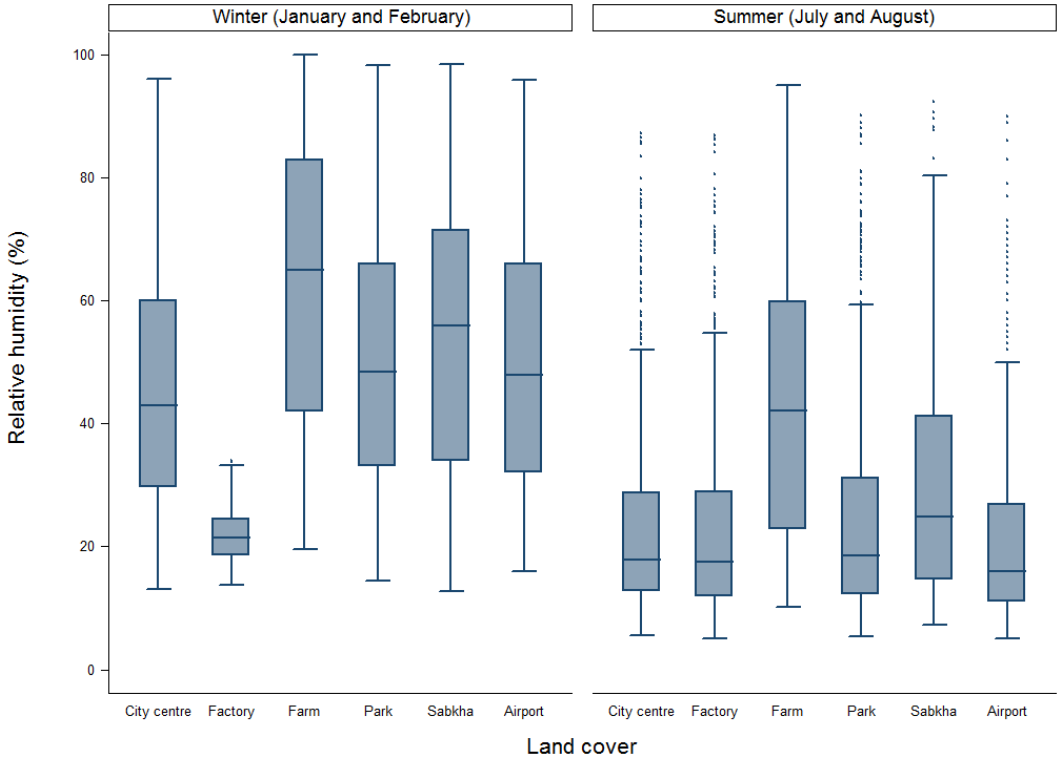

Table 4-13 Results of Kruskal–Wallis tests of relative humidity during winter and summer seasons between each pair of land cover areas

Location	Season	City centre	Sabkha	Park	Farm	Factory	Airport
City centre							
Sabkha	Winter	≠(0.000)					
	Summer	≠(0.000)					
Park	Winter	≠(0.000)	≠(0.000)				
	Summer	=(0.483)	≠(0.000)				
Farm	Winter	≠(0.000)	≠(0.000)	≠(0.000)			
	Summer	≠(0.000)	≠(0.000)	≠(0.000)			
Factory	Winter	≠(0.000)	≠(0.000)	≠(0.000)	≠(0.000)		
	Summer	=(0.278)	≠(0.000)	=(0.085)	≠(0.000)		
Airport	Winter	≠(0.000)	≠(0.000)	=(0.371)	≠(0.000)	≠(0.000)	
	Summer	≠(0.000)	≠(0.000)	≠(0.000)	≠(0.000)	≠(0.010)	

Note: '=' indicates no difference (accept – H_0) and '≠' indicates significant difference (accept - H_1). Values in parentheses indicate calculated P values. Adjusted probability (P'=0.0033).

4.4.4 Wind and gust speed variation

There are statistically significant differences in wind and gust speed among different land cover during the winter and the summer season. Table 4-14 and Table 4-15 indicate the result of Kruskal-Wallis test between each pair in order of the wind and gust speed during both

seasons. The Kruskal-Wallis test shows that the wind and gust speed at all locations are significantly different between each pair (P=0.000). However, some of the locations indicate no significant difference of the wind and gust speed such as between city centre and park; farm and park; and city centre and farm with (P=0.902, P=0.432, and P=0.360) during winter respectively. While, the equal locations of the gust speed included between city centre and park in the summer; city centre and farm in the winter; and farm and park in the winter with (P=0.356, P=0.032, and P=0.955) respectively. That might be explained by the similarity of the canopy level of these locations for example the height of the trees might interrupt the wind and gust speed in the farm and park.

Table 4-14 Results of Kruskal–Wallis tests of wind speed during winter and summer seasons between each pair of land cover areas

Location	Season	City centre	Sabkha	Park	Farm	Factory	Airport
City centre							
Sabkha	Winter	≠(0.000)					
	Summer	≠(0.000)					
Park	Winter	=(0.902)	≠(0.000)				
	Summer	≠(0.001)	≠(0.000)				
Farm	Winter	=(0.360)	≠(0.000)	=(0.432)			
	Summer	≠(0.000)	≠(0.000)	≠(0.000)			
Factory	Winter	≠(0.000)	≠(0.000)	≠(0.000)	≠(0.000)		
	Summer	≠(0.000)	≠(0.000)	=(0.152)	≠(0.000)		
Airport	Winter	≠(0.000)	≠(0.000)	≠(0.000)	≠(0.000)	≠(0.000)	
	Summer	≠(0.000)	≠(0.000)	≠(0.000)	≠(0.000)	≠(0.000)	

Note: '=' indicates no difference (accept – H_0) and '≠' indicates significant difference (accept - H_1). Values in parentheses indicate calculated P values. Adjusted probability (P'=0.0033).

Table 4-15 Results of Kruskal–Wallis tests of gust speed during winter and summer seasons between each pair of land cover areas

Location	Season	City centre	Sabkha	Park	Farm	Factory	Airport
City centre							
Sabkha	Winter	≠(0.000)					
	Summer	≠(0.000)					
Park	Winter	=(0.003)	≠(0.000)				
	Summer	=(0.356)	≠(0.000)				
Farm	Winter	=(0.032)	≠(0.000)	=(0.955)			
	Summer	≠(0.000)	≠(0.000)	≠(0.000)			
Factory	Winter	≠(0.000)	=(0.021)	≠(0.000)	≠(0.000)		
	Summer	=(0.029)	≠(0.000)	=(0.689)	≠(0.000)		
Airport	Winter	≠(0.000)	≠(0.000)	≠(0.000)	≠(0.000)	=(0.039)	
	Summer	≠(0.000)	=(0.180)	≠(0.001)	≠(0.000)	≠(0.000)	

Note: '=' indicates no difference (accept – H_0) and '≠' indicates significant difference (accept - H_1). Values in parentheses indicate calculated P values. Adjusted probability (P'=0.0033).

4.4.5 Intensity of local CLHIs

4.4.5.1 *Air temperature*

The means of air temperature during January and February in 2011 range from 11.4 °C at the Farm site at 6am, to 24.5 °C at the Factory site at 3pm. Conversely, air temperature mean values range from 25.2 °C at the Farm site at 6am to 47.7 °C at the Factory at 2pm during July and August in 2011. All the selected land cover types (City centre, Factory, Farm, Park, Sabkha, and Airport) show a similar pattern during both winter and summer - lowest air temperature at night, starting to increase around 7am to reach a maximum temperature around 2 to 3pm, and then starting to decrease again after sunset, around 5pm in the winter and 6:30pm in the summer (Figure 4-16).

The intensity of local CLHIs can be measured by the difference between the rural and urban stations (Yagüe et al., 1991, Jauregui et al., 1992, Karaca et al., 1995). The difference between the mean air temperature of the urban sites from the mean of the airport weather station, located in a rural area, show that the city centre and factory sites were the highest compared to the airport weather station in both winter and summer. The farm and park sites show the opposite result, having the lowest difference compared to the airport site. Through Figure 4-17 we can see that the local CLHI effect appears weaker during winter than in summer. In general, the difference in mean air temperature is greater during the night and becomes smaller during the day. The difference in mean air temperature from the airport mean is largest at the farm site (-7.9 °C at 7 a.m. in the summer and -2.2 °C at 6 p.m. in the winter) during the summer and winter and at the farm and park respectively. However, the lowest difference of the mean from the airport mean is reported in the city centre during the summer season (4 °C) and at the factory site during the winter season (2.2 °C) (Figure 4-17).

Figure 4-16 Hourly mean air temperature at fixed weather stations during winter and summer

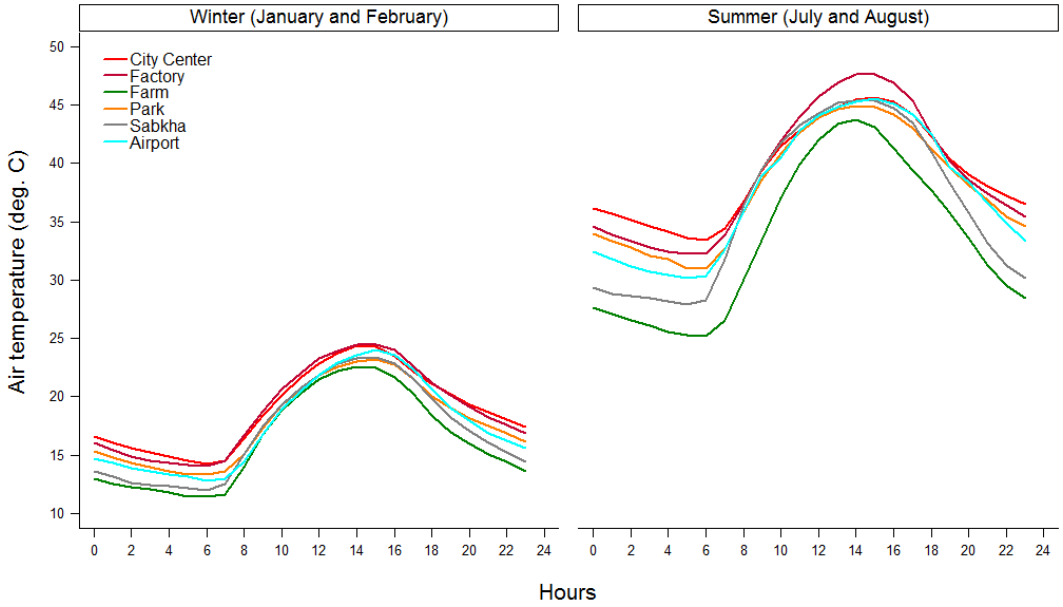

Figure 4-17 Hourly difference in air temperature means from the airport weather station during winter and summer

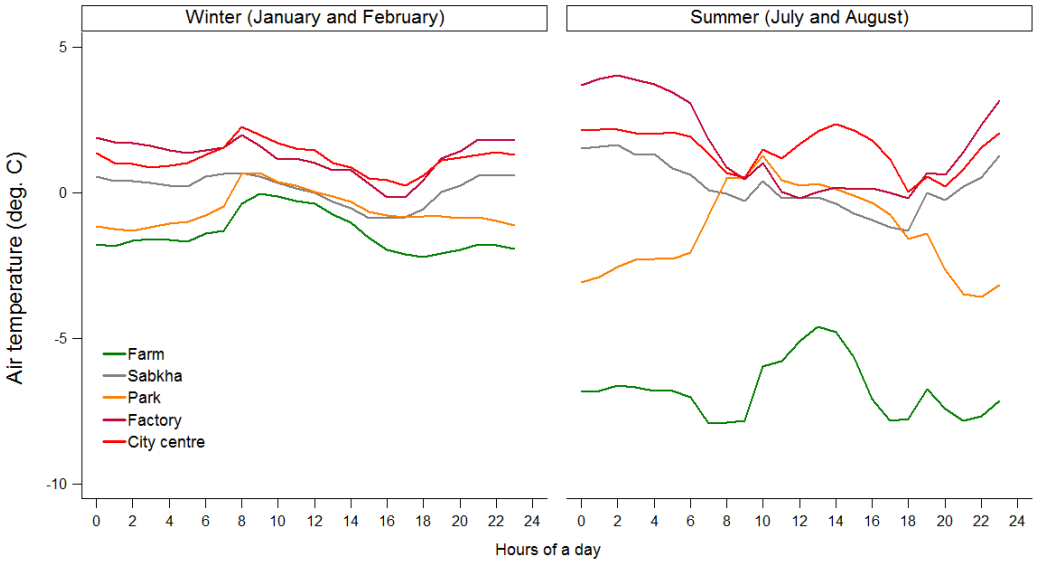

4.4.5.2 *Surface temperature*

During the winter, the mean surface temperature reaches a maximum at the city centre site (27.9 °C at 1pm) while the minimum value is recorded at the farm site (13.1 °C at 6am). However, during the summer, the maximum mean surface temperature is recorded at the city centre and sabkha sites (48.2 °C at 2pm), while the lowest value is observed at the farm site (28.4 °C at 6am). All sites show a similar diurnal pattern of surface temperature variation, dropping at night time and increasing after sunrise to reach a maximum around 1 to 2pm.

The farm and park sites show the lowest surface temperatures compared to the sabkha, factory, and city centre sites (Figure 4-18). This might relate to differences between land cover types, such as concrete, asphalt, grass, and wet sand. In addition, vegetation plays a major role in regulating temperature, since at the farm site incoming radiation energy can be converted into latent heat during the daytime. Thus, the sensible heat flux will be lower than at the factory and city centre sites, which are covered by asphalt or concrete (Wilmers, 1990, Jonsson, 2004). Also, the shade of palm trees at the farm site and the reflection of solar radiation from the surface vegetation reduce radiant absorption at the ground (Oke, 1987). At night, a farm or park with short plants or an area of open bare ground such as the sabkha may cool rapidly due to a higher radiative cooling rate (Spronken-Smith and Oke, 1999), whereas a built-up area, such as the city centre and factory sites, with a relatively low sky view factor may cool more slowly (Oke, 1981). We can see in Figure 4-19 that the differences in mean surface temperature from the overall mean varied between locations, in terms of the different land covers (farm, sabkha, park, factory, and city centre). The difference in mean surface temperature from the total mean of all sites shows the city centre and factory sites with the highest value compared to the farm, park, and sabkha sites.

Figure 4-18 Hourly of mean surface temperature at fixed weather stations during winter and summer

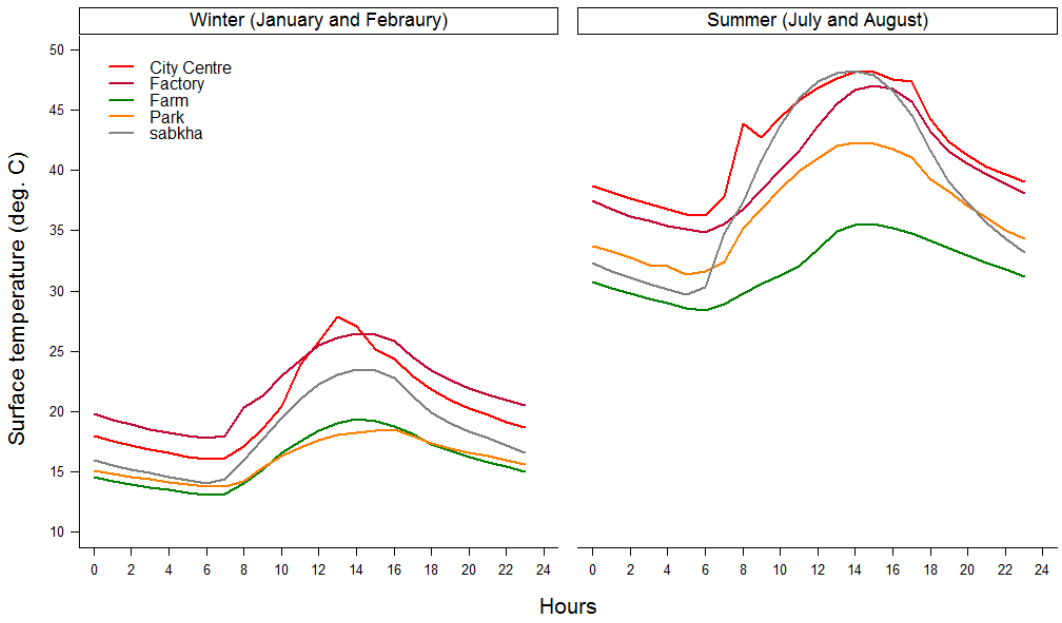

The biggest difference in mean surface temperature from the total mean is recorded in the farm site (-9 °C below the total mean at 12pm) and in the city centre (7.2 °C above the total mean at

8am) during the summer. During the winter, the mean surface temperature in the park has the lowest value (-4.8 °C below the total mean at 1am), while the city centre site has the highest difference of 5 °C above the total mean at 1am.

Figure 4-19 Hourly mean surface temperature difference from total mean during winter and summer

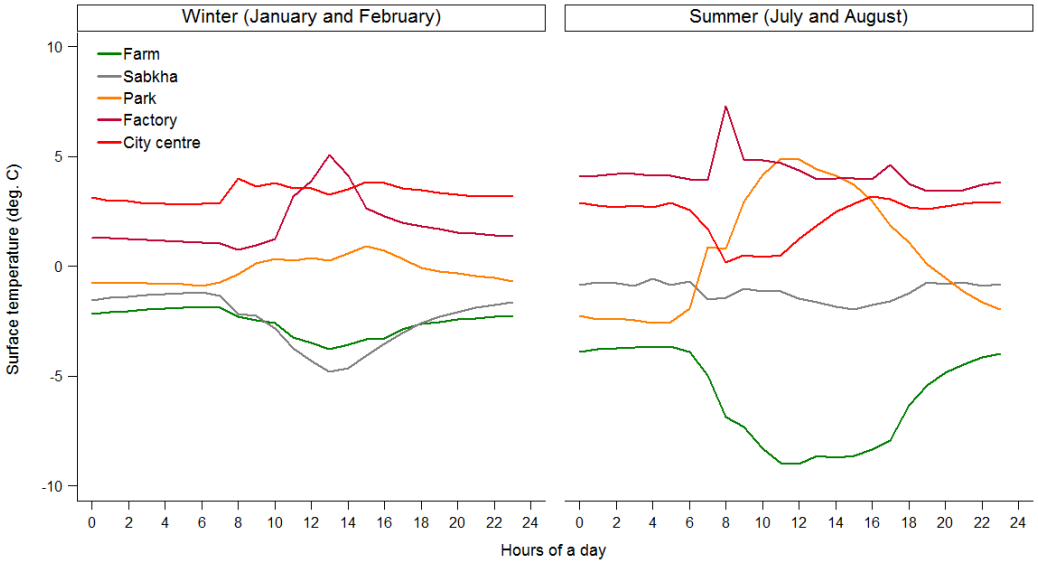

4.4.5.3 *Relative humidity*

In general, mean relative humidity shows the opposite relationship to air and surface temperature during both seasons. When the temperature increases, the relative humidity decreases. Mean relative humidity at all the sites shows an increase during the night hours and starts to drop around 7am, to reach a minimum value at 2pm either in the winter and summer seasons. The relative humidity value is affected by the pressure and wind systems that impact the whole region, as mentioned in Chapter Two (Section 2.4.1.4). The maximum mean relative humidity value is recorded at the farm site, with 80% and 70.7% at 7am in the winter and summer respectively, whilst the minimum value during winter is recorded at the factory site with 17% at 6am, and during summer with 9.6% at 3pm in the airport weather station (Figure 4-20).

Figure 4-20 Hourly graph of mean relative humidity at fixed weather stations during winter and summer

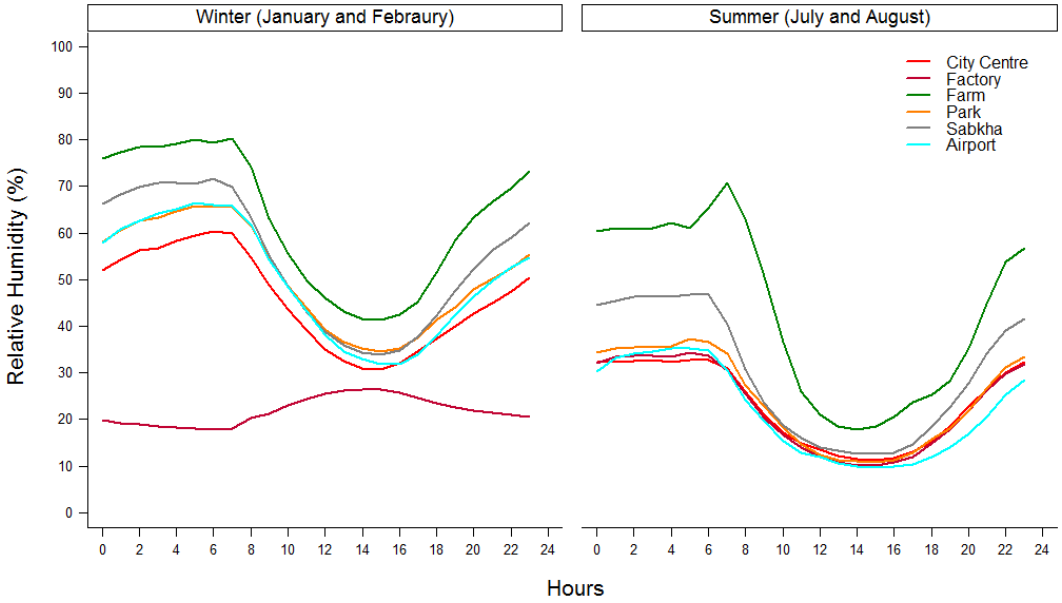

Figure 4-21 Hourly mean relative humidity difference from airport weather station during winter and summer

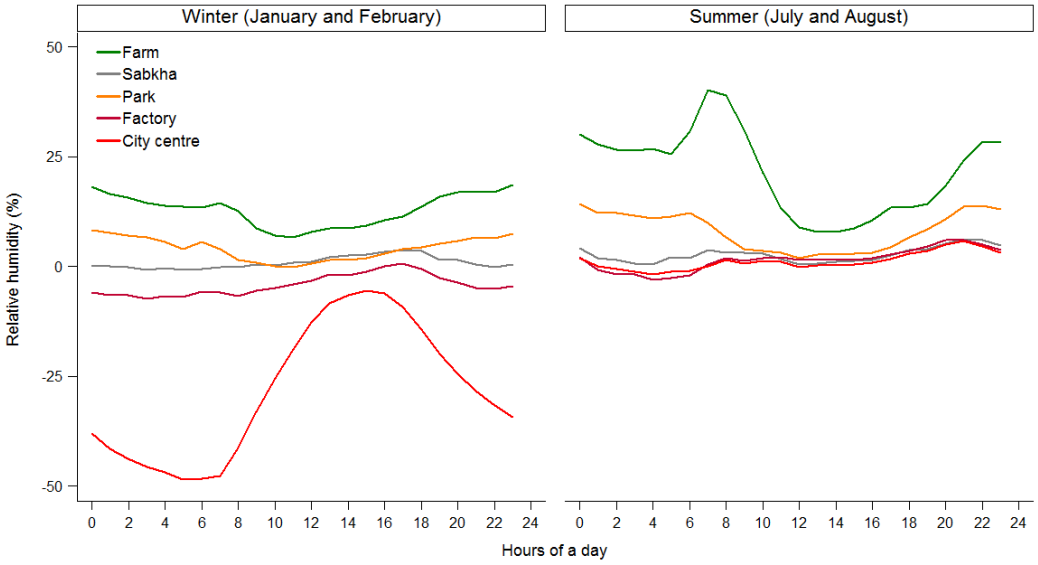

By comparing the mean relative humidity at the airport weather stations and other sites, it is seen that the biggest negative difference occurs at the city centre and factory sites, while the largest positive difference was at the farm and park sites. The city centre shows a difference in mean relative humidity which is greater during the night and early morning, but reduces between sunrise and sunset in the winter season (Figure 4-21). During the summer season, the difference between the airport and all urban locations is very small except for the farm site, which indicates a positive difference, especially during the night and early morning.

4.5 **Summary**

This chapter presents data on variations in air temperature, surface temperature, and relative humidity during two seasons (summer and winter) in 2011 and how they vary among key urban land cover types. In general terms, the data shows the existence of CLHI and SUHI effect in the study area at both seasonal and diurnal scale during the selected period, using data from fixed weather stations collected in different land cover types. Statistically, there is a significant difference between the median groups of air temperature, surface temperature, and relative humidity data from the fixed weather stations during the winter and summer seasons. The local urban heat island effect is stronger in the summer than in the winter, and more clear at night and early in the morning than during the day time. The average of air and surface temperatures and relative humidity indicated variation between the rural station (airport weather station) and the other fixed stations, factoring in the different urban land covers (park, sabkha, factory, city centre, and farm). The greatest intensity of urban heat islands is seen in the city centre and factory sites during both seasons, while the farm and park sites represented the lowest intensity of heat islands in the study area.

Chapter 5: Spatial and Temporal Distribution of Air UHI

5.1 Introduction

This chapter discusses the spatial and temporal distributions of local CLHIs. The aim of this chapter is to investigate the effect of land cover types on the air temperature and relative humidity of the study area. The main land covers found in the study area are sabkha, sand, built-up areas, vegetation, and water. The main land covers types are classified using the Landsat 8 image of 2013. Mobile air temperature and relative humidity were measured over the course of 46 traverses through the study area of Al Ahsa during January and February (winter) and August (summer) of 2011.

5.2 Summer mobile data

During the summer season (August 2011), twenty traverses were carried out in the study area. The air temperature and relative humidity were collected every 30 seconds, twice a day. The first traverse was made at night, approximately two to three hours before sunrise, while the second was after sunset. The duration of each traverse was between one and 2.5 hours. Each traverse took the same path during the night and after sunset, to pass through the same land covers as much as possible. Table 5-1 shows the date, period, start and end times, duration, and times of sunrise and sunset during the summer traverses.

Table 5-1 Mobile traverses schedule during August 2011 (after sunset and night-time)

Date	Period	Starting time	Ending time	Duration	Sunrise	Sunset
02/Aug	After sunset	18:33:59	20:58:36	02:24:37	05:09	18:27
	Night	01:47:15	04:43:28	02:56:13		
07/Aug	After sunset	19:00:45	20:52:35	01:51:50	05:11	18:23
	Night	02:45:17	04:21:04	01:35:47		
09/Aug	After sunset	19:14:31	21:29:31	02:15:00	05:12	18:22
	Night	02:11:05	04:25:05	02:14:00		
12/Aug	After sunset	18:56:47	21:25:17	02:28:30	05:14	18:19
	Night	02:28:29	04:48:59	02:20:30		
16/Aug	After sunset	19:01:16	20:48:46	01:47:30	05:15	18:16
	Night	02:27:41	04:03:11	01:35:30		
18/Aug	After sunset	18:58:01	21:31:31	02:33:30	05:16	18:14
	Night	02:20:07	04:47:07	02:27:00		
20/Aug	After sunset	18:48:41	21:10:11	02:21:30	05:17	18:13
	Night	02:35:50	04:39:50	02:04:00		
23/Aug	After sunset	18:54:54	21:15:54	02:21:00	05:18	18:10
	Night	02:27:06	04:24:06	01:57:00		
25/Aug	After sunset	18:57:27	20:57:57	02:00:30	05:19	18:08
	Night	02:26:52	04:28:52	02:02:00		
28/Aug	After sunset	18:43:38	19:58:08	01:14:30	05:20	18:05
	Night	02:45:51	04:20:21	01:34:30		

Note: Sunrise and sunset times obtained from the Weather Underground Inc. website: http://www.wunderground.com/

5.3 **Winter mobile data**

In the winter season (January and February 2011), twenty six traverses were considered in the study area. The air temperature and relative humidity were collected every 30 seconds, twice a day. The first time was at night, approximately two to four hours before sunrise, while the second was immediately after sunset. The duration of each traverse was between one and 2.5 hours. The path of each traverse was the same during the night and after sunset, so as to pass through the same land covers as much as possible. Table 5-2 shows the date, period, start and end times, duration, and times of sunrise and sunset during the winter traverses.

Table 5-2 Mobile traverses schedule during January and February 2011 (after sunset and night-time)

Date	Period	Starting time	Ending time	Duration	Sunrise	Sunset
27/Jan	After sunset	17:34:15	19:43:45	02:09:30	06:27	17:22
	Night	01:50:52	03:55:52	02:05:00		
02/Feb	After sunset	17:59:50	19:12:12	01:12:22	06:24	17:26
	Night	02:57:37	04:43:07	01:45:30		
06/Feb	After sunset	18:18:43	20:23:13	02:04:30	06:22	17:29
	Night	02:28:53	04:41:53	02:13:00		
08/Feb	After sunset	18:10:38	20:04:09	01:53:31	06:21	17:31
	Night	03:25:37	05:16:35	01:50:58		
12/Feb	After sunset	18:15:52	20:04:22	01:48:30	06:19	17:33
	Night	02:15:50	04:05:50	01:50:00		
15/Feb	After sunset	18:22:38	20:39:38	02:17:00	06:17	17:35
	Night	00:10:35	02:18:05	02:07:30		
18/Feb	After sunset	18:10:27	19:50:57	01:40:30	06:14	17:37
	Night	03:47:45	05:24:15	01:36:30		
19/Feb	After sunset	17:57:32	20:23:02	02:25:30	06:14	17:38
	Night	01:16:05	03:29:35	02:13:30		
20/Feb	After sunset	18:22:15	20:13:45	01:51:30	06:13	17:38
	Night	00:04:49	01:48:49	01:44:00		
21/Feb	After sunset	18:42:38	21:04:08	02:21:30	06:12	17:39
	Night	00:00:39	02:12:09	02:11:30		
22/Feb	After sunset	18:44:14	21:09:14	02:25:00	06:11	17:39
	Night	00:16:05	02:42:35	02:26:30		
23/Feb	After sunset	18:53:53	22:44:23	03:50:30	06:10	17:40
	Night	00:01:14	03:59:14	03:58:00		
24/Feb	After sunset	20:06:04	20:57:34	00:51:30	06:10	17:41
	Night	03:24:43	04:12:43	00:48:00		

Note: Sunrise and sunset times obtained from the Weather Underground Inc. website: http://www.wunderground.com/

5.4 **Land cover types from Landsat data**

The first source of land cover types of the study area is the Landsat data. The Landsat 8 Image 2013 classified using two different programmes: ENVI and Definiens Professional-5. As a result of the classification, both forms of software show accurate depictions of the main land cover types of the study area (Sabkha, Sand, Urban, Vegetation, and Water). However, the Definiens Professional-5 software shows more details of these classes, especially for Urban and Sabkha areas (Figure 5-1).

Figure 5-1 Supervised classification of Landsat 8 using ENVI (left) and Definiens professional software (right)

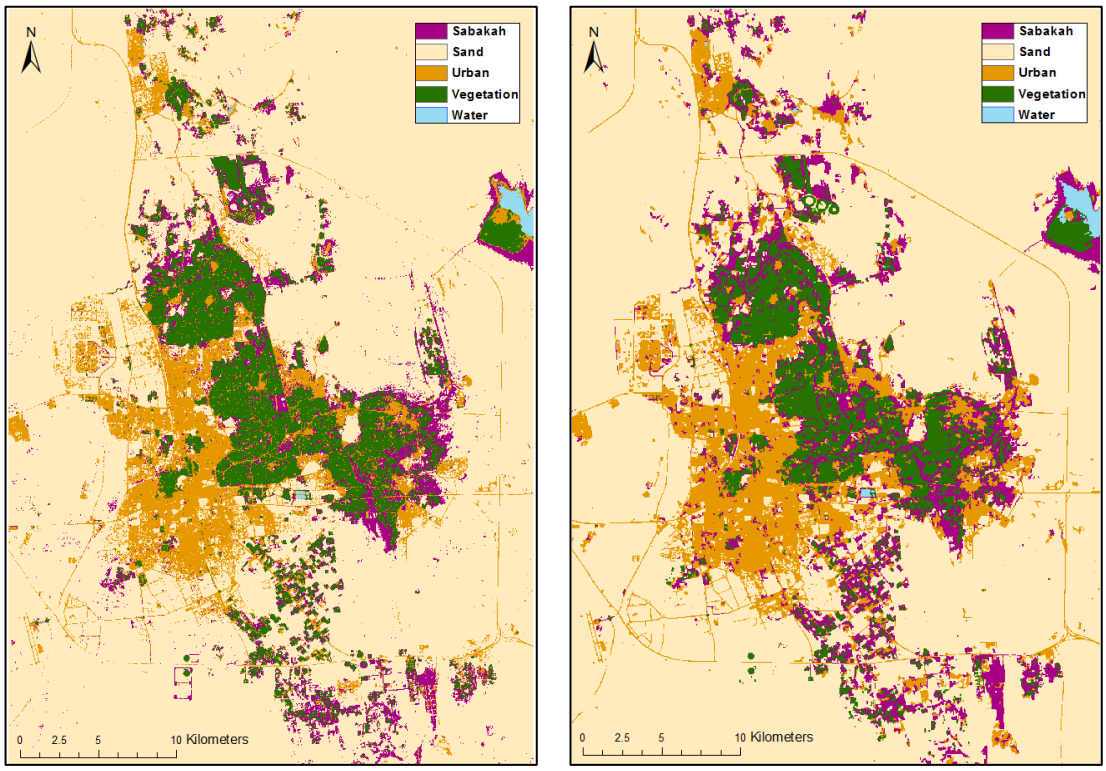

5.5 **Land cover types from GeoEye data**

The second source of land cover data of the study area is the GeoEye image. The GeoEye data at a spatial resolution of 0.5 metres shows more detail of land cover in the study area. The data set was used with mobile data to present the local CLHI profile and validate the classification results of the Landsat 8 image. The main land covers of the study area as mentioned before are: sand, sabkha, vegetation, built-up area, and water. However, to understand the effect of the different land covers on the air temperature and CLHIs intensity, the built-up of the study area are identified to sub-classes using GeoEye image as high resolution image (Oke, 2006). These classes are classified based on the intensity of the houses, vegetation, sand, and sabkha. Moreover, the classes and sub-classes are (1) vegetation (palm trees), class (2) water (evaporation lakes), class (3) sabkha, class (4) houses with vegetation, class (5) sand, class (6) sabkha mixed houses, class (7) sand with houses, class (8) low density of houses, and class (9) most the area is houses (Figure 5-2).

Figure 5-2 Sub-classes of the main land covers of the study area

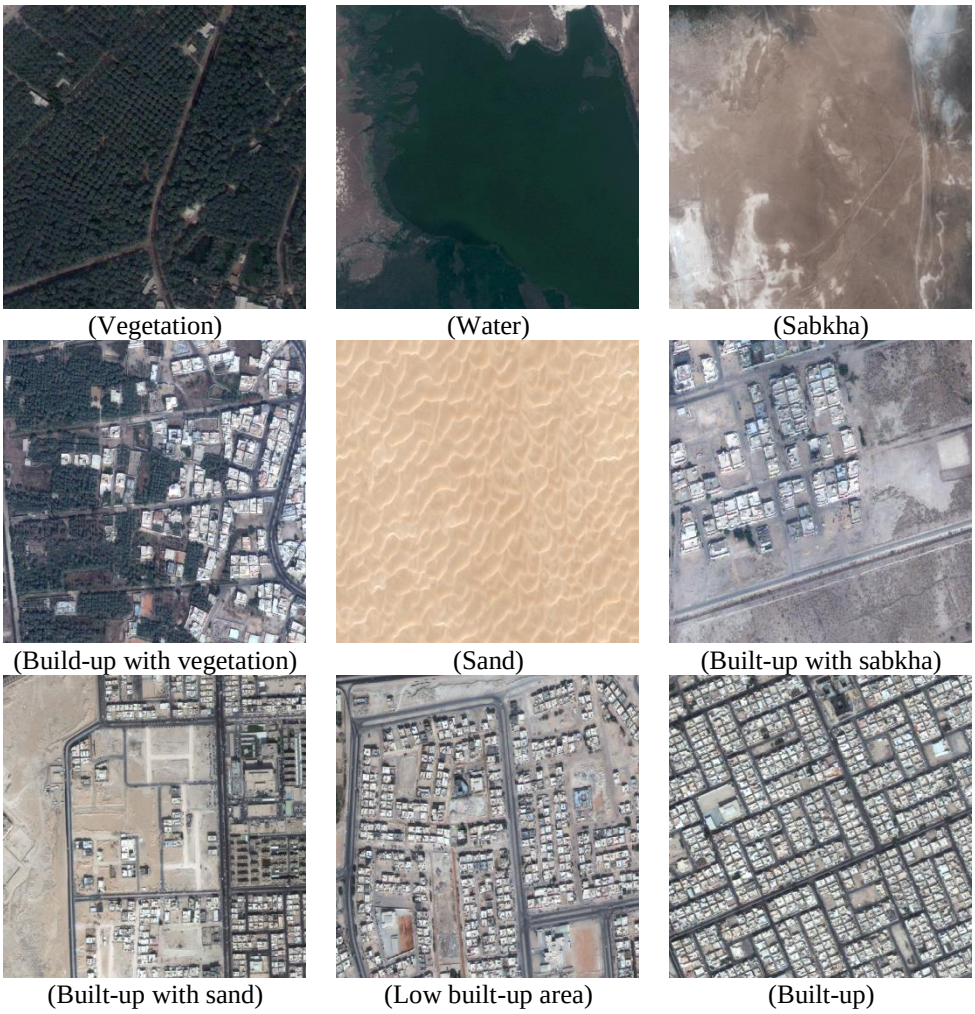

5.6 **Descriptive statistics and accuracy of mobile data**

Table 5-3 summarises air temperature and relative humidity during the night-time and after-sunset traverses in both winter and summer. In both traverses during both seasons, the difference between maximum, minimum, and mean air temperatures between night-time and after-sunset ranges from 4 °C to 7 °C. Meanwhile, the difference between maximum, minimum, and mean relative humidity between night-time and after-sunset ranges from 4% to 17%. Relative humidity percentages during winter were higher than in summer. Maximum relative humidity was 89.1% in the winter, compared to 77.1% in the summer. Also, relative humidity was higher at night-time than after sunset in both seasons (Table 5-3).

Table 5-3 Statistics summary of air temperature and relative humidity for mobile data during winter

Variable	Night Temperature (°C)		Sunset Temperature (°C)		Night RH (%)		Sunset RH (%)	
	Winter	Summer	Winter	Summer	Winter	Summer	Winter	Summer
Maximum	19.31	36.33	25.13	41.64	89.10	77.10	85.00	59.70
Minimum	8.56	23.88	13.16	30.95	28.10	16.40	19.60	9.70
Mean	14.60	30.85	19.94	36.87	54.94	34.32	37.37	24.87
Median	14.55	30.90	19.96	37.04	53.65	32.50	31.00	21.30
SD*	2.54	2.50	2.60	2.21	16.45	14.37	15.61	12.46
Range	10.75	12.45	11.97	10.69	61.00	60.70	65.40	50.00
Skewness	-.06	-.18	-.11	-.20	.46	1.07	1.32	0.97
Kurtosis	2.30	2.34	2.49	2.20	2.15	3.68	3.82	3.15

Note: SD = Standard deviation

The accuracy of mobile traverses data are examined by comparing them with fixed weather stations data when they match closely in time and location during the winter and summer seasons. The comparison shows close agreements between data measured by HOBO data loggers and mobile or fixed weather station data. During the winter the mean different between mobile data and fixed weather stations of air temperature is 0.28 °C at night and 0.43 °C after sunset and -2.1% at night and -1.0% after sunset for the relative humidity (Table 5-4). During the summer the mean difference in air temperature between mobile data and fixed weather station data is 0.05 °C at night and 0.10 °C after sunset and -0.7% at night and -0.4% after sunset for the relative humidity (Table 5-5).

Table 5-4 Air and relative humidity comparison between mobile and fixed weather stations data during winter at night and after sunset

Date	Time of observation				Air temperature in (°C)						Relative humidity (%)								
	Night		After sunset		Night			After sunset			Night			After sunset					
	MB	FWS	MB	FWS	MB	FWS	DI	MB	FWS	DI	MB	FWS	DI	MB	FWS	DI	WSL	LCT	DFFWS
27/01/11	02:14	02:00	17:49	20:00	15.99	15.80	0.19	20.41	18.41	2.00	87.6	94.6	-7.0	82.5	90.3	-7.8	FAR	BUP	480
02/02/11	03:54	04:00	18:58	19:00	13.16	12.94	0.22	18.49	19.63	-1.14	80.2	84.0	-3.8	59.1	51.1	8.0	SAB	SAB	421
06/02/11	03:37	04:00	19:12	19:00	14.58	12.97	1.61	15.77	14.96	0.81	78.0	80.6	-2.6	56.8	59.5	-2.7	PAR	BUP	1,457
08/02/11	03:53	04:00	18:34	19:00	10.86	10.08	0.78	23.64	22.71	0.93	52.0	56.8	-4.8	29.5	34.0	-4.5	FAC	VEG	949
12/02/11	03:08	03:00	19:11	19:00	12.27	12.05	0.22	17.51	18.39	-0.88	58.1	63.7	-5.6	34.2	35.0	-0.8	FAC	BUP	201
	03:21	03:00	19:21	19:00	12.05	12.05	0.00	17.37	18.39	-1.02	60.9	63.7	-2.8	36.7	35.0	1.7	CC	BUP	155
15/02/11	02:01	02:00	20:14	20:00	13.21	12.12	1.09	18.87	18.65	0.22	38.6	40.3	-1.7	28.3	19.7	8.6	CC	BUP	1,538
	00:53	01:00	19:17	19:00	12.82	11.47	1.35	20.10	18.3	1.80	37.5	45.1	-7.6	24.9	31.6	-6.7	FAC	BUP	1,741
18/02/11	05:18	05:00	19:45	20:00	15.27	15.06	0.21	20.82	19.51	1.31	57.6	58.0	-0.4	30.6	32.9	-2.3	CC	BUP	238
	05:16	05:00	19:42	20:00	15.37	15.06	0.31	20.72	19.51	1.21	57.4	58.0	-0.6	30.7	32.9	-2.2	CC	BUP	339
19/02/11	02:24	02:00	19:21	19:00	09.04	08.92	0.12	16.94	14.82	2.12	88.5	88.3	0.2	50.0	55.1	-5.1	FAR	VEG	1,407
20/02/11	00:55	01:00	19:11	19:00	14.12	15.80	-1.68	23.18	23.93	-0.75	46.4	41.4	5.0	20.7	21.0	-0.3	CC	BUP	1,186
21/02/11	01:54	02:00	20:45	21:00	19.27	18.94	0.33	22.25	20.94	1.31	29.1	30.1	-1.0	25.9	28.8	-2.9	CC	BUP	2,339
22/02/11	01:21	02:00	19:42	20:00	18.44	17.92	0.52	20.60	20.15	0.45	37.4	39.5	-2.1	32.9	34.9	-2.0	CC	BUP	531
	02:14	02:00	20:36	20:00	18.08	17.92	0.16	19.65	20.15	-0.50	37.9	39.5	-1.6	34.6	34.9	-0.3	CC	BUP	595
23/02/11	01:02	01:00	19:28	20:00	16.87	16.42	0.45	21.15	21.41	-0.26	45.2	45.3	-0.1	28.7	27.4	1.3	CC	BUP	2,051
24/02/11	03:29	03:00	20:11	20:00	15.68	16.82	-1.14	24.68	24.97	-0.29	39.1	38.4	0.7	27.6	27.6	0.0	PAR	BUP	2,482
Minimum							**-1.68**			**-1.14**			**-7.6**			**-7.8**			
Maximum							**1.61**			**2.12**			**5.0**			**8.6**			
Mean							**0.28**			**0.43**			**-2.1**			**-1.0**			

Note: MB = Mobile, FWS = Fixed weather station, DI = Different, WSL = Weather station location, LCT = Land cover type, DFFWS = Distant from weather station, FAR = Farm, SAB = Sabkha, BUP = Built-up area, VEG = Vegetation, CC = City centre, FAC = Factory.

Table 5-5 Air and relative humidity comparison between mobile and fixed weather stations data during summer at night and after sunset

Date	Time of observation				Air temperature in (°C)						Relative humidity (%)								
	Night		After sunset		Night			After sunset			Night			After sunset					
	MB	FWS	MB	FWS	MB	FWS	DI	MB	FWS	DI	MB	FWS	DI	MB	FWS	DI	WSL	LCT	DFFWS
02/08/11	04:28	04:00	20:43	21:00	34.05	35.8	-1.75	40.00	40.03	-0.03	34.2	33.0	1.2	15.4	16.7	-1.3	CC	BUP	48
	02:13	02:00	18:56	19:00	25.82	26.82	-1.00	38.39	37.32	1.07	68.5	67.6	0.9	25.6	28.2	-2.6	FAR	VEG	1,400
	02:29	03:00	19:07	19:00	26.26	28.05	-1.79	39.12	40.43	-1.31	46.9	55.2	-8.3	18.8	21.4	-2.6	SAB	SAB	20
07/08/11	03:34	03:00	19:52	20:00	25.28	26.52	-1.24	34.62	34.26	0.36	64.3	60.7	3.6	29.0	30.8	-1.8	FAR	VEG	262
09/08/11	02:18	02:00	19:21	19:00	35.69	35.00	0.69	38.81	39.63	-0.82	17.5	18.7	-1.2	17.2	17.4	-0.2	PAR	BUP	1,574
	04:18	04:00	21:21	21:00	34.15	35.61	-1.46	35.00	38.95	-3.95	19.4	17.9	1.5	30.9	29.4	1.5	CC	BUP	2,761
12/08/11	04:38	05:00	21:12	21:00	32.18	31.07	1.11	39.66	37.40	2.26	35.0	39.6	-4.6	12.6	14.2	-1.6	PAR	BUP	241
	03:57	04:00	20:29	20:00	31.13	30.87	0.26	39.63	38.31	1.32	36.8	39.4	-2.6	14.6	13.5	1.1	PAR	VEG	1,700
16/08/11	03:23	03:00	20:00	20:00	34.89	34.78	0.11	40.66	40.80	-0.14	18.0	17.8	0.2	10.6	10.4	0.2	CC	BUP	97
	03:08	03:00	19:46	20:00	30.75	31.82	-1.07	39.32	40.03	-0.71	21.2	19.7	1.5	11.2	10.6	0.6	FAC	BUP	608
	02:36	03:00	19:09	19:00	34.12	32.00	2.12	40.06	39.94	0.12	18.8	19.8	-1.0	9.90	9.30	0.6	PAR	BUP	353
18/08/11	03:56	04:00	20:33	21:00	34.78	34.68	0.10	37.84	37.07	0.77	19.0	19.5	-0.5	19.7	21.1	-1.4	CC	BUP	141
	04:34	04:00	21:18	21:00	34.6	34.05	0.55	37.48	36.88	0.60	19.3	19.5	-0.2	20.0	20.5	-0.5	FAC	BUP	579
	03:02	03:00	19:34	19:00	31.23	31.40	-0.17	37.07	39.30	-2.23	21.0	19.0	2.0	20.0	19.0	1.0	AIP	SAN	1,466
20/08/11	04:35	05:00	21:04	21:00	32.51	32.38	0.13	34.20	35.85	-1.65	23.5	23.7	-0.2	34.2	37.5	-3.3	CC	BUP	655
23/08/11	02:27	02:00	18:55	19:00	33.89	33.00	0.89	37.51	37.89	-0.38	62.7	69.7	-7.0	29.3	29.5	-0.2	CC	BUP	1,370
25/08/11	04:28	04:00	20:57	21:00	27.75	26.63	1.12	32.95	29.67	3.28	57.5	57.3	0.2	53.1	49.1	4.0	FAR	VEG	1,622
28/08/11	04:17	04:00	19:56	20:00	25.45	25.02	0.43	31.31	31.64	-0.33	38.3	37.5	0.8	23.4	24.4	-1.0	FAR	VEG	1,381
Minimum							**-1.79**			**-3.95**			**-8.3**			**-3.3**			
Maximum							**2.12**			**3.28**			**3.6**			**4.0**			
Mean							**-0.05**			**-0.10**			**-0.7**			**-0.4**			

Note: MB = Mobile, FWS = Fixed weather station, DI = Different, WSL = Weather station location, LCT = Land cover type, DFFWS = Distant from weather station, FAR = Farm, SAB = Sabkha, BUP = Built-up area, VEG = Vegetation, CC = City centre, FAC = Factory, SAN = Sand, AIP = Airport.

5.7 **Summer and winter mobile data distribution**

The mobile data distribution for both seasons indicates that the air temperature and relative humidity data are not normally distributed, either in the night-time or after-sunset periods. Probability plots (Figure 5-3 and Figure 5-4) as well as quantile distribution plots (also see appendix 5.1) clearly show skewness of the data in the tail and the centre of the mobile data distribution, for both air temperature and relative humidity in both seasons. In addition, the data skewness is greater during the winter for both variables. The log temperature and square root transformation methods of both air temperature and relative humidity indicate the same result, that the data is not normally distributed (Figure 5-3 and Figure 5-4). The Figure 5-3 and Figure 5-4 indicate that the data distribution of both air temperature and relative humidity are not normally distributed. The normal probability plot is generally not straight with two distinct peaks and that sort as curvature evinces bimodality.

Statistically, the air temperature and relative humidity based on original data, log temperature and square root transformation methods are not normally distributed. Skewness/Kurtosis tests showed "fail to accept" for the null hypothesis ("Air temperature and relative humidity observations at night and after sunset are normally distributed") at $P<0.05$ level, for both air temperature and relative humidity for the three different methods in both seasons (Table 5-6 and Table 5-7). Although some individual variables show a statistically normal distribution, such as air temperature during winter, the probability and Quantile distribution plots indicate that these are not in fact normally distributed. The decision to reject normal distribution was thus based on both graphic and statistical methods, to meet the good complete normality test (D'Agostino et al., 1990).

Figure 5-3 Probability distribution plots of air temperature (°C) during winter traverses

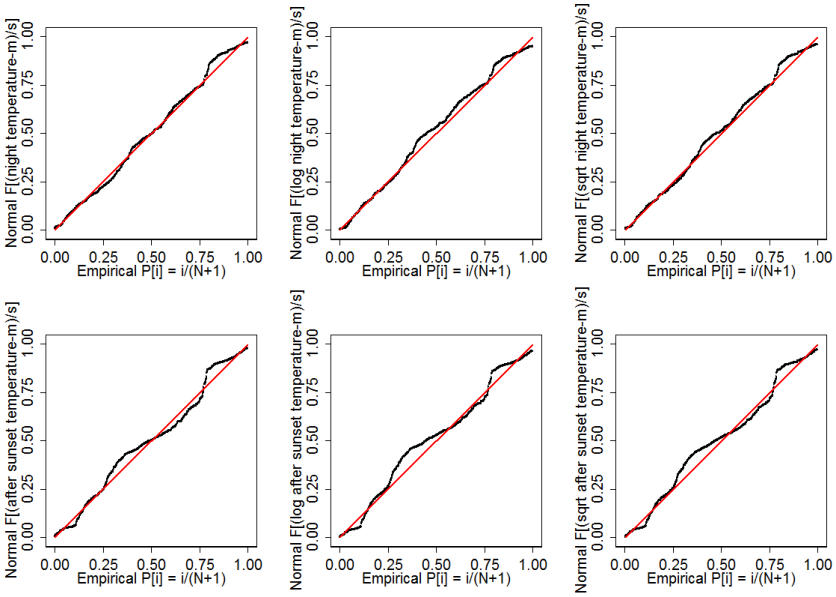

(a) Winter season

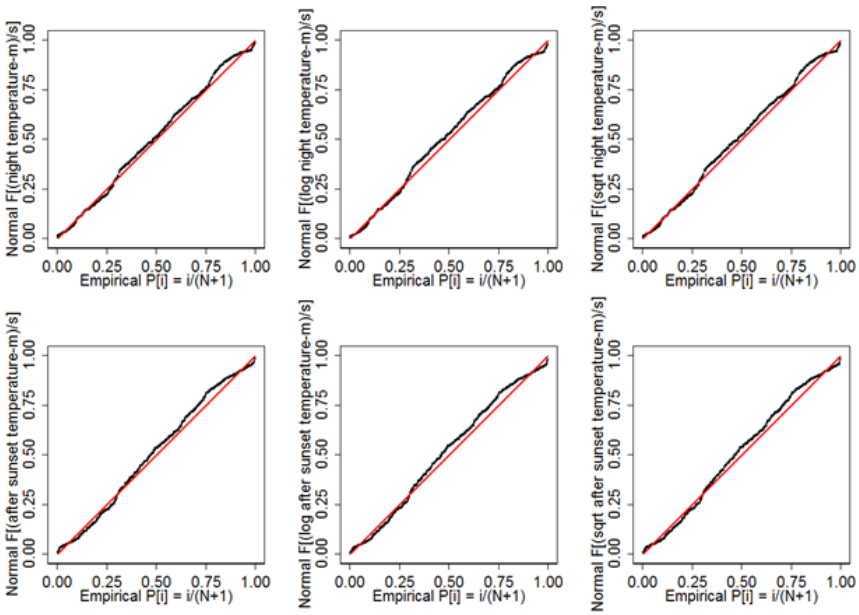

(b) Summer season

Note: at night and after sunset (a) and during summer traverses at night and after sunset (b). Original data left, log temperature in the middle, and square root transformation of air temperature right.

Figure 5-4 Probability distribution plots of relative humidity (%) during winter traverses

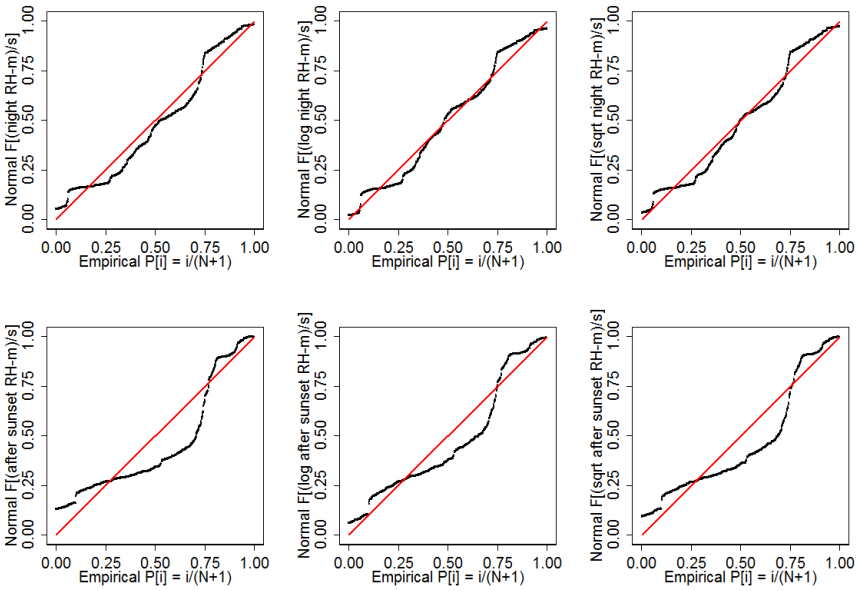

(a) Winter

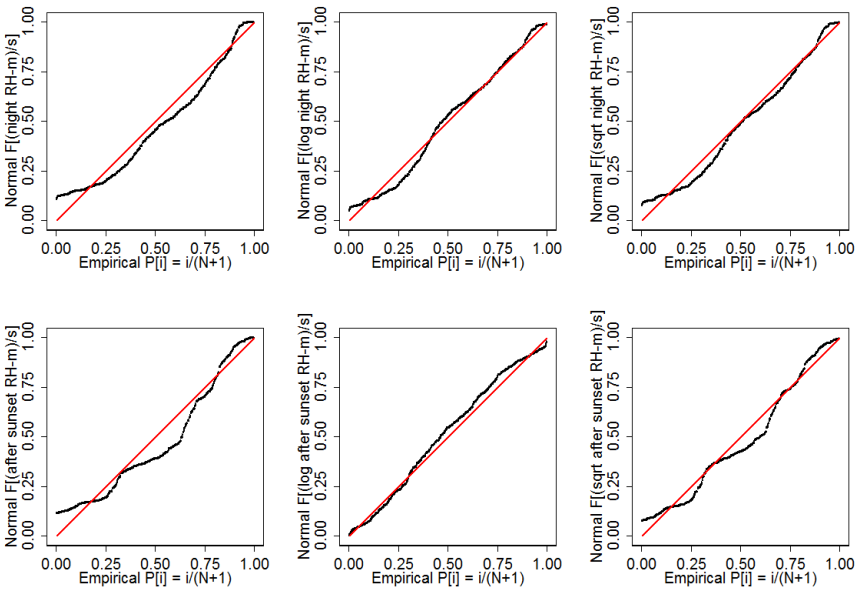

(b) Summer

Note: at night and after sunset (a) and during traverses at night and after sunset (b). Original data left, log relative humidity in the middle, and square root transformation of relative humidity right.

Table 5-6 Air temperature Skewness/Kurtosis tests for normality during winter and summer

Season	Air temperature	Obs	Pr (Skewness)	Pr (Kurtosis)	Adj chi2 (2)	Prob>chi2
Winter	Original data at night	972	0.4417	0.0000	40.29	0.0000
	Original data after sunset	972	0.1405	0.0000	18.30	0.0001
	Log at night	972	0.0000	0.0496	28.40	0.0000
	Log after sunset	972	0.0000	0.0853	25.73	0.0000
	SQRT at night	972	0.0020	0.0000	26.78	0.0000
	SQRT after sunset	972	0.0008	0.0016	18.74	0.0001
Summer	Original data at night	698	0.0494	0.0000	26.96	0.0000
	Original data after sunset	698	0.0271	0.0000	47.17	0.0000
	Log at night	698	0.0002	0.0003	22.81	0.0000
	Log after sunset	698	0.0009	0.0000	36.60	0.0000
	SQRT at night	698	0.0047	0.0000	24.16	0.0000
	SQRT after sunset	698	0.0056	0.0000	41.54	0.0000

Table 5-7 Relative humidity Skewness/Kurtosis tests for normality during winter and summer seasons

Season	Relative Humidity	Obs	Pr (Skewness)	Pr (Kurtosis)	Adj chi2 (2)	Prob>chi2
Winter	Original data at night	972	0.0000	0.0000	.	0.0000
	Original data after sunset	972	0.0000	0.0001	.	0.0000
	Log at night	972	0.9760	0.0000	.	0.0000
	Log after sunset	972	0.0000	0.0131	65.22	0.0000
	SQRT at night	972	0.0024	0.0000	.	0.0000
	SQRT after sunset	972	0.0000	0.3637	.	0.0000
Summer	Original data at night	698	0.0000	0.0029	.	0.0000
	Original data after sunset	698	0.0000	0.3627	65.65	0.0000
	Log at night	698	0.0011	0.0000	40.54	0.0000
	Log after sunset	698	0.0402	0.0000	66.20	0.0000
	SQRT at night	698	0.0000	0.3701	37.66	0.0000
	SQRT after sunset	698	0.0000	0.0002	39.94	0.0000

5.7.1 Seasonal variation of mobile data in different land cover

A non-parametric test of the median values for air temperature and relative humidity of each land cover area (Sabkha, Sand, Urban, and Vegetation) for both seasons (winter and summer) showed that there is a statistically significant difference among these groups. The results of a Kruskal–Wallis test for median comparison of air temperatures and relative humidity indicates $\lambda 2=47.128$ with (3) *d.f.* $P=0.0001$ and $\lambda 2=62.263$ with (3) *d.f.* $P=0.0001$ respectively during the winter, while the same test during summer indicates $\lambda 2=127.477$ with (3) *d.f.* $P=0.0001$ and $\lambda 2=60.432$ with (3) *d.f.* $P=0.0001$ respectively.

5.7.2 Air temperature variation

There are statistically significant differences in air temperature between each pair of land covers during both seasons (Table 5-8 and Table 5-9). The Kruskal-Wallis test shows that the air temperature at all land covers is significantly different, with P=0.000 except between sand and sabkha; P=0.015 during summer at night and P=0.134 during winter after sunset. Also, there are no significant differences between urban and sand land covers, with P=0.300 during summer after sunset, P=0.648 during winter at night, and P=0.709 after sunset. Neither are there significant differences between vegetation and sabkha during summer after sunset with P=0.409 (Table 5-8 and Table 5-9). The equal medians of air temperature over land covers mentioned above can be explained by the similarity of conditions between them; for example, between vegetation and sabkha on one hand, and sand and sabkha on the other. However, the equal medians between urban and sand areas might be also be explained by the location of most areas classified as sand inside the urban areas. In summary, these results strongly support the effect of land cover on air temperature during both winter and summer.

Table 5-8 A result of the Kruskal–Wallis test of air temperature at night and after sunset during summer between each pair of land covers of mobile data

Time	Variable	Sand	Urban	Vegetation
At night	Sabkha	=(0.015)	≠(0.000)	≠(0.000)
	Sand		≠(0.000)	≠(0.000)
	Urban			≠(0.000)
After sunset	Sabkha	≠(0.000)	≠(0.000)	=(0.409)
	Sand		=(0.300)	≠(0.000)
	Urban			≠(0.000)

Note: '=' indicates no difference (accept – H_0) and '≠' indicates significant difference (accept - H_1). Values in parentheses indicate calculated P values. Adjusted probability (P'=0.0083).

Table 5-9 A result of the Kruskal–Wallis test of air temperature at night and after sunset during winter between each pair of land covers of mobile data

Time	Variable	Sand	Urban	Vegetation
At night	Sabkha	≠(0.000)	≠(0.000)	≠(0.000)
	Sand		=(0.648)	≠(0.000)
	Urban			≠(0.000)
After sunset	Sabkha	=(0.134)	≠(0.000)	≠(0.000)
	Sand		=(0.709)	≠(0.000)
	Urban			≠(0.000)

Note: '=' indicates no difference (accept – H_0) and '≠' indicates significant difference (accept - H_1). Values in parentheses indicate calculated P values. Adjusted probability (P'=0.0083).

5.7.3 Relative humidity variation

There are also statistically significant differences in relative humidity between each pair of land covers during both seasons (Table 5-10 and Table 5-11). The Kruskal-Wallis test indicates that relative humidity over all land covers is significantly different with P=0.000. However, there are statistically no differences in relative humidity between the vegetation and sabkha during both seasons, with P=0.055 during summer after sunset, P=0.040 during winter at night, and P=0.095 during winter after sunset. Neither are there significant differences between urban and sand areas during winter, with P=0.312 at night and P=0.284 after sunset (Table 5-10 and Table 5-11). The equal medians for relative humidity between the vegetation and sabkha on one hand, and urban and sand on the other, is due to the similarity of conditions between these land covers areas. For example, vegetation and sabkha are similar as both locations feature include wet sand, an irrigation method used in farms and also a natural feature of sabkha land. Sabkha areas also contain large areas of sand. Similarly, the equal medians found in urban and sand measurements might be explained by the location of most sand areas inside urban areas, classified as sand.

Table 5-10 A result of the Kruskal–Wallis test of relative humidity at night and after sunset during summer between each pair of land covers of mobile data

Time	Variable	Sand	Urban	Vegetation
At night	Sabkha	≠(0.000)	≠(0.000)	≠(0.000)
	Sand		≠(0.000)	≠(0.000)
	Urban			≠(0.000)
After sunset	Sabkha	≠(0.000)	≠(0.000)	=(0.055)
	Sand		≠(0.000)	≠(0.000)
	Urban			≠(0.000)

Note: '=' indicates no difference (accept – H_0) and '≠' indicates significant difference (accept - H_1). Values in parentheses indicate calculated P values. Adjusted probability (P'=0.0083).

Table 5-11 A result of the Kruskal–Wallis test of relative humidity at night and after sunset during winter between each pair of land covers of mobile data

Time	Variable	Sand	Urban	Vegetation
At night	Sabkha	≠(0.000)	≠(0.000)	=(0.040)
	Sand		=(0.312)	≠(0.000)
	Urban			≠(0.000)
After sunset	Sabkha	≠(0.000)	≠(0.000)	=(0.095)
	Sand		=(0.284)	≠(0.000)
	Urban			≠(0.000)

Note: '=' indicates no difference (accept – H_0) and '≠' indicates significant difference (accept - H_1). Values in parentheses indicate calculated P values. Adjusted probability (P'=0.0083).

5.8 **Seasonal air temperature and relative humidity profiles**

The mobile data from the summer traverses show variations in air temperature and relative humidity between the different land cover areas. Most of the mobile traverses (see appendix 5.2) show an increase in air temperature in the urban areas and decreases in the sand, sabkha, and vegetation areas. For example, during day two (2nd August 2011) of the summer traverses, the maximum air temperature in the built-up area was 34 °C and the minimum air temperature was 25 °C in the vegetation area at night, while the maximum air temperature in the built-up area was 42 °C and the minimum air temperature was 36 °C in the vegetation area after the sunset. Therefore, the different between daytime and night-time air temperatures for the same day is 17 °C. Figure 5-5 shows an example of one day of data from summer traverses, with the tracking points overlaid on the GeoEye image.

Similarly, day eight of the summer traverses supports the influence of different land covers on air temperature. The data from this traverse show the stability of air temperature during both day-time and night-time as we move through the urban areas. The maximum air temperature during the night-time was 33 °C and the minimum was 30 °C, while the air temperature ranged from 35 °C to 37 °C after sunset. Hence, the range of air temperatures in urban areas over both day and night is only 7 °C.

The relative humidity data show a strong and clear relationship with air temperature. When the air temperature increases, the relative humidity decreases (Lawrence, 2005). The levels of relative humidity are high in both vegetation and sabkha sites, while it is less in the urban and sand areas. On day two of the summer traverses, maximum relative humidity was 64% at night and 29% after sunset in the vegetation areas, while the minimum relative humidity was recorded as 29% at night and 17% after sunset. For day eight, relative humidity ranged from 77% at night to 28% after sunset; most the land cover of this traverse was urban areas (Figure 5-5).

Figure 5-5 Air temperature, relative humidity, and land cover profile chart of the mobile traverse day two during summer season (7 August 2011)

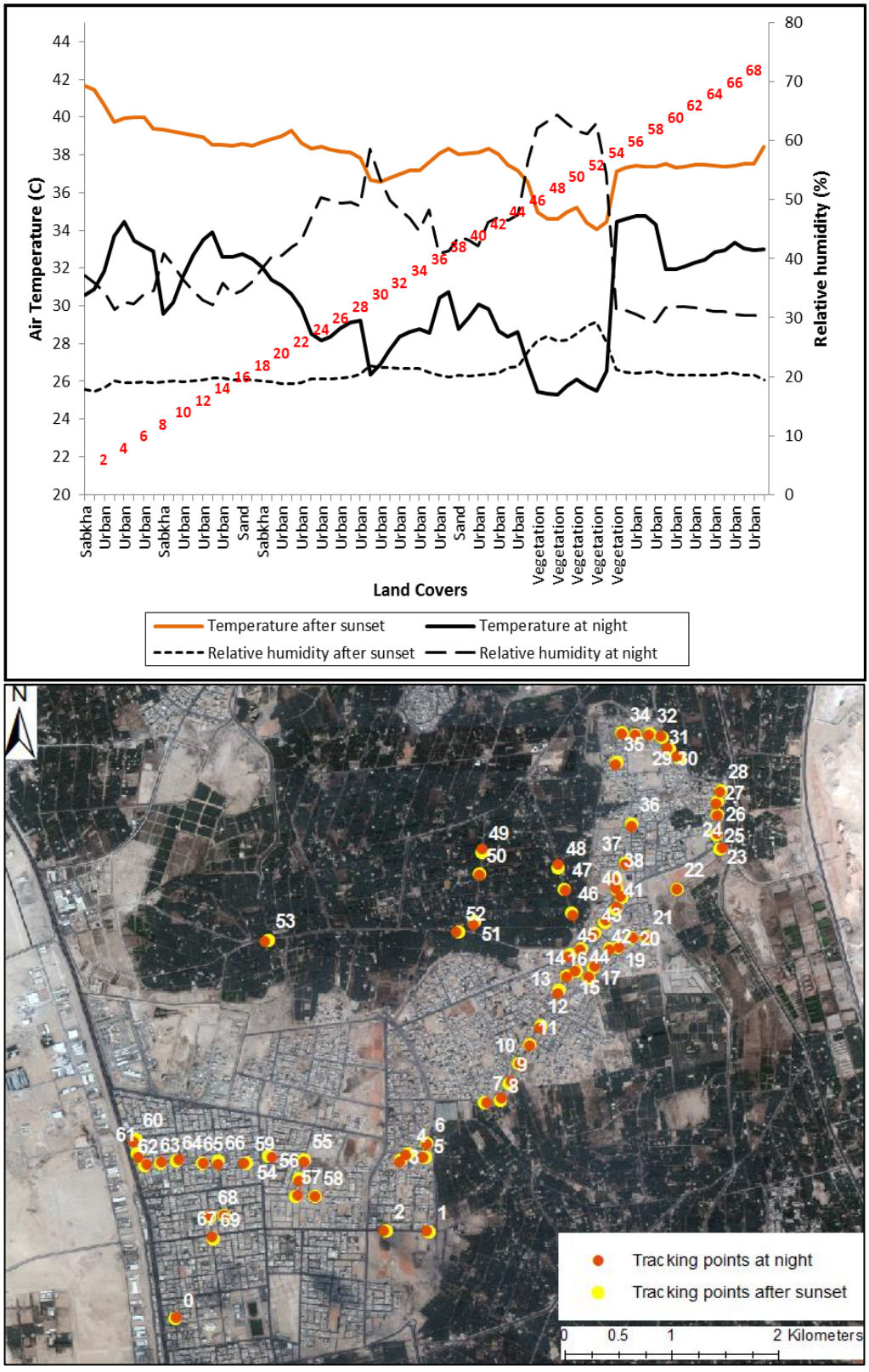

Note: GeoEye data below shows the tracking of the same traverse.

Data from the winter traverses also indicate that air temperature and relative humidity differed over the various land cover areas. The mobile data from the winter traverses also show increases in air temperature as we move in or around the built-up areas, while air temperature decreases in the vegetation, sand, and sabkha areas (see appendix 5.2). An example of the air temperature and relative humidity profile is shown in Figure 5-6. During day eight (19th February 2011) both air temperature and relative humidity were clearly fluctuated among different land covers types. The maximum air temperature during this traverse was observed in built-up areas (14 °C at night and 21 °C after sunset), while the minimum air temperature was recorded in vegetation areas of 8 °C at night and 13 °C after sunset. Therefore, the range of air temperatures for the same day's traverses was 13 °C (Figure 5-6).

The relative humidity data in the winter also showed a clear relationship with both air temperature and land cover. When the air temperature decreases, relative humidity increases (Lawrence, 2005, Valsson and Bharat, 2011). The highest relative humidity values are recorded at vegetation and sabkha sites, while it is lower in urban and sand areas. During day eight of the winter traverses, maximum relative humidity reached 83% at night and 60% after sunset in the vegetation areas, while minimum relative humidity was recorded as 54% at night and 26% after sunset (Figure 5-6).

Figure 5-6 Air temperature, relative humidity, and land cover profile chart of the mobile traverse day eight during winter season (19 February 2011)

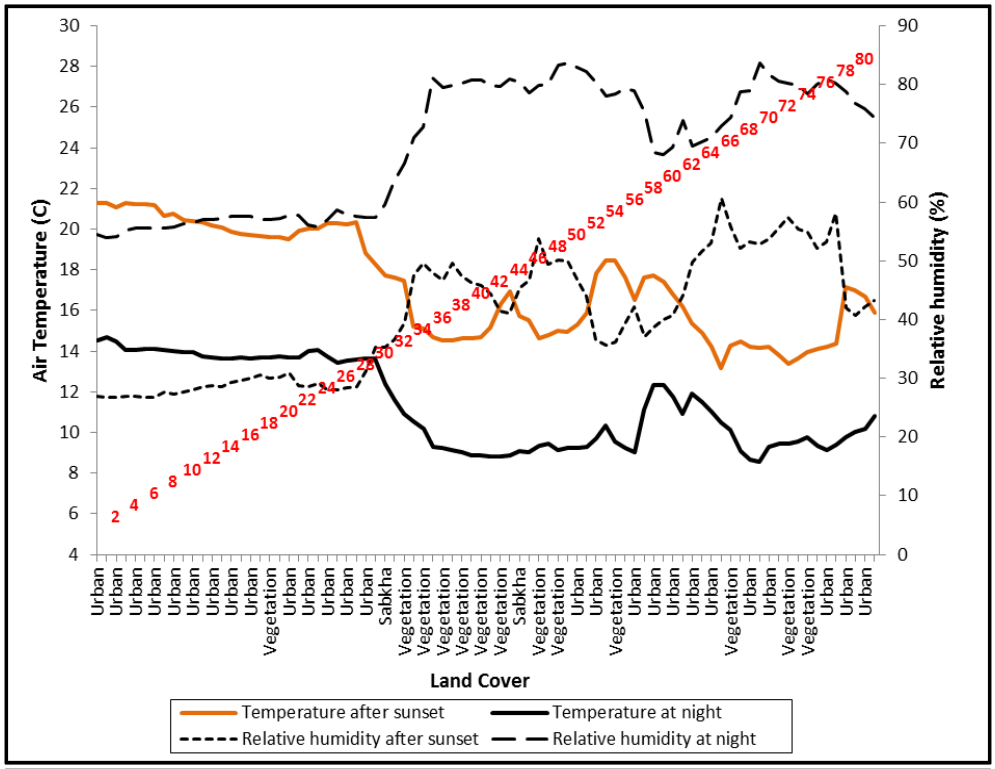

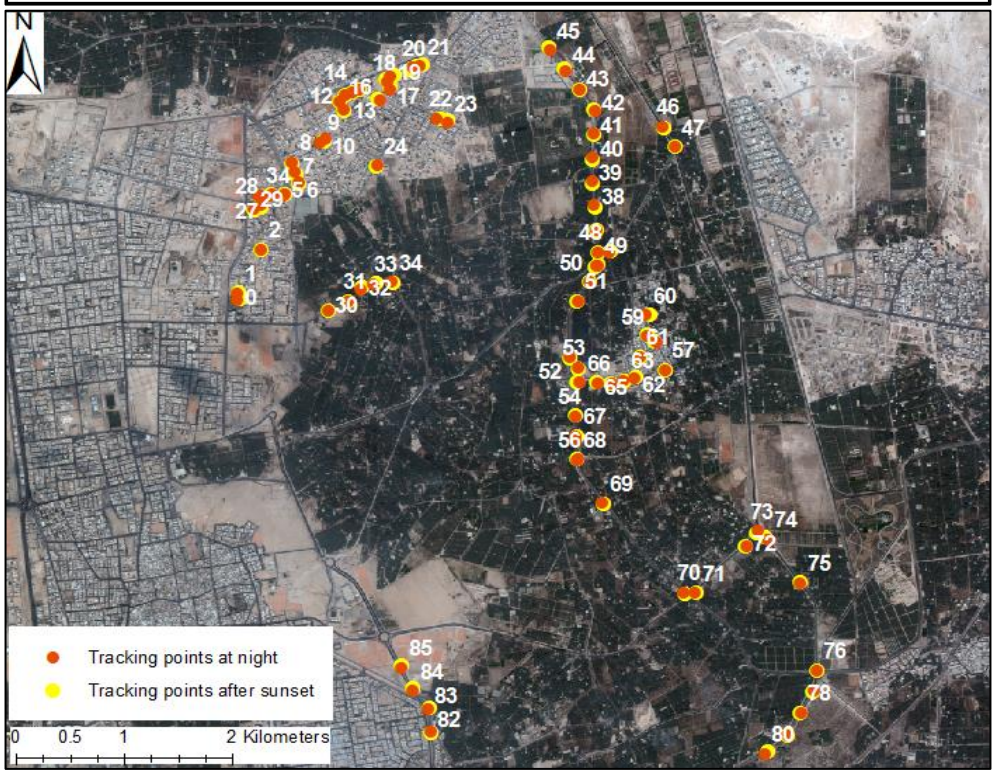

Note: GeoEye data below shows the tracking of the same traverse.

5.9 **Intensity of summer CLHIs**

The intensity of CLHIs is described as the difference in temperature between pairs of fixed weather stations, with the first one representing an “urban” area and the second a “rural” area (Oke, 1998). In this study, data from the mobile traverses (night and after sunset) during both winter and summer recorded in different land cover areas were compared two times. First time is with the fixed weather station located at the palm tree farm, which represents an oasis situation and second with airport weather station, which is located outside the urban area.

All the mobile data, comparing with both stations (Airport and Farm), show high intensity of CLHIs in the built-up areas (classes 4, 6, 7, and 9), and low or negative heat islands in the vegetation, sabkha, mixed building and vegetation class, and sand areas during summer (Figure 5-7). The intensity of CLHIs is higher during the night in the built-up areas than after sunset and similar or close in other land covers based on the farm fixed weather station and airport weather station as control variables. The different in the air temperature, during the summer, between mobile data in different land covers and from fixed weather station ranges between +9.1 ℃ to -1.0 ℃ at night and +8.0 ℃ to -2.5 ℃ after sunset (Figure 5-7). While the different in the air temperature between, during the summer, mobile data in different land covers and airport fixed weather station ranges between +6.1 ℃ to -5.7 ℃ at night and +2.6 ℃ to -7.2 ℃ after sunset (Figure 5-8).

Figure 5-7 CLHI intensity among different land covers for day one during summer (02 August 2011) based on farm as control

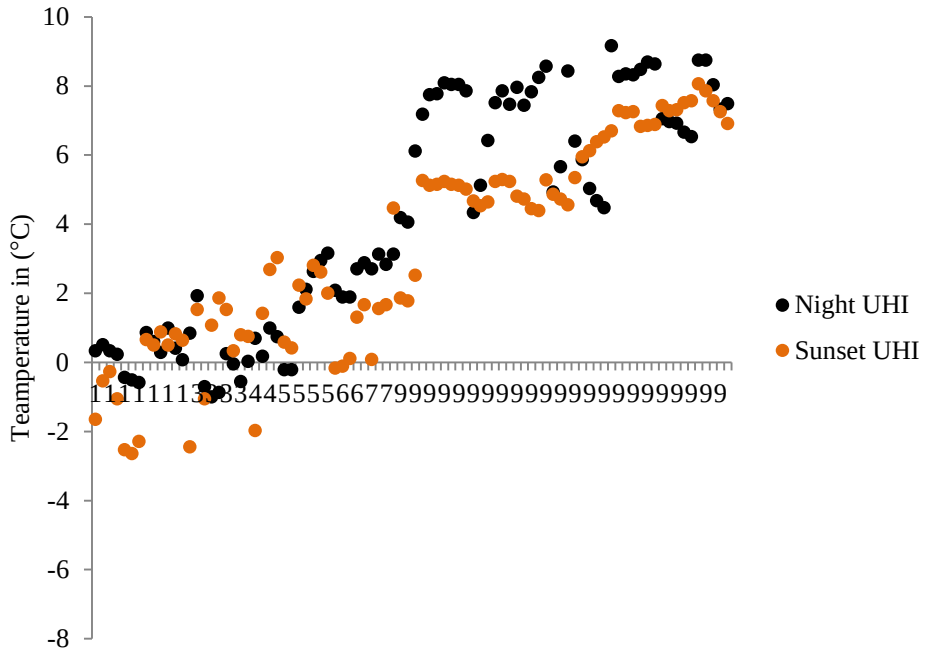

Note: 1=Vegetation, 3=Sabkha, 4=Built-up 1, 5=Sand, 6=Built-up 2, 7=Built-up 3, and 9=Built-up 5. Night-time between 01:49:29am and 04:42:29am and Sunset-time between 18:36:05pm and 20:58:36pm.

Figure 5-8 CLHI intensity among different land covers for day one during summer (02 August 2011) based on airport as control

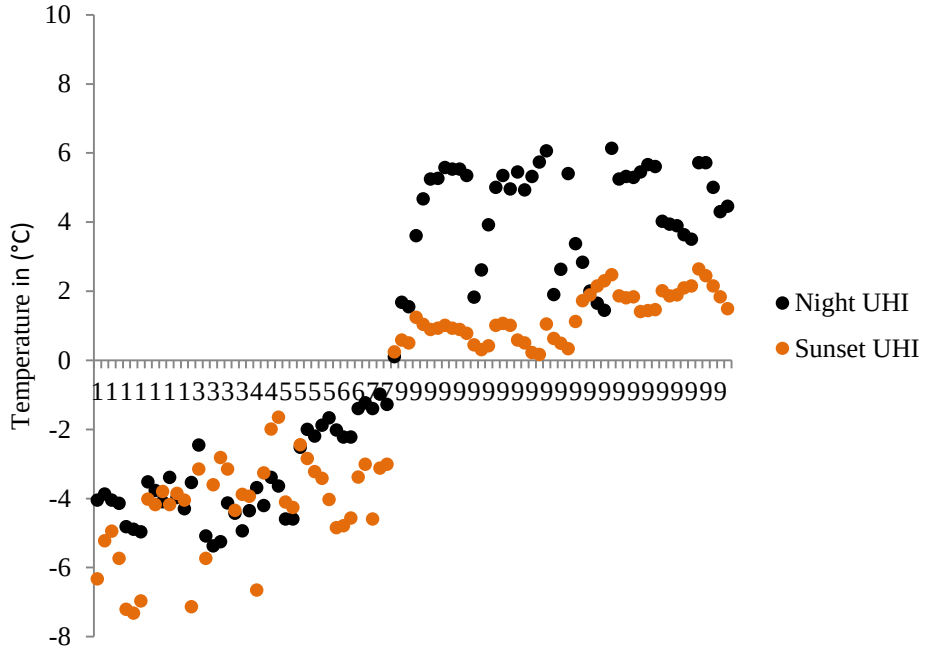

Note: 1=Vegetation, 3=Sabkha, 4=Built-up 1, 5=Sand, 6=Built-up 2, 7=Built-up 3, and 9=Built-up 5. Night-time between 01:49:29am and 04:42:29am and Sunset-time between 18:36:05pm and 20:58:36pm.

The intensity of CLHIs during summer indicates the same temporal pattern in both night-time and after-sunset traverses for all the mobile data comparing with the farm and airport weather stations. All the traverses during the night and after sunset, based on the farm or airport as control, show the same patterns that UHI intensity is higher at night than after sunset and associated with different land covers. The highest CLHIs exist in built-up areas especially at the class 5 of the built-up area which represents the high intensity of building and population. While the minimum or negative CLHIs occur at the vegetation and sabkha which have less building and more trees with wet soils. For example, the maximum of UHI intensity based on farm and airport control variables, in the day selected below (August 2nd 2011) (Figure 5-9 and Figure 5-10), is +9.0 °C to +8.0 °C and +6.0 °C to +3.0 °C at night and after sunset, respectively. While the minimum or negative UHI intensity, observed in same day, is -1.0 °C to -3.0 °C and -6.0 °C to -7.0 °C at night and after sunset, respectively.

Figure 5-9 Temporal CLHI intensity on day one among different land cover areas

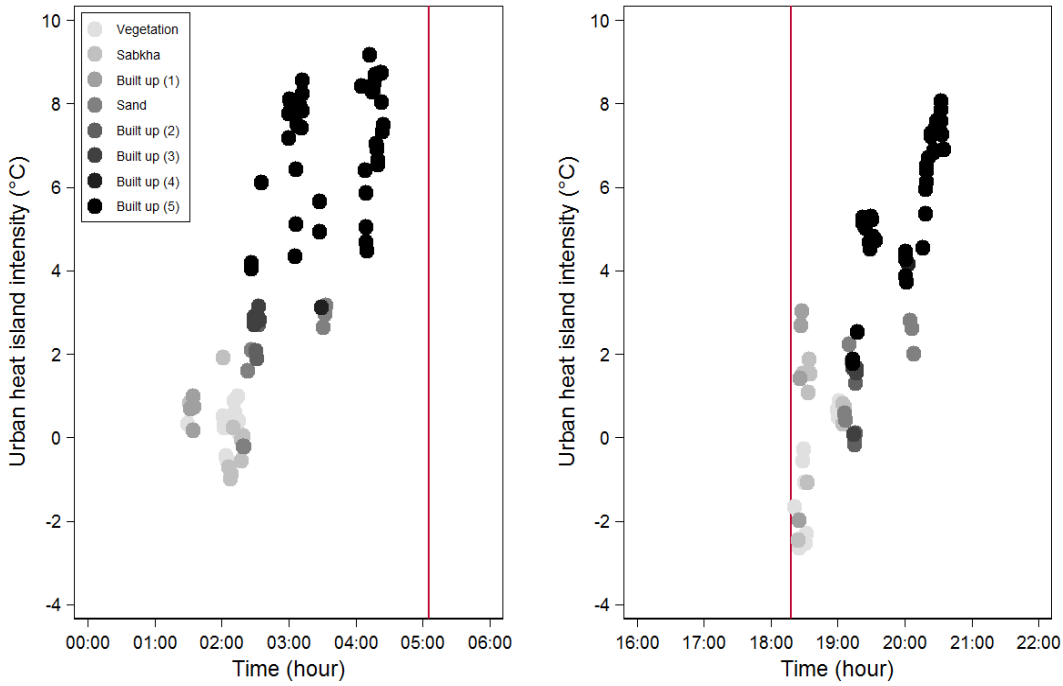

Note: (night and after-sunset traverses during summer) (Farm as control). Reference lines indicate time of sunrise (05:09am) and sunset (18:27pm).

Figure 5-10 Temporal CLHI intensity on day one among different land cover areas

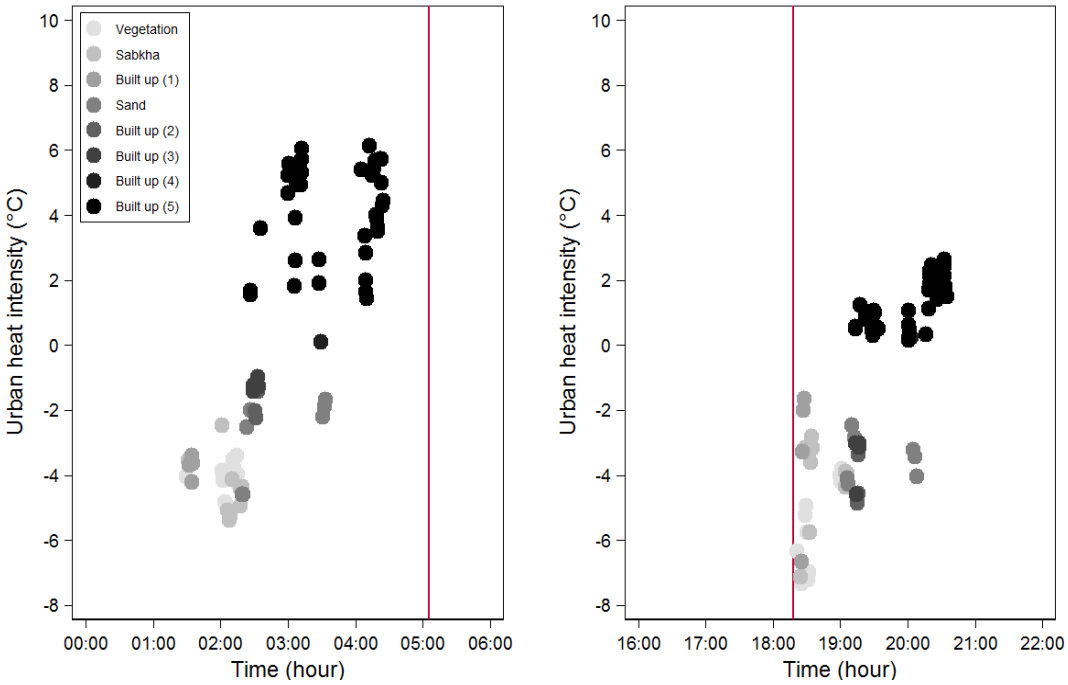

Note: (night and after-sunset traverses during summer) (Airport as control). Reference lines indicate time of sunrise (05:09am) and sunset (18:27pm).

The spatial distribution of CLHI intensity during summer traverses at night and after sunset is shown in (Figure 5-11 and Figure 5-12). Based on the range of CLHI intensity, local urban heat islands can be divided into three different categories: hot, mild, and cool heat islands according to both methods of identifying UHI intensity (farm and airport weather stations). During summer traverses (August), the hot zone of CLHIs is clearly visible in the western region of the study area over the largest cities in the study area: Al Hufuf and Al Mubarraz, which have a population of 660,788 in 2010 (Ministry of Economy and Planning, 2010).

The intensity of CLHIs in the hot zone ranges from +5.1 °C to +10.5 °C at night and +3.7 °C to +10.4 °C after sunset as farm site is the control, and ranges from +2.5 °C to +4.8 °C at night and +0.6 °C to +2.6 °C after sunset as airport weather station is the control. The hot zone of the CLHIs also appears in the north, east, and north-east of the study area at night. This zone includes the cities and villages that have less population and housing intensity. Examples of these cities are Al Uyun in the north, Al Killabiyah in the north-east, and Al Umran in the east of the study area with populations of 33,042, 16,984, and 17,410 respectively.

The mild zone of local CLHIs covers most of the study area, including within the boundaries of the hot zone mentioned above. Most settlements located in the east, southeast, and north of the study area represent the mild CLHIs zone. The mild region includes most the small villages such as Al Qaraah, Al Fadooel, and Al Mutayrifi with 9702, 6609, and 6371 inhabitants respectively (Ministry of Economy and Planning, 2010). The intensity of CLHIs in the mild zone ranges from +1.0 °C to +5.1 °C at night and +0.2 °C to +3.7 °C after sunset as farm site is the control, and ranges from +1.3 °C to +2.5 °C at night and -0.5 °C to +0.6 °C after sunset as airport weather station is the control.

The third category of CLHIs is the cool zone. This zone is found on the edges of the mild zone and over the vegetation areas which extend from the north and north-east to the south and south-east of the study area. The intensity of CLHIs in the cool zone ranges from -1.0 °C to +1.0 °C at night and -2.5 °C to +0.2 °C after sunset as farm site is the control, and ranges from -6.4 °C to 1.3 °C at night and -7.2 °C to -0.5 °C after sunset as airport weather station is the control (Figure 5-11 and Figure 5-12).

Figure 5-11 Distribution of CLHIs for the mobile data during summer season August 2011at night-time and after sunset where Farm as control

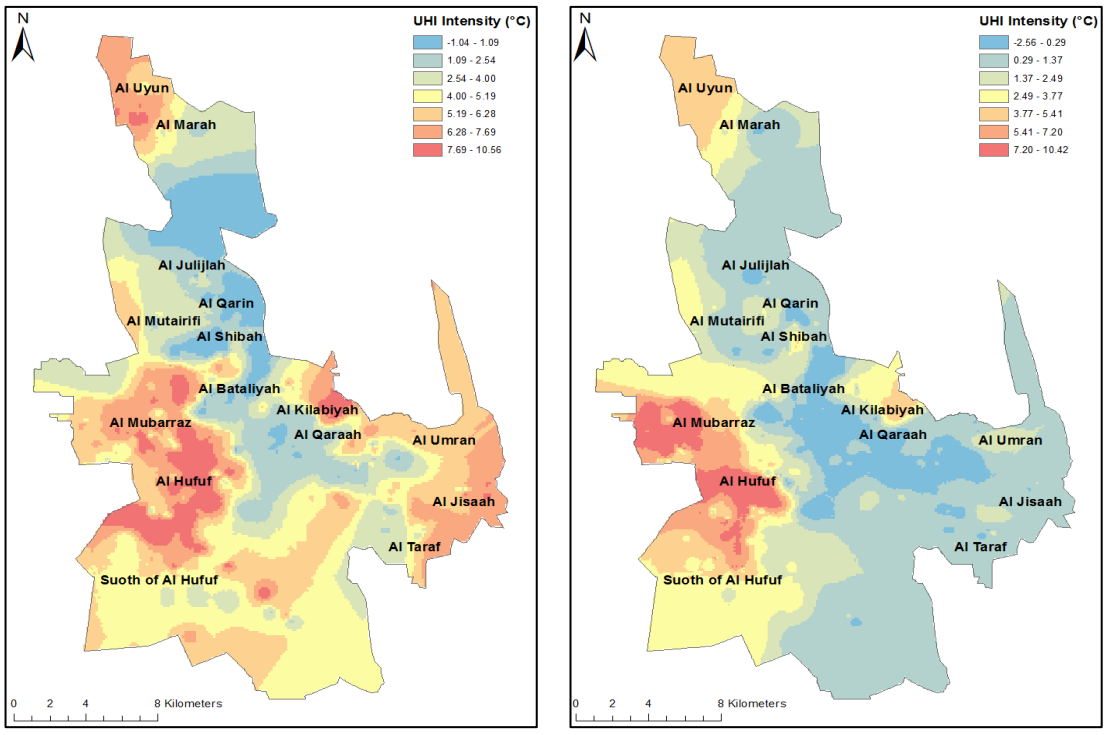

(a) At night (b) After sunset

Figure 5-12 Distribution of CLHIs for the mobile data during summer season August 2011 at night-time and after sunset where Airport as control

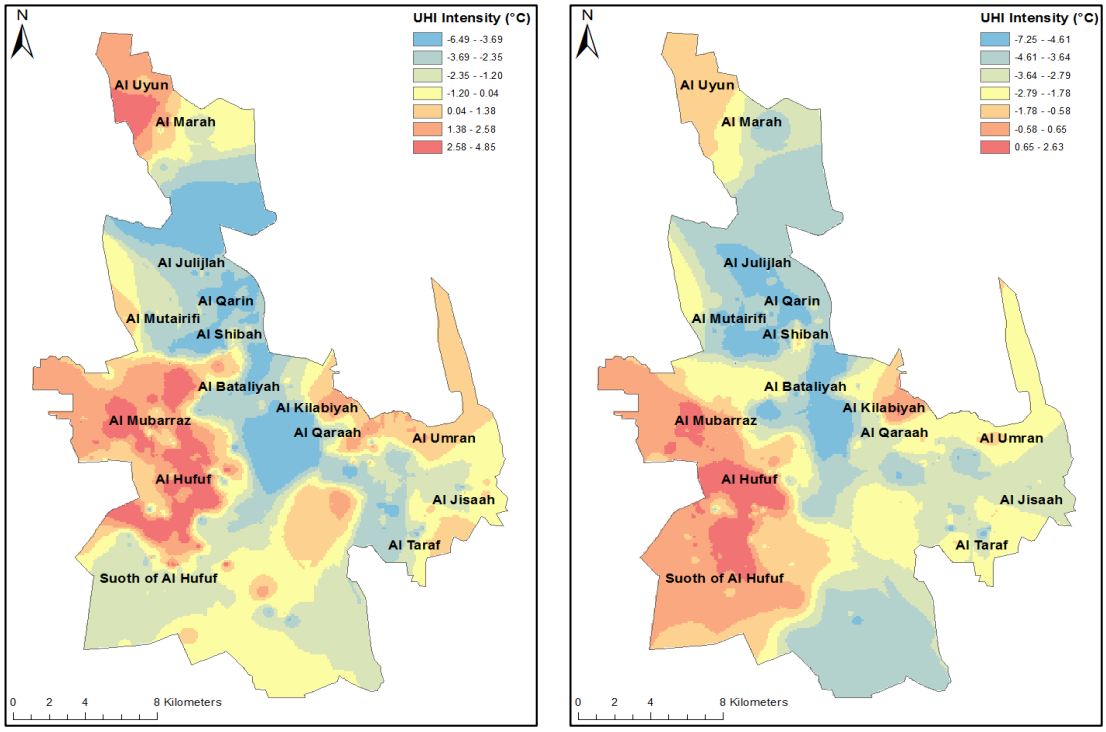

(a) At night (b) After sunset

5.10 **Intensity of winter CLHIs**

During winter, data from the mobile traverses (night and after sunset) in different land covers are compared with the fixed weather station located in the farm site and with the airport weather station located outside the urban area. Comparison indicates the presence of CLHIs during winter season based on both control variables farm and airport but with less intensity compared to summer season. The mobile data indicates high CLHI intensity in the built-up areas (class 4, 8, and 9), and low or negative heat islands in the vegetation and sabkha areas during winter based on both control variables farm and airport (Figure 5-13). The intensity of CLHIs shows similarity of the different in the air temperature during the night and after sunset in the winter. The different in the air temperature during winter between mobile data in different land covers and farm fixed weather station ranges between +4.9 °C to -0.1 °C at night and +4.8 °C to -0.2 °C after sunset (Figure 5-13). While the difference in the air temperature during winter between mobile data in different land covers and airport fixed weather station ranges between +2.5 °C to -3.1 °C at night and +2.1 °C to -5.0 °C after sunset (Figure 5-14).

Figure 5-13 CLHI intensity among different land cover areas for day eight of winter (19 February 2011) based on farm as control

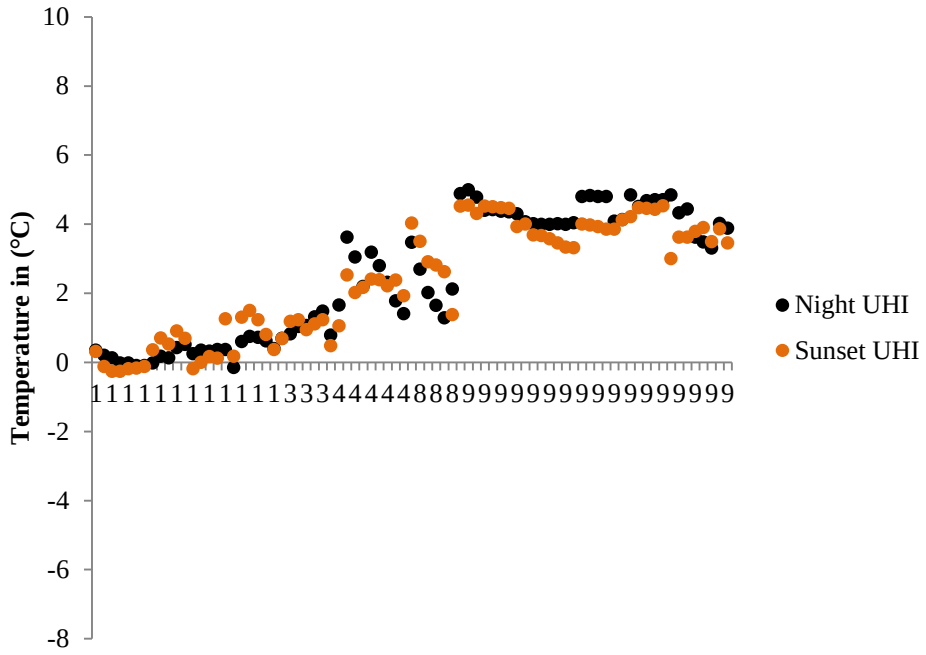

Note: 1=Vegetation, 3=Sabkha, 4=Built-up 1, 8=Built-up 4, and 9=Built-up 5. Night-time between 01:17:35am and 03:25:35am and Sunset-time between 20:06:34pm and 20:57:34pm.

Figure 5-14 CLHIs intensity among different land cover areas for day eight of winter (19 February 2011) based on airport as control

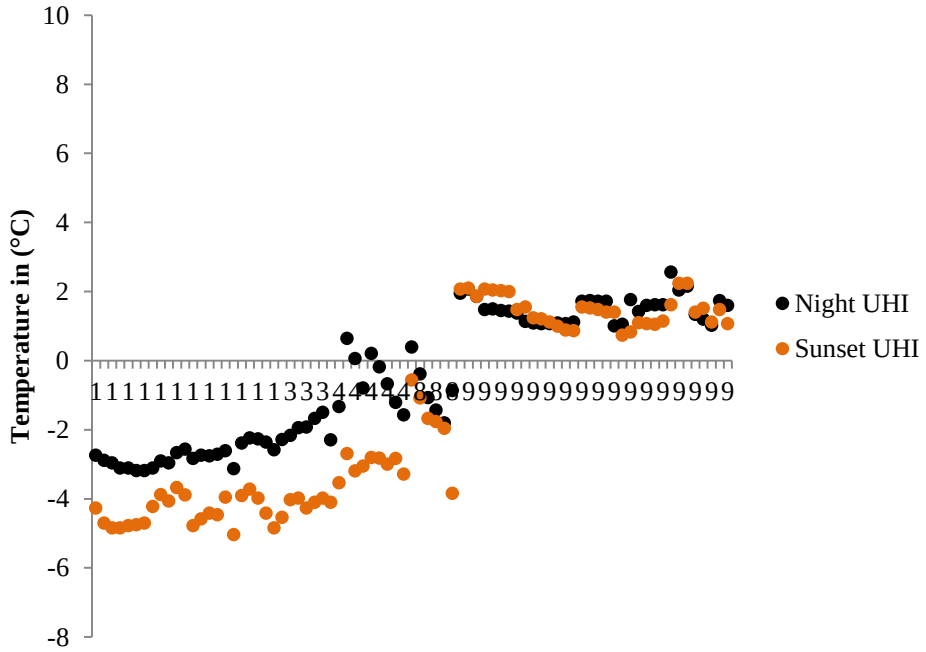

Note: 1=Vegetation, 3=Sabkha, 4=Built-up 1, 8=Built-up 4, and 9=Built-up 5. Night-time between 01:17:35am and 03:25:35am and Sunset-time between 20:06:34pm and 20:57:34pm.

The intensity of CLHIs during winter show the same temporal pattern in both night-time and after-sunset traverses for all the mobile data comparing with the farm and airport weather stations. All the mobile data during the night and after sunset traverses, based on the farm or airport as control, indicate that CLHI intensity is higher at night than after sunset and related with different land covers classes. Moreover, the maximum CLHIs intensity exists in built-up areas which have high intensity of building and population. While the minimum or negative CLHIs occur at the vegetation and sabkha areas which have less building and more trees with wet soils. For example, the maximum of UHI intensity based on farm and airport control variables, in the day selected below (February 19th 2011) (Figure 5-15 and Figure 5-16), is +5.0 °C to +4.5 °C and +2.3 °C to +2.2 °C at night and after sunset, respectively. While the minimum or negative UHI intensity, observed in same day, is -0.1 °C to -0.2 °C and -3.0 °C to -5.0 °C at night and after sunset, respectively.

Figure 5-15 Temporal CLHI intensity on day eight among different land cover areas

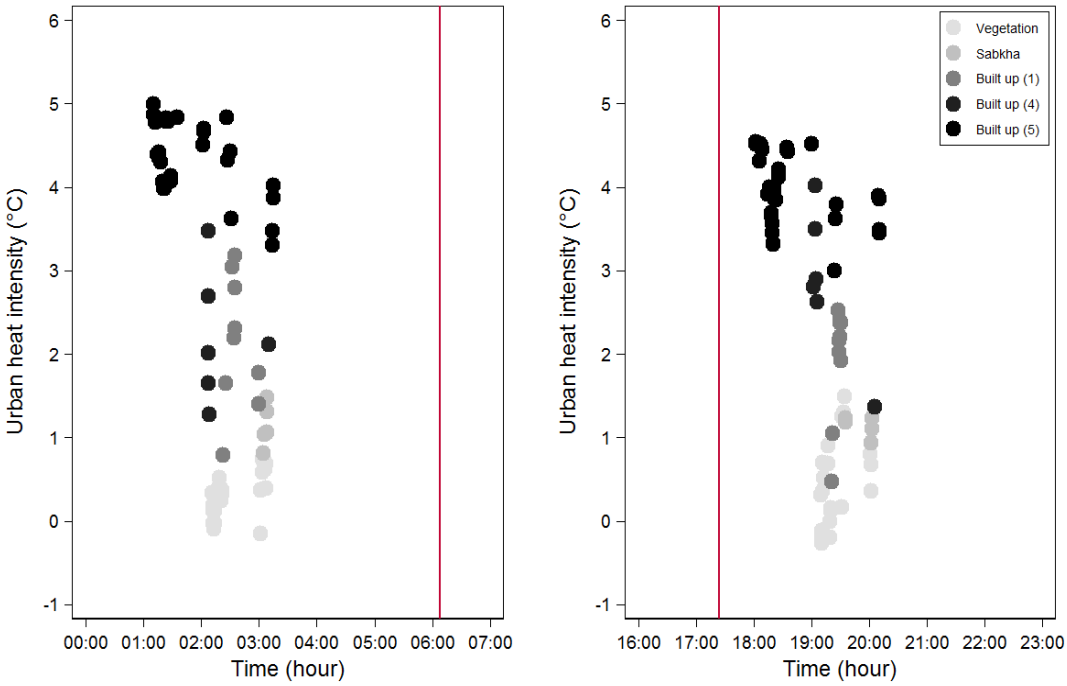

Note: (night and after-sunset traverses during winter). (Farm as control). Reference lines indicate time of sunrise (05:09am) and sunset (18:27pm).

Figure 5-16 Temporal CLHI intensity on day eight among different land cover areas

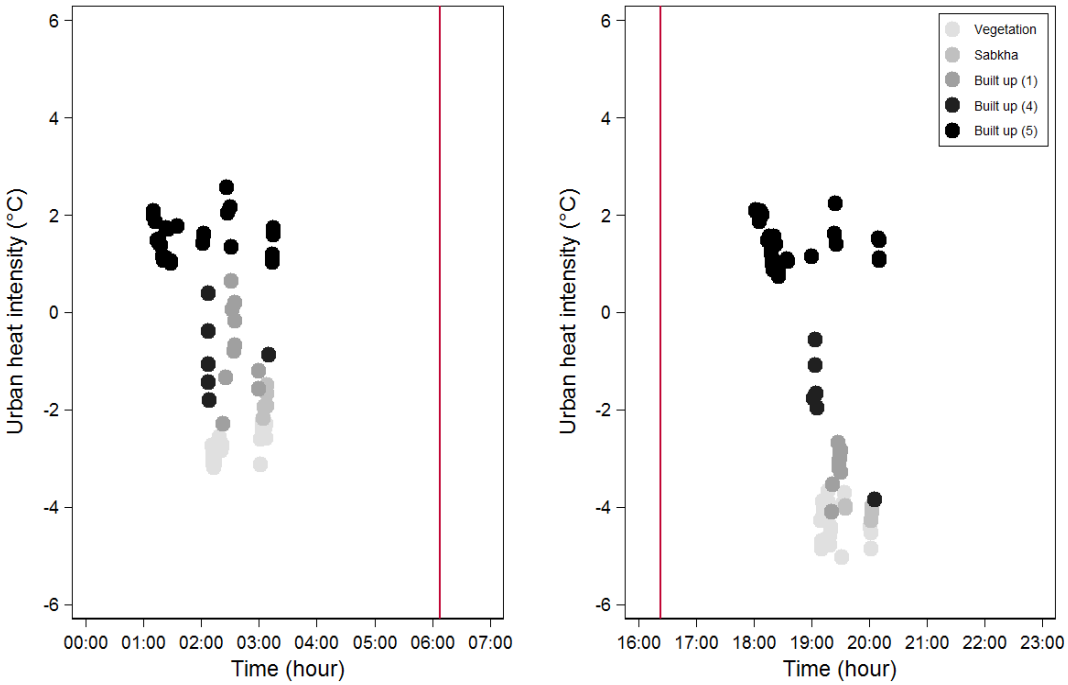

Note: (night and after-sunset traverses during winter). (Airport as control). Reference lines indicate time of sunrise (06:14am) and sunset (17:38pm).

The spatial distribution of CLHI intensity during winter traverses at night and after sunset is shown in (Figure 5-17 and Figure 5-18). Also, based on the range of CLHI intensity, the local CLHIs can be divided into three different zones: warm, mild, and cool heat islands. During the winter traverses (February), the warm zone of CLHIs is centred over the largest cities of the study area, Al Hufuf and Al Mubarraz. However, in this season the peak of CLHIs moved slightly to the south, both at night and after sunset and based on the farm or airport as control. The intensity of CLHIs in the warm zone ranges from +3.1 °C to +7.8 °C at night and +2.1 °C to +7.3 °C after sunset as farm site is the control, and ranges from +1.8 °C to +4.8 °C at night and +1.3 °C to +3.4 °C after sunset as airport weather station is the control (Figure 5-17 and Figure 5-18).

The majority of the study area is classified under the mild zone of CLHIs, which is located between the two zones the edges of the warm and cool zones. The villages and small settlements e.g. Al Qaraah, Al Fadooel, and Al Mutayrifi are examples of the mild zone areas. The formation of the mild zone of heat islands refers to the size of the area and population of these villages comparing with the main and large cities of the study area areas. The intensity of urban heat islands in the mild zone ranges from +1.0 °C to +3.1 °C at night and +0.1 °C to +2.1

°C after sunset as farm site is the control, and ranges from +0.6 °C to +1.8 °C at night and +0.4 °C to +1.3 °C after sunset as airport weather station is the control.

The third category of CLHIs is the cool region. This zone is recognized on the edges of the study area and over the vegetation region which extends from the north and north-east to the south and south-east of the study area. The intensity of CLHIs in the cool zone ranges from -2.1 °C to +1.0 °C at night and -3.5 °C to +0.1 °C after sunset as farm site is the control, and ranges from -3.1 °C to +0.6 °C at night and -4.9 °C to +0.4 °C after sunset as airport weather station is the control (Figure 5-17 and Figure 5-18).

Figure 5-17 Distribution of CLHIs for the mobile data during winter (February) 2011, night-time and after sunset where Farm as a control

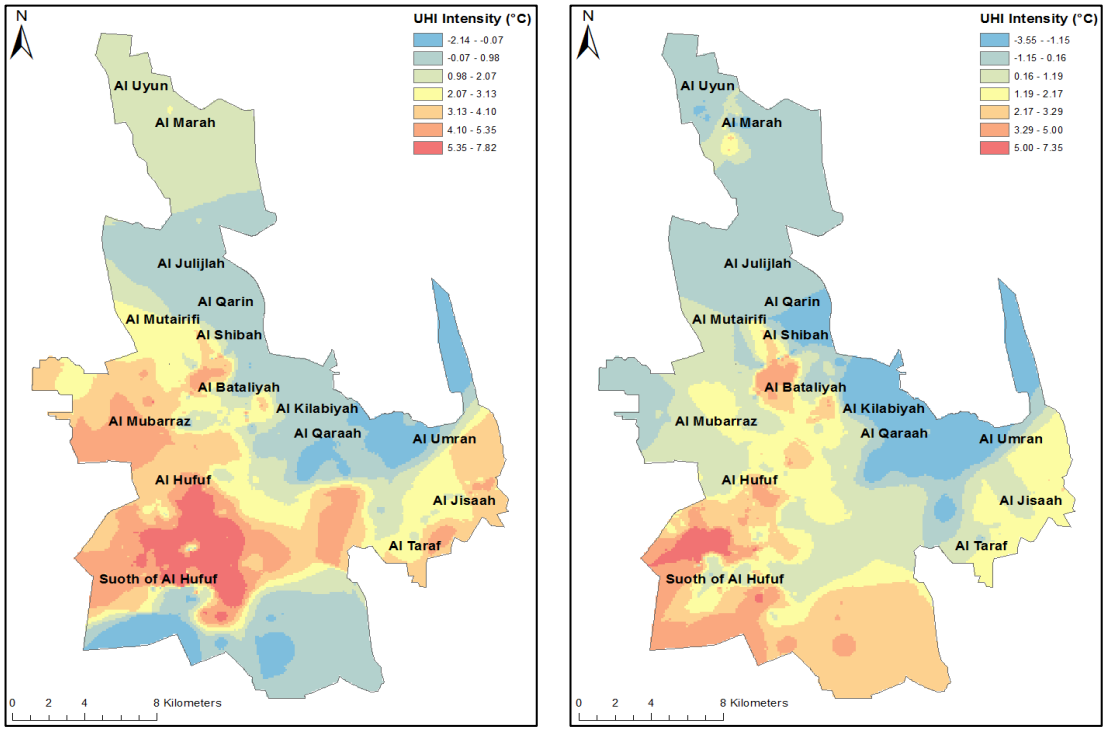

(a) At night (b) After sunset

Figure 5-18 Distribution of CLHIs for the mobile data during winter (February) 2011, night-time and after sunset where Airport as a control

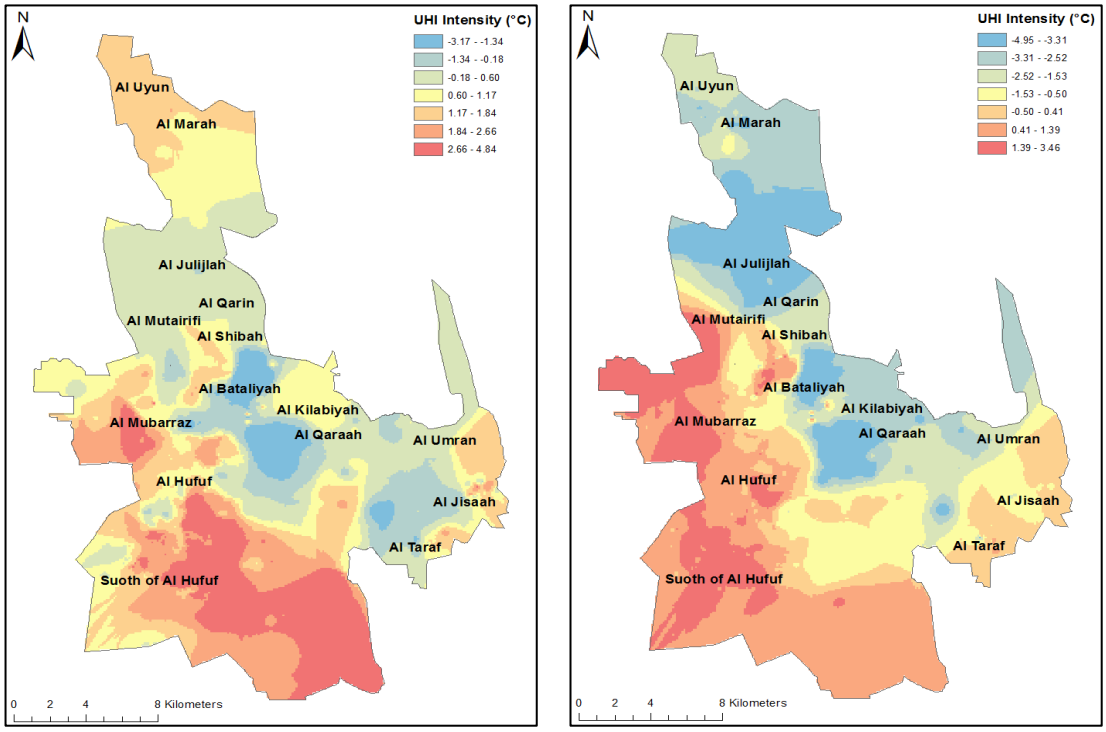

(a) At night (b) After sunset

5.11 **Summary**

In this chapter, temporal and spatial distributions of CLHIs are addressed. There are statistically significant differences in both air temperature and relative humidity during the winter and summer seasons among the different land cover types. The differences in air temperature suggest the existence of urban heat islands in the study area during both winter and summer. There is a strong relationship between air temperature, relative humidity, and the different land covers (sabkha, sand, built-up areas, vegetation, and water).

The spatial distribution of CLHIs intensity during both winter and summer, based on the farm or airport as control variables, shows a clear link between air temperature and land cover type. There are four zones of CLHIs over the study area during the winter and summer: hot, warm, mild, and cool zones. The hot and warm zones are recognized in the largest cities of the study area (Al Hufuf and Al Mubarraz). The mild zone was observed in the small settlements and villages such as Al Qaraah, Al Fadooel, and Al Mutayrifi. Finally, the cool zone of CLHIs was located in the farm regions, extending from the north and north-east to the south and south-east

of the study area during winter and summer and based on both methods. Finally, more discussions of these results will be included in Chapter Seven.

Chapter 6: Estimating Surface Temperature

6.1 Introduction

This chapter addresses the regional surface temperature of the study area using the remote sensing approach during the winter (February) and summer (August) seasons in 2011. The aim of this chapter is to present estimations of surface temperature using satellite data from the Landsat 7 ETM+ and the Moderate Resolution Imaging Spectroradiometer (MODIS) sensors in order to measure the effect of (SUHIs) in the study area in both winter (February) and summer (August) in 2011. The use of different satellite data allows an understanding of the effect of local (SUHIs) at different spatial and temporal scales. The surface temperature obtained from the satellite data is used to evaluate the effect of land cover type on local surface temperatures. Also, where appropriate, the estimated surface temperature is compared with the temperature data obtained from mobile sensors described in chapter five to validate the accuracy of the satellites-derived surface temperatures. Representations of the surface temperatures and (SUHIs) are presented graphically using ArcMap 10.2 and statistically using Stata 12. Finally, the relationship between land cover type and SUHI intensity is presented and discussed for the day and night data.

6.2 Satellite data

Three types of satellite data at different spatial resolutions are used in this study for different purposes. The satellites are the Landsat 7 Landsat7 ETM+, MODIS and GeoEye-1. The Landsat 7 ETM+ images for February and August 2011 were obtained free of charge from the USGS website (Figure 6-1). The various bands of the Landsat 7 ETM+ are used for different purposes. Bands 1, 2, 3, 4 and 5, as multi-

spectral bands with 30 metres each of pixel resolution (NASA, 2013b) are used to classify the main land cover types of the study area for February and August 2011, while band 6 is the thermal band used to estimate the surface temperature, with a spatial resolution of 60 metres, resampled to 30 metres, for each pixel (Chander et al., 2009, United States Geological Survey, 2010).

Figure 6-1 USGS global visualization viewer (GloVis)

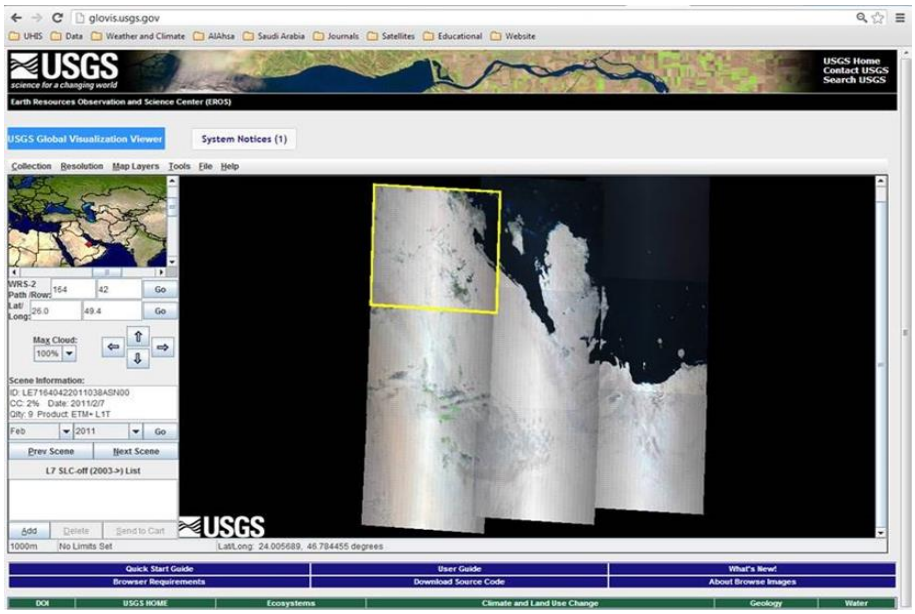

Source: (United States Geological Survey, 2011).

The MODIS (Figure 6-2) data are used to obtain quantitative data of land cover based on MODIS pixel size and to estimate the surface temperature of the study area to estimate the SUHI intensity. MODIS data can also be obtained free of charge from the USGS website. Daily MODIS images for February and August 2011, that are a product of MOY11A1 Aqua, at 1000 m spatial resolution, are used to estimate the surface temperature of the study area. The data and data preparation of the MODIS images are described in detail in chapter three (methodology).

Figure 6-2 Moderate Resolution Imaging Spectroradiometer (MODIS) of the study area

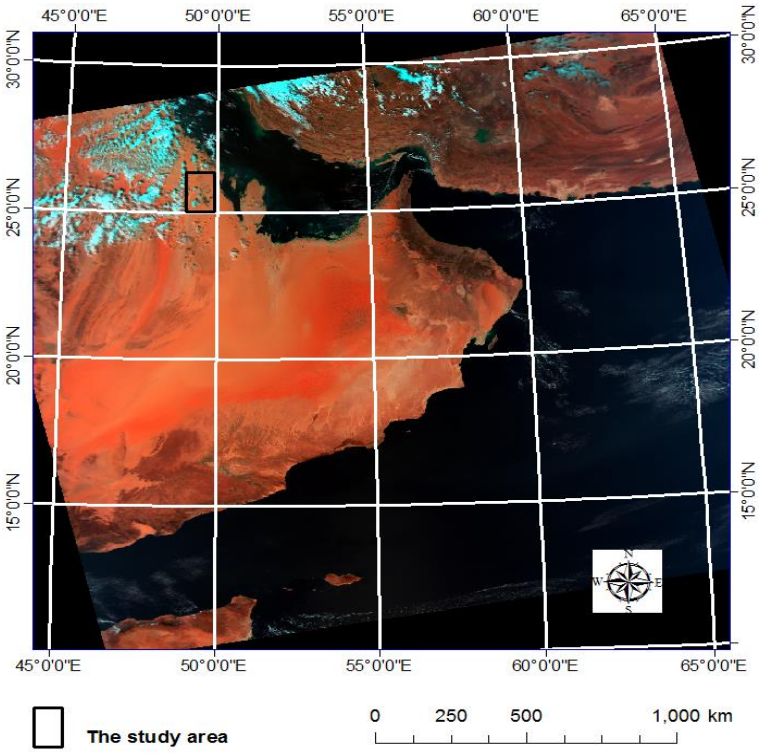

Source: (NASA, 2013b).

The third source of satellite data used in this study is from the GeoEye-1 sensor (Figure 6-3). The data were obtained with permission from the Al Ahsa Municipality in Saudi Arabia. GeoEye-1 data has a high spatial resolution of 0.5 metres and is used to validate the accuracy of the Landsat 7 ETM+ and MODIS land cover mapping. These data are also used to provide details of the surfaces and roof covers and to create the emissivity map in order to estimate the surface temperature and calculate the SUHI intensity of the study area.

Figure 6-3 GeoEye-1 satellite image of the Al Ahsa Oasis in 2010

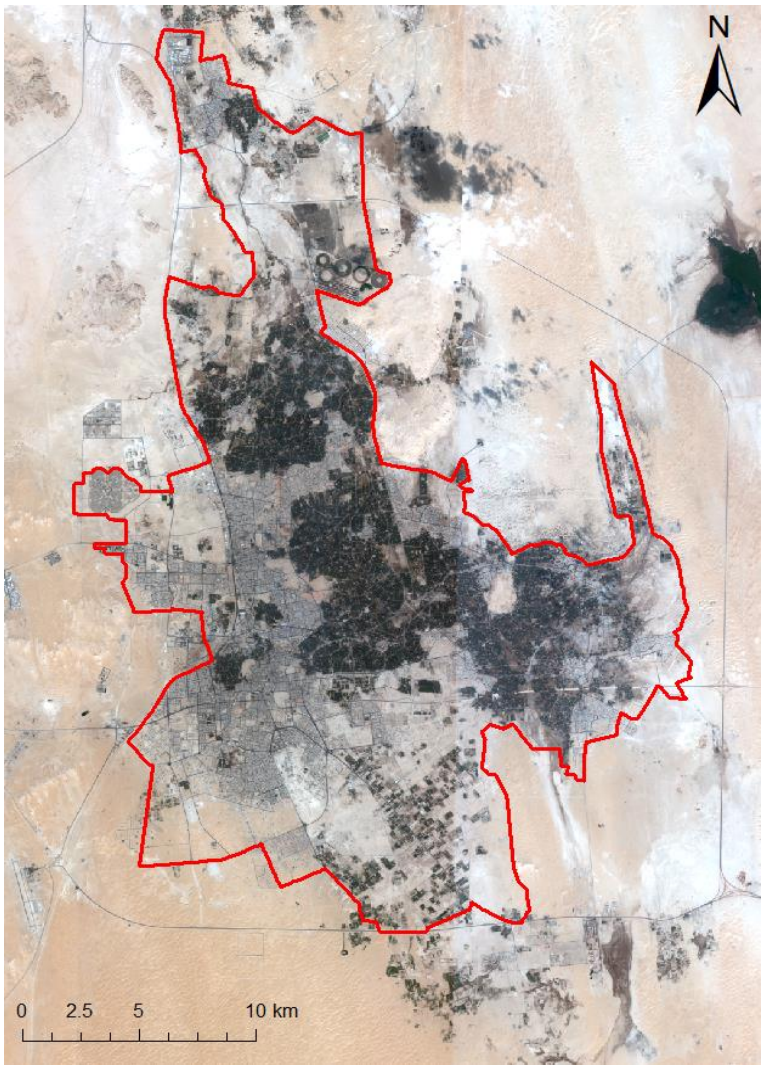

Image obtained from Al Ahsa Municipality in Saudi Arabia, 2010.

6.3 **Land cover classification**

Mapping land cover is an important step in obtaining the quantitative data needed to test the effect of the land cover on surface temperature (Chen et al., 2006, Adinna et al., 2009). Supervised classification is a well-established and reliable method typically used to classify the land cover types. It has been shown to provide accurate results, particularly when two or more scenes that are captured on different dates are used (Mas, 1999). The results of the maximum likelihood method for the Landsat7 ETM, with a spatial resolution of 30 m for each pixel, are presented in Figure 6-4 below. The main land cover types in the study area are sabkha, sand, vegetation (palm trees and parks), residential areas, and water (evaporation lakes).

However, some of these classes are sub-divided in order to provide more precision about the land cover of the study area and to create a more specific emissivity map. Estimating emissivity is a vital step in determining land surface temperature using satellite data. These sub-classes of the main land cover types are sand dunes, sandstone, red sand, a built-up area (1) where most of the area consists of houses, built-up areas (2) where most of the area is asphalt (e.g. parking lots and streets), vegetation (1), consisting of palm trees, and vegetation (2) where the most of the area is grass (e.g. parks, football fields and irrigated crop fields) (Figure 6-5).

Figure 6-4 The main land cover type classifications of the study area, using Landsat7 ETM+ 18th August 2011

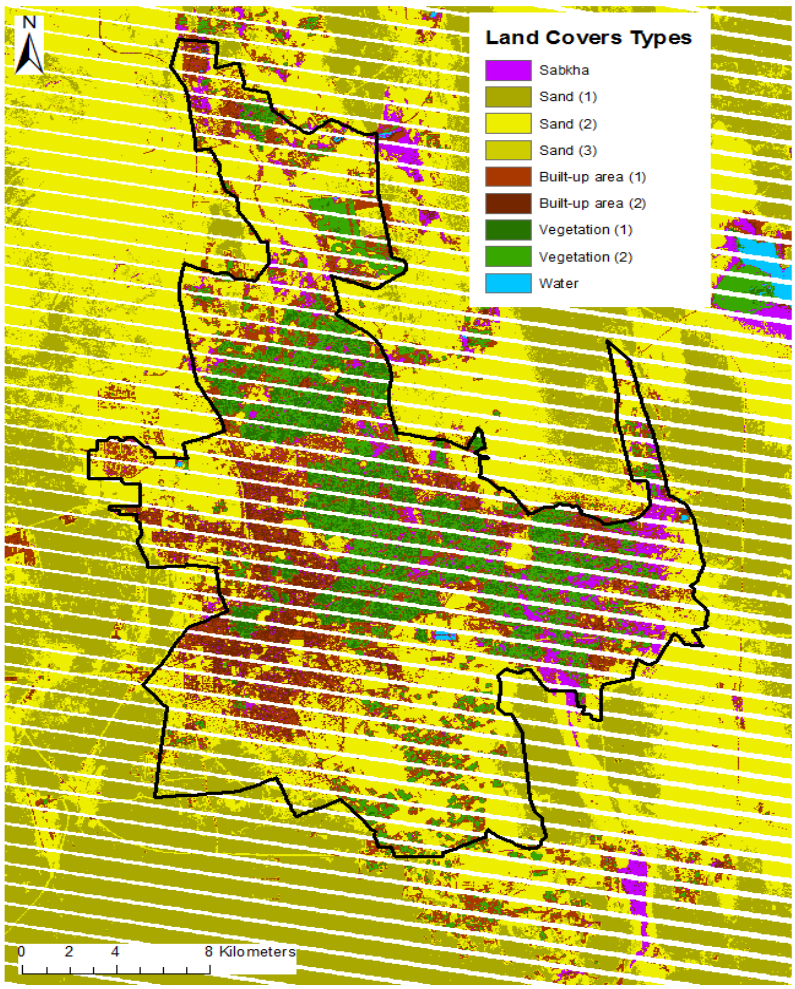

Note: Built-up area (1) mostly houses and concrete; Built-up (2) most of the area is asphalt; Vegetation (1) palm trees; Vegetation (2) parks and irrigated crop fields.

Figure 6-5 Samples of the main and sub-classes of land cover types of the study area

MODIS satellite images are also used to map the land cover of the study area at 1000 m resolution, to provide quantitative data and create an emissivity map to estimate the surface temperature. In order to investigate the thermal characteristics of different land cover types, every pixel in each of the images is classified with respect to the common land cover schema (Bradley et al., 2002) and considered the land cover details of each pixel (Oke, 2006, Owen et al., 2006). Figure 6-6 shows the maximum likelihood results used to classify each pixel of the MODIS image; then each pixel was edited based on main and sub-classes of the study area land covers (Figure 6-7). The classified image was edited based on the common land cover of each pixel and consider the pixel details, such as the density of the buildings, sand, sabkha, and vegetation area, in the sub-classes step (Oke, 2006, Owen et al., 2006), then each pixel was validated with a high spatial resolution image (GeoEye-1 image).

Figure 6-6 Land cover types of the study area (Al Ahsa oasis) based on MODIS data

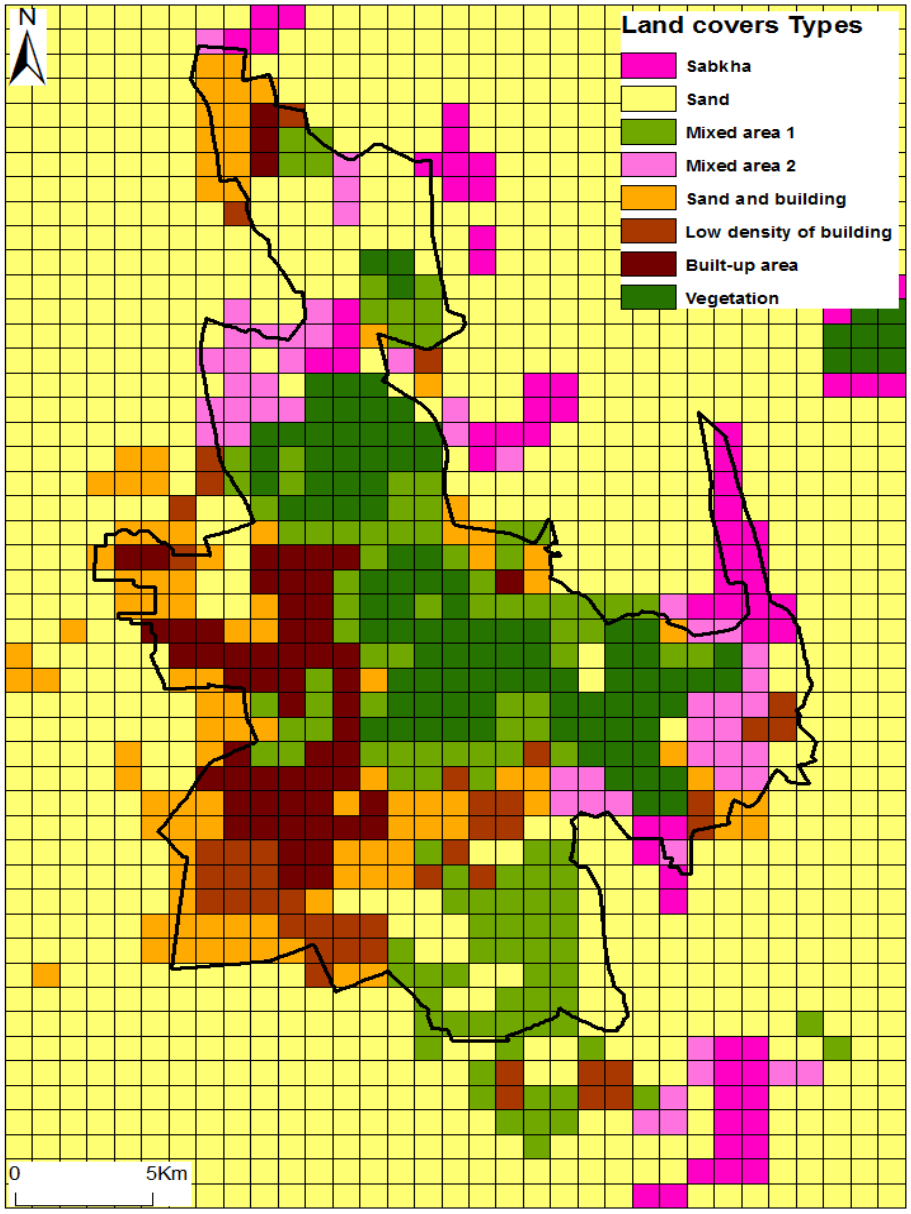

Note: (1) Sabkha, (2) Sand dunes, (3) Mixed area 1 (vegetation, buildings, sand, and sabkha), (4) Mixed area 2 (sabkha, sand, buildings, and vegetation), (5) Sand and buildings, (6) Low density of buildings, (7) Built-up area (houses and asphalt), (8) Vegetation area (farm).

Figure 6-7 Samples of the main and sub-classes of land cover types of the study area based on MODIS pixel 1 km X 1 km resolution.

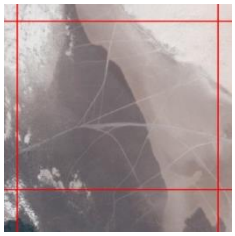
Sabkha

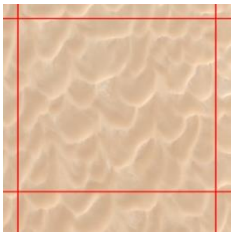
Sand dunes


Mixed area 1


Mixed area 2


Sand and buildings


Low density of buildings


Built-up area

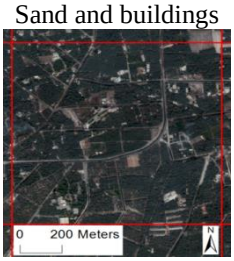

Vegetation area (farm)

Note: Mixed area 1 - vegetation, buildings, sand and sabkha; and mixed area 2 - sabkha, sand, buildings and vegetation.

6.4 **Accuracy assessment of the classification**

The step following classification is the accuracy assessment. The land cover classification results from Landsat 7 are tested using real-world land cover data using high spatial resolution images (GeoEye-1 and Google Earth images). The accuracy assessment used a simple random sampling (SRS) framework and the results indicates that 438 of 500 random sample points are identical with those of the real world, while only 62 sample points show a dissimilarity to the reference points (GeoEye-1 and Google Earth images) (Table 6-1). In other words, the accuracy assessment of the land cover classification using the Landsat 7 data for the study area is 87% accurate against the reference data. Moreover, the most errors of the classification results appear among the sand and sabkha classes. That refers to the close similarity of both classes, which represent sand surfaces but the sabkha includes some wet salty surfaces. An example of the random sample units is shown in Figure 6-8.

Table 6-1 Error matrices comparing, on a class-by-class basis

		Reference map data (GeoEye and Google Earth image)						
	Classes	Sabkha	Sand	Vegetation	Built-up	Water	Total	(%)
Classified map data	Sabkha	20	13	3	6	0	42	48%
	Sand	5	193	8	0	0	206	94%
	Vegetation	1	14	95	1	0	111	86%
	Built-up	5	5	1	129	0	140	92%
	Water	0	0	0	0	1	1	100%
Total		31	225	107	136	1	500	
(%)		65%	86%	89%	95%	100%		87%

Note: The relationship between known reference data (ground true GeoEye and Google Earth data) and the corresponding results of the classification procedure for the study area.

Figure 6-8 An example of random sample points of classified images with the decision about being identical to or dissimilar from the real world

Class name	Google Earth	GeoEye	Classified	Decision
Vegetation			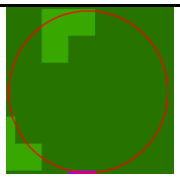	Identical
Built-up area			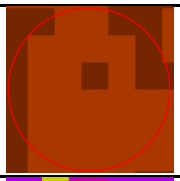	Identical
Sabkha and sand		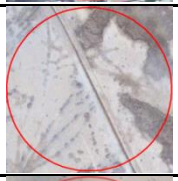	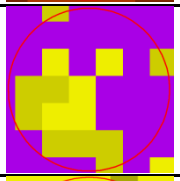	Identical
Vegetation and sand	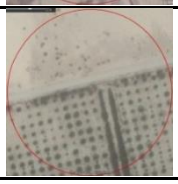	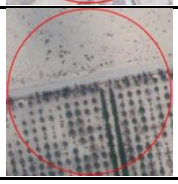	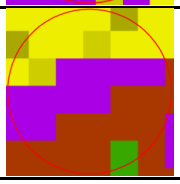	Dissimilar

Note: Green = vegetation, Brown = built-up area, Purple = sabkha, and Yellow = sand. The real scale of each image is 180 m width and 180 m height.

6.5 **Mapping the emissivity (εσ)**

Mapping the emissivity values is the next step followed the supervised classification in order to estimate the surface temperature using Landsat 7 ETM+ and MODIS thermal data. The emissivity value of each land cover class is identified after classification step based on look up tables and previous studies of the emissivity values in arid region (Zhang, 2011). Each class in the Landsat 7 ETM+ and MODIS

classified images integrates its own emissivity value using the ENVI software to produce the emissivity map (Shunlin, 2001, Janet, 2009, Sobrino et al., 2012). The results of the emissivity maps using both images Landsat 7 ETM+ and MODIS is shown in (Figure 6-9 and Figure 6-10). The emissivity value ranges between 0.95 and 0.99 during the summer (18 August 2011) and between 0.93 and 0.98 during the winter (7 February 2011) for the Landsat 7 ETM+. While the emissivity value ranges between 0.94 and 0.97 during the summer (1 July 2011) and between 0.93 and 0.98 during the winter (1 February 2011) (Figure 6-9 and Figure 6-10).

Figure 6-9 Emissivity values of different land covers of the study area, using Landsat 7 ETM+

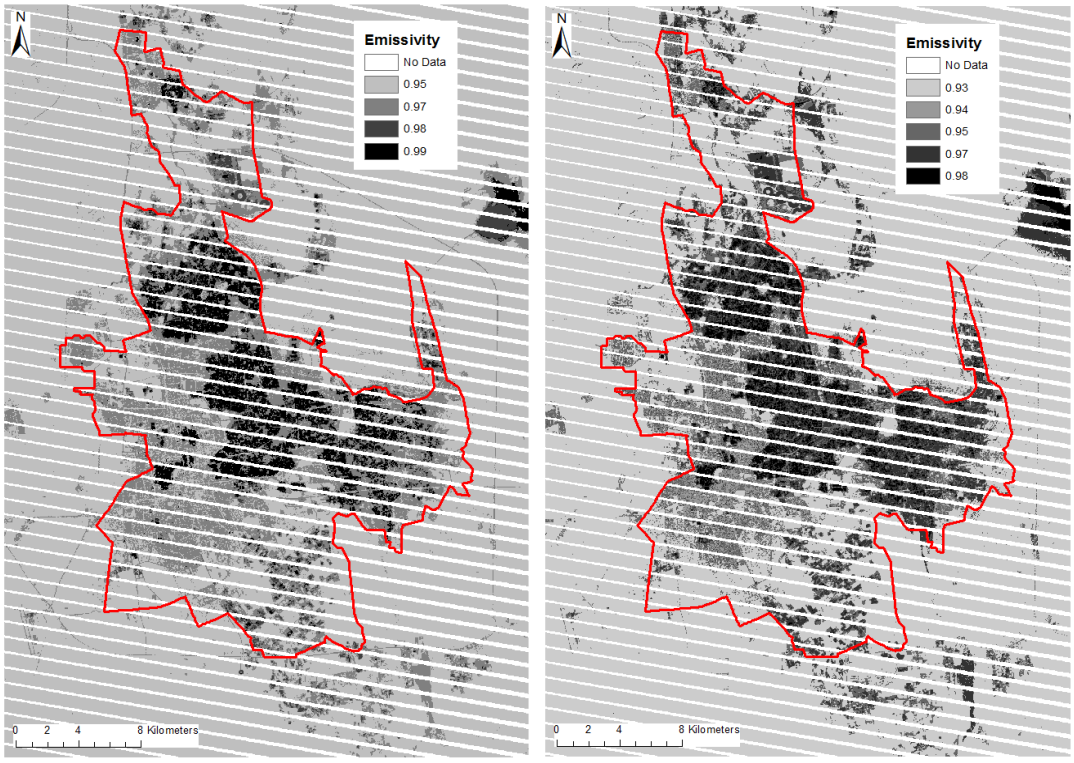

Note: Left: during the summer (18 August 2011); Right: during the winter (7 February 2011).

Figure 6-10 Emissivity values of different land covers of the study area using MODIS data

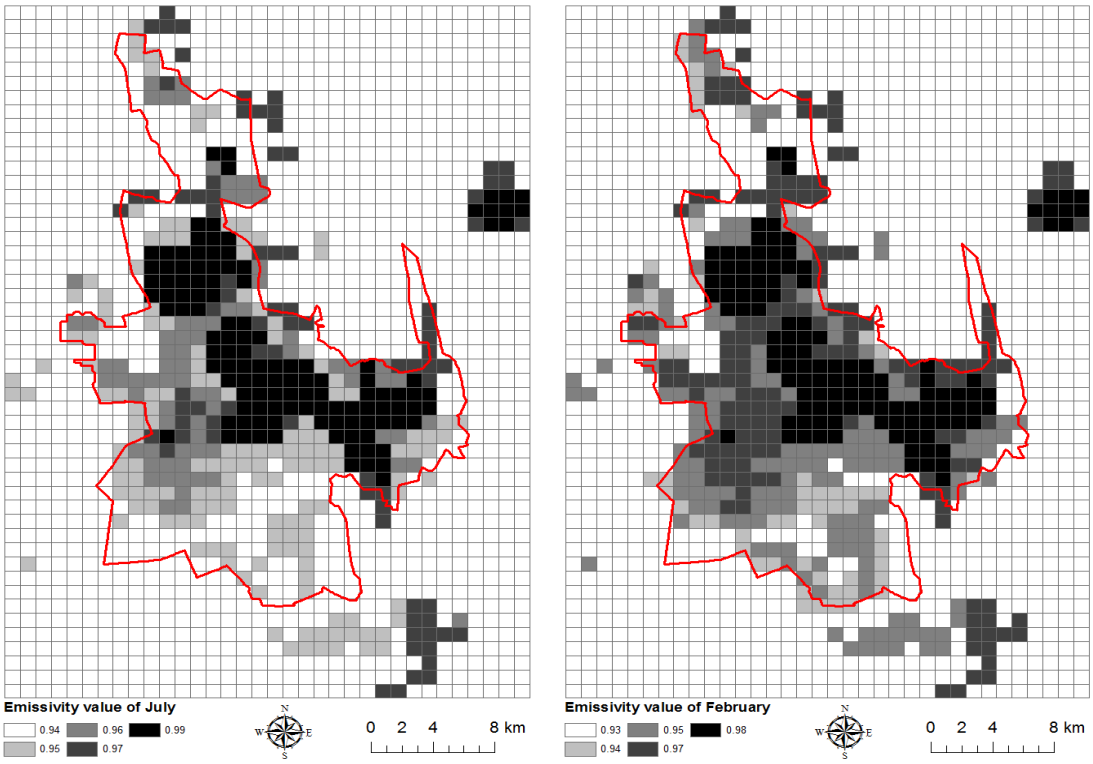

Note: Left: during the summer (1 July 2011); Right: during the winter (1 February 2011).

6.6 **Estimating surface temperature using Landsat7 ETM+**

The Landsat 7 ETM+ thermal band 6 data refer to the gain value and settings when the data are acquired. The thermal band is acquired in two different gain values high and low then stored in two different channels 61 for lower radiometric resolution and sensitivity and 62 for higher radiometric resolution and sensitivity (Barsi et al., 2003). Following the previous steps of classification and emissivity, it is possible to estimate the surface temperature by converting the digital numbers to radiance values using published parameters (Coll et al., 2010). (See chapter three: Data sources and Methodology-section 3.5 for more details with respect to the estimation of the surface temperatures from spectral radiance data).

The surface temperature is estimated seasonally during the winter and summer 2011. The surface temperature estimation result is shown in Figure 6-11. During the winter season (7 February 2011) the surface temperature of the study area, Al Ahsa Oasis,

ranged between 12 °C and 31 °C at 11:00 AM, while the surface temperature ranged between 28 °C and 58 °C during the summer season (18 August 2011).

The surface temperature in the study area can be classified into four categories: cool, mild, high and extremely high. The first category includes the surface temperature ranging from 12 °C to 20 °C during the winter and from 28 °C to 42 °C during the summer. This category is located at the green vegetated areas and the area that is close to the palm tree farms. The second category represents the mild zone, where the surface temperature ranges from 20 °C to 22 °C during the winter and from 42 °C to 46 °C during the summer; this zone extends between the green area and the built-up area. The third category is the high zone, where the surface temperatures range between 22 °C and 24 °C during the winter and between 46 °C and 48 °C during the summer. The last category is the extremely high area, which is located on the sand and sabkha sites during either the winter or the summer season. The surface temperature in this area ranges from 24 °C to 31 °C in the winter and from 48 °C to 58 °C in the summer (Figure 6-11).

These previous results for the surface temperature were expected due to the time of the satellite overpass, which is 11:00 AM, and from estimating the surface temperature during the period of direct sun during the day (Mildrexler et al., 2011). The nature of the surface temperature in the desert regions, where sand is the main land cover, is that it quickly heats up to high temperatures during the daytime and drops rapidly during the night, which explains the results for the surface temperature of the study area (Alavipanah et al., 2007).

Figure 6-11 Surface temperature of the study area estimated from Landsat7 ETM+ 2011

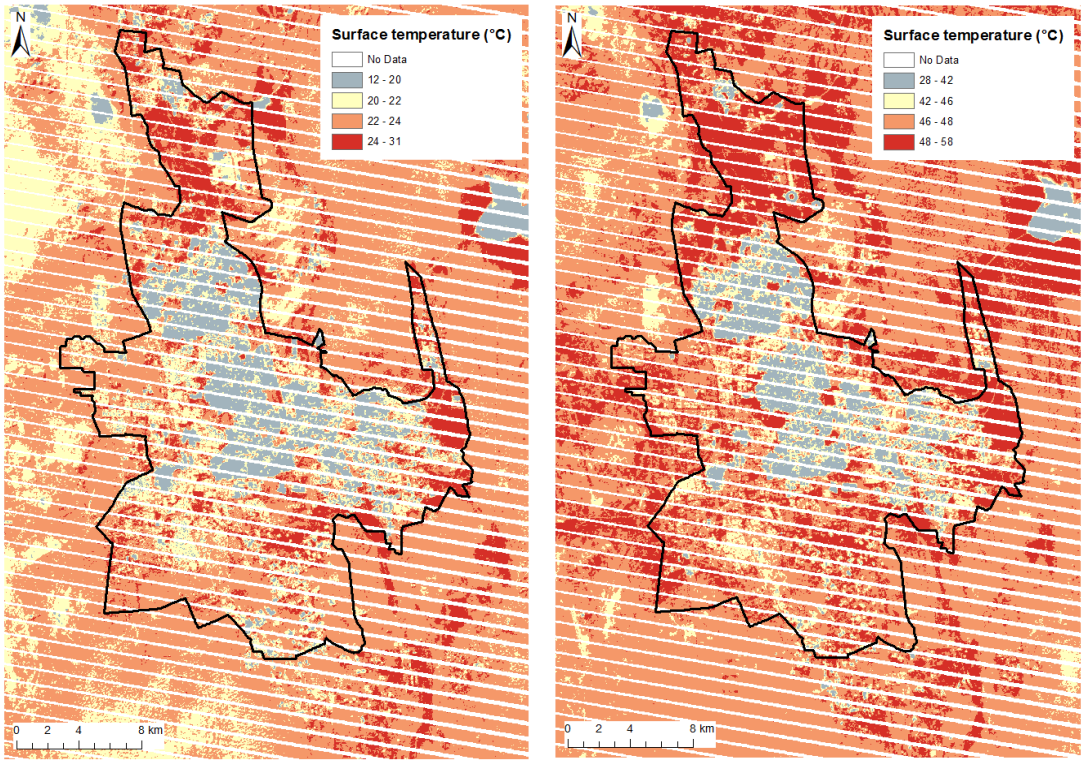

Note: 7 February (left) 18 August (right) at 11:00 AM local time). The two images are in different scales.

6.7 **Estimating surface temperature using MODIS data**

Another method of estimating the surface temperature using MODIS data is to use a generalized split-window LST algorithm (Zhengming and Dozier, 1996, Wan et al., 2002). Although the MODIS data do not have a high spatial resolution, being 1000 m compared to the Landsat 7 ETM+ at 60 m, they have a high temporal resolution, as the data are available on a daily basis for both day and night (Roy et al., 2002). The surface temperature of the study area during the winter (February) and summer (August) was estimated daily, for the day and the night. An example of the brightness temperature, estimated using MODIS data, is shown in Figure 6-12 for both day- and night-time on two selected days in each season, 4 and 20 February and 4 and 20 August.

Figure 6-12 Night-time and daytime brightness temperature of the study area using MODIS data during February and August in 2011

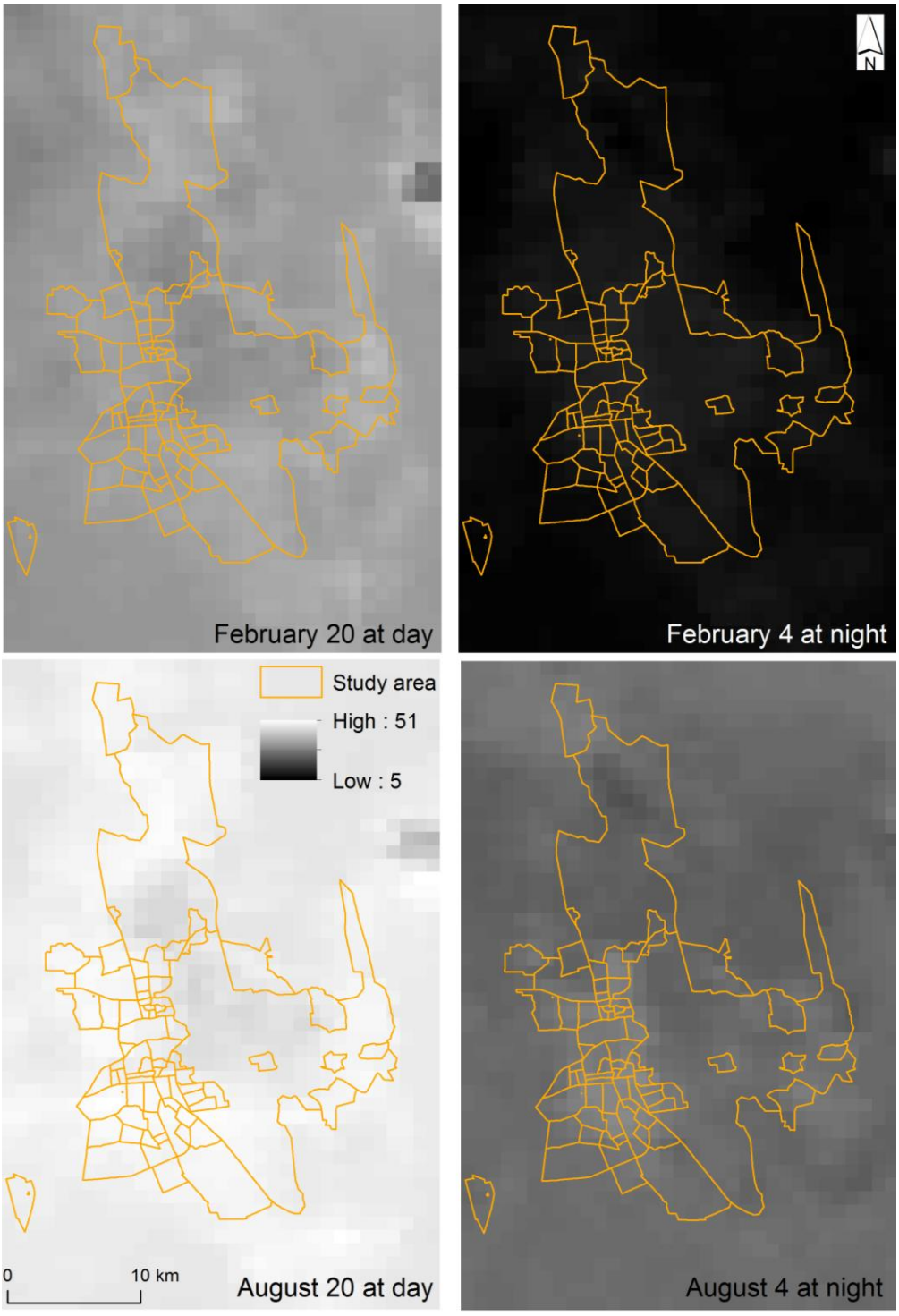

Both brightness temperature images during the daytime and night-time indicate the presence of SUHI in the study area. The maximum surface temperature during the two selected days, presented in a light colour, is distributed outside and on the open sand and sabkha areas during the day, while it is centred on the built-up area and

residential area during the night. However, the minimum surface temperature, presented in the dark colour, was observed over the vegetated areas and water bodies during the day and became cooler during the night in the same area, including the sand covered area. The difference between the maximum and minimum surface temperatures during the two selected days is 15 °C in the day and 6 °C in the night in February and is 10 °C in both day and night in August.

6.8 **Comparison between ground and satellite surface temperature estimates**

The results of surface temperature obtained from the Landsat 7 ETM+ and MODIS satellites were compared to the real-time ground temperature measurements, recorded at six fixed weather stations and from mobile data. Thist allows satellite surface temperature estimates to be compared against ground (Orhan et al., 2014). The comparison of the results of Landsat with those of the fixed weather stations, including the airport, indicates a close agreement, ranging between 1 °C and 6 °C during August and between 1 °C and 5 °C during winter (Figure 6-13), while the comparison of results between mobile and MODIS data shows that agreement ranged between 0.03 °C and 4.16 °C during the winter and summer selected days (2 August and 19 February 2011) (Figure 6-14 and Figure 6-15). These differences or disagreements between fixed weather stations and Landsat 7 ETM+ observations might refer to the sensitivity of the method that used to estimate the surface temperature by converting the radiation to brightness temperature comparing with ground-based method and to the small sample of the points which are presenting in this comparison. The largest different between the satellite and fixed weather stations observations occurred on the sabkha and farm sites and that supports the argument about the sensitivity of the measurements especially if we consider the time of the satellite overpass which is about 11am. The disagreement between MODIS and mobile observations might refer to the pixel size of MODIS which covers 1000 metres and represents different land covers compared to mobile data. That might be confirmed by the largest disagreement between both MODIS and mobile observations being recorded in mixed areas in both seasons (Figure 6-14 and Figure 6-15).

Figure 6-13 Relationships between real-time (in situ) fixed weather station and land surface temperatures calculated from Landsat-7 thermal infrared band

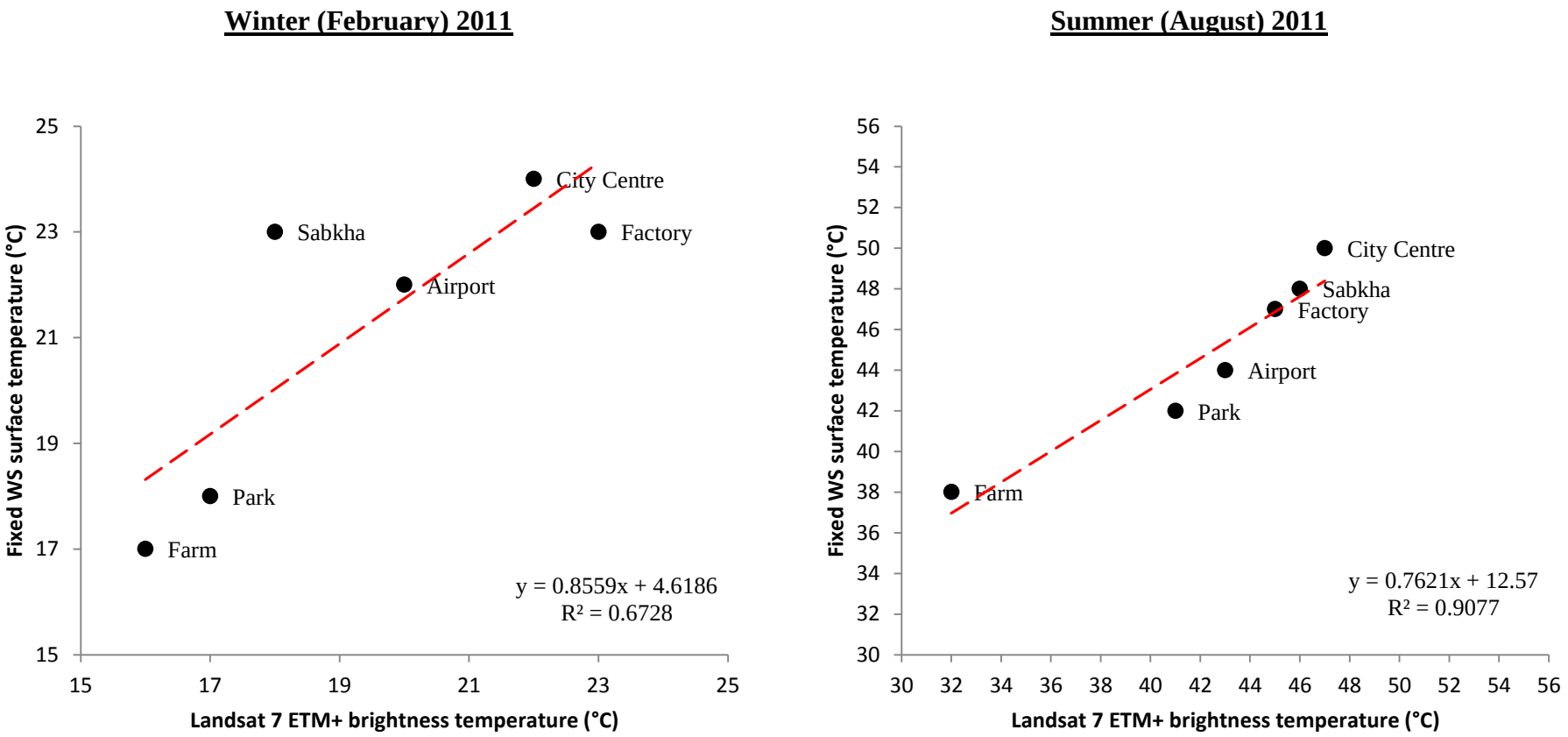

Note: (real-time measurements were collected on 7 February 2011 and 18 August 2011 (11:00 AM), GMT+3). Landsat-7 overpass: (07:04 AM).

Figure 6-14 Comparison between real-time (in situ) mobile data and brightness surface temperature estimated from MODIS image on 2nd August 2011

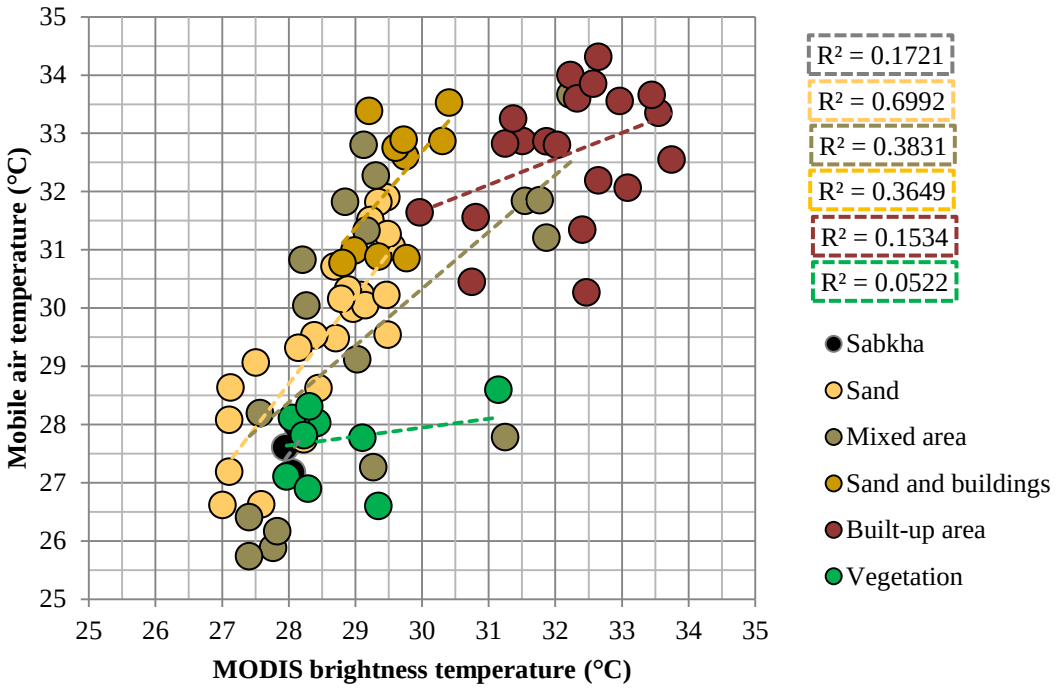

Note: (real-time of mobile data at 01:47 AM and MODIS overpass at 01:40 AM).

Figure 6-15 Comparison between real-time (in situ) mobile data and brightness surface temperature estimated from MODIS image on 19th February 2011

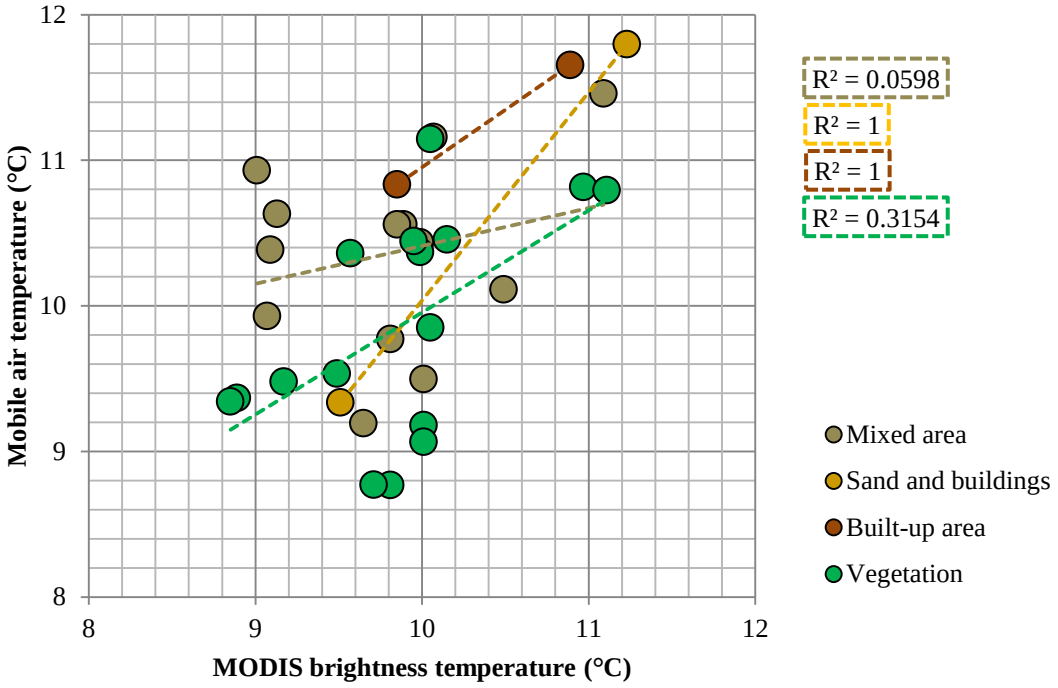

Note: (real-time of mobile data at 01:16 AM and MODIS overpass at 01:10 AM).

6.9 **The relationship between SUHI intensity and different land cover**

Land cover change is one of the most important factors of urban climate change, usually presented as (SUHIs) (Laras et al., 2012). After estimating the brightness temperature using Landsat 7 and MODIS thermal band data, the SUHI intensity is calculated by subtracting the pixel value of the rural area (the airport area) from the urban area of the study area (Oke, 1998). The relationship between the UHI intensity and different land cover types is tested two times based on two different spatial resolutions, first with Landsat at 60 metres and second with MODIS at 1000 metres of spatial resolution.

6.9.1 Landsat 7 ETM+

The SUHI intensity data distribution indicates a significant relationship among different land cover types based on Landsat 7 data. Although the Landsat overpass time was 11:00 AM local time, when the SUHI intensity was weak (Oke, 1982), there is a clear picture of the effect of the different land cover types on the (SUHIs). The median of the SUHI intensity ranged between -7 °C and 1 °C during February and between -18 °C and 2 °C during August at the water body and sabkha sites and at the water body and residential areas, respectively. The minimum of SUHI intensity is observed at the water body, palm tree sites, residential areas, and irrigated areas during February, while the maximum is recorded in the sabkha, sandstone, residential areas, and parking lot and asphalt areas during August. For example, the minimum value of SUHI intensity was recorded in the residential areas during February (-10 °C) and in the water bodies during August (-18 °C), while the maximum values were observed at the sandstone area (8 °C) during February and at the parking lot and asphalt areas during August (10 °C) (Figure 6-16). These results are expected, because the time of the satellite overpass is 11.00 AM local time, when the surface is receiving direct sunlight. Moreover, different materials on the Earth's surface absorb solar radiation differently. For example, water heats up more slowly and to a lower temperature than other materials such as sand or sabkha areas (Bland et al., 2004).

Figure 6-16 Summary of SUHI intensity distribution during February and August among different land cover types

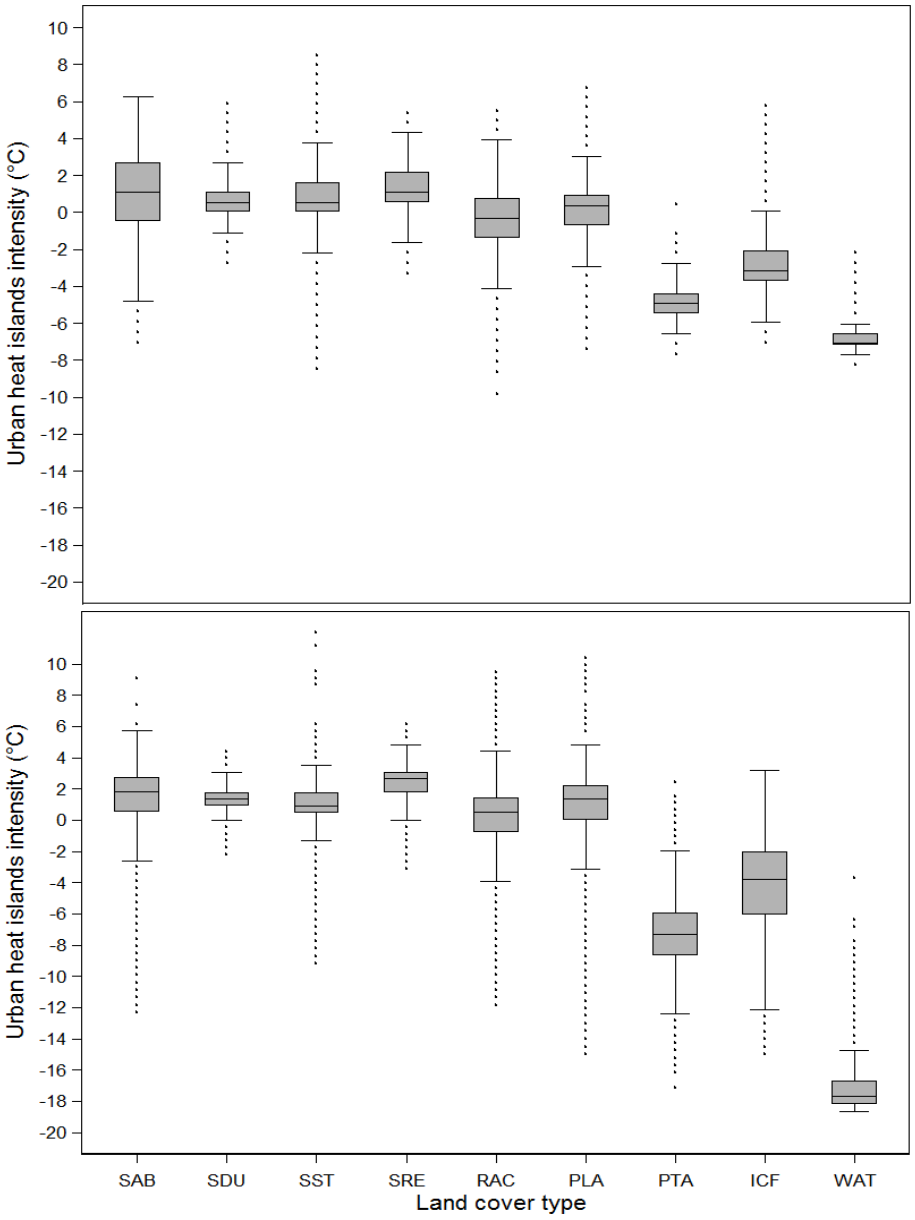

Note: 7 February (top) and 18 August (bottom). SAB = Sabkhas, SDU = Sand dunes, SST = Sandstone, SRE = Red Sand, RAC = Resident area (most of it buildings), PLA = Parking lot area (most of it asphalt), PTA = Palm tree areas, ICF = irrigated crop fields, and WAT = water.

Similarly, Figure 6-17 shows the intensity of (SUHIs) in the study area, Al Ahsa Oasis, during February and August. Through the images, we can divide the (SUHIs) into three categories: 1) cool (SUHIs), which range between -10 °C and 0 °C during February and from -18 °C to 0 °C during August; 2) a no SUHI zone, which is at 0 °C during February and August; and 3) hot (SUHIs), which range between 0 °C and 8 °C during February and from 0 °C to 12 °C during August. The cool category centres on the water, palm trees and irrigated areas, while the hot zone is located on

the three types of sands (sand dunes, sandstone and red sand areas), including the sabkha sites; however, the no SUHI zone is located between the hot and cool zones and is made up of the areas close to the vegetation and the edges of the urban and resident areas.

Figure 6-17 SUHI intensity of the study area using Landsat 7 ETM+ data

Note: 7 February (winter), left, and 18 August (summer), right. The overpass of the satellite is 11:00 AM local time.

Statistical test indicates that heat islands intensity data are not normally distributed based on Landsat 7 ETM+ data. The result of a Skewness/Kurtosis test showed that the null hypothesis cannot be accepted at $P<0.05$ level for HII in different land cover areas during both February and August. A non-parametric test of the median values for HII among different land cover area (Sabkha, Sand dunes, Sandstone, Red Sand, Resident area, Parking lots, Palm tree areas, Irrigated crop fields, and water) for both seasons (February and August), showed that there is a statistically significant difference among these groups. The results of a Kruskal–Wallis test for median

comparison of HII indicates λ2 = 1.15e+05 with (8) *d.f.* *P*=0.0001 for February and λ2 = 1.29e+05 with (8) *d.f.* *P*=0.0001 for August. There are statistically significant differences in HII between each pair of land cover areas during both February and August (Table 6-2). The Kruskal-Wallis test showed that the HII at all locations is significantly different, with (*P*=0.0001) except between Sandstone and Parking lots areas during August (*P*=0.0025). The equal medians of these mentioned sites might be explained by the similarity of the conditions between them as the parking lots area represent asphalt while the other site is the sand mixed with stones. These results strongly indicate the effect of the land cover types on the SUHI intensity during both seasons based on Landsat 7 ETM+ data.

Table 6-2 A result of the Kruskal–Wallis test of SUHI intensity between each pair of land cover areas during February and August based on Landsat 7 ETM+ data.

Land cover	Season	SAB	SDU	SST	SRE	RAC	PLA	PTA	ICF
SDU	Feb.	≠							
	Aug.	≠	≠						
SST	Feb.	≠	≠						
	Aug.	≠	≠						
SRE	Feb.	≠	≠	≠					
	Aug.	≠	≠	≠					
RAC	Feb.	≠	≠	≠	≠				
	Aug.	≠	≠	≠	≠				
PLA	Feb.	≠	≠	≠	≠	≠			
	Aug.	≠	≠	=	≠	≠			
PTA	Feb.	≠	≠	≠	≠	≠	≠		
	Aug.	≠	≠	≠	≠	≠	≠		
ICF	Feb.	≠	≠	≠	≠	≠	≠	≠	
	Aug.	≠	≠	≠	≠	≠	≠	≠	
WAT	Feb.	≠	≠	≠	≠	≠	≠	≠	≠
	Aug.	≠	≠	≠	≠	≠	≠	≠	≠

Note: '=' indicates no difference (accept – H_0) and '≠' indicates significant difference (accept - H_1). Values in parentheses indicate calculated *P* values. Adjusted probability (P'=0.001). SAB = Sabkhas, SDU = Sand dunes, SST = Sandstone, SRE = Red Sand, RAC = Resident area (most of it buildings), PLA = Parking lot area (most of it asphalt), PTA = Palm tree areas, ICF = irrigated crop fields, and WAT = water.

6.9.2 MODIS data

MODIS data, with a 1000-metre pixel size and daily revisits (day and night), are used to investigate the relationship between SUHI intensity and land cover type. The land cover types are divided into seven classes, based on the majority land cover

type evaluated over the area of a MODIS pixel size (1000 m): sabkha, sand, vegetation, mixed area, sand and buildings, low density of buildings, and built-up area. The land cover is classified, using a grid overlaid on a high spatial resolution image (GeoEye-1) in order assess the precise area of each type of land within each grid (Oke, 2006). These results indicate a significant relationship between the land cover type and SUHI intensity, based on MODIS data during February and August, for both day and night observations. For the sand and residential land cover types, the median of the SUHI intensity ranged between 1 °C and 2 °C respectively during the day and between 0.30 °C and 3 °C at night, during the nine selected days of February. For the vegetation, sabkha, sand land cover types, the median of the SUHI intensity ranged from -1.30 °C to 1.50 °C in daytime and from 0.65 °C to 2.40 °C at night during for the same nine days The minimum SUHI intensity is observed over the vegetated areas (-10 °C) and the sand areas (-3 °C) during February daytime and night-time, respectively. The maximum HII is recorded over the sand (11 °C) and mixed area (7 °C) land cover types during February. The minimum SUHI intensity is observed over the vegetated areas (-12 °C) and sabkha areas (-10 °C) during August daytime and night-time, respectively, while the maximum is recorded in the sand (6 °C) and residential areas (7 °C) during August daytime and night-time, respectively (Figure 6-18).

Figure 6-18 Summary of SUHI intensity distribution among different land cover in the nine selected days of 31 days during August and of 28 days of February 2011

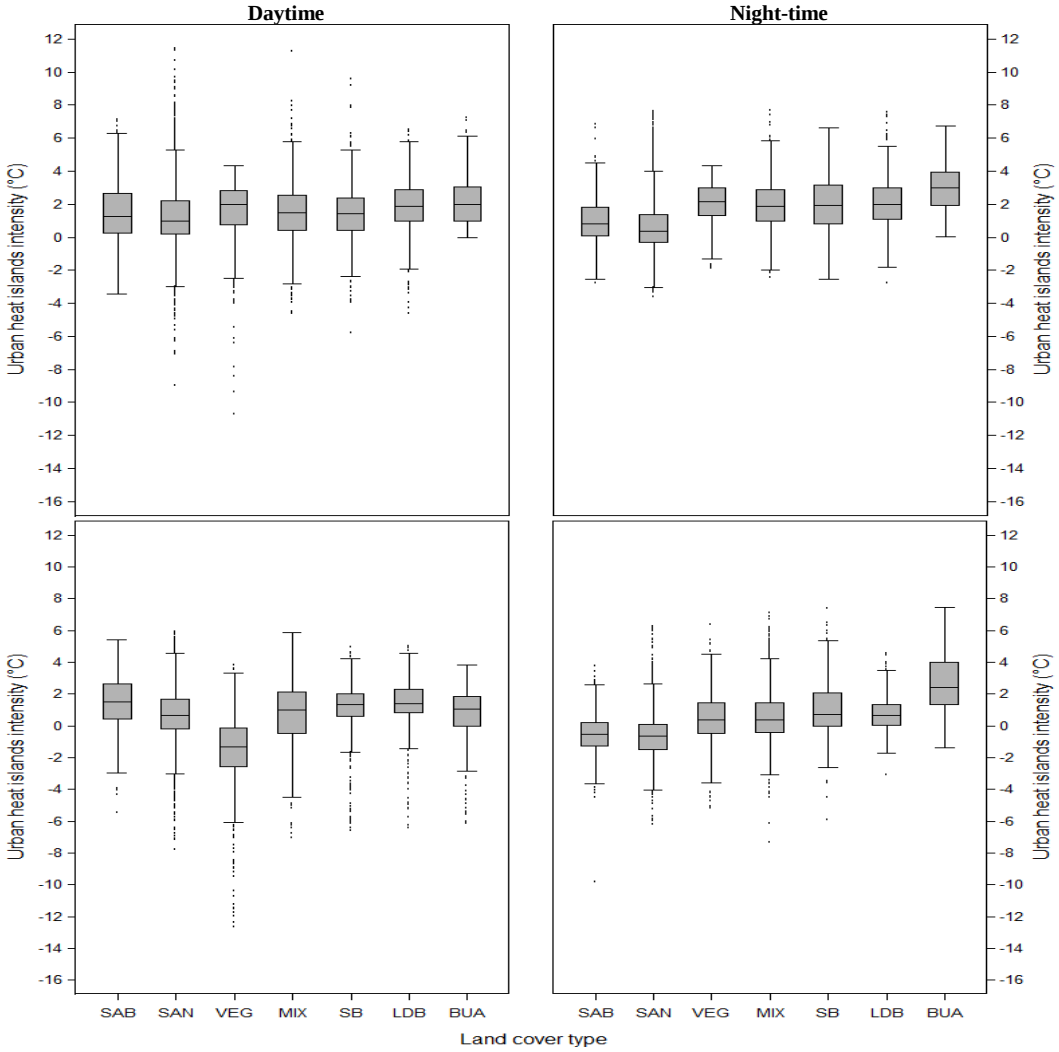

Note: February (top) and August (bottom), in daytime (left) and night-time (right). SAB = Sabkha, SAN = Sand, VEG = Vegetation, MIX = Mixed area, SB = Sand and buildings, LDB = Low density of buildings, and BUA = Built-up areas.

An example of mapping SUHI intensity using MODIS imagery is shown in Figure 6-19. The figure indicates that during the night the positive SUHI intensity is centred over the residential area, which represents the main two urbanized centres of the oasis (Al Hufuf and Al Mubarraz), and the weaker heat islands are centred over the vegetated area and water body during the day and over the sand at night during both seasons, February and August 2011.

Figure 6-19 SUHI intensity of the study area using MODIS data

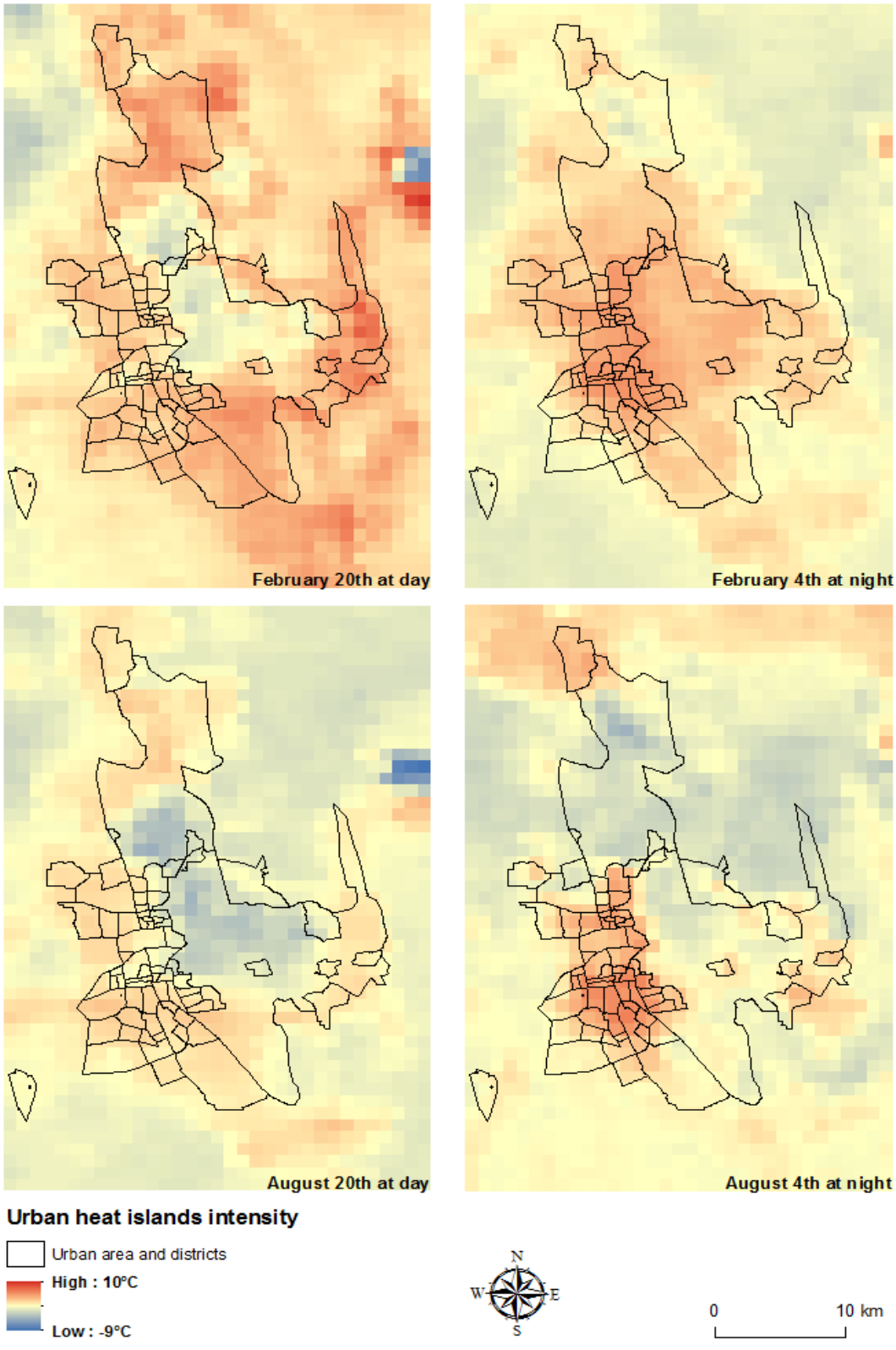

Note: during 20 February and 4 February (winter), top, and 20 August and 4 August (summer), bottom. The overpass of the satellite is at 13:00 and 01:10 local time during February and is at 13:20 and 01:40 local time during August, day- and night-time, respectively.

The distribution of MODIS data indicates that heat islands intensity data are not normally distributed. The result of a Skewness/Kurtosis test shows that the null hypothesis cannot be accepted at $P<0.05$ level for HII in different land cover areas during both February and August at the day and night data based on MODIS data. A non-parametric test of the median values for HII among different land cover area (Sabkha, Sand, Vegetation, Mixed area, Sand and buildings, Low density of buildings, and built-up area) for both seasons (February and August) during the day and night, indicates that there is a statistically significant difference among these groups. The results of a Kruskal–Wallis test for median comparison of HII are $\lambda 2 = 1979.409$ with (6) *d.f.* $P=0.0001$, $\lambda 2 = 2779.990$ with (6) *d.f.* $P=0.0001$, $\lambda 2 = 1363.365$ with (6) *d.f.* $P' =0.0001$, and $\lambda 2 = 3035.303$ with (6) *d.f.* $P=0.0001$ during February and August at the day and night respectively.

Moreover, comparing each pair of land cover during both periods also indicates that there are statistically significant differences of the heat island intensity among these land covers. The Kruskal-Wallis test shows that the HII at most of the sites is significantly different, with $P=0.0001$ except between some of the land covers classes. These classes that include the equal medians, are sand and buildings with mixed area, and vegetation; low density of buildings with sabkha, mixed area, sand and buildings, and vegetation during February; and sand with sabkha, vegetation with mixed area, low density of buildings with sabkha, sand and buildings, mixed area, and vegetation, and finally mixed area with built-up area during August (Table 6-3 and Table 6-4). The equal medians of these mentioned sites might be refer to the effect of the differences of the spatial resolution between MODIS (1000 meter), which represent several land covers within each pixel, comparing with Landsat 7 ETM+ (30 meter). Overall, the statistic outcomes support the effect of the land covers types on the (SUHIs) intensity based on MODIS data for both seasons at the day and night time.

Table 6-3 A result of the Kruskal–Wallis test of SUHI intensity between each pair of land cover areas during February (nine selected days) at the day and night-time based on MODIS data.

Land cover	Time	SAB	SAN	VEG	MIX	SB	LDB
SAN	Day	≠(0.0001)					
	Night	≠(0.0001)					
VEG	Day	≠(0.0001)	≠(0.0001)				
	Night	≠(0.0001)	≠(0.0001)				
MIX	Day	≠(0.0001)	≠(0.0001)	≠(0.0001)			
	Night	≠(0.0001)	≠(0.0001)	≠(0.0004)			
SB	Day	≠(0.0001)	≠(0.0001)	≠(0.0001)	=(0.4892)		
	Night	≠(0.0001)	≠(0.0001)	=(0.0251)	=(0.6730)		
LDB	Day	=(0.1269)	≠(0.0001)	≠(0.0001)	≠(0.0001)	≠(0.0001)	
	Night	≠(0.0001)	≠(0.0001)	=(0.2710)	=(0.1648)	=(0.2524)	
BUA	Day	≠(0.0001)	≠(0.0001)	≠(0.0001)	≠(0.0001)	=(0.9658)	≠(0.0001)
	Night	≠(0.0001)	≠(0.0001)	≠(0.0001)	≠(0.0001)	≠(0.0001)	≠(0.0001)

Note: '=' indicates no difference (accept – H_0) and '≠' indicates significant difference (accept - H_1). Values in parentheses indicate calculated P values. Adjusted probability (P'=0.002).

Table 6-4 A result of the Kruskal–Wallis test of SUHI intensity between each pair of land cover areas during August (nine selected days) at the day and night-time based on MODIS data.

Land cover	Time	SAB	SAN	VEG	MIX	SB	LDB
SAN	Day	≠(0.0001)					
	Night	=(0.0021)					
VEG	Day	≠(0.0001)	≠(0.0001)				
	Night	≠(0.0001)	≠(0.0001)				
MIX	Day	≠(0.0001)	≠(0.0002)	≠(0.0001)			
	Night	≠(0.0001)	≠(0.0001)	=(0.5713)			
SB	Day	=(0.0033)	≠(0.0001)	≠(0.0001)	≠(0.0001)		
	Night	≠(0.0001)	≠(0.0001)	≠(0.0001)	≠(0.0001)		
LDB	Day	=(0.4488)	≠(0.0001)	≠(0.0001)	≠(0.0001)	=(0.0518)	
	Night	≠(0.0001)	≠(0.0001)	=(0.0030)	=(0.0035)	=(0.0044)	
BUA	Day	≠(0.0001)	≠(0.0012)	≠(0.0001)	=(0.9848)	≠(0.0001)	≠(0.0001)
	Night	≠(0.0001)	≠(0.0001)	≠(0.0001)	≠(0.0001)	≠(0.0001)	≠(0.0001)

Note: '=' indicates no difference (accept – H_0) and '≠' indicates significant difference (accept - H_1). Values in parentheses indicate calculated P values. Adjusted probability (P'=0.002).

The SUHI intensity is higher during the daytime in both February and August. The SUHI intensity ranged between -7 °C and 10 °C and between -9 °C and 4 °C in 20th of February and 20th of August respectively at the daytime. While, the SUHI intensity ranged from -2 °C to 6 °C and from -4 °C to 6 °C in 4th of February and 4th of August respectively at the night-time (Figure 6-19). Similarly to Landsat 7 observations, the MODIS thermal data also shows a similar pattern, relating land cover type and SUHI intensity. Three zones of SUHI intensity can be identified. The first zone is the sabkha and sand areas, which heat up quickly during the daytime and

cool down rapidly at night. The second zone is the vegetated and water body areas, which show a stable relationship with SUHI intensity during both day and night; this zone can be classified as the lowest zone of SUHI intensity values. The third zone is the built-up areas, which include the zone that receives energy and heat during the day and releases it during the night; this applies to both seasons, February and August (Figure 6-19).

The daily distribution of SUHI intensity among different land cover types either during February or August at day or night indicates a fluctuating distribution, especially during February daytime. Figure 6-20 shows that the median HII in the areas of sand and low density of buildings during the daytime ranged between 0.30 °C and 3.65 °C. The minimum HII values were recorded over low density buildings and sand areas on different days during February. For example, at -4 °C on 2 February for the low density buildings; at -9 °C on 22 February for sand; at -10 °C on 27 February for vegetation. The maximum values were observed over sand on 4 February at 11 °C; 6 °C over sand and buildings on 19 February; 7 °C over sabkha on 20 February (Figure 6-20).

However, the medina HII in the regions of sand and built-up during the night ranged between -0.40 °C and 4 °C. The minimum HII values were observed at also different land covers during February. For example, at -4 °C on 2 February for the sand area, -3 °C on 15 February for the sabkha area and at -2 °C on 11 February for the sand and buildings areas. The maximum HII values were recorded over built-up and low density of buildings areas on 22 February at 8 °C and 7 °C over the mixed area site on 19 February (Figure 6-20).

Figure 6-20 The data distribution of the SUHI intensity among the different land cover types on the nine selected days of 28 days during February 2011

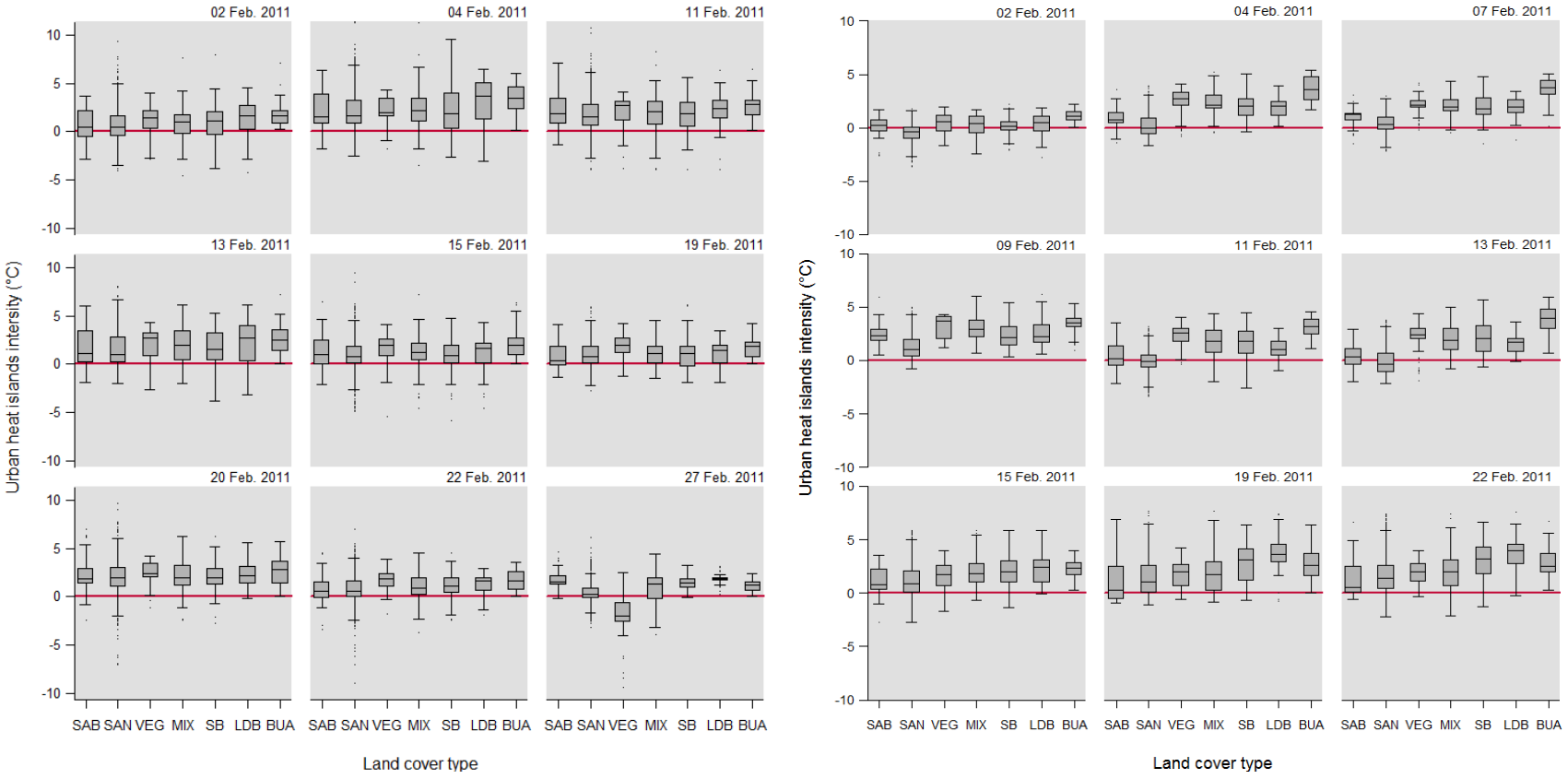

Note: Daytime (left) and night-time (right). SAB = Sabkha, SAN = Sand, VEG = Vegetation, MIX = Mixed area, SB = Sand and buildings, LDB = Low density of buildings, and BUA = Built-up areas.

During August, the daily distribution of urban HII values among different land cover types fluctuates, especially during the day. The night data, however, show a more stable pattern with less variation among the land cover types. Figure 6-21 shows that the median night HII values ranged between -3 °C and 3 °C at the vegetation and sabkha areas, respectively, and between -2 °C and 4 °C at the sabkha and built-up areas, respectively. The minimum HII values were recorded over different land cover types on different days (Figure 6-21).

At August night the land cover shows a clear effect on the pattern (SUHIs) intensity. The distribution of the minimum, maximum, and the median of (SUHIs) indicate an increase starting from the first land cover sabkha to reach the peak value at the built-up area during the night-time. The minimum values of SUHI intensity during the night were also noted in different land covers and on different days during this month, for example, at -10 °C on 23 August at the sabkha area, at -6 °C on 18 August at the sand area and at -5 °C on 18 August at the vegetation areas. However, the maximum values were observed in the built-up area class on 20 August at 8 °C, at the low density of buildings area on 20 August at 7 °C and at the sand and buildings site on 23 August at 6 °C (Figure 6-21).

Figure 6-21 The data distribution of the SUHI intensity among the different land cover types on the nine selected days of 31 days during August 2011

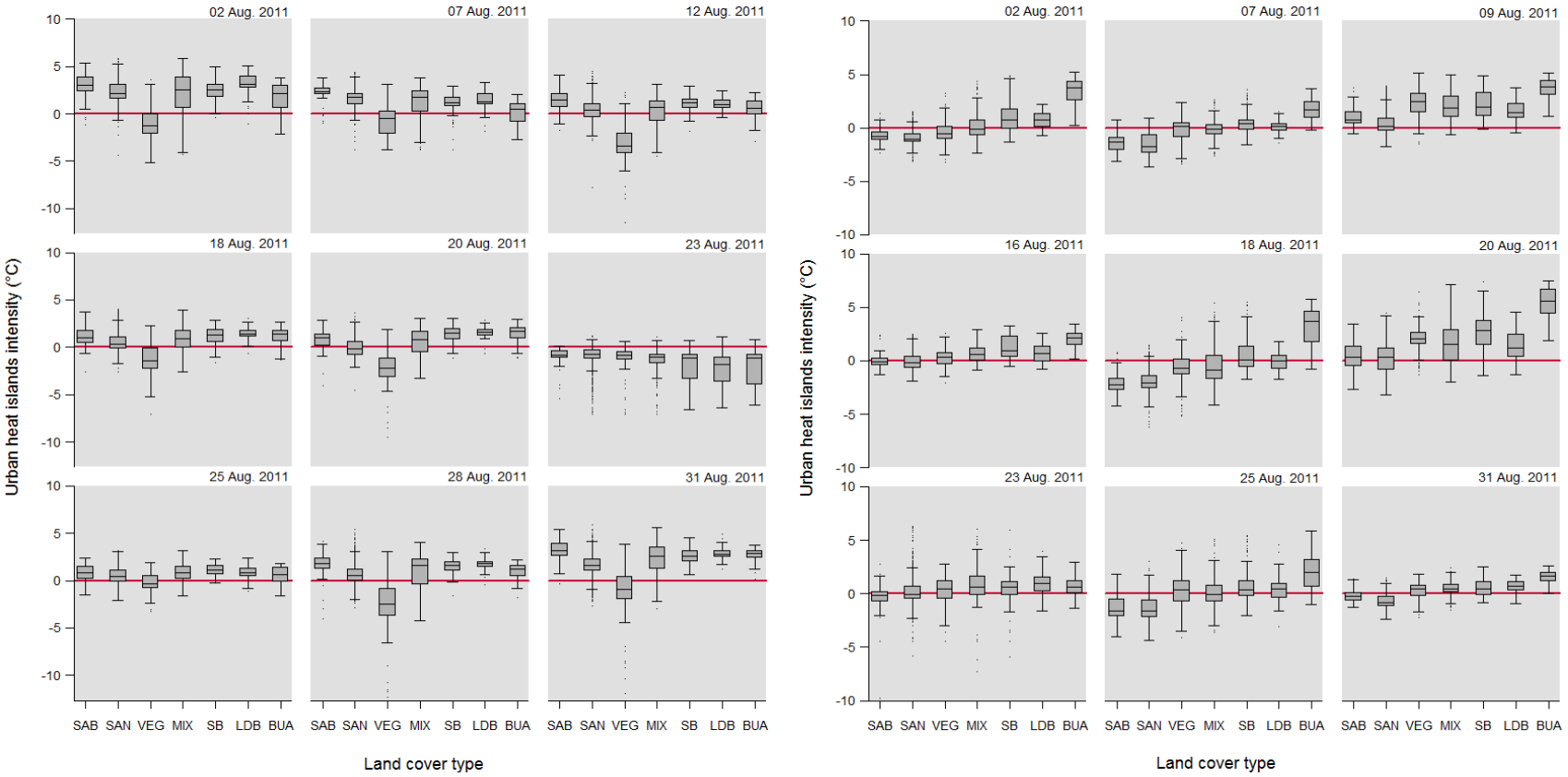

Note: Daytime (left) and night-time (right) during August 2011. SAB = Sabkha, SAN = Sand, VEG = Vegetation, MIX = Mixed area, SB = Sand and buildings, LDB = Low density of buildings, and BUA = Built-up areas.

Another way to determine the effect of land cover on UHI intensity is to compare the percentage of land cover for each class with the UHI intensity values derived from satellite observation (Yokobori and Ohta, 2009). The percentage of each land cover class is calculated based on both MODIS and Landsat pixel sized classified images. For more details about this analysis, see the methodology chapter (section 3.4.3.3). The relationship between the percentages of different land cover types and UHI intensity for the selected days of February and August is shown in Figure 6-22 and Figure 6-23. During the daytime, the UHI intensity increases as the area of sabkha cover increases. On the other hand, there is a strong decrease in UHI intensity as the percentage of vegetation cover increases. During the night, the UHI intensity increases as area of built-up area increases. Also, during the night, the percentage of sand and vegetation appear to have an influence on UHI intensity which can be summarized as an inverse relationship (the more sand, the less SUHI intensity), (Figure 6-22and Figure 6-23).

The above-mentioned results are logically consistent with the expected thermal behaviour of desert land cover types; sabkha and sand usually heat up quickly during under strong direct sunlight and cool down rapidly at night (Bland et al., 2004). Vegetation is a typical land cover type in many oases and plays a major role in surface cooling both during the day and the night. Moreover, the built-up area shows a significant relationship with UHI intensity at night; as the percentage of built-up areas increases, the UHI intensity values increase. This refers to the concrete and asphalt as the most commons materials in the modern cities, which make a primary contribution to increase the city temperature by absorbing a large percentage of solar heat during the daytime and emit it at night-time (Gore, 2008).

Figure 6-22 The relationship between the percentage of the land cover types and SUHI intensity on the nine selected days during February 2011

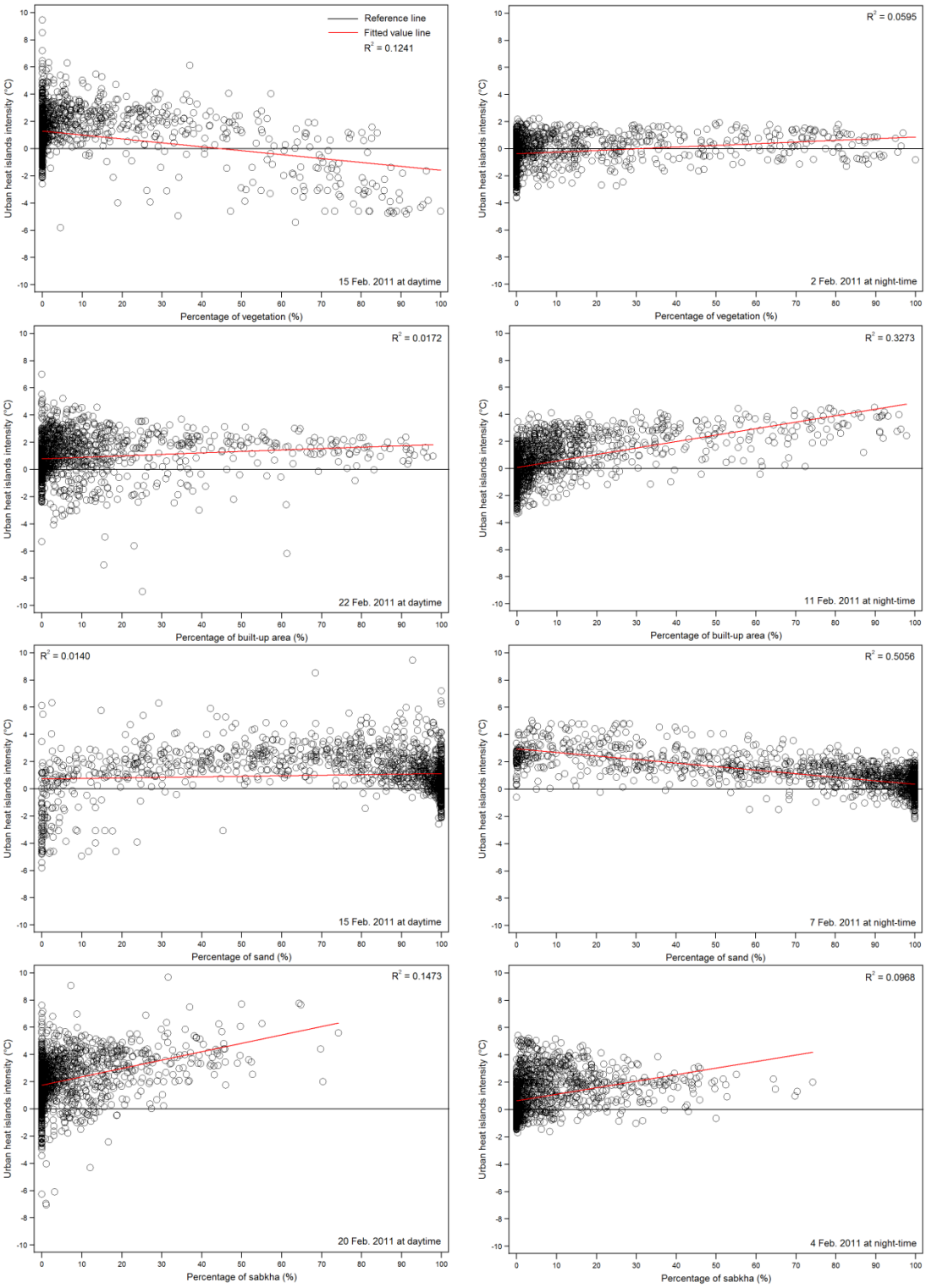

Note: The land cover types are (vegetation, built-up area, sand and sabkha) and daytime (left) and night-time (right).

Figure 6-23 The relationship between the percentage of the land cover types and SUHI intensity on the nine selected days during August 2011

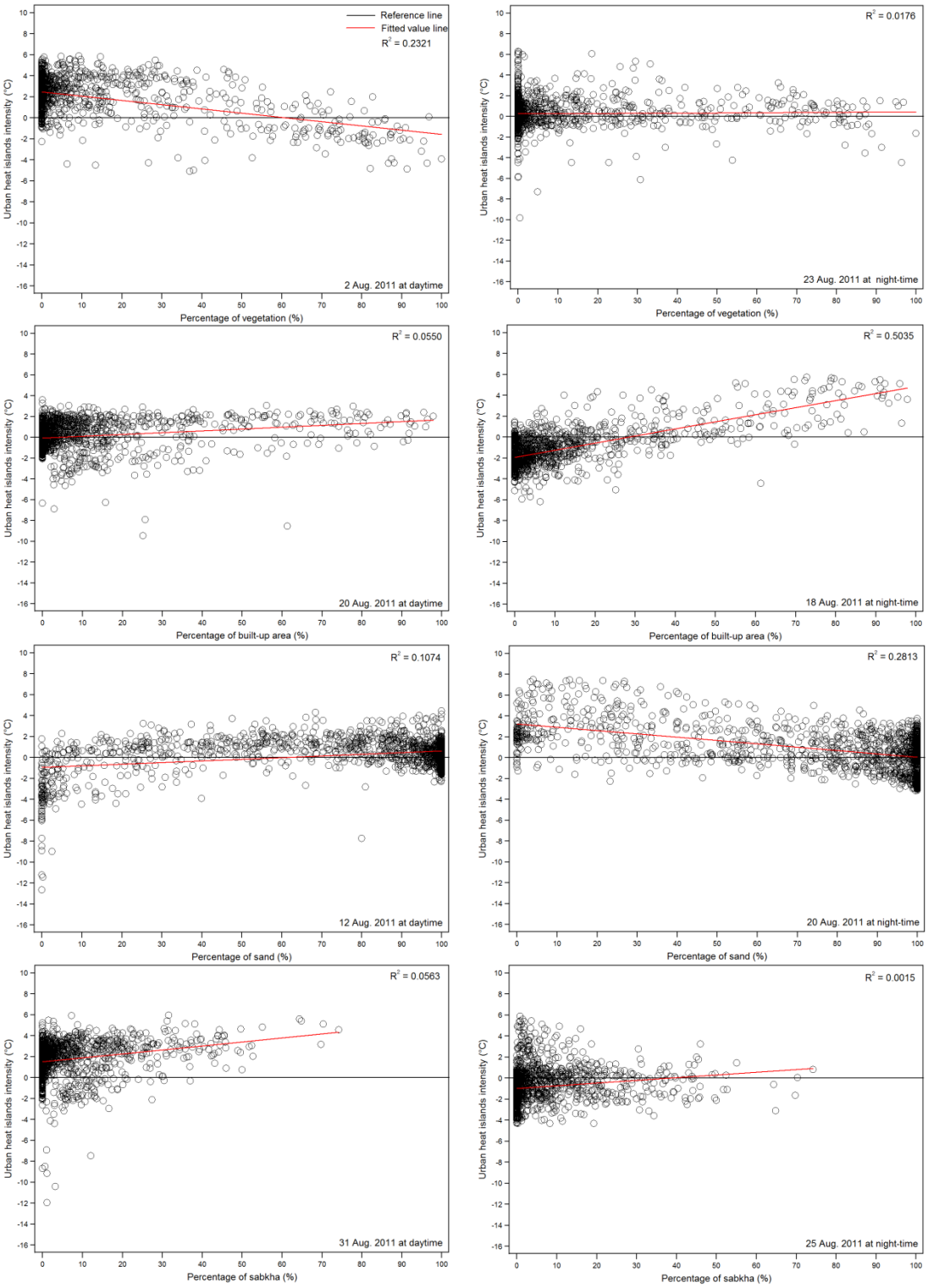

Note: The land cover types are (vegetation, built-up area, sand and sabkha) and daytime (left) and night-time (right).

6.10 **Summary**

In this chapter, the surface temperature (brightness temperature), using two different satellite sensors, the Landsat 7 ETM+ and the Moderate Resolution Imaging Spectroradiometer (MODIS), is estimated from the thermal bands of each satellite. The results indicate that the highest surface temperatures were estimated using Landsat 7 ETM+ are located outside the built-up areas over the sabkha and sand areas; they range between 12 °C and 31 °C during February and between 28 °C and 58 °C during and August. Also, the highest surface temperature which is estimated using the MODIS data are located over the sand and sabkha areas during both season at the day, while, located over the built-up area during both season at the night-time. The lowest surface temperatures which are estimated using both sensors, (Landsat 7 ETM+ and MODIS), centred over the water bodies and vegetation during both season at the day and night; however, the sand area is added to the lowest land covers at night which is determined using MODIS data. Therefore, the Landsat 7 ETM+ data are useful to estimate the surface temperature as high spatial resolution but limited with day time observation. On other hand, the MODIS data are useful to estimate the surface temperature tow times day and night but with 1000-metre spatial resolution.

The SUHI intensity using Landsat 7 ETM+ ranges between -10 °C and 8 °C during February and between -18 °C and 12 °C during August lowest at the water and vegetation and highest at the sabkha and sand areas. While based on MODIS data UHI intensity ranges between -7 °C and 10 °C and between -9 °C and 4 °C during the day and between -2 °C and 6 °C and between -4 °C and 6 °C during the night in February and August, respectively. Also, the highest UHI located over the sabkha and sand during the day and over the built-up area during the night, while the lowest centred over the water, vegetation, and sand at the night.

Statistically, there are significant differences of the heat island intensity among most of the land covers. The Kruskal-Wallis test shows that the UHI intensity at most of the sites is significantly different, with P=0.0001 of both data from Landsat 7 ETM+ and MODIS except some of the land covers classes. These differences indicate that

there is effect of land cover types on the (SUHIs) intensities in the study area. The SUHI intensity distribution among the different land covers indicates a strong relationship between them in both seasons and during both the day and night. The percentage of each class of land cover also shows a clear effect of the land cover on the (SUHIs) during both day and night. More discussion of details about the results can be found in the following chapter (discussion chapter).

Chapter 7: Discussions and Conclusions

7.1 Introduction

Different data sets including five fixed weather stations, the airport weather station, mobile data, and satellites images (MODIS and Landsat 7 ETM+), were used to map and investigate (SUHIs) in the arid region Al Ahsa oasis, Saudi Arabia. The lack of investigations at high temporal and spatial resolution provided the need for this type of research for more understanding of the urban heat island phenomenon in arid regions such as Al Ahsa oasis. Moreover, less attention has been paid to urban heat islands in arid zones compared to the humid tropical and mid-latitude regions (Figure 7-1). This study has several unique features in relation to the investigation of the effect of different land covers on UHI intensity. Besides its location in the arid region where the temperature is extremely high, the study area is located on a flat area which limits the effect of topography on near-surface temperature. Also, the study area has different land covers, sand, sabkha, vegetation, water, and built-up area, help to identify the effect on the UHI, Thus, this thesis is the first study to attempt to provide high temporal and spatial resolution of an arid-zone urban heat island. The results should assist local government agencies to mitigate the urban heat island effect.

The multi-sensor data used in this study, along with the assessment of methods for processing MODIS and Landsat7 ETM+ imagery for mapping (SUHIs) (chapters 4, 5, and 6), has demonstrated a methodology for using remote sensing to improve our understanding of (SUHIs) in arid regions at high temporal and spatial resolutions.

Figure 7-1 Distribution of world cities that UHI has reported overlaid over world climate zone

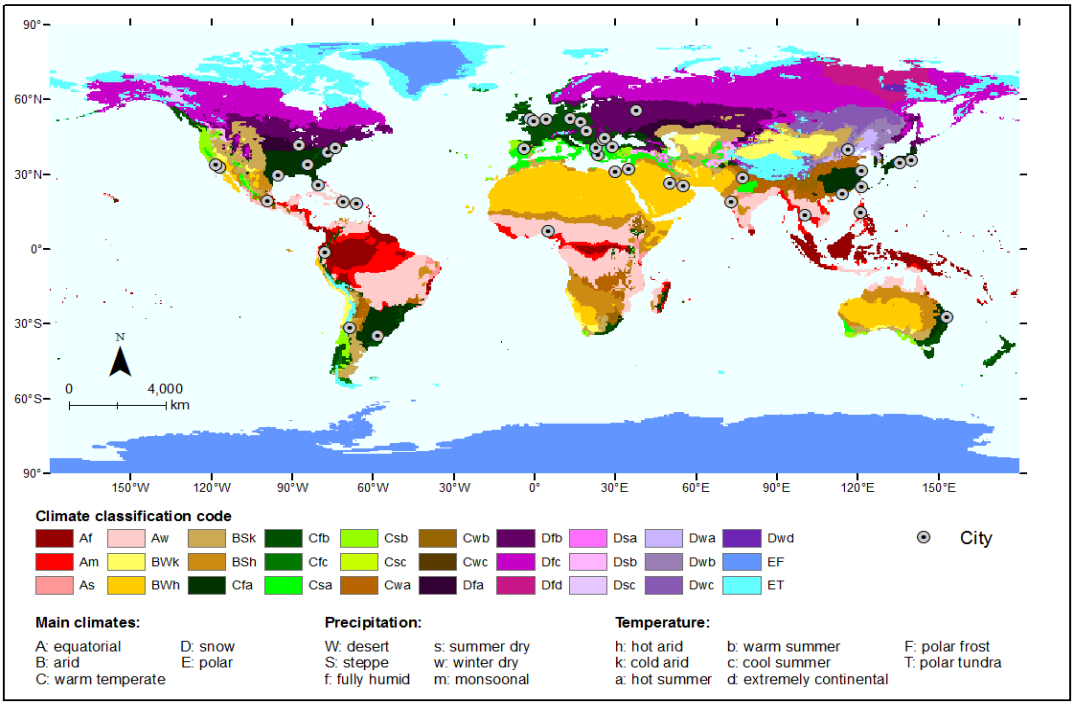

Note: The cities is based on the last review of the world UHI by (Wong et al., 2013) and the climate zone map modified after (Kottek et al., 2006).

7.2 Structure of the local urban heat islands

The evaluation of the spatial variability of different climate factors such as air and surface temperatures, wind, relative humidity, and precipitation are important aspects in order to understand the patterns and structure of microclimates of an urban area. One of the simplest methods to study urban heat islands is the fixed weather station (Oke, 2006, Gartland, 2008). The benefits of using fixed stations in this study are:

(1) To quantify the urban heat island intensity;
(2) To compare results with mobile and satellite data;
(3) To determine the effect of different land cover on the urban heat island;
(4) To investigate seasonal variation in the urban heat island.

Five micro stations were established in different locations. The locations of these fixed weather stations were chosen based on the main land covers which represents the nature of the study area. These locations are farm, park, sabkha, factory, and city

centre (Figure 7-2). In addition to these fixed weather stations, the airport weather station was used as reference to calculate the magnitude of CLHIs in this study as it is located outside the urban area of the study area (Voogt, 2000, Kim and Baik, 2005). The data obtained from theses fixed weather stations are hourly air and surface temperature, relative humidity, and wind and gust speed of each location for the period of the study (January and February for winter season) and (July and August for summer season) in 2011. More details on these fixed weather stations are mentioned in Chapter 3, (Data Sources and Methodology) section 3.2.1 for airport weather station and 3.2.2 for fixed weather stations.

Figure 7-2 The location of the fixed and airport weather stations among the urban and rural areas of the study area Al Ahsa Oasis

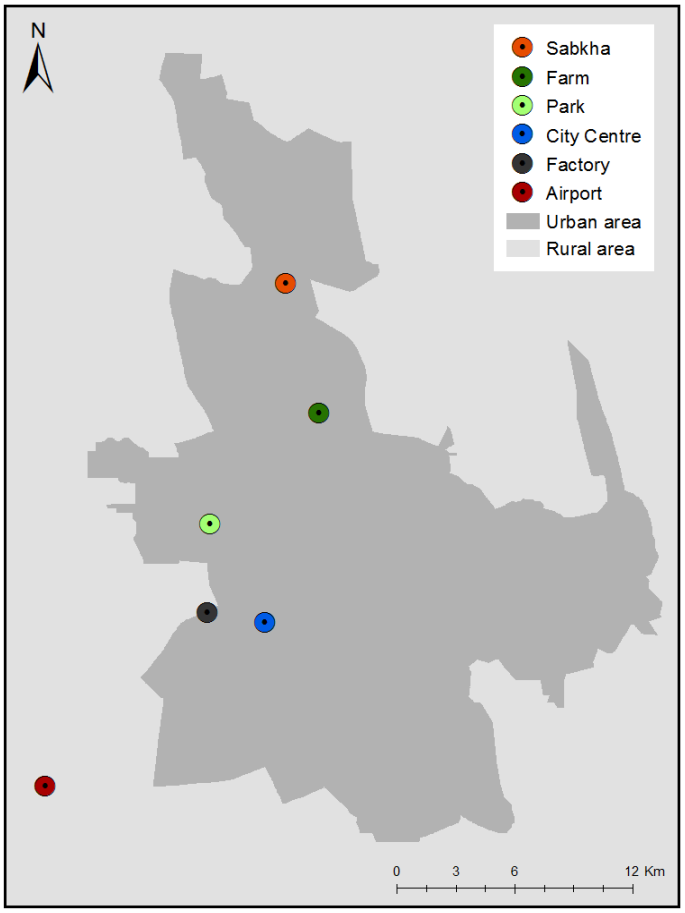

7.2.1 Evaluation of the air and surface temperature variation

The data distribution analysis of the fixed and airport weather stations indicates the variations of air temperature, surface temperature, relative humidity, and wind and

gust speed between each location during both periods of the study (January and February for winter) and (July and August for summer) in 2011. The histograms and probability distribution of all the variables indicate that the data are not normally distributed in either summer or winter. On the other hand, the results show that the air and surface temperatures in the city centre and factory are the highest during both periods of the study while, the farm and park locations are the lowest. However, the sabkha location is between these two categories during the summer and winter seasons. The city centre, factory, and airport weather stations represent the lowest locations for relative humidity while the farm, park, and sabkha are the highest. The highest wind and gust speeds are recorded at the airport and sabkha locations while the lowest are observed in the city centre, farm, and park.

These results are expected because the high density of concrete and buildings in the city centre and industrial activities in the factory locations affect the air and surface temperatures, and relative humidity. The changing of the Earth's surface by replacing the natural vegetation with non-evaporating and non-transpiring surface such as asphalt, metal, and concrete will increase the solar radiation amount in the city centre and factory locations which is stored by the surface materials during the day and released by night (Weng, 2001). However, vegetated areas (palm trees farm in this study) and parks areas behave in the opposite way by cooling down the area and represent the lowest patterns and locations of air and surface temperature and relative humidity. The high leaf area and canopy thickness of the vegetation cover can be an important factor that influences air and surface temperature due to the effect of vegetation on relative humidity because of traditional irrigation used in the study area (Figure 7-3) and the wet surfaces (Zoulia et al., 2009, Al-ghannam and Al-Qahtnai, 2012). It is also expected that the vegetation will influence wind speed and gust speeds in and around the farms, city centre, and park areas due to the height and density of the buildings in the city centre and to the trees and palm trees in the park and farm locations respectively. Also, higher wind speeds and gusts levels were expected at the airport and sabkha locations because both locations are located in open areas (Heisler, 1990).

Figure 7-3 The irrigation method used to irrigate the farms in the study area

Looking at the seasonal variations of the fixed weather stations data within each land cover in statistical terms, there is a significant difference between the median groups of air temperature, surface temperature, and relative humidity during the winter and summer seasons. More details of the significant values are mentioned in chapter 4 sections 4.3, 4.3.1, 4.3.2, 4.3.3, and 4.3.4. Therefore, the results of the analysis support the existence of an urban heat island effect in the study area at both seasonal and diurnal scale during the selected period, using fixed weather stations data which are collected in different land cover types.

Comparison of the hourly air temperature means between the reference weather stations (airport) and others fixed weather stations quantifies the local CLHIs intensity. The results show that the highest difference between the two means of air temperature is in the city centre and factory 4°C in the summer and 2.2°C in the winter respectively while the lowest is in the farm -7.9°C in the summer and -2.2°C in the winter (Figure 7-4). These results are similar to the previous studies where city centre and industrial areas present the hottest zones due to the tallest and the highest density of buildings with less green space heat emissions from traffic and commercial activities (Pinho and Orgaz, 2000, Saaroni et al., 2000). This study

found the similar results to previous studies carried out in arid regions: the intensity of CLHIs is weaker during winter than summer season (Sofer and Potchter, 2006). This may relate to the differential of the amount of solar gain during both seasons.

Figure 7-4 Hourly difference in air temperature means from the airport weather station during winter and summer.

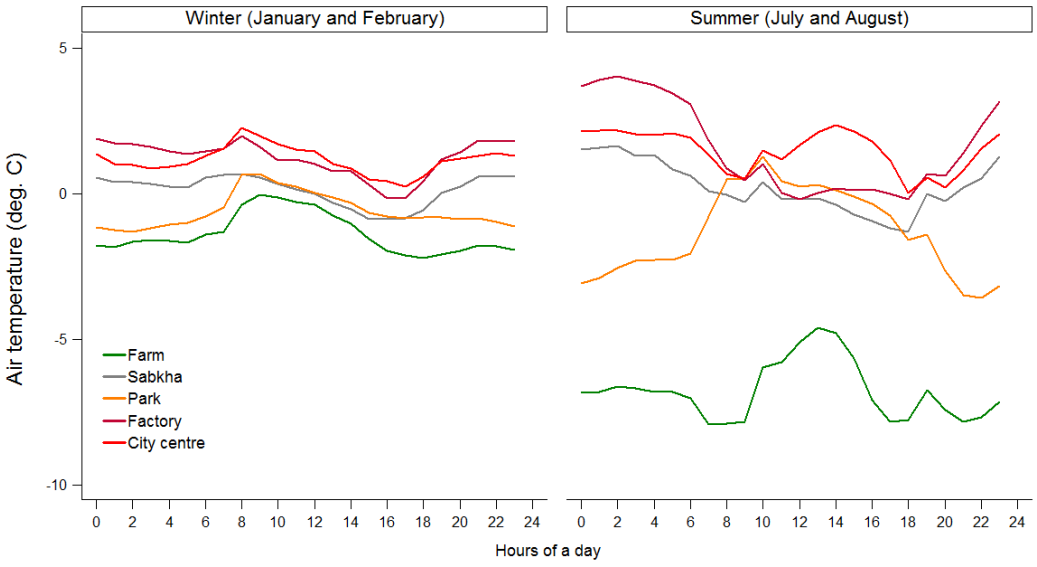

7.2.2 Advantages and limitations of fixed weather stations

Although the fixed weather stations are one of the most useful tools for measuring urban heat islands, there are some limitations using this method. These can be summarized in the following points:

1. The cost of these stations;
2. The numbers of the stations needed;
3. The spatial coverage of these stations.

In other words, it is impossible to establish enough fixed weather stations to cover the whole study area such Al Ahsa oasis because the cost and the effort needed. Therefore, mobile data collection is another tool that can be used to investigate the spatial and temporal distribution of the local urban heat islands.

7.3 **The profile of local and seasonal UHIs**

Forty six traverses were carried out in this study during February and August (2011) to investigate the distribution of the local UHIs at the local scale. The forty six traverses covered almost the whole study area (Figure 7-5) and were not only limited to just a few transects (Yokobori and Ohta, 2009, Charabi and Bakhit, 2011, Brandsma and Wolters, 2012). The number of mobile traverses and the ability to revisit the same locations (at night and immediately after sunset), helped to give better understanding of the temporal and spatial distribution of the local UHIs and to investigate the effect of the land cover on the UHI intensity (Gartland, 2008).

To understand the local UHI and its distribution at the local scale, the land cover conditions needed to be identified. The high spatial resolution obtained from GeoEye image [give the pixel size here] of the study area were used to classify each pixel by its dominant land cover for the whole study area. It has been reported that the cooling effect of different land cover types cannot be detected at less than 150metre resolution (Yokohari et al., 2001). Therefore, sub-classes of different main land covers were created based on GeoEye imagery especially for the built-up area. For example, the area that is located close to the vegetation or is mixed with other classes such sabkha or sand need to be classified in separate class in order to understand of the effect of different land cover on the UHI (Oke, 2006, Hart and Sailor, 2009). In this study, the distance between each point of the mobile data at night and after sunset is considered to be within the range of 35 metres to ensure that each point of the mobile data properly represents the same land cover type.

Figure 7-5 The tracking of the mobile transect during February 2011 after sunset and at the night-time

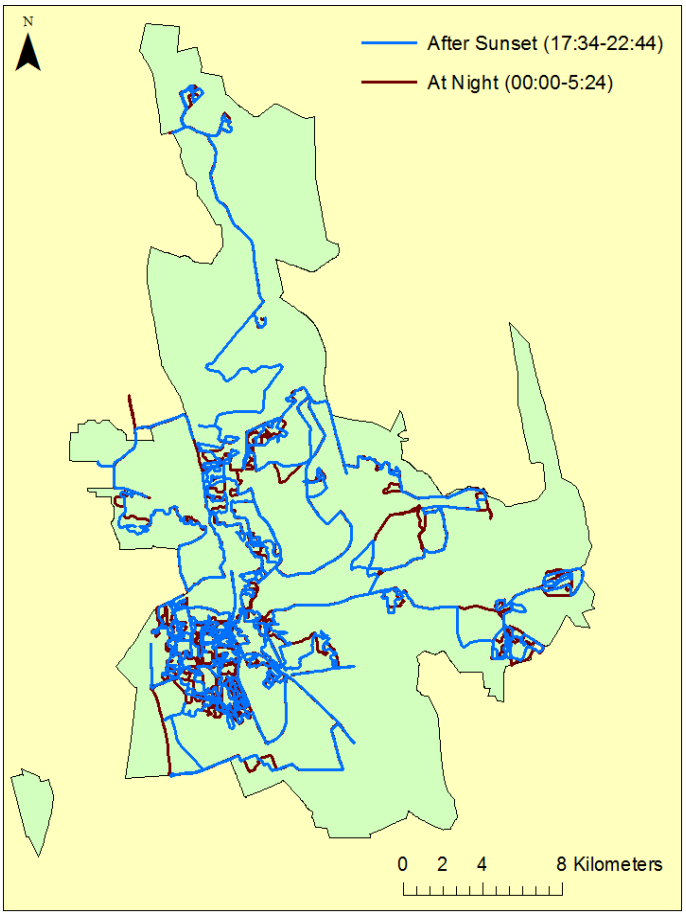

Seasonally, the UHI intensity is higher in the summer than winter season. The maximum UHI intensity during the summer ranged between 6 °C and 9 °C at night and between 3 °C and 8 °C after sunset based on the farm and airport as reference respectively. The maximum UHI intensity during the winter ranged between 2.5 °C and 5 °C at night and between 2 °C and 5 °C after sunset based on the farm and airport as reference respectively. The UHI intensity is weak during the winter and strong during the summer and that might be related to the amount of the radiative cooling which is higher during the winter than summer and to the influence of the different of the seasonal solar period which is longer in the summer than winter. Therefore, UHI intensity during the summer and winter season has a tendency to be stronger at night.

7.3.1 UHI intensity during the day and night

Diurnal variations of the UHIs intensity during the winter (February) and summer (August) have been observed in this study using data from 46 traverses; at night before sunrise and soon after sunset. It has been reported that the maximum of the UHI intensity occurs approximately 3 to 5 hours after sunset (Oke, 1987). Some recent studies have found that the maximum UHI intensity occurs around midnight (Runnalls and Oke, 2000, Chow and Roth, 2006) or shortly before sunrise (Erell and Williamson, 2007). The UHI intensity has been also found to be negative during the daytime (Chow and Roth, 2006, Erell and Williamson, 2007) which is then named as an urban cool island.

Similarly to previous studies mentioned above, this study found that the maximum UHI intensity occurs during the night compared with the daytime in both seasons (Figure 7-6 and Figure 7-7). This is due to the rapid cooling of the sand area, vegetation, and sabkha sites at night compared to the built-up area which releases heat energy and long-wave radiation at this time to create the heat island. In addition, UHI intensity is higher when the farm is used as reference to calculate the UHI intensity compared to the airport weather station.

Figure 7-6 Urban heat island intensity among different land covers for day one during summer (02 August 2011) where farm is control

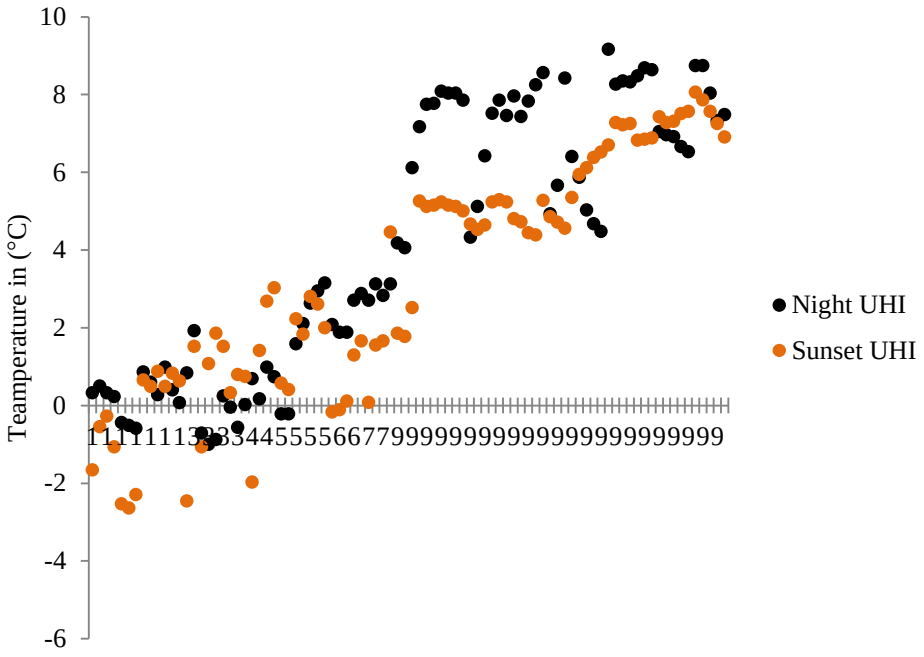

Note: 1=Vegetation, 3=Sabkha, 4=Built-up 1, 5=Sand, 6=Built-up 2, 7=Built-up 3, and 9=Built-up 5. Night-time between 01:49:29am and 04:42:29am and Sunset-time between 18:36:05pm and 20:58:36pm.

Figure 7-7 Urban heat island intensity among different land cover areas for day eight of winter (19 February 2011) where airport is control

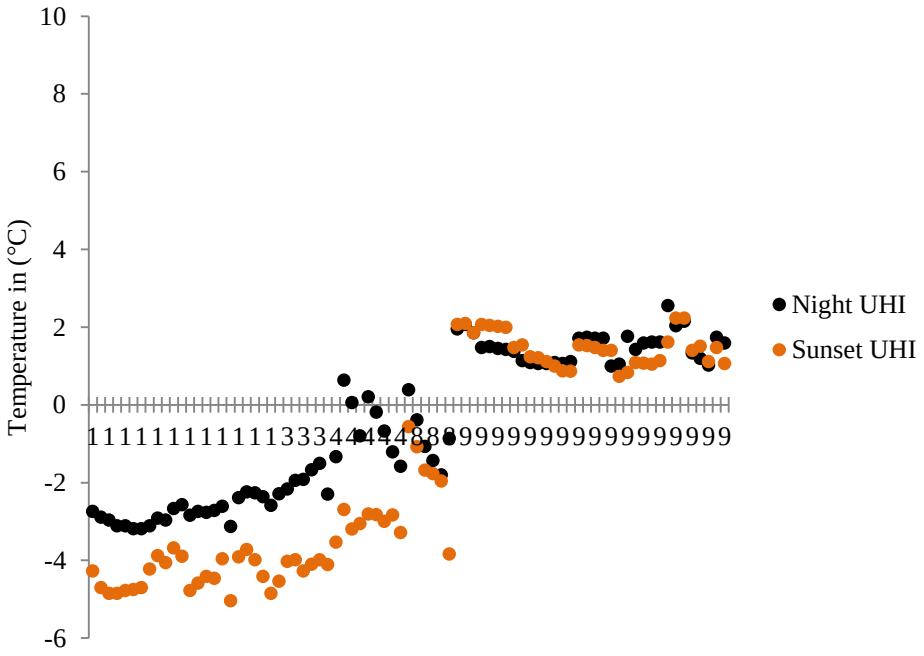

Note: 1=Vegetation, 3=Sabkha, 4=Built-up 1, 8=Built-up 4, and 9=Built-up 5. Night-time between 01:17:35am and 03:25:35am and Sunset-time between 20:06:34pm and 20:57:34pm.

7.3.2 The relationship between land cover and UHIs intensity

The effects of land cover on ambient air temperatures has been reported in many previous studies (Saito et al., 1990, Eliasson, 1996, Upmanis and Chen, 1999, Unger et al., 2001, Jonsson, 2004, Bottyán et al., 2005, Hart and Sailor, 2009). In this study, as shown in Figure 7-6 and Figure 7-7, the UHI intensity varied significantly according to different land cover types. The UHI intensity is higher in the built-up area (class 9 which represent the most common area: buildings) and lower in the vegetation, sabkha, sand, and sub-classes of built-up area. In other words, the built-up areas are warming due to an increase in non-natural land covers, and the vegetated areas have moderating effects on ambient air temperatures. In general, the moderating effects were slightly stronger in August than February. Therefore, it seems that the moderating effect produced by a higher cooling rate in the vegetated area at night during the summer could be larger than that produced by evapotranspiration and the blocking of incident solar radiation during the day. This might relate to the stability of the air temperature during the night rather than the advection (Yokobori and Ohta, 2009).

7.3.3 The spatial distribution of local UHI

The surrounding rural areas, such as the airport (sand area), the farm (palm tree area), and the sabkha area, are more open to the sky than the built-up area. This led to a rapid cooling during the night for these land cover types. However, there is increase of the UHI intensity as we move through the built-up sub-classes, which regulate long-wave radiative heat loss at the same time (Oke, 1981, Oke, 1982). As a result, there is a large UHI intensity difference between the built-up and the references (airport and farm). In this study, the UHI intensity at night in the vegetation, sabkha, and sand during both seasons is lower than the temperatures in the both references the airport and the farm, due to the high rate of radiative cooling. Similarly, (Spronken-Smith and Oke, 1998, Hedquist, 2005, Yokobori and Ohta, 2009) found night maximum cooling in vegetation and open grass parks areas, due to low thermal effect, compared to built-up area and mixed area. In addition, the farm

site with tree canopy cover has a daytime maximum cooling due to a combination of shade and evapotranspiration effect.

Location, topography and wind direction - all together can play a significant role to effect on the UHI intensity and its spatial distribution (Charabi and Bakhit, 2011). Figure 7-8 (top) shows the state of UHI affected by topography and land cover in Muscat measured by mobile traverse. The warmest UHI intensity zones include: Wadi Al-Kabir and in Ruwi, Matrah, Bait Al-Falaj and Darsit that are located in narrow valleys in the high lands (Figure 7-8 top). These are the locations of business centres in Muscat where high buildings those trap heat and increase the effect of the UHI. The outcomes of their study in terms of the UHI spatial distribution revealed a similar pattern with the current study but with a higher value of UHI intensity and influence of vegetation in controlling UHI as mentioned above (Figure 7-8 below). During the summer seaso, the UHI intensity can reach a maximum of 7.5 °C at night and 5.2 °C after sunset for Al Ahsa oasis while, 4.8 °C at night and 3.5 °C at the daytime for Muscat. According to this comparison, along with distance from the urban centres, topography and wind direction (Charabi and Bakhit, 2011), vegetation cover played an influential factor in reducing UHI intensity in the study area.

Figure 7-8 Thermal difference between mobile traverses and the reference point in Muscat city (top) Oman and the study area Al Ahsa oasis (bottom) during summer

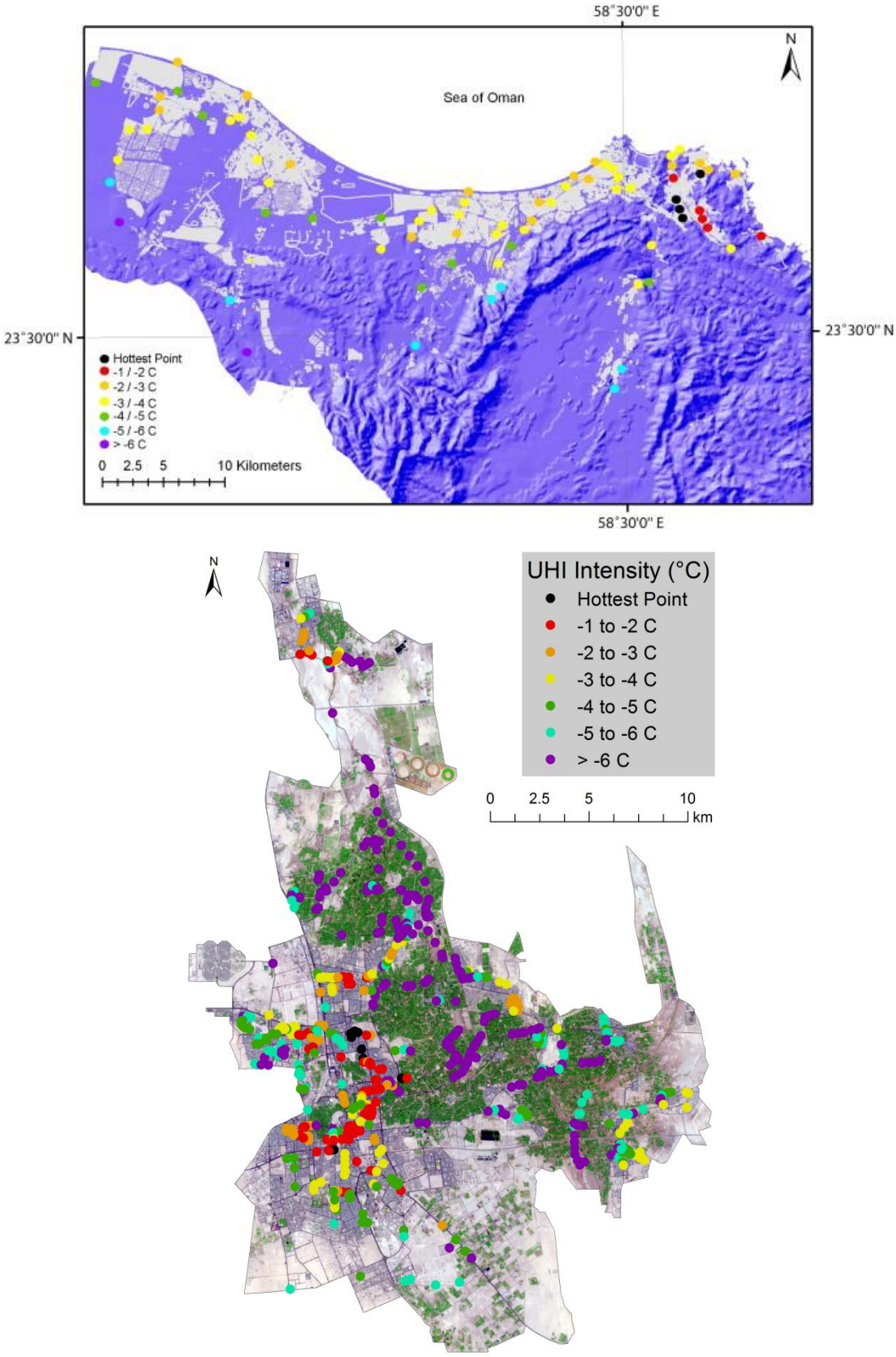

Note: Source of Muscat map: (Charabi and Bakhit, 2011).

The maximum UHI intensity has been linked to the city size which can be measured by its population (Oke, 1973, Oke, 1981, Oke, 1982, Fukuoka, 1983). Oke (1973) indicated that maximum UHI intensity was related to the size of the population of many North American and European settlements. As mentioned before, a maximum UHI intensity of nearly 10°C was observed in the two main settlements of the study area (Al Hufuf and Al Mubarraz), which have populations of about 660,788 based on 2010 residential census (Ministry of Economy and Planning, 2010). In a similar study in Tokorozawa, Japan, (Yokobori and Ohta, 2009) also found a maximum UHI intensity of nearly 10 °C in a study area with 40 000 population and an area of approximately 10 km^2. In a recent study in an arid region, Muscat, Oman,(Charabi and Bakhit, 2011) found that maximum UHI intensity ranged between 4 °C and 6 °C. However, the low value of UHI intensity might be due to the effect of the topography and coastal location of this city (Muscat) compared to these capital cities of the study area (Al Ahsa oasis) which are located on a flat, inland area. Finally, the spatial distribution of maximum UHI intensity is clearly linked to the size of the settlements and villages of Al Ahsa oasis as suggested in previous studies such as (Oke, 1973).

The maximum UHI intensity is recorded in the large cities of the study area during both seasons and the UHI decreases in the small cities such as Al Uyun in the north, Al Killabiyah in the north-east, and Al Umran in the east of the study area with populations of 33,042, 16,984, and 17,410 respectively. Moreover, the effect of the vegetation on the UHI intensity during both seasons at the night and day-time is clearly identified by the low UHI intensity in the small villages such as the Al Qaraah, Al Julijlah, and Al Shibah, which are surrounded by the palm trees from almost every direction (Figure 7-9).

Figure 7-9 Distribution of urban heat islands for the mobile data during summer season August 2011, night-time left and after sunset right. (Farm as control)

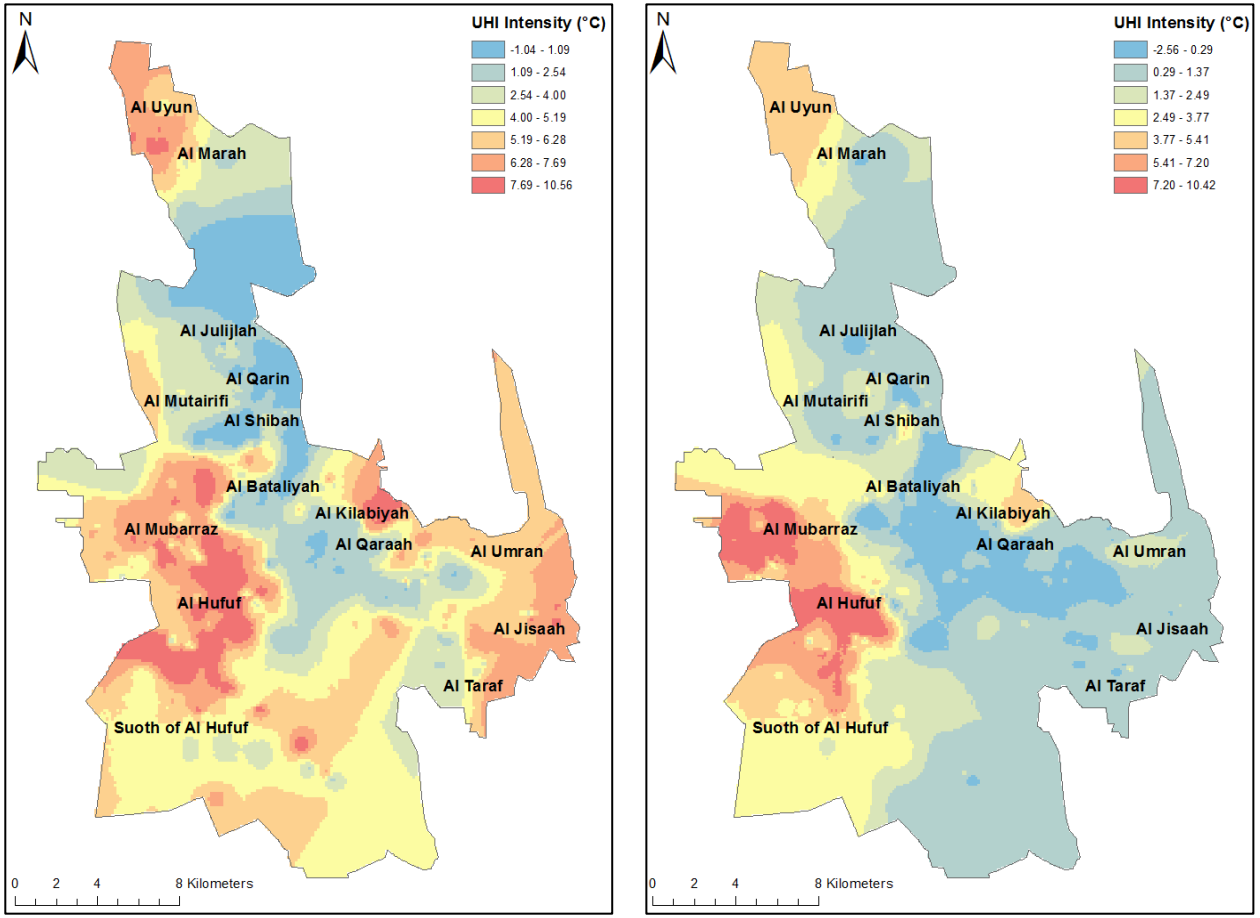

7.3.4 Advantages and limitations of mobile traverses

Mobile sensor data are another method to measure the UHI. It is an economical method to investigate the UHI of an urban area and its suburban and rural area, whether walking or cycling in a small area (Spronken-Smith and Oke (1998) or by public transportation or car for large area (Chandler, 1960, Hutcheon et al., 1967, Yamashita, 1996, Stewart, 2000). This method also can be carried out at any time day or night, although sometimes this is dependent upon local factors such as traffic.

The limitation of the mobile traverses can be highlighted by the difficultly of making simultaneous measurements at different locations. It is possible to overcome this issue by using two or more sets of equipment at the same time but this will be expensive compared to the fixed weather station method. Another limitation of this method is the time of the traverses which dependent on the traffic conditions which can vary. Finally, the recorded temperature usually needs to be adjusted to a reference time either by comparing the data with other measurements or to a fixed weather station (Gartland, 2008).

7.4 Mapping the UHIS in arid regions using remote sensing

Remote sensing can be used to investigate the characteristics of the surface temperature such as the roofs, pavements, vegetation, and bare ground by measuring the reflected and emitted energy for each pixel in an image. Special equipment is used to capture imagery at both visible and infrared (reflected and emitted) wavelengths. Also, there are several types of satellite sensors with varying spatial resolution orbiting the Earth (Gartland, 2008). In this study, two different satellites sensors were used: Landsat 7 ETM+ and MODIS. These two sensors were selected because of their high spatial resolution (Landsat 7 ETM+) and their high temporal resolution (MODIS) beside the availability as public data.

The detail of the land cover of the study area is an important factor for modelling the UHI for two main reasons. The first is to identify the appropriate emissivity values in order to estimate the surface temperature using the satellite data (Zhengming and Dozier, 1996, Li et al., 2013). The second is to investigate the effect of land cover type on the local UHI intensity (Voogt and

Oke, 2003). There is no difficulty in integrating the emissivity value of Landsat 7 ETM+ or MODIS for the pixels that present one land cover. However, the emissivity of mixed classes of the land cover pixels especially for MODIS where the pixel size is about 1000 metres is problematic and is normally calculated based on the average of each land cover (Zhengming and Dozier, 1996). Mapping the emissivity of the study area was based on an approach that used a look-up table of emissivity values derived from a land cover classification. This approach was designed to reduce errors or uncertainties based on crude assumption of emissivity values for arid and semi-arid regions (Gillespie et al., 1999, Li et al., 2013).

In this study, satellite images were used to investigate the UHI magnitude and determine the effect of different land cover type on the local UHI intensity at the city scale including the urban, sub-urban, and the surroundings areas of the study area. The results largely support findings from previous studies (Hu and Jia, 2009, Rajasekar and Weng, 2009, Kaya et al., 2012, Laras et al., 2012, Jamil et al., 2012, Tomlinson et al., 2012, Effat et al., 2014) which can be summarized as a strong relationship between UHI intensity and the different land covers. The outcomes of the satellite data analysis support the findings based on the ground data and fixed weather stations method. The surface temperature of different land cover varies and reflects the effect of the different land cover on the surface temperature.

When comparing the land cover of the study area with UHI intensity, the results indicates similar outcomes to Tomlinson et al. (2012). The UHI magnitude increases across the land cover in the order 8 (woodland/open land), 3 (light suburban), 1 (villages/farms), 7 (light urban/open water), 2 (suburban), 4 (dense suburban), 6 (urban), 5 (urban/transport) (Figure 7-10) (Tomlinson et al., 2012). This study found a similar results which indicates that the UHI intensity median increases in the following order sand, sabkha, vegetation, mixed area, low density of buildings, sand and buildings, and built-up areas at the night-time. However, in the day time this order is slightly different vegetation, sand, mixed area, built-up area, sand and buildings, low density of buildings, and sabkha (Figure 7-11). This conclusion suggests that the land covers respond in different ways between day and night. For example, the sand and sabkha areas in a desert region heat up during the day time and cool down very quickly at night. Also, the results bring to our attention that even though night images more appropriate for land surface temperature as Rigo et al. (2006) suggest, the day time also might help for more understanding of the response of the different land covers.

Figure 7-10 SUHI Magnitude for each Pasquill-Gifford class, distributed by Owens land and plotted in order of ascending mean SUHI magnitude

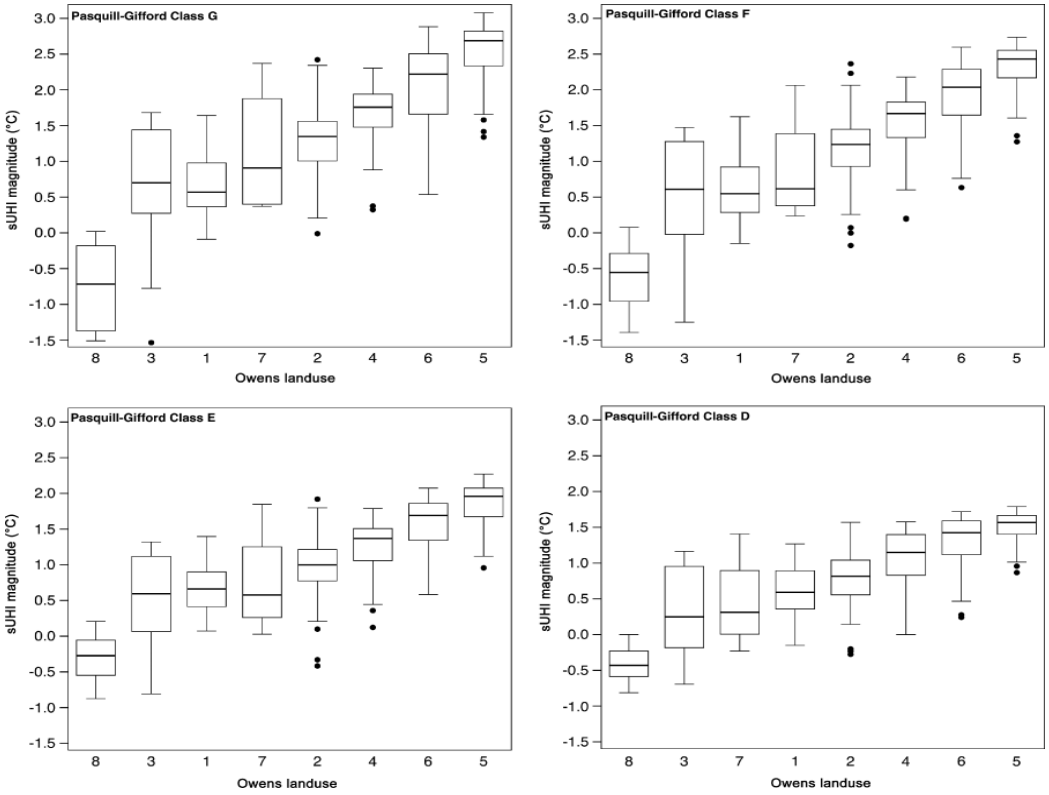

Note: 1 (villages/farms), 2 (suburban), 3 (light suburban), 4 (dense suburban), 5 (urban/transport), 6 (urban), 7 (light urban/open water), 8 (woodland/open land). (Tomlinson et al., 2012).

Figure 7-11 August urban heat island intensity distribution among different land cover types on the nine selected days, in daytime (left) and night-time (right)

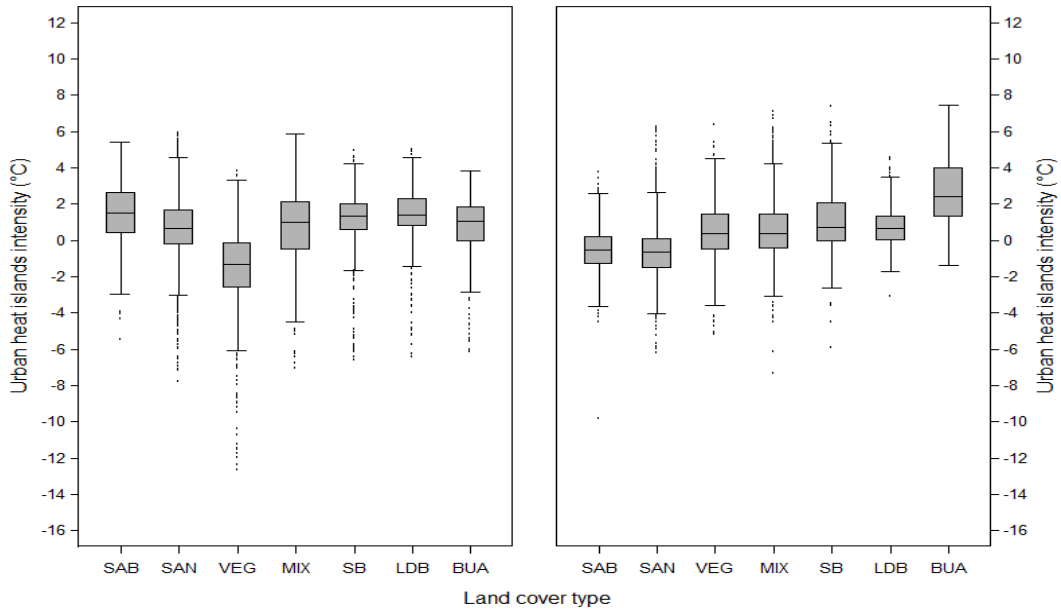

Note: SAB = Sabkha, SAN = Sand, VEG = Vegetation, MIX = Mixed area, SB = Sand and buildings, LDB = Low density of buildings, and BUA = Built-up areas.

The distribution of the UHI intensity shows a clear response of the different land cover and the city size as well as the location of the small villages and settlements in the study area. The relationship between the land cover and the surface temperature is determined in similar study in Atlanta city (Quattrochi, 2009) Figure 7-12 (d). The relationship between UHI intensity and land cover using Landsat 7 ETM+ is limited to the day time only; however, the results indicates a significant response of the different land covers during the summer and winter. The UHI intensity can be divided to three categories, first hot UHI located over the sand and sabkha areas, cool UHI centred over the water and vegetation, and mild UHI represented over the built-up area Figure 7-12 (a), (b), and (c).

Night-time images of MODIS are the most appropriate solutions to calculate the UHI intensity (Oke, 1987). MODIS land surface temperature is more accurate at night than day time (Rigo et al., 2006) because at night there is no incoming solar radiation to affect the surface radiation budget. The distribution of the maximum UHI intensity found over the two main cities of the study area are similar to another study has been done in Birmingham, UK (Tomlinson et al., 2012).

Figure 7-13 shows both aspects the land cover and UHI intensity of Birmingham and the current study. It is clear that similar results have been achieved, but the maximum of UHI intensity is higher in the Al Ahsa oasis (10 °C) than in Birmingham (5 °C), which might relate to the different of the locations and effect of the density of the trees and vegetation. That also indicates the important of studying and focusing on the UHI in the arid regions which might be a larger effect than in humid tropical or mid-latitude regions.

Figure 7-12 UHI intensity using Landsat data during February (a) and August (b) and corresponding land cover responses of the study area (c) and comparing to Atlanta, GA results using similar data (d)

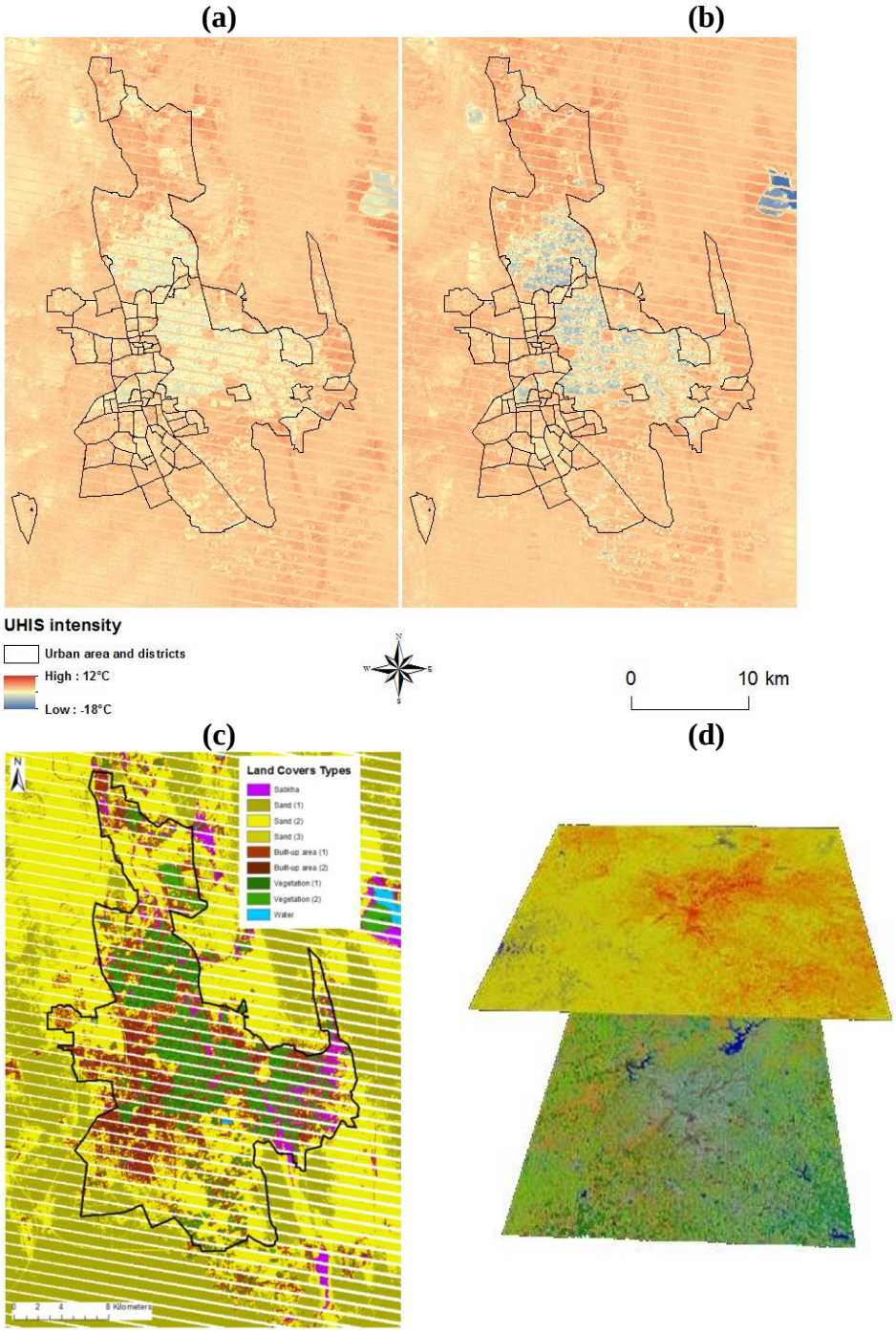

Note: Surface temperature and land cover of Atlanta, GA (d) obtained from (Quattrochi, 2009).

Figure 7-13 Comparison of UHI magnitude between Al Ahsa oasis and Birmingham city with land cover data

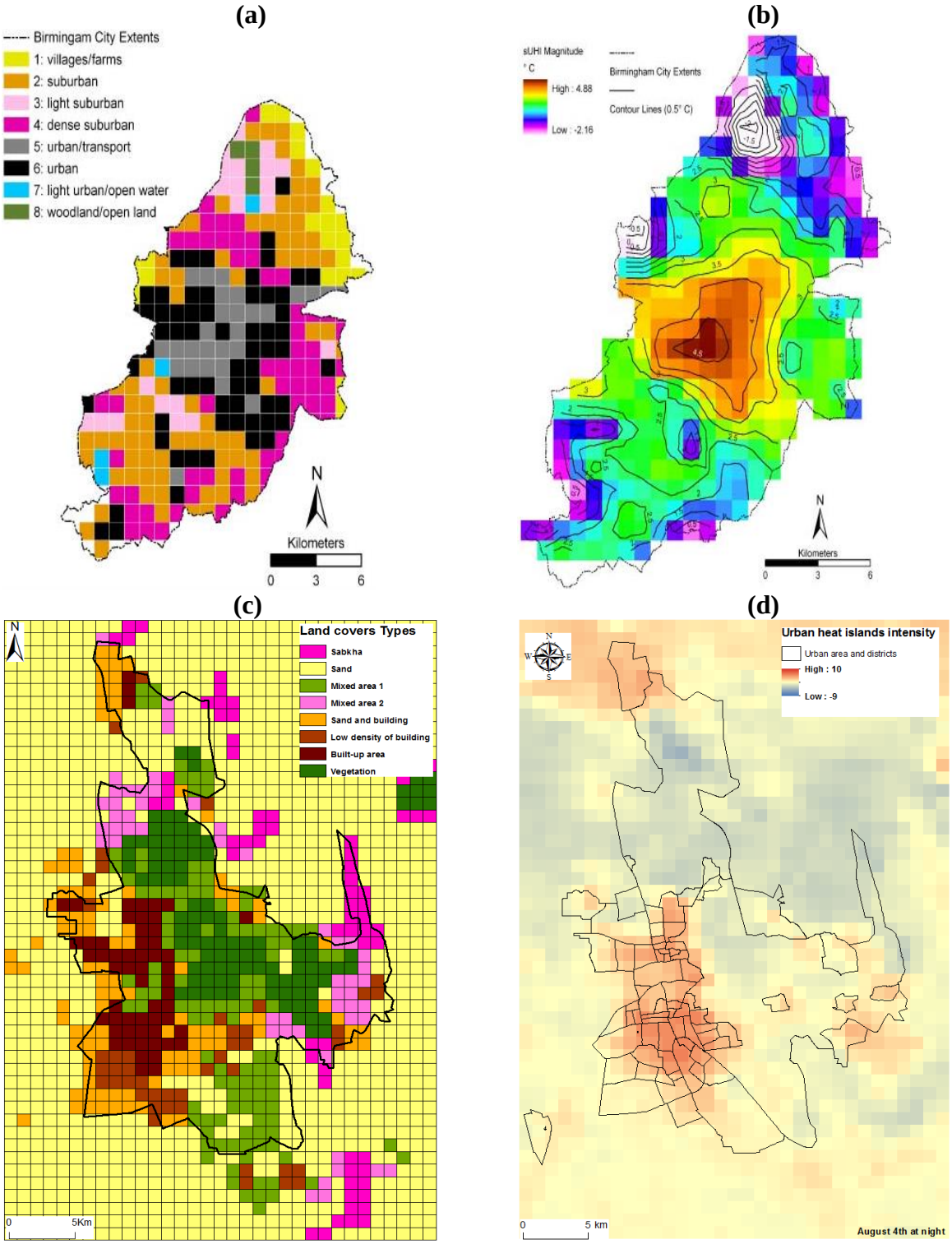

Note: Spatial distribution of Owens land classification across Birmingham (a) and SUHI magnitude of Birmingham during heatwave event 18 July 2006 (b) and land cover classification of the study area (c) and corresponding UHI intensity of the study area during 4 August 2011(d). (a) and (b) obtained from (Tomlinson et al., 2012).

7.4.1 Advantages and limitations of remote sensing

One of the most important advantages of using remote sensing to investigate the UHI is its power to visualize the surface temperature over a large area. However, this is offset by the long time between revisiting the same area and the short period of overpass time e.g. 16 days revisit for Landsat 7 ETM+ and only few minutes to overpass small selected study areas such as the one presented here. Moreover, some satellites' overpass is only available during the day time which is limited to measure UHI during the day time only. In addition, remote sensing shows only the urban temperature as a birds'-eye view leaving out the temperatures of walls and vegetation and the temperature under the trees. This information is also important to fully study the urban heat island and there is some work that has been done to cover this issue such in Vancouver, British Columbia (Voogt and Oke, 1997). Also, the spatial resolution of the thermal data of different satellites is one of the limitations in order to estimate and measure the urban heat island. While the Landsat 7 ETM+ has 60 metre of the thermal data and resampled to 30 metre, the MODIS has poor thermal spatial resolution.

7.5 UHI and some of related environment issues

These days, the Ministry of Housing in Saudi Arabia is planning and establishing new housing projects, Figure 7-14, at all Saudi Arabia districts and cities (Table 7-1). One of these districts is the study area (Al Ahsa oasis), which is located in the eastern province, five projects with a total number of 9017 units (Ministry of Housing of Saudi Arabia, 2014). These houses will be built of cement and concrete and the projects will establish new networks (roads) which mean more asphalt and pavement. Therefore and according to the outcome of this study, the thermal budget and the balance of the heat will be affected by these materials and contribute to building the local urban heat island. In addition, these units and houses will be provided with air conditioning which leads to heat emission especially during the summer season when the air temperature reaches about 50 °C and make the UHI even worse.

Figure 7-14 An example of the new house project of ministry of housing in Saudi Arabia

Source: (Ministry of Housing of Saudi Arabia, 2014).

Table 7-1 The number of the new projects and unites in the main Saudi Arabia regions.

Region	Province	Project	Unite
Makkah	10	23	56926
Al Madinah	7	15	17581
Al Riyadh	21	21	18083
Eastern region	10	17	43256
Al Qassim	12	26	21979
Hail	8	9	12289
Tabuk	6	10	10399
Northern region	4	7	8301
Al Jouf	4	8	4084
Al Baha	7	13	7381
Asir	10	20	21200
Najran	4	5	7184
Total	103	174	228663

Source: (Ministry of Housing of Saudi Arabia, 2014).

Moreover, this brings to our attention the important of studying the urban heat islands in arid region in term of the global warming issue. Although there is a big debate whether there is link between the urban heat island and the global warming (Alcoforado and Andrade, 2008), the air temperature of the study area has been investigated by Nasrallah and Balling (1993) who found there is increase of the air temperature in the Middle East. The air temperature of the Middle East region over the period 1950-1990 increases of 0.07 °C per decade. Most of the increase

has occurred in the spring season, with moderate amount of warming recorded in the summer and fall seasons, and weak no warming during the winter (Nasrallah and Balling, 1993).

Another environment problem that related to the urban heat island is the human health and stress issue. The extreme heat waves and heat island has been reported in different places in the world and at different climate regions e.g. Tel-Aviv, Israel, Los Angeles, USA, Istanbul, Turkey, Muscat, Oman, Moscow, Russia, London, UK, Bangkok, Thailand, Brisbane, Australia, Hong Kong, China, Bangladesh, and Delhi, India (Wong et al., 2013). In addition, the urban heat island intensity is recorded in Shanghai, Bangkok, Beijing, Tel-Aviv, and Tokyo of 3.5 °C to 7.0 °C, 3.0 °C to 8.0 °C, 5.5 °C to 10 °C, 10 °C, and 12°C, respectively (Wong et al., 2013). Moreover, the mortality rates and human health problems have been linked to the increase and events of the heat weaves and heat islands phenomenon in several places in the world. e.g. the mortalities rates increased from 4.1% to 5.8% per 1 °C over a temperature threshold of about 29 °C in cities such as Hong Kong, Bangkok, and Delhi (Wong et al., 2013).

Extremely high temperatures have caused excess deaths in Europe, North-eastern, and United States. More than 4,780 deaths were reported in United States between the period of 1979-2002 due to heat weaves condition (CDC, 2006). During the summer 2003, the heat wave caused up to 70,000 deaths over four months in Central and Western Europe (Brucker, 2005, Sardon, 2007, Robine et al., 2008) and an estimated death of 55,000 was reported again in 2010 for the same reason in the Eastern Europe (Barriopedro et al., 2011). Most the deaths among these people are from the elderly, e.g. there were about extra deaths of 600 people all of the age in London (Ken Livingstone, 2006). These days, more than 2,300 are death in India and some of the roadways in Delhi were melted due to the recent heat waves that hit the region and the country (Figure 7-15) (Sean Breslin, 2015).

Figure 7-15 Some of the roadways in India are melting because of the recent heat waves that hit the regions

Source: (Sean Breslin, 2015).

According to the above environmental problems, it is important to bring the importance of the urban heat island issue to the local government's agencies in order of planning and developments the local cities and communities in a friendly environments ways. This research is the first study in the region and might provide baseline for other similar studies in the near future in the region to achieve its recommendations.

7.6 **Main findings**

The main findings of this study can be summarized in the following points:

1. There are statistical differences in the hourly air temperature, surface temperature, relative humidity, and wind and gust speed between different fixed weather stations and the airport weather station, which indicate the existence of the local urban heat island in the study area during the summer (July) and winter (February).

2. The hourly analysis of the differences during both seasons, whether from the airport weather station values or from the calculated means of the air temperature, surface temperature, relative humidity, and wind and gust speed indicates similar pattern during

the early morning and midday for all the fixed weather stations; however, the city centre, factory, and sabkha show an increase of the air and surface temperature both seasons especially during the summer.

3. There is a statistically significant difference between the air temperature and relative humidity data, based on mobile method, among different land cover (Sabkha, Sand, Urban, and Vegetation) during winter and summer at night and or after sunset.

4. The profile of the air temperature and relative humidity shows a strong effect of different land covers on air temperature and relative humidity during both seasons at night and after sunset, either based on the farm site or airport as control.

5. The temporal urban heat island intensity, based on mobile method, appears to be highest 2 to 3 hours before the sunrise and after the sunset; however, it is stronger during the summer than winter and at night than after sunset.

6. The highest UHI intensity is located over the largest settlements, Al Hufuf and Al Mubarraz, while the mild UHI intensity is centred on the smaller towns and villages that are surrounded by the farms and vegetation, and the last type of UHI intensity is recorded over the vegetation region which extends from the north and north-east to the south and south-east of the study area during both seasons at the night and after the sunset.

7. The spatial distribution of the surface temperature using the remote sensing method either by Landsat 7 ETM+ or MODIS indicate promising results to investigate the UHI in the large scale comparing with ground data whether fixed stations or mobile data.

8. Although there is a temporal limitation of Landsat 7 ETM+, which is a daytime observation about 11:00am local time, the surface temperature varies between different land cover; however, MODIS covers both day and night which is important time for observing and investigating the UHI.

9. Statistically, there is a significant difference between the median of UHI intensity and land covers based on both sensors during winter and summer, which suggests the effect of the land cover on the UHI intensity.

10. The highest UHI intensity appears over the built-up area in general and at night time in particular; while the lowest area of UHI intensity is represented as the vegetation and mixed area during the day and sabkha, sand, vegetation, and mixed area at the night-time.

11. The percentage of different land covers during the day and night-time is linked with the UHI intensity; e.g. with the percentage of built-up also increases the UHI intensity increases especially at night and when the percentage of the sand area increases the UHI intensity decreases at the night.

7.7 **Evaluation of Aim and Objectives**

This study has confirmed that combined remote sensing and ground data including fixed weather stations and mobile traverses are important method to investigate and study the effect of land cover on urban heat island in general and in arid regions in particular. There are two main conclusions can be drawn from this study:

1. In this study an integrates between remote sensing (satellite images) and ground data (fixed weather station and mobile data) has been developed and confirmed for estimating the air and surface temperature in order to investigate and study urban heat island in arid regions.

2. The present study has demonstrated that there is a strong relationship between different land cover and urban heat island intensity and its temporal and spatial distribution during both seasons winter and summer and at day and night-time; however, this relationship appears to be stronger during the summer and at the night.

3. The study confirms the benefit of investigating UHI intensity and its spatial distribution using different scales to provide better understanding of the UHI phenomenon in arid regions as presented in this study.

7.8 **Conclusions**

Al Ahsa oasis, which has more than 2 million palm trees, is one of the main regions in Saudi Arabia that has a rapid development of urbanization. That brings to our attention the important of studying UHI in such oases and investigating the effect of this change on the thermal budget of the study area. This thesis has investigated the effect of different land cover on the urban heat island intensity in the arid region Al Ahsa oasis, Saudi Arabia during winter and summer seasons. Less attention has been paid to UHIs in arid regions, where daytime surface and air temperatures can be extremely high, and to investigate the effect of different land cover on UHI intensity using ground data and multi-scale and multi-temporal satellite thermal imagery. Moreover, this study have used a high spatial resolution image (GeoEye) to identify the ground data in order to investigate the effect of the different land covers on UHI intensity.

The findings of this study have emphasized the effectiveness of combining ground and satellites data to investigate the relationship between the land cover and UHI intensity. Studying UHI needs high-resolution thermal data in two aspects, spatial and temporal. Fixed weather stations and mobile traverses provide continuation observations of air and surface temperatures and link the data with high spatial resolution (GeoEye) for better understanding of the effect of the land cover of UHI intensity. The cost of fixed weather stations and mobile data is an issue here, but this cost may be out-weighted as it provides the good quality data needed and also it is a low cost when compared to the cost of some satellite images such as ASTER or SPOT per unit for long period of time. Different satellite sensors with high spatial resolution (Landsat 7 ETM+) and high temporal resolution (MODIS) seems to be the best option to map the UHI in the large scale.

The local UHI intensity is determined using ground data as a rural reference (airport weather station) and at the farm site. Both methods show the same results but the intensity of the UHI is higher with the farm, which is to be expected because of the effect of the vegetation. There is a

significant relationship between distribution of the UHI and land cover by using the mobile traverses and the remote sensing approaches. The UHI intensity is higher during the summer than the winter and at the night-time than the daytime. The highest UHI intensity is located over the two major cities in the oasis (Al Hufuf and Al Mubarraz) while the lowest UHI is recorded over the small villages and vegetated areas. The outcomes of this thesis can be used in future urban development and planning projects and draw the framework for implementing rules and regulations by government agencies for a sustainable urban development approach.

7.9 **Recommendations and directions for future study**

The aim of this study was to integrate both methods remote sensing and ground based data including the fixed weather stations and mobile data for better understating of the effect of the different land cover on urban heat island; however, the research project was challenging. According to the main limitations of both methods, studying urban heat island needs tools that have high resolution in both temporal and spatial information at the same time.

The ground data seem to be more accurate and easier to calibrate in order to study urban heat islands; however, this method needs large numbers of fixed weather stations and several mobile traverses day and night to gather the data needed and that costs a lot of money. But according to this study, it is recommended the large cities should have at least enough numbers of these fixed weather stations established on different locations to predict the heat waves and minimise the risk of urban heat island.

Remote sensing is a very good method to estimate the surface temperature and investigates the urban heat island at a large scale. However, there are a number of limitations, which have been mentioned before, which need to be improved in two aspects, the temporal and the spatial resolution. The two satellites images that used in this study are the highest temporal and spatial resolution available to study the UHI in the present study area Al Ahsa oasis. The Landsat 7 ETM+ has two thermal bands of 60 metres of spatial resolution and resampled to 30 metres and MODIS with daily revisit day and night but with poor spatial resolution.

Future studies should consider using ground-based thermal images for better understanding of the different land cover responses during the day and night-time. These thermal images will provide detailed surfaces temperatures with high temporal and spatial resolution to quantify the outgoing radiation budget at specific locations (Figure 7-16). These thermal images have some limitations related to the spatial coverage of small areas compared with the satellite observations. Moreover, if we need to collect data for several sites at the same time, it will need more thermal cameras but that will increase the cost.

NASA organized a workshop, which was held on October, 2008 in Monrovia, California in United States, to confirm and clarify the science requirements for the new Hyperspectral Infrared Imager (HyspIRI) mission (Figure 7-17). The HyspIRI will be launched between 2013-2016 and have eight spectral bands of which seven of them are located in the thermal infrared part of the spectrum between 7 and 13 μm, while the last band in located in the mid infrared part with electromagnetic spectrum of 4 um. The TIR instrument will have a swath width of 600 km with 60 meters spatial resolution and temporal revisit of 5 days. Moreover, the instrument will capture images over the entire surface of the earth during the day and night time (NASA, 2010). Therefore, this satellite will help to collect day and night observations with high spatial resolution which will allow better investigation and understanding of urban heat islands at different scales.

Figure 7-16 Thermal images of city centre site with snapshot of the location and thermal data during the morning and afternoon of February 6th and 7th 2011

Digital snapshot of the site

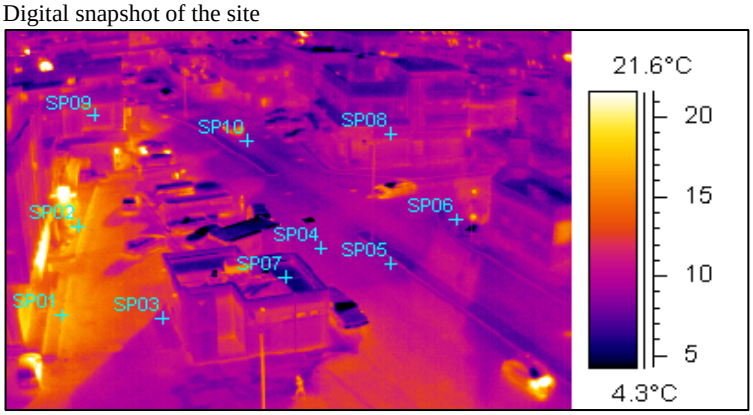

7-Feb-2011. 7:55 AM-Spot (1=16) (2=15) (3=9) (4=11) (5=8) (6=7) (7=9)

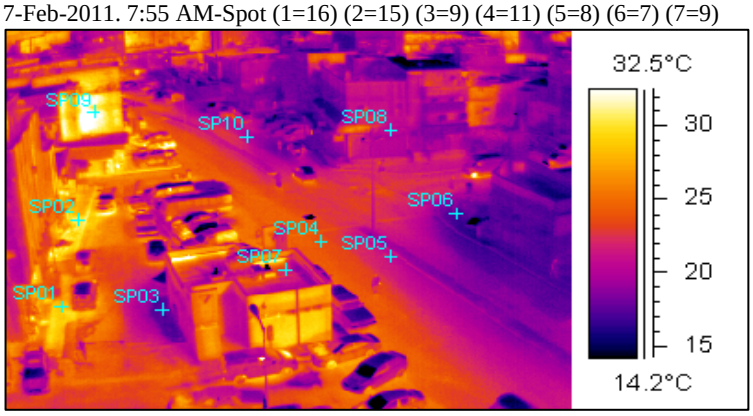

6-Feb-2011. 4:15PM-Spot (1=25) (2=30) (3=23) (4=24) (5=17) (6=19) (7=21)

Figure 7-17 Image and thermal infrared measurement characteristics of HyspIRI

Spectral	
Bands (8) μm	3.98 μm, 7.35 μm, 8.28 μm, 8.63 μm, 9.07 μm, 10.53 μm, 11.33 μm, 12.05 μm
Bandwidth	0.084 μm, 0.32 μm, 0.34 μm, 0.35 μm, 0.36 μm, 0.54 μm, 0.54 μm, 0.52 μm
Accuracy	<0.01 μm
Spatial	
IFOV	60 m
Swath Width	600 km (±25.5° at 623 km altitude)
Swath Length	15.4 km (± 0.7 degrees at 623 km altitude)
Temporal	
Orbit Crossing	11 a.m. Sun synchronous descending
Global Land Repeat	5 days at Equator
Data Collection	
Time Coverage	Day and Night
Land Coverage	Land surface above sea level
Water Coverage	Coastal zone minus 50 m and shallower
Open Ocean	Averaged to 1-km spatial sampling

Source: (NASA, 2010, NASA, 2015).

This study recommends the following recommendations in order of future study and research:

1. Establish more of micro weather stations in different land covers in the study area (Al Ahsa oasis) to record high temporal meteorological data including air and surface temperatures, relative humidity, sun radiation, wind and gust speed, and precipitation to help investigate the current and future local urban heat islands and the heat waves.

2. Investigate the effect of different land cover types on the local urban heat island using high spatial and temporal sensors that have multispectral bands such as Hyperspectral Infrared Imager (HyspIRI) for more understanding and studying the urban heat island.

3. Increase the awareness of the local government agencies about the urban heat island issue by establishing research centres, such Environmental Protection Agency, that provide the information needed and encourage the future research of related problems of heat island.

4. As the main findings of this study is that the built-up areas are the highest in UHI intensity, it is important to investigate more and in details of the different roofs, roads, pavements, and buildings materials which effects the heat balance of the city and that need special tools such as Hyperspectral Infrared Imager (HyspIRI) or thermal camera.

5. The effect of vegetation, in relation to evaporation and shading the surface from the sun's rays, helps keep the area cool (Gartland, 2008). Therefore, it is important to keep the existing palm trees in the oasis and increase the numbers of the trees in desert cities and built-areas to minimise the air and surface temperatures and the UHI intensity. Moreover, the vegetation has a key role to play in contributing to the overall temperature of the cities. The trees and green spaces can reduce the UHI and cool the air by between 2 °C and 8 °C, which leads to reduced heat-related stress and human deaths during extreme temperature events (Doick and Hutchings, 2013).

7.10 **Bibliography**

ABDELRAHMAN, M., SAID, S., AHMAD, A., INAM, M. & ABUL-HAMAYEL, H. 1990. Thermal conductivity of some major building materials in Saudi Arabia. *Journal of Building Physics,* 13**,** 294-300.

ABOLKHAIR, Y. M. S. 1981. *SAND ENCROACHMENT BY WIND IN AL-HASA OF SAUDI ARABIA.* 8119015 Ph.D., Indiana University.

ADINNA, E., CHRISTIAN, E. I. & OKOLIE, A. T. 2009. Assessment of urban heat island and possible adaptations in Enugu urban using landsat-ETM. *Journal of Geography and Regional Planning,* 2**,** 030-036.

AHMAD, A. 2004. ENERGY SIMULATION FOR A TYPICAL HOUSE BUILT WITH DIFFERENT TYPES OF MASONRY BUILDING MATERIALS. *Arabian Journal for Science & Engineering* 29**,** 113.

AIT BELAID, M. M., M.A 2002. Investigation of the impact of Urbanization on Agricultural Lands in AL-Ahsa Oasis Using Geographic Information Systems and Remote Sensing Technologies. *Annual ESRI Middle East & Africa User Conference.* Dubai.

AKBARI, H. 2005. Energy Saving Potentials and Air Quality Benefits of Urban Heat IslandMitigation.

AKHOONDZADEH, M. & SARADJIAN, M. 2008. Comparison of land surface temperature mapping using MODIS and ASTER images in semi-arid area. *Int Arch Photogram Remote Sens Spat Inf Sci XXXVII Part B,* 8**,** 873-876.

AL-ABDEEN, Z., ABDULRAHMAN 1986. *Al-Ahsa Oasis: Study in its Water Recourses and its effects in urban,* Riyadh, Saudi Arabia, Imam Muhammad Ibn Saud Islamic University.

AL-BUT'HIE, I. M. & EBEN SALEH, M. A. 2002. Urban and industrial development planning as an approach for Saudi Arabia: the case study of Jubail and Yanbu. *Habitat International,* 26**,** 1-20.

AL-FARRAJ, A. 2005. An evolutionary model for sabkha development on the north coast of the UAE. *Journal of Arid Environments,* 63**,** 740-755.

AL-GHANNAM, A. R. O. & AL-QAHTNAI, M. R. A. 2012. Impact of vegetation cover on urban and rural areas of arid climates. *Australian Journal of Agricultural Engineering,* 3**,** 1-5.

AL-MASS, A. 1999. *Agriculture and Sand Incursion in the Al-Ahsa, Saudi Arabia.* MA, Indiana State University.

AL-MUBARAK, F. A. 1999. Oil, urban development and planning in the eastern province of Saudi Arabia: the case of the Arab American oil company in the 1930's-1970's. *Journal of King Saud University*.

AL-OMEER, A. 1987. *Urban Geography of Al-Ahsa Oases.* Phd, Imam Muhammad Ibn Saud Islamic University.

AL-TAHER, A. 1999. *Al-Ahsa a Geographical Study,* Al Riyahd, Saudi Arabia, King Saud University Radmk for Publishing.

ALAVIPANAH, S., SHAMSIPOUR, A. & AMIRI, R. 2007. A study of the relationship among temperatures of surface features and its application in remote sensing study of Lut desert. *DESERT (BIABAN)***,** 85-97.

ALCOFORADO, M. & ANDRADE, H. 2008. Global Warming and the Urban Heat Island. *In:* MARZLUFF, J., SHULENBERGER, E., ENDLICHER, W., ALBERTI, M., BRADLEY, G., RYAN, C., SIMON, U. & ZUMBRUNNEN, C. (eds.) *Urban Ecology.* Springer US.

ALGHANNAM, A. R. O. & AL-QAHTNAI, M. R. A. 2012. Impact of vegetation cover on urban and rural areas of arid climates. *Australian Journal of Agricultural Engineering,* 3**,** 1-5.

ALTMAN, D. G. & BLAND, J. M. 2009. Parametric v non-parametric methods for data analysis. *BMJ,* 338.

ANONYMOUS 2006. MODIS Level 1B Product User's Guide. *In:* CENTER, N. G. S. F. (ed.). Greenbelt, Md, USA: NASA.

ARNFIELD, A. J. 2003. Two decades of urban climate research: a review of turbulence, exchanges of energy and water, and the urban heat island. *International Journal of Climatology,* 23**,** 1-26.

AUER, A. H. 1978. Correlation of Land Use and Cover with Meteorological Anomalies. *Journal of Applied Meteorology,* 17**,** 636-643.

AVISSAR, R. 1996. Potential effects of vegetation on the urban thermal environment. *Atmospheric Environment,* 30**,** 437-448.

BADARINATH, K., CHAND, T., MADHAVILATHA, K. & RAGHAVASWAMY, V. 2005. Studies on urban heat islands using envisat AATSR data. *Journal of the Indian Society of Remote Sensing,* 33**,** 495-501.

BAILLY, J. S., ARNAUD, M. & PUECH, C. 2007. Boosting: a classification method for remote sensing. *International Journal of Remote Sensing,* 28**,** 1687-1710.

BALLING, R. C. A. S. W. B. 1986. 'New' weather in Phoenix? Myths and realities. *Weatherwise,* 39**,** 86-90.

BARRIOPEDRO, D., FISCHER, E. M., LUTERBACHER, J., TRIGO, R. M. & GARCÍA-HERRERA, R. 2011. The hot summer of 2010: redrawing the temperature record map of Europe. *Science,* 332**,** 220-224.

BARSI, J. A., SCHOTT, J. R., PALLUCONI, F. D., HELDER, D. L., HOOK, S. J., MARKHAM, B. L., CHANDER, G. & O'DONNELL, E. M. 2003. Landsat TM and ETM+ thermal band calibration. *Canadian Journal of Remote Sensing,* 29**,** 141-153.

BECKER, F. & LI, Z. L. 1995. Surface temperature and emissivity at various scales: Definition, measurement and related problems. *Remote Sensing Reviews,* 12**,** 225-253.

BERDAHL, P. & BRETZ, S. E. 1997. Preliminary survey of the solar reflectance of cool roofing materials. *Energy and Buildings,* 25**,** 149-158.

BEST, M. J. 2006. Progress towards better weather forecasts for city dwellers: from short range to climate change. *Theoretical and Applied Climatology,* 84**,** 47-55.

BINDA, P. L. 1983. On the Skewness of Some Eolian Sands from Saudi Arabia. *In:* BROOKFIELD, M. E. & AHLBRANDT, T. S. (eds.) *Developments in Sedimentology*. Elsevier.

BLAND, P. A., MCBRIDE, N., MOORE, E. A., ROTHERY, D. A., WIDDOWSON, M., WRIGHT, I., ROTHERY, D. A., MCBRIDE, N. & GILMOUR, I. 2004. *An introduction to the solar system*, Open University.

BOTTYÁN, Z., KIRCSI, A., SZEGEDI, S. & UNGER, J. 2005. The relationship between built-up areas and the spatial development of the mean maximum urban heat island in Debrecen, Hungary. *International Journal of Climatology,* 25**,** 405-418.

BRADLEY, A. V., THORNES, J. E., CHAPMAN, L., UNWIN, D. & ROY, M. 2002. Modelling spatial and temporal road thermal climatology in rural and urban areas using a GIS. *Climate Research,* 22**,** 41-55.

BRANDSMA, T. & WOLTERS, D. 2012. Measurement and Statistical Modeling of the Urban Heat Island of the City of Utrecht (the Netherlands). *Journal of Applied Meteorology and Climatology,* 51**,** 1046-1060.

BRUCKER, G. 2005. Vulnerable populations: lessons learnt from the summer 2003 heat waves in Europe. *Euro Surveill,* 10**,** 147.
BUECHLEY, R. W., VAN BRUGGEN, J. & TRUPPI, L. E. 1972. Heat ISLAND = death island? *Environmental Research,* 5**,** 85-92.
CDC. 2006. *Extreme Heat: A Prevention Guide to Promote Your Personal Health and Safety* [Online]. United States Center for Disease Control and Prevention. Available: http://www.bt.cdc.gov/disasters/extremeheat/heat_guide.asp [Accessed 26 February 2013].
CHANDER, G., MARKHAM, B. L. & HELDER, D. L. 2009. Summary of current radiometric calibration coefficients for Landsat MSS, TM, ETM+, and EO-1 ALI sensors. *Remote Sensing of Environment,* 113**,** 893-903.
CHANDLER, T. J. 1960. WIND AS A FACTOR OF URBAN TEMPERATURES—A SURVEY IN NORTH-EAST LONDON. *Weather,* 15**,** 204-213.
CHANGNON, S. A. 1995. Applied climatology: A glorious past, and uncertain future. Historical Essays in Meteorology,. *American Meteorological Society***,** 379-393.
CHANGNON, S. A. J., KUNKEL, K. E. & REINKE, B. C. 1996. Impacts and responses to the 1995 heat wave: A call to action. *Bulletin of the American Meteorological Society,* 77**,** 1497–1506.
CHARABI, Y. & BAKHIT, A. 2011. Assessment of the canopy urban heat island of a coastal arid tropical city: The case of Muscat, Oman. *Atmospheric Research,* 101**,** 215-227.
CHEN, E. & ALLEN JR, L. H. 1987. Comparison of HCMM and GOES satellite temperatures and evaluation of surface statistics. *Remote Sensing of Environment,* 21**,** 341-353.
CHEN, X.-L., ZHAO, H.-M., LI, P.-X. & YIN, Z.-Y. 2006. Remote sensing image-based analysis of the relationship between urban heat island and land use/cover changes. *Remote Sensing of Environment,* 104**,** 133-146.
CHEVAL, S., DUMITRESCU, A. & BELL, A. 2009. The urban heat island of Bucharest during the extreme high temperatures of July 2007. *Theoretical and Applied Climatology,* 97**,** 391-401.
CHOW, W. T. L. & ROTH, M. 2006. Temporal dynamics of the urban heat island of Singapore. *International Journal of Climatology,* 26**,** 2243-2260.
CLARKE, J. F. 1972. Some effects of the urban structure on heat mortality. *Environmental Research,* 5**,** 93-104.
COLL, C., CASELLES, V., GALVE, J. M., VALOR, E., NICLÒS, R., SÁNCHEZ, J. M. & RIVAS, R. 2005. Ground measurements for the validation of land surface temperatures derived from AATSR and MODIS data. *Remote Sensing of Environment,* 97**,** 288-300.
COLL, C., GALVE, J. M., SANCHEZ, J. M. & CASELLES, V. 2010. Validation of Landsat-7/ETM+ Thermal-Band Calibration and Atmospheric Correction With Ground-Based Measurements. *Geoscience and Remote Sensing, IEEE Transactions on,* 48**,** 547-555.
COTTON, W. P., RA 1995. Human Impacts on Weather and Climate. Cambridge UK: Cambridge University Press.
CRITCHFIELD, H. J. 1983. *General Climatology*, Prentice Hall, Englewood Cliffs, N.J.
CRUTZEN, P. J. P. J. 2004. New Directions: The growing urban heat and pollution "island" effect--impact on chemistry and climate. *Atmospheric Environment,* 38**,** 3539-3540.
D'AGOSTINO, R. B., BELANGER, A. & D'AGOSTINO, R. B., JR. 1990. A Suggestion for Using Powerful and Informative Tests of Normality. *The American Statistician,* 44**,** 316-321.
DA CUNHA, A. 2015. Evaluation of measurement errors of temperature and relative humidity from HOBO data logger under different conditions of exposure to solar radiation. *Environmental Monitoring and Assessment,* 187**,** 1-11.

DAVENPORT, A. G., C.S.B. GRIMMOND & WIERINGA, T. R. O. J. Estimating the roughness of cities and sheltered country. Proceedings 12th Conference on Applied Climatology, 2000 Asheville, NC, Boston. American Meteorological Society, 96-99.

DAVID, S. 2007. The Urban Heat Island (UHI) – Causes, Impacts, and Mitigation Strategies. *State Clean Energy-Environment Technical Forum U.S. EPA.* United State: Portland State University.

DAVIS, J. C. 2002. *Statistics and data analysis in Geology,* New York, John Wiley & Sons.

DOICK, K. & HUTCHINGS, T. 2013. Air temperature regulation by urban trees and green infrastructure. England: Forestry Commission.

EDGELL, H. S. 1992. Basement Tectonics of Saudi Arabia as Related to Oil Field Structures. *In:* RICKARD, M. J., HARRINGTON, H. J. & WILLIAMS, P. R. (eds.) *Basement Tectonics 9.* Springer Netherlands.

EFFAT, H. A., TAHA, L. G. E.-D. & MANSOUR, K. F. 2014. Change Detection of Land cover and Urban Heat Islands using Multi-Temporal Landsat Images, application in Tanta City, Egypt. *Open Journal of Remote Sensing and Positioning,* 1**,** 1-15.

ELIASSON, I. 1996. Intra-urban nocturnal temperature differences: a multivariate approach. *CLIMATE RESEARCH,* 7**,** 21-30.

ELLEFSEN, R. 1991. Mapping and measuring buildings in the canopy boundary layer in ten U.S. cities. *Energy and Buildings,* 16**,** 1025-1049.

EPA. 2013. *Heat Island Impacts* [Online]. United States: United States Envirnmental Protection Agency. Available: http://www.epa.gov/heatisland/impacts/index.htm#2 [Accessed 26/02/ 2013].

ERELL, E. & WILLIAMSON, T. 2007. Intra-urban differences in canopy layer air temperature at a mid-latitude city. *International Journal of Climatology,* 27**,** 1243-1255.

ESCOBEDO, F., AND MARIELLE DUBBELING 2014. Guideline 2: Methodological guidelines for monitoring of temperature effects. November 2014 ed. UK: RUAF Foundation-Resource Centres on Urban Agriculture and Food Security.

FRYBERGER, S. G., AL-SARI, A. M. & CLISHAM, T. J. 1983. Eolian dune, interdune, sand sheet, and siliciclastic sabkha sediments of an offshore prograding sand sea, Dhahran area, Saudi Arabia. *AAPG Bulletin,* 67**,** 280-312.

FUKUOKA, Y. 1983. *Physical climatological discussion on causal factors of urban temperature,* Hiroshima Univ.

GARTLAND, L. 2008. *Heat Islands: Understanding and Mitigating Heat in Urban Areas*, Taylor & Francis.

GILLESPIE, A. R., ROKUGAWA, S., HOOK, S. J., MATSUNAGA, T. & KAHLE, A. B. 1999. Temperature/emissivity separation algorithm theoretical basis document, version 2.4.

GIVONI, B. 1976. *Man, climate and architecture* London, Applied Science Publishers.

GLENNIE, K. W. & SINGHVI, A. K. 2002. Event stratigraphy, paleoenvironment and chronology of SE Arabian deserts. *Quaternary Science Reviews,* 21**,** 853-869.

GLUCH, R., QUATTROCHI, D. A. & LUVALL, J. C. 2006. A multi-scale approach to urban thermal analysis. *Remote Sensing of Environment,* 104**,** 123-132.

GOGGINS, G. 2009. *Impacts of city size and vegetation coverage on the urban heat island using Landsat satellite imagery.* M.S. 1462620, Mississippi State University.

GOOD, E. 2015. Daily minimum and maximum surface air temperatures from geostationary satellite data. *Journal of Geophysical Research: Atmospheres,* 120**,** 2306-2324.

GORE, A. S., A 2008. *World Changing: A User's Giode for the 21st Century,* New York: Abrams.

GPS UTILITY. 2013. *GPS Utility - A program for handling GPS information* [Online]. Available: http://www.gpsu.co.uk/index.html 2013].
GRIMMOND, C. S. B. 2006. Progress in measuring and observing the urban atmosphere. *Theoretical and Applied Climatology,* 84**,** 3-22.
GRIMMOND, S. U. E. 2007. Urbanization and global environmental change: local effects of urban warming. *Geographical Journal,* 173**,** 83-88.
GUPTA, R. P. 2005. *Remote Sensing Geology,* Verlag Berlin Heidelberg, Springer International Edition.
HABIB, B. M. 2007. Study of Urban Heat Island of Dammam City, Saudi Arabia Using Remote Sensing and GIS. Saudi Arabia: Dammam University.
HART, M. & SAILOR, D. 2009. Quantifying the influence of land-use and surface characteristics on spatial variability in the urban heat island. *Theoretical and Applied Climatology,* 95**,** 397-406.
HEDQUIST, B. C. 2005. Assessment of the Urban Heat Island in Casa Grande, Arizona. *Journal of the Arizona-Nevada Academy of Science* 38**,** pp 29-39.
HEISLER, G. 1990. Mean wind speed below building height in residential neighborhoods with different tree densities. *ASHRAE transactions,* 96**,** 1389-1396.
HOFFMANN, P., KRUEGER, O. & SCHLÜNZEN, K. H. 2012. A statistical model for the urban heat island and its application to a climate change scenario. *International Journal of Climatology,* 32**,** 1238-1248.
HSU, S.-I. 1984. VARIATION OF AN URBAN HEAT ISLAND IN PHOENIX. *The Professional Geographer,* 36**,** 196-200.
HU, Y. & JIA, G. 2009. Influence of land use change on urban heat island derived from multi-sensor data. *International Journal of Climatology,* 9999**,** n/a.
HUMAIDAN, S. 1980. *Policies and Management Guidelines for Optimum Resource Utilization at Al-Hasa Irrigation and Drainage Project.* PhD, Oklahoma State University.
HUSSAIN, Z. 1982. Problems of irrigated agriculture in Al-Hassa, Saudi Arabia. *Agricultural Water Management,* 5**,** 359-374.
HUTCHEON, R., JOHNSON, R., LOWRY, W., BLACK, C. & HADLEY, D. 1967. Observations of urban heat island in a small city. *Bulletin of the American Meteorological Society,* 48**,** 7-&.
JABLONSKY, D. L. 2013. *GeoEye Imagery Collection Systems Inc. Private Remote Sensing System License Summary of GeoEye-1* [Online]. Longmont, United State: DigitalGlobe Available: www.digitalglobe.com 2013].
JAMES, W. 2002. Green Roads: Research Into Permeable Pavers An investigation of infiltration capacity, pavement leachate, and runoff temperature. *Stormwater The Journal For Surface Water Quality Professionals.*
JAMIL, A., AHMAD, M. A., MOHAMMAD, F. R. & SAIED, P. 2012. Land Surface Temperature Assessment in Semi-Arid Residential Area of Tehran, Iran Using Landsat Imagery. *World Applied Sciences Journal* 20**,** 319-326.
JANET, N. 2005. Remote Sensing of Urban Heat Islands by Day and Night. *Photogrammetric Engineering and Remote sensing,* 71**,** 613-621.
JANET, N. 2009. An Emissivity Modulation Method for Spatial Enhancement of Thermal Satellite Images in Urban Heat Island Analysis. *Photogrammetric Engineering and Remote sensing,* 75**,** 547-556.
JAUREGUI, E. 1990. Influence of a large urban park on temperature and convective precipitation in a tropical city. *Energy and Buildings,* 15**,** 457-463.

JAUREGUI, E., GODINEZ, L. & CRUZ, F. 1992. Aspects of heat-island development in Guadalajara, Mexico. *Atmospheric Environment. Part B. Urban Atmosphere,* 26**,** 391-396.

JEFFREY K. SONNE, R. K. V. 2000. Cool Neighborhoods: The Measurement of Small Scale Heat Islands. Florida Solar Energy Center: American Council for an Energy-Efficient Economy.

JENSEN, J. R. 2005a. *Introduction Digital Image Processing A Remote Sensing Perspective* United State, Pearson Education Inc.

JENSEN, J. R. 2005b. *Thematic Information Extraction: Pattern Recognition. – A Remote Sensing Perspective. Prentice Hall Series in Geographic Information Science.*

JONSSON, P. 2004. Vegetation as an urban climate control in the subtropical city of Gaborone, Botswana. *International Journal of Climatology,* 24**,** 1307-1322.

JR, R. C. B. & BRAZEL, S. W. 1987. Time and Space Characteristics of the Phoenix Urban Heat Island. *Journal of the Arizona-Nevada Academy of Science,* 21**,** 75-81.

JUDAH, H., JUDAH 1989. *Climatology and Biogeography,* Alexandria, Egypt, Alexandria University Dar Al-Marefa Al Gamieyah.

KALKSTEIN, L. S. & SMOYER, K. E. 1993. The impact of climate change on human health: Some international implications. *Experientia,* 49**,** 969-979.

KALNAY, E., KANAMITSU, M., KISTLER, R., COLLINS, W., DEAVEN, D., GANDIN, L., IREDELL, M., SAHA, S., WHITE, G., WOOLLEN, J., ZHU, Y., LEETMAA, A., REYNOLDS, R., CHELLIAH, M., EBISUZAKI, W., HIGGINS, W., JANOWIAK, J., MO, K. C., ROPELEWSKI, C., WANG, J., JENNE, R. & JOSEPH, D. 1996. The NCEP/NCAR 40-Year Reanalysis Project. *Bulletin of the American Meteorological Society,* 77**,** 437-471.

KANDA, M. 2006. Progress in the scale modeling of urban climate: Review. *Theoretical and Applied Climatology,* 84**,** 23-33.

KARACA, M., TAYANC, M. & TOROS, H. 1995. Effects of urbanization on climate of Istanbul and Ankara. *Atmospheric Environment,* 29**,** 3411-3421.

KARDINAL, J., STEVE, WONG, N. H., HAGEN, E., ANGGORO, R. & HONG, Y. 2007. The influence of land use on the urban heat island in Singapore. *Habitat International,* 31**,** 232-242.

KAWASHIMA, S. 1990. Effect of vegetation on surface temperature in urban and suburban areas in winter. *Energy and Buildings,* 15**,** 465-469.

KAYA, S., BASAR, U. G., KARACA, M. & SEKER, D. Z. 2012. Assessment of urban heat islands using remotely sensed data. *Ekoloji,* 84**,** 107-113.

KEN LIVINGSTONE 2006. London's Urban Heat Island: A Summary for Decision Makers. Hall, UK.

KIM, H. H. 1992. Urban heat island. *International Journal of Remote Sensing,* 13**,** 2319 - 2336.

KIM, J. 2009. *Land-use planning and the urban heat island effect.* Ph.D. 3382376, The Ohio State University.

KIM, Y.-H. & BAIK, J.-J. 2002. Maximum Urban Heat Island Intensity in Seoul. *Journal of Applied Meteorology,* 41**,** 651-659.

KIM, Y.-H. & BAIK, J.-J. 2005. Spatial and Temporal Structure of the Urban Heat Island in Seoul. *Journal of Applied Meteorology,* 44**,** 591-605.

KING ABDULAZIZ CITY FOR SCIENCE AND TECHNOLOGY 2010. Image data for Landsat-5 EOSAT 1996. *In:* INSTITUTE, S. R. (ed.). Riyadh, Saudi Arabia.

KOTTEK, M., GRIESER, J., BECK, C., RUDOLF, B. & RUBEL, F. 2006. World Map of the Köppen-Geiger climate classification updated. *Meteorologische Zeitschrift,* 15**,** 259-263.

KRUSKAL, W. H. & WALLIS, W. A. 1952. Use of Ranks in One-Criterion Variance Analysis. *Journal of the American Statistical Association,* 47**,** 583-621.

LAND INFO WORLDWIDE MAPPING. 2013. *GeoEye-1 High-Resolution Satellite Imagery, GeoEye-1 Specifications* [Online]. Highlands Ranch, United State. Available: http://www.landinfo.com/geo.htm 2013].

LANDSBERG, H. E. 1981. *The Urban Climate,* New York, Academic Press.

LARAS, T., JOSAPHAT, T. S. S., HIROAKI, K. & ERNA, S. A. 2012. Relationship between Urban Heat Island Phenomenon and Land Use/Land Cover Changes in Jakarta – Indonesia. *Journal of Emerging Trends in Engineering and Applied Sciences* 3**,** 645-653.

LAWRENCE, M. G. 2005. The Relationship between Relative Humidity and the Dewpoint Temperature in Moist Air: A Simple Conversion and Applications. *Bulletin of the American Meteorological Society,* 86**,** 225-233.

LAZZARINI, M., MARPU, P. R. & GHEDIRA, H. 2013. Temperature-land cover interactions: The inversion of urban heat island phenomenon in desert city areas. *Remote Sensing of Environment,* 130**,** 136-152.

LEICHTWEISS, I. 1973. Agro-meteorology of the Al-Hassa oasis In: Report on the work of Leichtweiss Institute Research Team. Hofuf, Saudi Arabia: Leichtweiss Institute Research Team.

LEICHTWEISS, I. 1978. Agro-meteorology of the Al-Hassa oasis In: Report on the work of Leichtweiss Institute Research Team. Hofuf, Saudi Arabia: Leichtweiss Institute Research Team.

LI, Z.-L., TANG, B.-H., WU, H., REN, H., YAN, G., WAN, Z., TRIGO, I. F. & SOBRINO, J. A. 2013. Satellite-derived land surface temperature: Current status and perspectives. *Remote Sensing of Environment,* 131**,** 14-37.

LILLESAND, T. M. K., R.W. 2000. *Remote sensing and image interpretation,* New York, John Wiley and Sons.

LO, C. P. & QUATTROCHI, D. A. 2003. Land-use and land-cover change, urban heat island phenomenon, and health implications: a remote sensing approach. *Photogrammetric Engineering and Remote Sensing,* 69**,** 1053-1063.

LO, C. P., QUATTROCHI, D. A. & LUVALL, J. C. 1997. Application of high-resolution thermal infrared remote sensing and GIS to assess the urban heat island effect. *International Journal of Remote Sensing,* 18**,** 287 - 304.

MALLESWARA RAO, T. C., NARASIMHA RAO, K. & MOHANA RAO, K. V. K. 1986. Georeference correction on landsat imagery. *Journal of the Indian Society of Remote Sensing,* 14**,** 67-76.

MARKHAM, B. L. & BARKER, J. L. 1986. Landsat MSS and TM post-calibration dynamic ranges,exoatmospheric reflectances and at-satellite temperatures *EOSAT Landsat Technical Notes, no.1.* Lanham, MD 20706: EOSAT.

MAS, J. F. 1999. Monitoring land-cover changes: A comparison of change detection techniques. *International Journal of Remote Sensing,* 20**,** 139-152.

MASSON, V. 2000. A Physically-Based Scheme For The Urban Energy Budget In Atmospheric Models. *Boundary-Layer Meteorology,* 94**,** 357-397.

MASSON, V. 2006. Urban surface modeling and the meso-scale impact of cities. *Theoretical and Applied Climatology,* 84**,** 35-45.

MEIER, F. S., DIETER RICHTERS, JOCHEN 2010. Determination of persistence effects in spatio-temporal patterns of upward long-wave radiation flux density from an urban courtyard by means of Time-Sequential Thermography. *Remote Sensing of Environment,* 114**,** 21-34.

MILDREXLER, D. J., ZHAO, M. & RUNNING, S. W. 2011. Satellite Finds Highest Land Skin Temperatures on Earth. *Bulletin of the American Meteorological Society,* 92**,** 855-860.

MILLS, G. 2008. Luke Howard and The Climate of London. *Weather,* 63**,** 153-157.

MINISTRY OF ECONOMY AND PLANNING 2010. *Annual Statistical Yearbook,* Kingdom of Saudi Arabia, Central Department of Statistics and Information.

MINISTRY OF HOUSING OF SAUDI ARABIA. 2014. *Statistics of Projects* [Online]. Saudi Arabia: Ministry of Housing Available: http://housing.gov.sa/ar/Pages/default.aspx 2014].

MINISTRY OF MUNICIPAL AND RURAL AFFAIRS 2013. Statistics Report for Saudi Arabia Divisions- Number of licenses issued for different shops from (1987-2011) Saudi Arabia.

MISHRA, R. K., BAHUGUNA, P. P. & SINGH, V. K. 2011. Detection of coal mine fire in Jharia Coal Field using Landsat-7 ETM+ data. *International Journal of Coal Geology,* 86**,** 73-78.

MONTÁVEZ, J. P., RODRÍGUEZ, A. & JIMÉNEZ, J. I. 2000. A study of the Urban Heat Island of Granada. *International Journal of Climatology,* 20**,** 899-911.

MP, M. O. P. 1992. This is Our Country. Saudi Arabia: Saudi Desert House for Publishing and Distribution.

MUFAREH, A. R. 2002. *Investigation of the impact of Urbanization on Land Use in AL Ahsa Oasis Using Remote Sensing and Geographic Information Systems Technologies* [Online]. Manama: Arabian Gulf University. MA].

NASA 2008. Hyspiri Whitepaper and Science Workshop Report. *In:* LABORATORY, J. P. (ed.). California Institute of Technology.

NASA 2012. How to find, understand, and use the quality assurance information for MODIS land products. *MODIS Land Products Quality Assurance Tutorial: Part:1.* United State: NASA LP DAAC USGS EROS Center,Sioux Falls South Dakota.

NASA. 2013a. *Landsat 7 Webpage* [Online]. United State: National Aeronautics and Space Administration. Available: http://landsat.gsfc.nasa.gov/about/landsat7.html 2013].

NASA. 2013b. *Moderate Resolution Imaging Spectroradiometer (MODIS) website* [Online]. United State: National Aeronautics and Space Administration-The Land Processes Distributed Active Archive Center (LP DAAC). Available: https://lpdaac.usgs.gov/ 2013].

NASA. 2015. *YyspIRI Mission Study Website* [Online]. United States California Institute of Technology U.S. Available: http://hyspiri.jpl.nasa.gov/ 2015].

NASA, N. A. A. S. A. 2010. Hyspiri Whitepaper and Science Workshop Report. *In:* LABORATORY, J. P. (ed.). California Institute of Technology.

NASRALLAH, H. & BALLING, R., JR. 1993. Spatial and temporal analysis of Middle Eastern temperature changes. *Climatic Change,* 25**,** 153-161.

NASRALLAH, H. A., BRAZEL, A. J. & JR., R. C. B. 1990. Analysis of the Kuwait city urban heat island. *International Journal of Climatology,* 10**,** 401-405.

NICHOL, J. E., FUNG, W. Y., LAM, K.-S. & WONG, M. S. 2009. Urban heat island diagnosis using ASTER satellite images and 'in situ' air temperature. *Atmospheric Research,* 94**,** 276-284.

OGAWA, K., SCHMUGGE, T. & ROKUGAWA, S. 2008. Estimating Broadband Emissivity of Arid Regions and Its Seasonal Variations Using Thermal Infrared Remote Sensing. *Geoscience and Remote Sensing, IEEE Transactions on,* 46**,** 334-343.

OGURO, Y., ITO, S. & TSUCHIYA, K. 2011. Comparisons of Brightness Temperatures of Landsat-7/ETM+ and Terra/MODIS around Hotien Oasis in the Taklimakan Desert. *Applied and Environmental Soil Science,* 2011.

OJIMA, T. 1990. Changing Tokyo Metropolitan area and its heat island model. *Energy and Buildings,* 15**,** 191-203.

OKE, T. R. 1973. City size and the urban heat island. *Atmospheric Environment (1967),* 7**,** 769-779.

OKE, T. R. 1981. Canyon geometry and the nocturnal urban heat island: Comparison of scale model and field observations. *International Journal of Climatology,* 1**,** 237-254.

OKE, T. R. 1982. The energetic basis of the urban heat island. *Quarterly Journal of the Royal Meteorological Society,* 108**,** 1-24.

OKE, T. R. 1987. *Boundary Layer Climates,* New York, Routledge.

OKE, T. R. 1997. Urban Climates and Global Environmental Change. *In:* PERRY, R. D. T. A. A. (ed.) *Applied Climatology: Principles & Practices.* New York, NY: Routledge.

OKE, T. R. 2006. Initial guidance to obtain representative meteorological observations at urban sites. *Instruments and Observing Methods.* Canada: World Meteorological Organisation.

OKE, T. R., GRIMMOND, C.S.B. & SPRONKEN-SMITH, R.A. 1998. On the confounding role of rural wetness in assessing urban effects on climate. *The Second Symposium on Urban Environment* Albuquerque NM: American Meteorological Society.

ONSET HOBO DATA LOGGERS COMPANY. 2013. *Specifications of HOBO Micro Station Data Logger - H21-002* [Online]. United State. Available: http://www.onsetcomp.com/products/data-loggers/h21-002 2013].

ORHAN, O., EKERCIN, S. & DADASER-CELIK, F. 2014. Use of Landsat Land Surface Temperature and Vegetation Indices for Monitoring Drought in the Salt Lake Basin Area, Turkey. *The Scientific World Journal,* 2014**,** 11.

OWEN, S. M., MACKENZIE, A. R., BUNCE, R. G. H., STEWART, H. E., DONOVAN, R. G., STARK, G. & HEWITT, C. N. 2006. Urban land classification and its uncertainties using principal component and cluster analyses: A case study for the UK West Midlands. *Landscape and Urban Planning,* 78**,** 311-321.

PEARSON, K. 1895. Contributions to the Mathematical Theory of Evolution. III. Regression, Heredity, and Panmixia. *Proceedings of the Royal Society of London,* 59**,** 69-71.

PEEL, M. C., FINLAYSON, B. L. & MCMAHON, T. A. 2007. Updated world map of the Köppen-Geiger climate classification. *Hydrol. Earth Syst. Sci.,* 11**,** 1633-1644.

PETITCOLIN, F. & VERMOTE, E. 2002. Land surface reflectance, emissivity and temperature from MODIS middle and thermal infrared data. *Remote Sensing of Environment,* 83**,** 112-134.

PINHO, O. S. & ORGAZ, M. D. M. 2000. The urban heat island in a small city in coastal Portugal. *International Journal of Biometeorology,* 44**,** 198-203.

POWERS, R., RAMIREZ, L., REDMOND, C. & ELBERG, E. 1966. Geology of the Arabian peninsula. *Geological survey professional paper,* 560**,** 1-147.

PRESIDENCY OF METEOROLOGY AND ENVIRONMENT 2011. Al Ahsa Weather Station Climate Data (1985-2012). *In:* DEPARTMENT, E. P. (ed.). Saudi Arabia.

QIAN, L.-X., CUI, H.-S. & CHANG, J. 2006. Impacts of Land Use and Cover Change on Land Surface Temperature in the Zhujiang Delta. *Pedosphere,* 16**,** 681-689.

QINA, Z., BERLINERB, P. & KARNIELIB, A. 2005. Ground temperature measurement and emissivity determination to understand the thermal anomaly and its significance on the development of an arid environmental ecosystem in the sand dunes across the Israel–Egypt border. *Journal of Arid Environments,* 6**,** 27-52.

QUATTROCHI, D. A., ANUPMA PRAKASH, MARIANA ENEVA, ROBERT WRIGHT, DOROTHY K. HALL, MARTHA ANDERSON, WILLIAM P. KUSTAS, RICHARD G. ALLEN, THOMAS PAGANO, AND MARK F. COOLBAUGH, 2009. *Thermal Remote Sensing: Theory, Sensors, and Applications (Chapter 3),* Falls Church, VA, (In Press), In Manual of Remote Sensing, American Society for Photogrammetry and Remote Sensing.

QUATTROCHI, R. D., ESTES M, CAYMON C, HOWELL B, LUVALL J 2000. A Decision Support information System for Urban Landscape Management Using Thermal Infrared data. *Photogrammetric Engineering and Remote sensing,* 66**,** 1195 – 1207.

RAJASEKAR, U. & WENG, Q. 2009. Spatio-temporal modelling and analysis of urban heat islands by using Landsat TM and ETM+ imagery. *Int. J. Remote Sens.,* 30**,** 3531-3548.

RIGO, G., PARLOW, E. & OESCH, D. 2006. Validation of satellite observed thermal emission with in-situ measurements over an urban surface. *Remote Sensing of Environment,* 104**,** 201-210.

ROA-ESPINOSA, A., WILSON, T., NORMAN, J. & JOHNSON, K. Predicting the impact of urban development on stream temperature using a thermal urban runoff model (TURM). National Conference on Urban Stormwater: Enhancing Programs at the Local Level. February, 2003. 17-20.

ROBINE, J. M., CHEUNG, S. L., LE ROY, S., VAN OYEN, H., GRIFFITHS, C., MICHEL, J. P. & HERRMANN, F. R. 2008. Death toll exceeded 70,000 in Europe during the summer of 2003. *C R Biol,* 331**,** 171-8.

ROHDE, R., MULLER, R., JACOBSEN, R., PERLMUTTER, S., ROSENFELD, A., WURTELE, J., CURRY, J., WICKHAM, C. & MOSHER, S. 2013. Berkeley earth temperature averaging process. *Geoinfor. Geostat.: An Overview,* 1**,** 1-13.

ROTH, M., OKE, T. R. & EMERY, W. J. 1989. Satellite-derived urban heat islands from three coastal cities and the utilization of such data in urban climatology. *International Journal of Remote Sensing,* 10**,** 1699 - 1720.

ROY, D. P., BORAK, J. S., DEVADIGA, S., WOLFE, R. E., ZHENG, M. & DESCLOITRES, J. 2002. The MODIS Land product quality assessment approach. *Remote Sensing of Environment,* 83**,** 62-76.

RUNNALLS, K. E. & OKE, T. R. 2000. DYNAMICS AND CONTROLS OF THE NEAR-SURFACE HEAT ISLAND OF VANCOUVER, BRITISH COLUMBIA. *Physical Geography,* 21**,** 283-304.

SAARONI, H., BEN-DOR, E., BITAN, A. & POTCHTER, O. 2000. Spatial distribution and microscale characteristics of the urban heat island in Tel-Aviv, Israel. *Landscape and Urban Planning,* 48**,** 1-18.

SABTAN, A. A. & SHEHATA, W. M. 2003. Hydrogeology of Al-Lith Sabkha, Saudi Arabia. *Journal of Asian Earth Sciences,* 21**,** 423-429.

SAILOR, D. J. 2002. URBAN HEAT ISLANDS Opportunities and Challenges for Mitigation and Adaptation. May 2002 ed. North American Urban Heat Island Summit Toronto,Canada: National Institute for Global Environmental Change School of Engineering, Tulane University.

SAITO, I., ISHIHARA, O. & KATAYAMA, T. 1990. Study of the effect of green areas on the thermal environment in an urban area. *Energy and Buildings,* 15**,** 493-498.

SANTAMOURIS, M. 2013. *Energy and climate in the urban built environment,* Routledge.

SARDON, J. P. 2007. The 2003 heat wave. *Euro surveillance : bulletin Europeen sur les maladies transmissibles = European communicable disease bulletin* [Online], 12. Available: http://europepmc.org/abstract/MED/17439811 [Accessed 2007/03//].

SEAN BRESLIN. 2015. *India Heat Wave, Now 5th Deadliest on Record, Kills More Than 2,300* [Online]. Weather.com. Available: http://www.weather.com/news/news/india-heat-wave-photos-news 2015].

SHAHMOHAMADI, P., CHE-ANI, A. I., ABDULLAH, N. A. G., MAULUD, K. N. A., TAHIR, M. M. & MOHD-NOR, M. F. I. 2010. The conceptual framework on formation of urban heat island in Tehran metropolitan, Iran: A focus on urbanization factor. *International Conference on Electric Power Systems, High voltages, Electric machines, International conference on Remote sensing - Proceedings.* Iwate; Japan: Iwate Prefectural University.

SHAHMOHAMADI, P., CHE-ANI, A. I., MAULUD, K. N. A., TAWIL, N. M. & ABDULLAH, N. A. G. 2011. The Impact of Anthropogenic Heat on Formation of Urban Heat Island and Energy Consumption Balance. *Urban Studies Research,* 2011.

SHARAF, M. 1997. *Studies in Applied Climatology-Climatic Hazards on Agriculture in Al-Hassa Oasis,* Egypt Faculty of Arts Magazine Dar Alexandria.

SHUNLIN, L. 2001. An optimization algorithm for separating land surface temperature and emissivity from multispectral thermal infrared imagery. *Geoscience and Remote Sensing, IEEE Transactions on,* 39**,** 264-274.

SKYE INSTRUMENTS LIMITED. 2013. *CHOOSING A SUITABLE LOCATION FOR AN AUTOMATIC WEATHER STATION* [Online]. United Kingdom: SKYE INSTRUMENTS LIMITED. Available: http://www.skyeinstruments.com/wp-content/uploads/LOCATING-A-WEATHER-STATION1.pdf 2013].

SMALL, C. 2006. Comparative analysis of urban reflectance and surface temperature. *Remote Sensing of Environment,* 104**,** 168-189.

SMOYER-TOMIC, K. E. & RAINHAM, D. G. 2001. Beating the heat: development and evaluation of a Canadian hot weather health-response plan. *Environ Health Perspect,* 109**,** 1241-8.

SOBRINO, J. A., OLTRA-CARRIÓ, R., JIMÉNEZ-MUÑOZ, J. C., JULIEN, Y., SORIA, G., FRANCH, B. & MATTAR, C. 2012. Emissivity mapping over urban areas using a classification-based approach: Application to the Dual-use European Security IR Experiment (DESIREX). *International Journal of Applied Earth Observation and Geoinformation,* 18**,** 141-147.

SOFER, M. & POTCHTER, O. 2006. The urban heat island of a city in an arid zone: the case of Eilat, Israel. *Theoretical and Applied Climatology,* 85**,** 81-88.

SOUCH, C. & GRIMMOND, S. 2006. Applied climatology: urban climate. *Progress in Physical Geography,* 30**,** 270-279.

SPRONKEN-SMITH, R. A. & OKE, T. R. 1998. The thermal regime of urban parks in two cities with different summer climates. *International Journal of Remote Sensing,* 19**,** 2085-2104.

SPRONKEN-SMITH, R. A. & OKE, T. R. 1999. Scale Modelling of Nocturnal Cooling in Urban Parks. *Boundary-Layer Meteorology,* 93**,** 287-312.

STATHOPOULOU, M. & CARTALIS, C. 2007. Daytime urban heat islands from Landsat ETM+ and Corine land cover data: An application to major cities in Greece. *Solar Energy,* 81**,** 358-368.

STEWART, I. D. 2000. Influence of meteorological conditions on the intensity and form of the urban heat island effect in Regina. *Canadian Geographer / Le Géographe canadien,* 44**,** 271-285.

STREUTKER, D. R. 2003. Satellite-measured growth of the urban heat island of Houston, Texas. *Remote Sensing of Environment,* 85**,** 282-289.
TAHA, H. 1997. Urban climates and heat islands: albedo, evapotranspiration, and anthropogenic heat. *Energy and Buildings,* 25**,** 99-103.
TARLETON, L. F. & KATZ, R. W. 1995. Statistical Explanation for Trends in Extreme Summer Temperatures at Phoenix, Arizona. *Journal of Climate,* 8**,** 1704-1708.
TOMLINSON, C. J., CHAPMAN, L., THORNES, J. E. & BAKER, C. J. 2012. Derivation of Birmingham's summer surface urban heat island from MODIS satellite images. *International Journal of Climatology,* 32**,** 214-224.
TSO, C. P. 1996. A survey of urban heat island studies in two tropical cities. *Atmospheric Environment,* 30**,** 507-519.
UNGER, J., SÜMEGHY, Z. & ZOBOKI, J. 2001. Temperature cross-section features in an urban area. *Atmospheric Research,* 58**,** 117-127.
UNION, E. 2009. *Saudi Arabia General information* [Online]. European Union in the world European Commission website. Available: http://ec.europa.eu/world/where/saudi_arabia/index_en.htm#.
UNITED STATE GEOLOGICAL SURVEY. 2011. *USGS Global Visualization Viewer* [Online]. United State: USGS. Available: http://glovis.usgs.gov/ 2011].
UNITED STATES GEOLOGICAL SURVEY. 2010. *Landsat Update-New Thermal Band Resampling: 30-meter pixels* [Online]. United State of America: USGS. Available: http://landsat.usgs.gov/about_LU_Vol_4_Issue_Special_Edition.php [Accessed 20 2013].
UNITED STATES GEOLOGICAL SURVEY. 2011. *USGS Global Visualization Viewer* [Online]. United State of America: USGS. Available: http://glovis.usgs.gov/ 2011].
UPMANIS, H. & CHEN, D. 1999. Influence of geographical factors and meteorological variables on nocturnal urban-park temperature differences-a case study of summer 1995 in Göteborg, Sweden. *Climate Research,* 13**,** 125-139.
VALSSON, S. & BHARAT, A. 2011. Impact of Air Temperature on Relative Humidity-A study. *ARCHITECTURE -TIME SPACE & PEOPLE.* India: Council of Architecture.
VAN WEVERBERG, K., DE RIDDER, K. & VAN ROMPAEY, A. 2008. Modeling the contribution of the Brussels heat island to a long temperature time series. *Journal of Applied Meteorology and Climatology,* 47**,** 976-990.
VARGHA, A. & DELANEY, H. D. 1998. The Kruskal-Wallis Test and Stochastic Homogeneity. *Journal of Educational and Behavioral Statistics,* 23**,** 170-192.
VICENTE SERRANO, S. M., CUADRAT, J. M. & SÁNCHEZ, S. 2005. Spatial patterns of the urban heat island in Zaragoza (Spain). *Climate Research,* 30**,** 61-69.
VOOGT, J. 2000. How Researchers Measure Urban Heat Islands. 2000 ed. United States Environmental Protection Agency, available online http://epa.gov/heatisland/resources/pdf/EPA_How_to_measure_a_UHI.pdf: EPA.
VOOGT, J. A. 2002. Urban Heat Island. *In Encyclopedia of Global Environmental Change* 3**,** 688.
VOOGT, J. A. 2004. *Urban Heat Islands: Hotter Cities* [Online]. Available: http://www.actionbioscience.org/environment/voogt.html 2010].
VOOGT, J. A. & GRIMMOND, C. S. B. 2000. Modeling Surface Sensible Heat Flux Using Surface Radiative Temperatures in a Simple Urban Area. *Journal of Applied Meteorology,* 39**,** 1679-1699.
VOOGT, J. A. & OKE, T. R. 1997. Complete Urban Surface Temperatures. *Journal of Applied Meteorology,* 36**,** 1117-1132.

VOOGT, J. A. & OKE, T. R. 2003. Thermal remote sensing of urban climates. *Remote Sensing of Environment,* 86**,** 370-384.
VUKOVICH, F. M. 1984. A comparison of surface temperature derived from HCMM infrared measurements with field data. *Remote Sensing of Environment,* 15**,** 63-76.
WAN, Z. 2008. New refinements and validation of the MODIS Land-Surface Temperature/Emissivity products. *Remote Sensing of Environment,* 112**,** 59-74.
WAN, Z., ZHANG, Y., ZHANG, Q. & LI, Z.-L. 2002. Validation of the land-surface temperature products retrieved from Terra Moderate Resolution Imaging Spectroradiometer data. *Remote Sensing of Environment,* 83**,** 163-180.
WAN, Z., ZHANG, Y., ZHANG, Q. & LI, Z. L. 2004. Quality assessment and validation of the MODIS global land surface temperature. *International Journal of Remote Sensing,* 25**,** 261-274.
WARE, C., KNIGHT, W. & WELLS, D. 1991. Memory intensive statistical algorithms for multibeam bathymetric data. *Computers & Geosciences,* 17**,** 985-993.
WENG, Q. 2001. A remote sensing?GIS evaluation of urban expansion and its impact on surface temperature in the Zhujiang Delta, China. *International Journal of Remote Sensing,* 22**,** 1999 - 2014.
WENG, Q. 2009. Thermal infrared remote sensing for urban climate and environmental studies: Methods, applications, and trends. *ISPRS Journal of Photogrammetry and Remote Sensing,* 64**,** 335-344.
WILMERS, F. 1990. Effects of vegetation on urban climate and buildings. *Energy and Buildings,* 15**,** 507-514.
WONG, E., AKBARI, H., BELL, R. & COLE, D. 2011. Reducing Urban Heat Islands: Compendium of Strategies. *Environmental Protection Agency, retrieved May,* 12**,** 2011.
WONG, K. V., PADDON, A. & JIMENEZ, A. 2013. Review of World Urban Heat Islands: Many Linked to Increased Mortality. *Journal of Energy Resources Technology,* 135**,** 11.
WONG, N. & JUSUF, S. GIS-based urban heat island study in University campus. In 2nd PALENC Conference and 28th AIVC Conference on Building Low Energy Cooling and Advanced Ventilation Technologies in the 21st Century, 2007. 1127-1131.
WONG, N. H. & YU, C. 2005. Study of green areas and urban heat island in a tropical city. *Habitat International,* 29**,** 547-558.
XIUPING, J. & RICHARDS, J. A. 1999. Segmented principal components transformation for efficient hyperspectral remote-sensing image display and classification. *Geoscience and Remote Sensing, IEEE Transactions on,* 37**,** 538-542.
XU, W., WOOSTER, M. J. & GRIMMOND, C. S. B. 2008. Modelling of urban sensible heat flux at multiple spatial scales: A demonstration using airborne hyperspectral imagery of Shanghai and a temperature-emissivity separation approach. *Remote Sensing of Environment,* 112**,** 3493-3510.
YAGÜE, C., ZURITA, E. & MARTINEZ, A. 1991. Statistical analysis of the Madrid urban heat island. *Atmospheric Environment. Part B. Urban Atmosphere,* 25**,** 327-332.
YAMASHITA, S. 1996. Detailed structure of heat island phenomena from moving observations from electric tram-cars in Metropolitan Tokyo. *Atmospheric Environment,* 30**,** 429-435.
YOKOBORI, T. & OHTA, S. 2009. Effect of land cover on air temperatures involved in the development of an intra-urban heat island. *Climate Research,* 39**,** 61-73.
YOKOHARI, M., BROWN, R. D., KATO, Y. & YAMAMOTO, S. 2001. The cooling effect of paddy fields on summertime air temperature in residential Tokyo, Japan. *Landscape and Urban Planning,* 53**,** 17-27.

ZAITCHIK, B. F., MACALADY, A. K., BONNEAU, L. R. & SMITH, R. B. 2006. Europe's 2003 heat wave: a satellite view of impacts and land–atmosphere feedbacks. *International Journal of Climatology*, 26**,** 743-769.

ZAITCHIK, B. F., MACALADY, A.K., BONNEAU, L.R. AND SMITH, R. B. 2006. Europe's 2003 Heat Wave: A Satellite View of Impacts and Land-Atmosphere Feedbacks. *Int. J. Climatol,* 26**,** 743–769.

ZHANG, Y. 2011. *MODIS UCSB Emissivity Library* [Online]. University of California, Santa Barbara: Institute for Computational Earth System Science. Available: http://www.icess.ucsb.edu/modis/EMIS/html/em.html.

ZHENGMING, W. & DOZIER, J. 1996. A generalized split-window algorithm for retrieving land-surface temperature from space. *Geoscience and Remote Sensing, IEEE Transactions on,* 34**,** 892-905.

ZHU, S., GUAN, H., BENNETT, J., CLAY, R., EWENZ, C., BENGER, S., MAGHRABI, A. & MILLINGTON, A. C. 2013. Influence of sky temperature distribution on sky view factor and its applications in urban heat island. *International Journal of Climatology*, 33**,** 1837-1843.

ZOULIA, I., SANTAMOURIS, M. & DIMOUDI, A. 2009. Monitoring the effect of urban green areas on the heat island in Athens. *Environmental Monitoring and Assessment,* 156**,** 275-292

7.11 **Appendices**

Appendix 4.1:

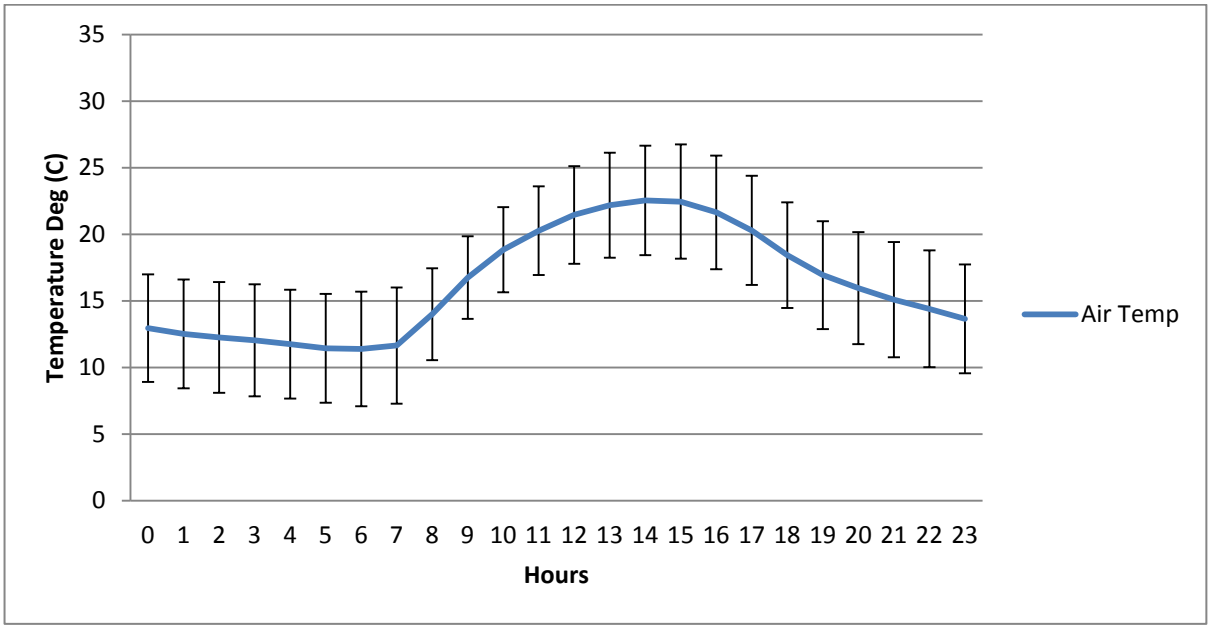

Mean and Standard Deviation of Air Temperature at Farm Site from 21/1/2011 to 28/2/2011.

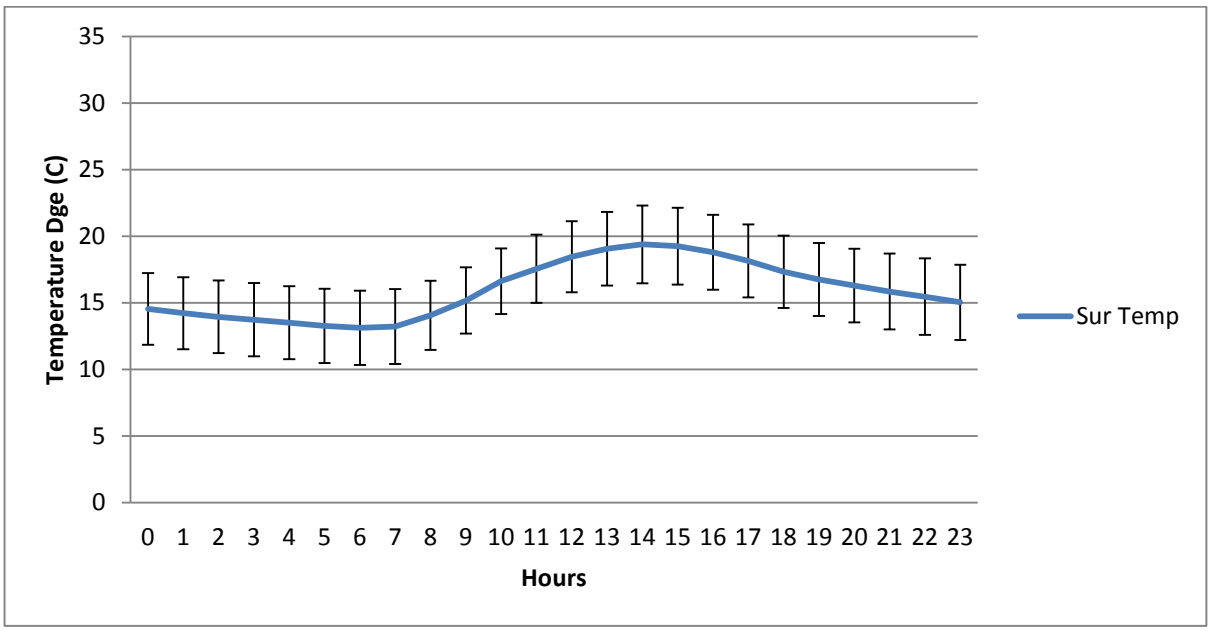

Mean and Standard Deviation of Surface Temperature at Farm Site from 21/1/2011 to 28/2/2011.

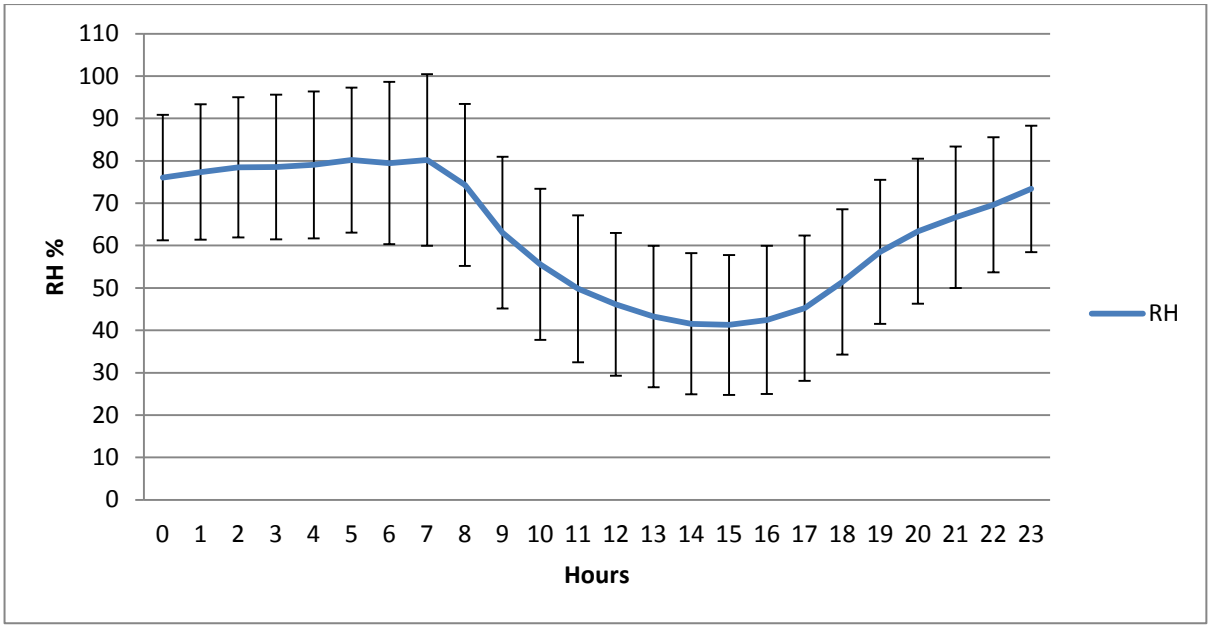

Mean and Standard Deviation of Relative Humidity at Farm Site from 21/1/2011 to 28/2/2011.

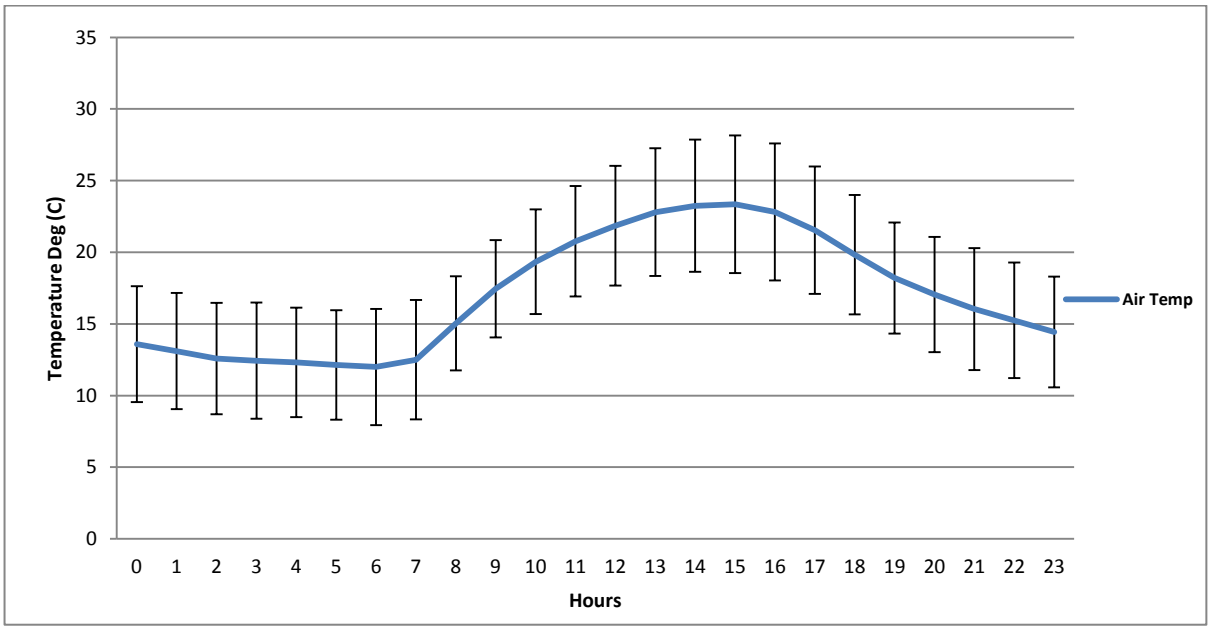

Mean and Standard Deviation of Air Temperature at Sabkha Site from 21/1/2011 to 28/2/2011.

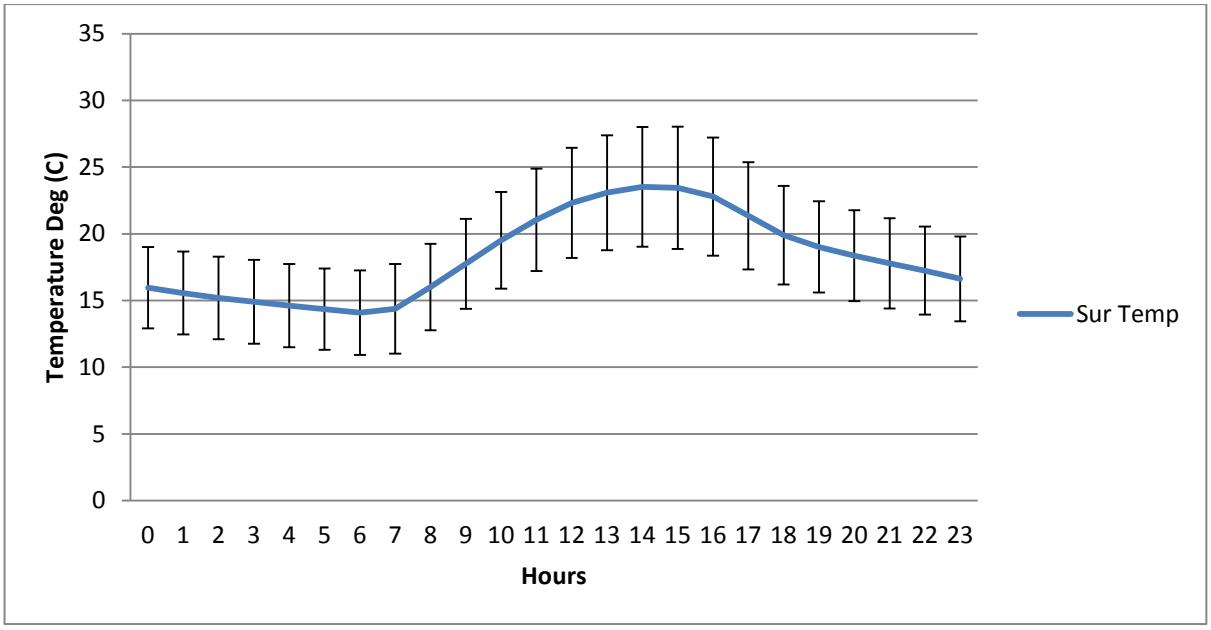

Mean and Standard Deviation of Surface Temperature at Sabkha Site from 21/1/2011 to 28/2/2011.

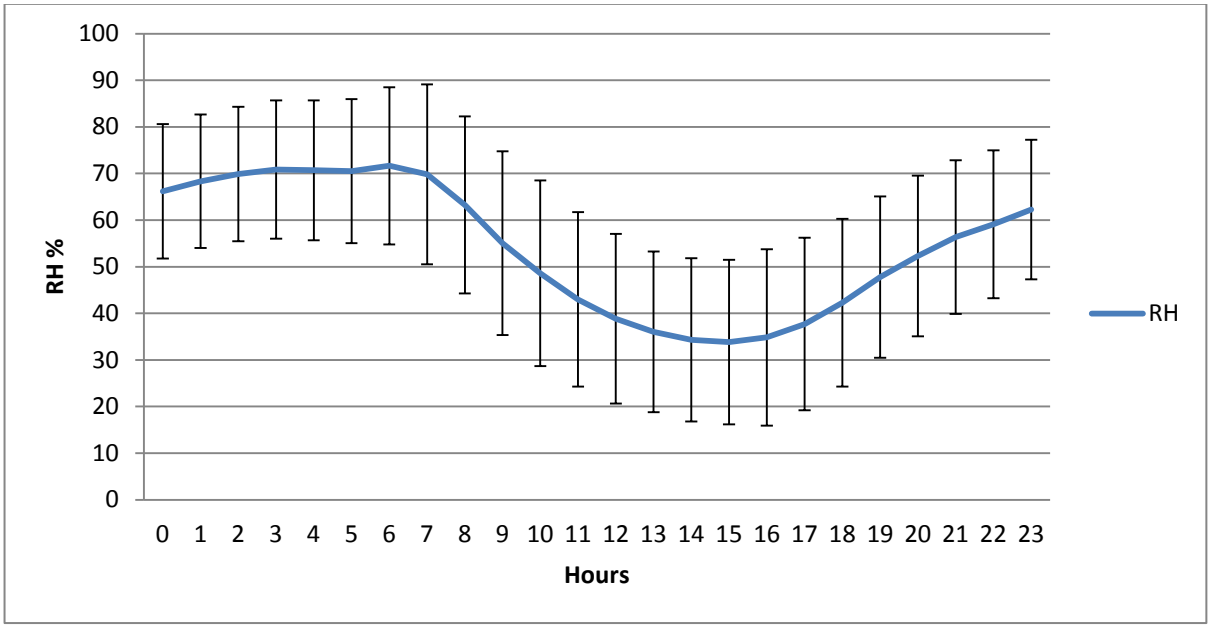

Mean and Standard Deviation of Relative Humidity at Sabkha Site from 21/1/2011 to 28/2/2011.

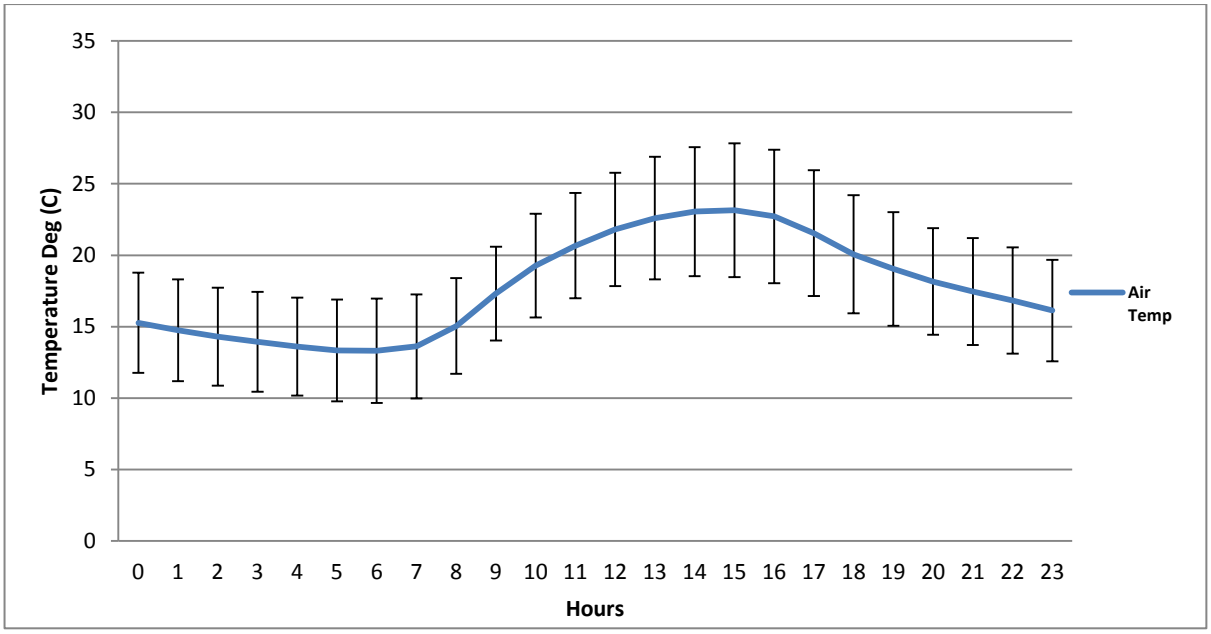

Mean and Standard Deviation of Air Temperature at Park Site from 21/1/2011 to 28/2/2011.

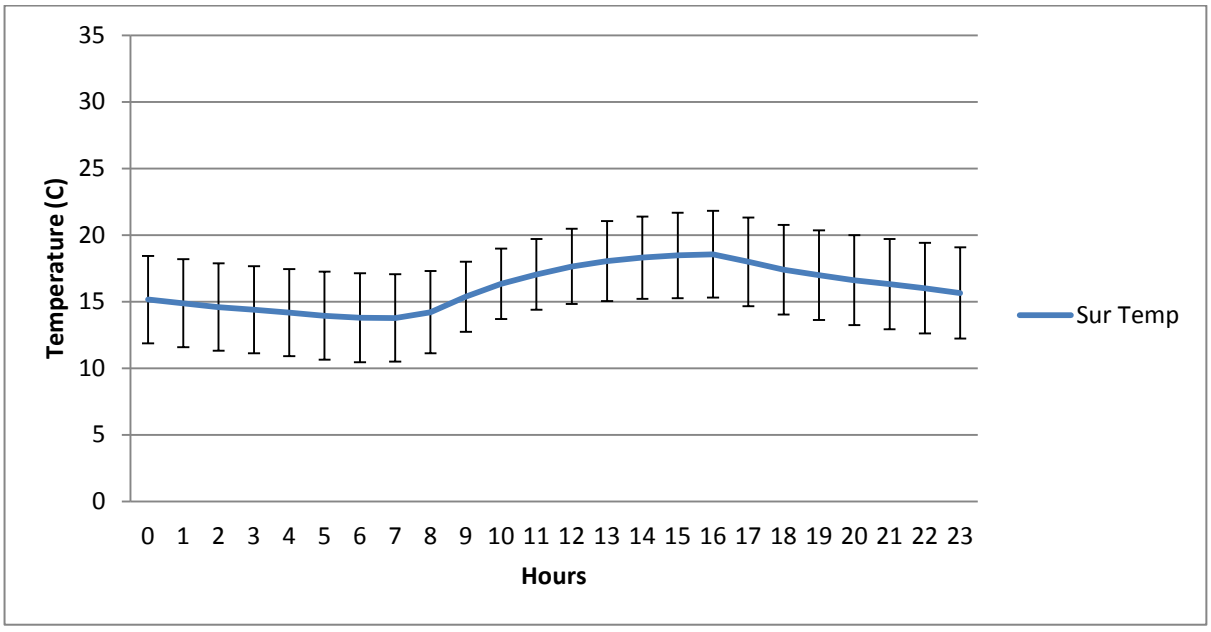

Mean and Standard Deviation of Surface Temperature at Park Site from 21/1/2011 to 28/2/2011.

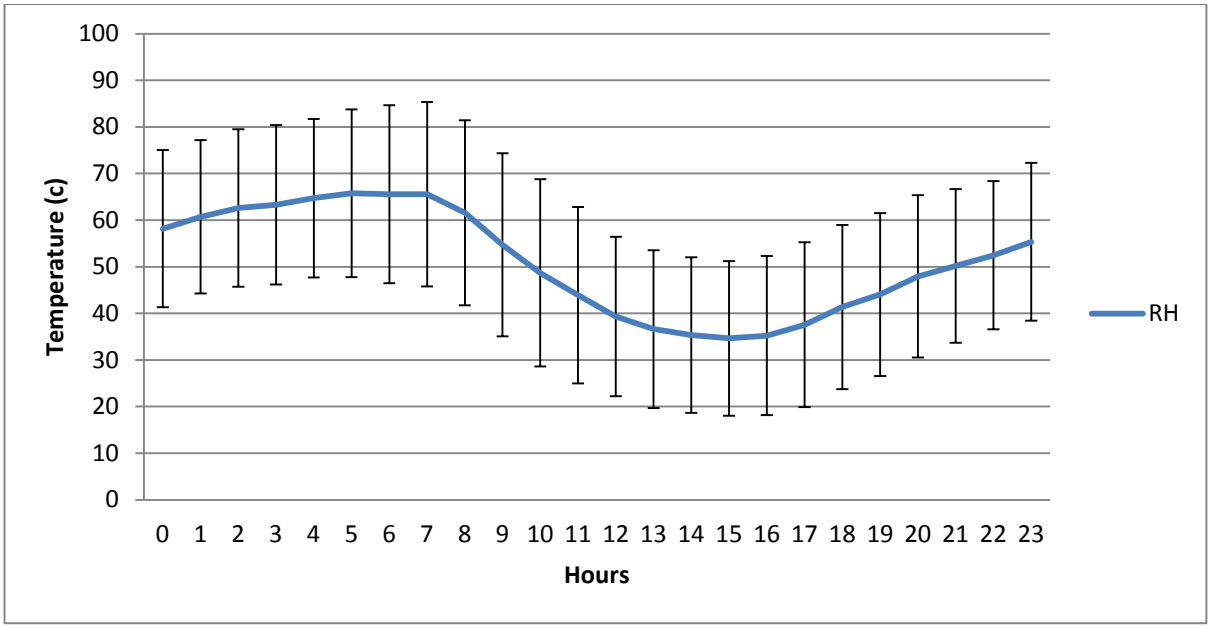

Mean and Standard Deviation of Relative Humidity at Park Site from 21/1/2011 to 28/2/2011.

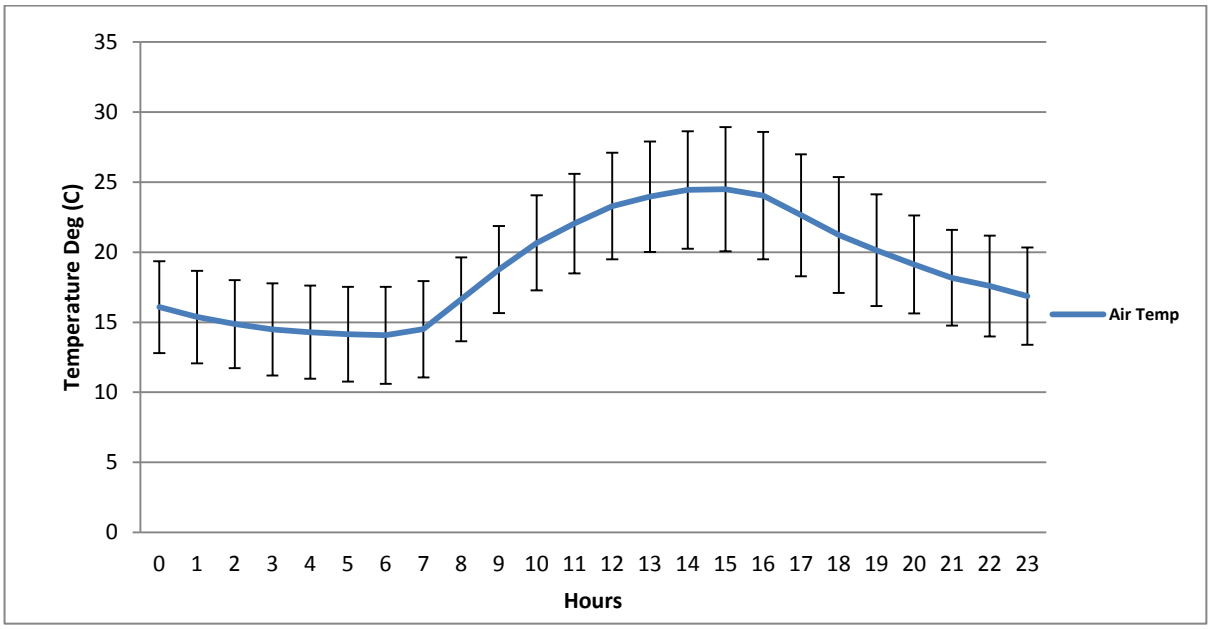

Mean and Standard Deviation of Air Temperature at Factory Site from 21/1/2011 to 28/2/2011.

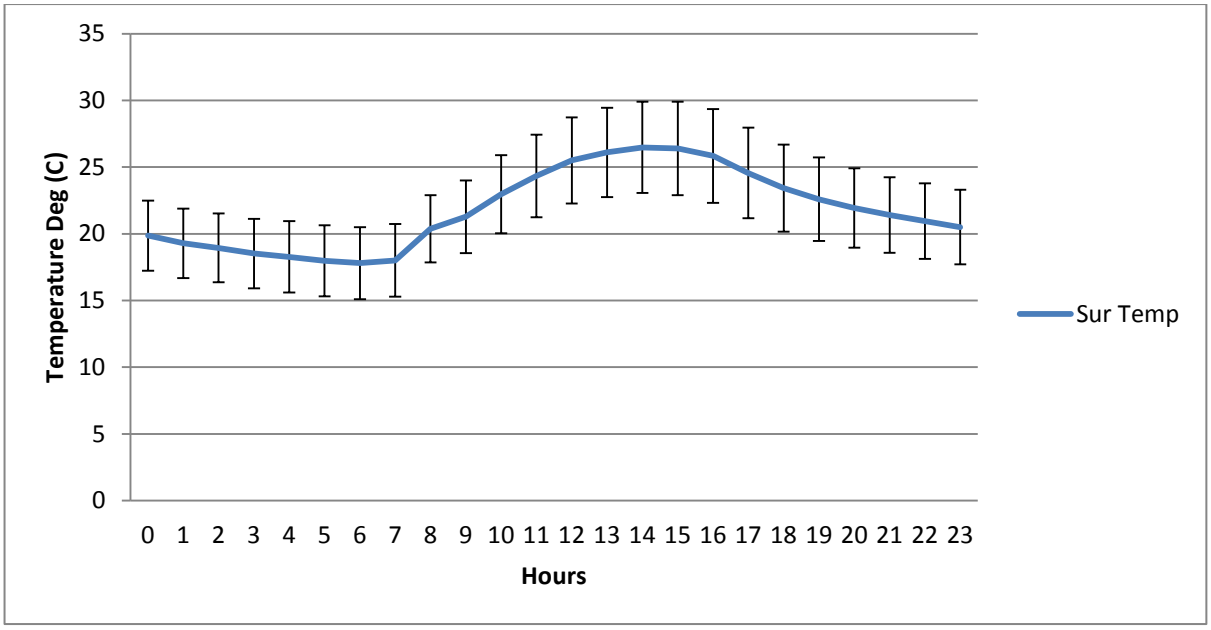

Mean and Standard Deviation of Surface Temperature at Factory Site from 21/1/2011 to 28/2/2011.

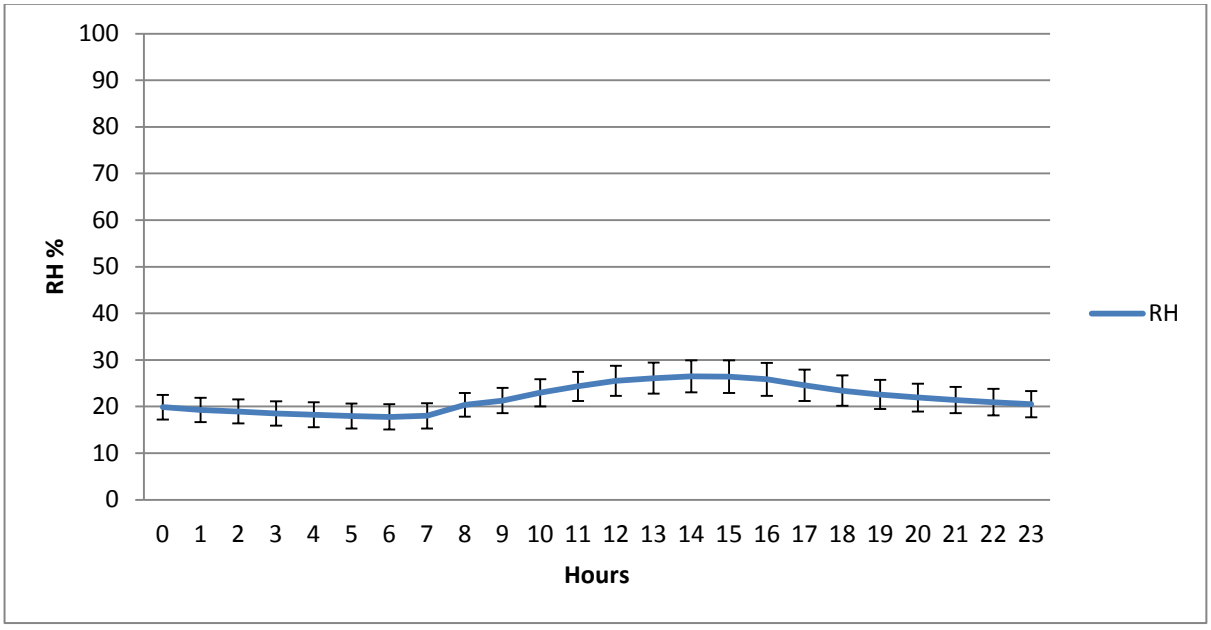

Mean and Standard Deviation of Relative Humidity at Factory Site from 21/1/2011 to 28/2/2011.

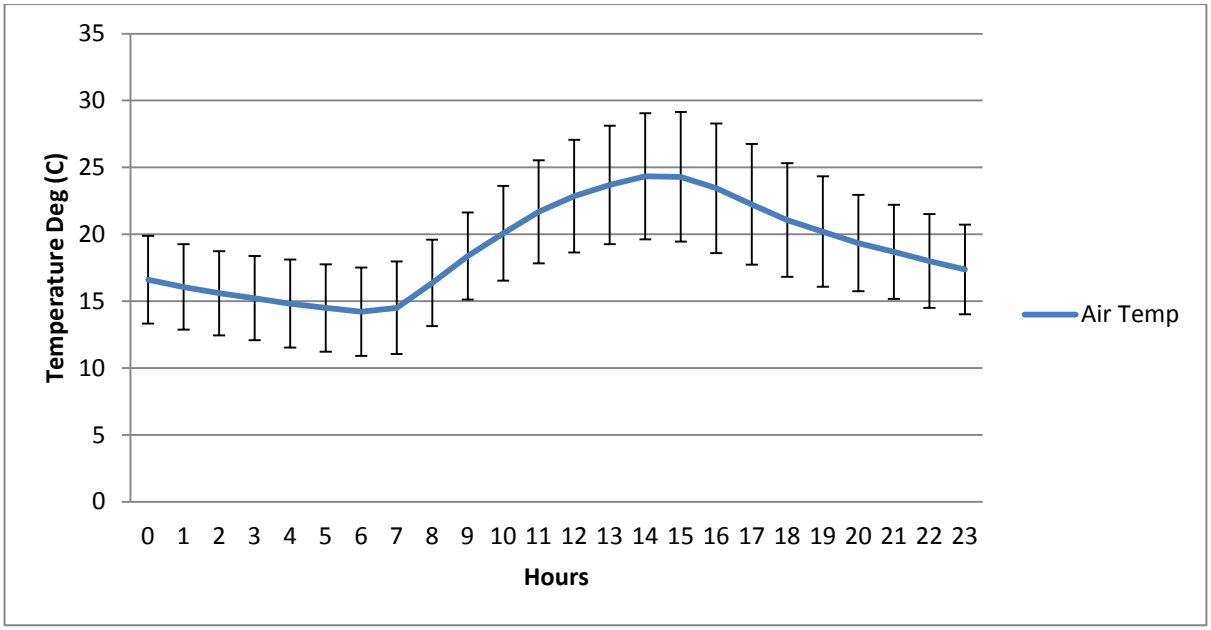

Mean and Standard Deviation of Air Temperature at City Centre Site from 21/1/2011 to 28/2/2011.

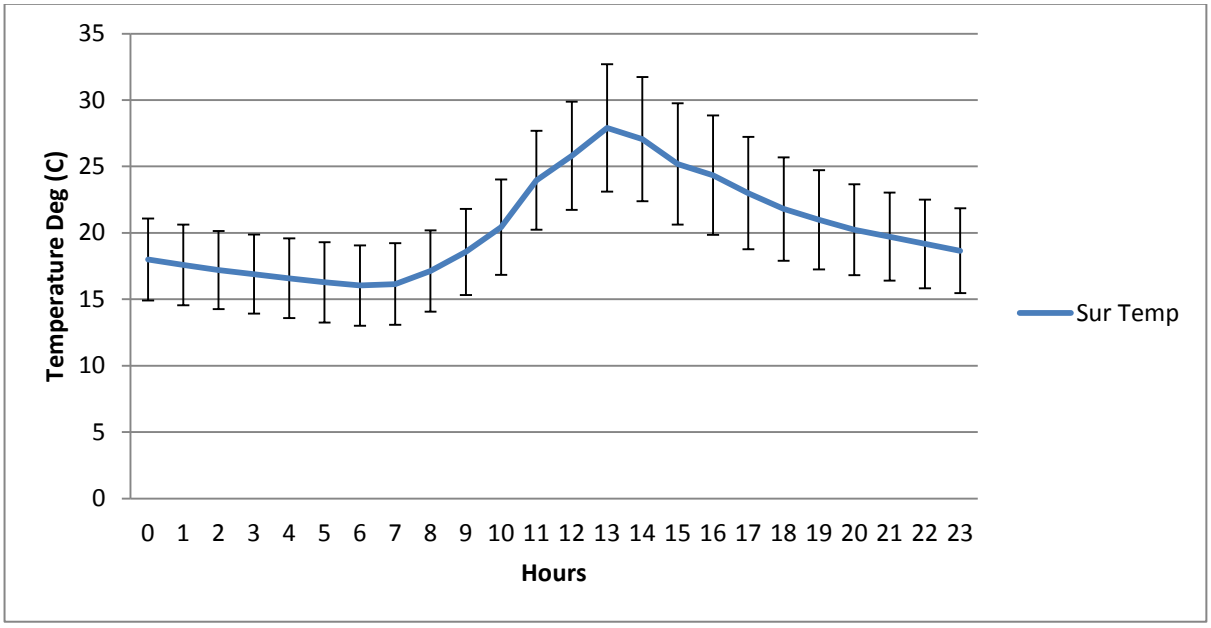

Mean and Standard Deviation of Surface Temperature at City Centre Site from 21/1/2011 to 28/2/2011.

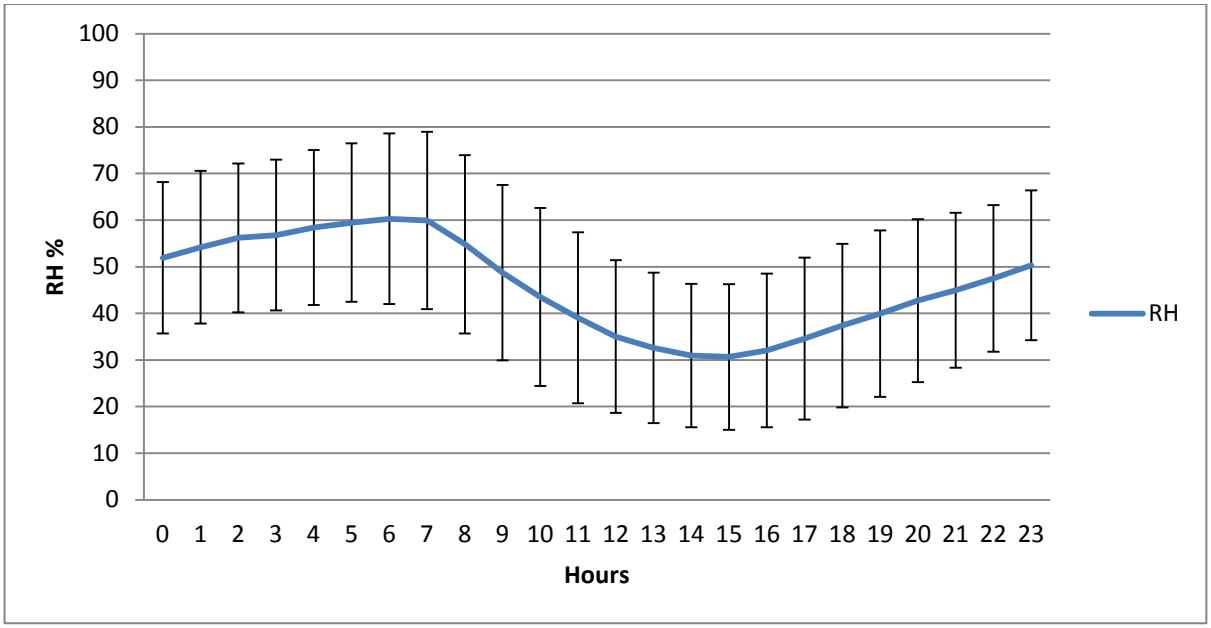

Mean and Standard Deviation of Relative Humidity at City Centre Site from 21/1/2011 to 28/2/2011.

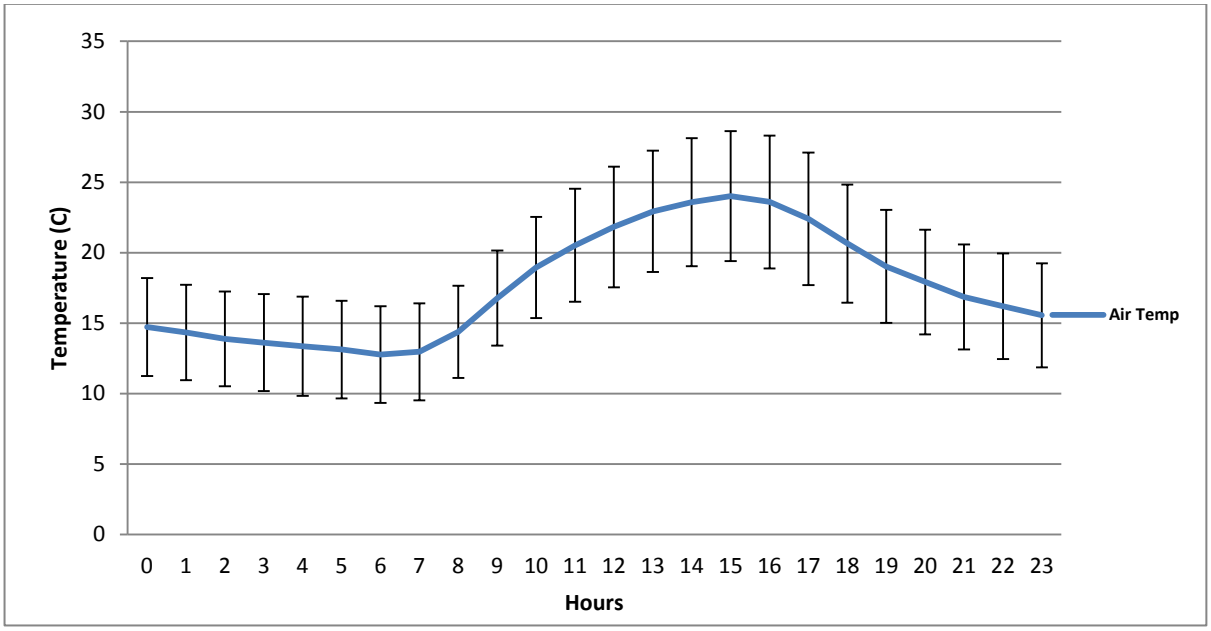

Mean and Standard Deviation of Air Temperature at Airport Weather Station 21/1/2011 to 28/2/2011.

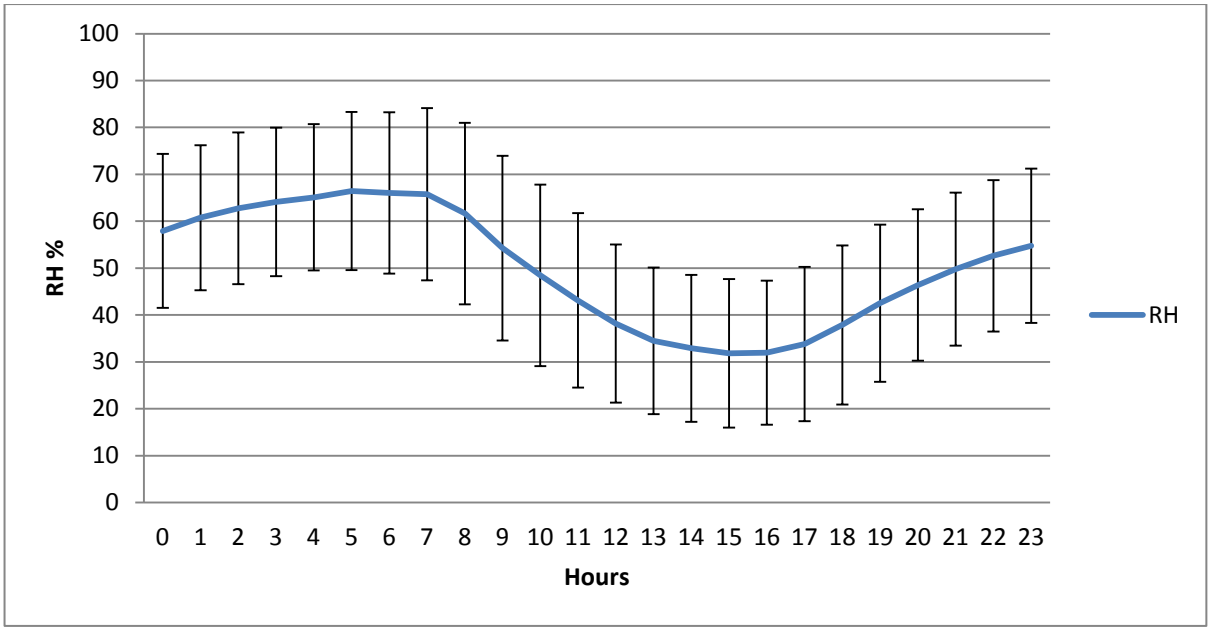

Mean and Standard Deviation of Relative Humidity at Airport Weather Station 21/1/2011 to 28/2/201

Appendix 4.2:

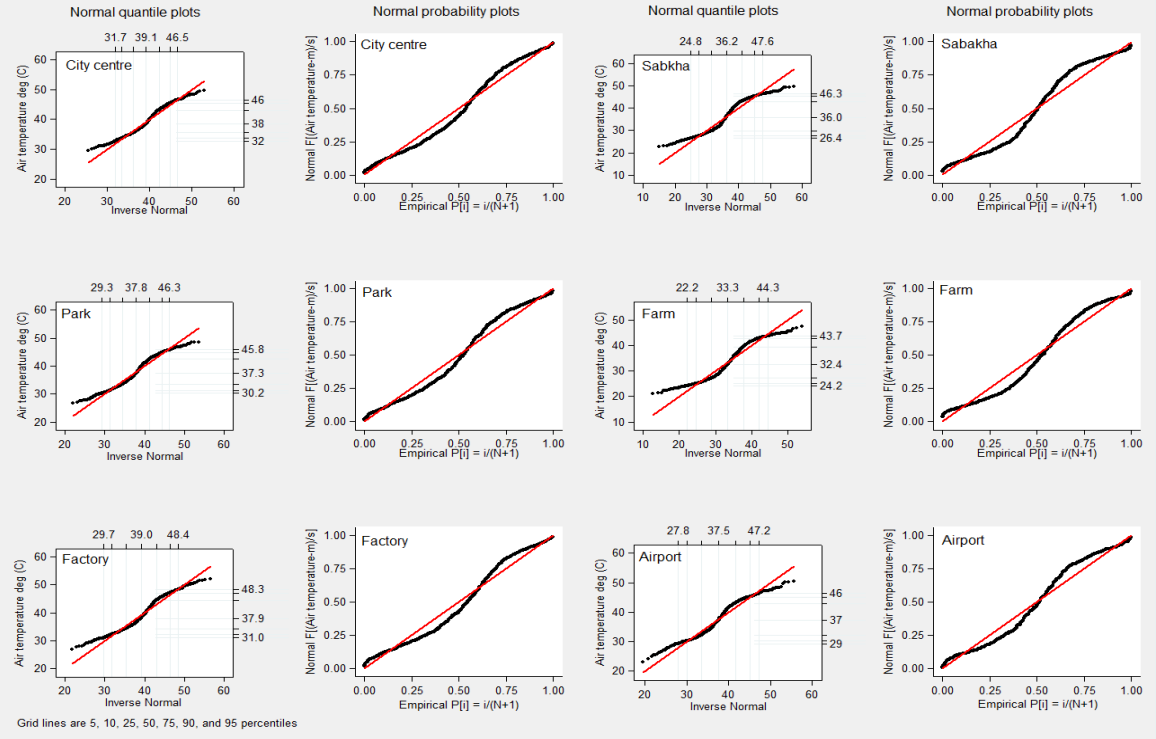

Quantile and probability distribution plots of air temperature (°C) during summer season (27 January 2011 to 31 August 2011) at different land use types.

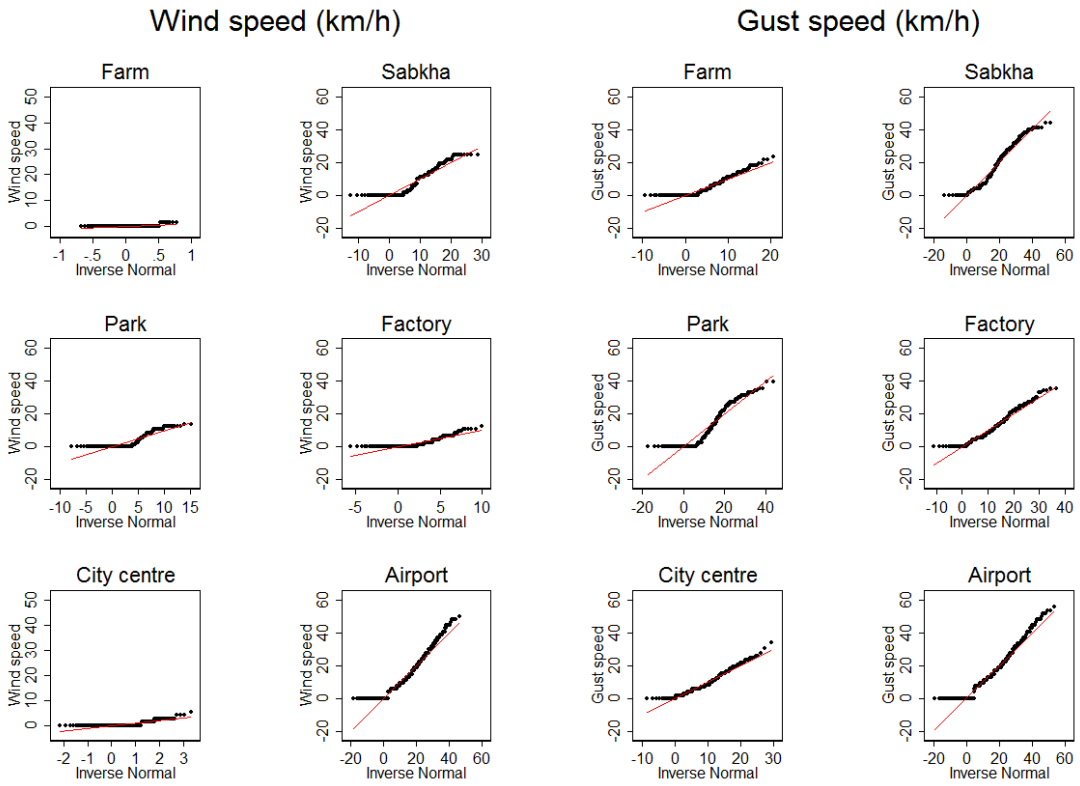

Quantile distribution plots of wind and gust speed (km/h) during summer (July and August 2011).

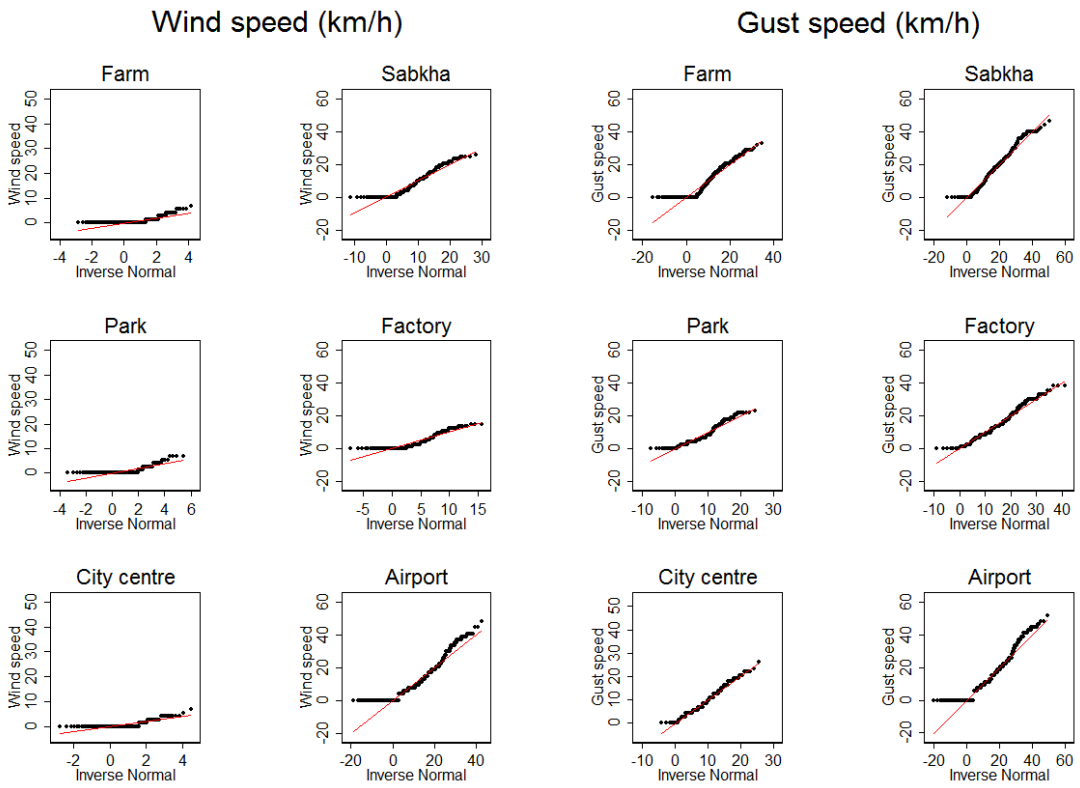

Quantile distribution plots of wind and gust speed (km/h) during winter (January and February 2011).

Appendix 4.3:

Results of Skewness/Kurtosis tests for normality (Air temperature (°C) during winter season) (21/01/2011 to 28/02/2011)

H_0 = Air temperature (°C) values in different land use have standard normal distribution

H_1 = Air temperature (°C) values in different land use does not have standard normal distribution

Variable	Obs	Pr (Skewness)	Pr (Kurtosis)	chi2 (2)	Prob>chi2
City centre	936	0.000	0.197	50.81	0.000
Sabkha	936	0.000	0.173	22.05	0.000
Park	936	0.000	0.667	31.69	0.000
Farm	936	0.003	0.002	18.50	0.000
Factory	936	0.000	0.199	29.27	0.000
Airport	936	0.000	0.683	40.13	0.000

Decision: Fail to accept null hypothesis at $P<0.05$ level. So, air temperature (°C) values in different land use have lack of normal distribution.

Kruskal–Wallis test for median comparison of air temperature (°C) among different land use types during winter (21/01/2011 to 28/02/2011) at $P\geq0.05$ level.

H_0 = Median values of air temperature (°C) in different land use are equal i.e. median (city centre) = median (sabkha) = median (park) = median (farm) = median (factory) = median (airport)

H_1 = Median values of air temperature (°C) in different land use are not equal or identical i.e. median (city centre) ≠ median (sabkha) ≠ median (park) ≠ median (farm) ≠ median (factory) ≠ median (airport)

Location	Observations	Rank sum
City centre	936	2.94e+06
Sabkha	936	2.44e+06
Park	936	2.64e+06
Farm	936	2.25e+06
Factory	936	2.93e+06
Airport	936	2.58e+06

λ^2 = 150.16 with (5) *d.f.* with P=0.0001
λ^2 with ties = 150.16 with (5) *d.f.* P=0.0001

Decision: Fail to accept H_0 at $P \geq 0.05$ level. So, significant difference exists in air temperature (°C) median values of at least one pair of land use types. To identify significant difference between groups from possible pairs, need to perform further post-hoc test on median comparison between different land use groups.

Results of Kruskal–Wallis test of air temperature during winter season between each two land use.

H_0 = between different land uses within a pair have identical distributions i.e. median values air temperature (°C) in different land use are equal or identical. For example, median air temperature (°C) of city centre = median air temperature (°C) of sabkha with respect to adjusted P' value less than (<) 0.0033

H_1 = between different land uses within a pair have different distributions i.e. median values air temperature (°C) in different land use are not equal. For example, median air temperature (°C) of city centre ≠ median air temperature (°C) of sabkha with respect to adjusted P' value greater than (>) 0.0033

Land use	City centre	Sabkha	Park	Farm	Factory	Airport
City centre						
Sabkha	≠ (0.000)					
Park	≠ (0.000)	= **(0.003)**				
Farm	≠ (0.000)	= **(0.007)**	≠ (0.000)			
Factory	= **(0.852)**	≠ (0.000)	≠ (0.000)	≠ (0.000)		
Airport	≠ (0.000)	= **(0.033)**	= **(0.384)**	≠ (0.000)	≠ (0.000)	

Note: '≠' indicates significant difference (fail to reject - H_1), '=' indicates insignificant difference (fail to reject – H_0) and values in paransethesis indicates calculated P values.

Adjusted probability (P'):

$$P' = \frac{P}{K(K-1)/2}$$

where, P =0.05 and K is the number of groups in sample. So, P' = 0.0033 @ K = 6 (no. of land use = 6)

Results of Skewness/Kurtosis tests for normality (Air temperature (°C) during summer season (26/07/2011 to 31/08/2011)

H_0 = Air temperature (°C) values in different land use have standard normal distribution

H_1 = Air temperature (°C) values in different land use does not have standard normal distribution

Variable	Obs	Pr (Skewness)	Pr (Kurtosis)	chi2 (2)	Prob>chi2
City centre	888	0.031	0.000	263.04	0.000
Sabkha	888	0.678	.	.	.
Park	888	0.329	0.000	552.79	0.000
Farm	888	0.020	0.000	3543.58	0.000
Factory	888	0.002	0.000	335.31	0.000
Airport	888	0.662	0.000	800.34	0.000

Decision: Fail to accept null hypothesis at $P<0.05$ level. So, air temperature (°C) values in different land use have lack of normal distribution.

Kruskal–Wallis test for median comparison of air temperature (°C) among different land use types during summer (26/07/2011 to 31/08/2011) at $P\geq0.05$ level.

H_0 = Median values of air temperature (°C) in different land use are equal i.e. median (city centre) = median (sabkha) = median (park) = median (farm) = median (factory) = median (airport)

H_1 = Median values of air temperature (°C) in different land use are not equal or identical i.e. median (city centre) ≠ median (sabkha) ≠ median (park) ≠ median (farm) ≠ median (factory) ≠ median (airport)

Location	Observations	Rank sum
City centre	888	2.80e+06
Sabkha	888	2.17e+06
Park	888	2.48e+06
Farm	888	1.59e+06
Factory	888	2.74e+06
Airport	888	2.42e+06

λ^2= 471.726 with (5) *d.f.* P=0.0001
λ^2 with ties = 471.727 with (5) *d.f.* P=0.0001

Decision: Fail to accept H_0 at $P\geq0.05$ level. So, significant difference exists in air temperature (°C) median values of at least one pair of land use types. To identify significant difference

between groups from possible pairs, need to perform further post-hoc test on median comparison between different land use groups.

Results of Kruskal–Wallis test of air temperature during summer season between each two land use.

H_0 = between different land uses within a pair have identical distributions i.e. median values air temperature (°C) in different land use are equal or identical. For example, median air temperature (°C) of city centre = median air temperature (°C) of sabkha with respect to adjusted P' value less than (<) 0.0033

H_1 = between different land uses within a pair have different distributions i.e. median values air temperature (°C) in different land use are not equal. For example, median air temperature (°C) of city centre ≠ median air temperature (°C) of sabkha with respect to adjusted P' value greater than (>) 0.0033

Land use	City centre	Sabkha	Park	Farm	Factory	Airport
City centre						
Sabkha	≠ (0.000)					
Park	≠ (0.000)	≠ (0.000)				
Farm	≠ (0.000)	≠ (0.000)	≠ (0.000)	≠ (0.000)		
Factory	= **(0.262)**	≠ (0.000)	≠ (0.000)	≠ (0.000)		
Airport	≠ (0.000)	≠ (0.000)	= **(0.281)**	≠ (0.000)	≠ (0.000)	

Note: '≠' indicates significant difference (fail to reject - H_1), '=' indicates insignificant difference (fail to reject – H_0) and values in paransethesis indicates calculated P values.

Adjusted probability (P'):

$$P' = \frac{P}{K(K-1)/2}$$

where, P =0.05 and K is the number of groups in sample. So, P' = 0.0033 @ K = 6 (no. of land use = 6)

Results of Skewness/Kurtosis tests for normality (surface temperature (°C) during winter season) (21/01/2011 to 28/02/2011)

H_0 = Surface temperature (°C) values in different land use have standard normal distribution

H_1 = Surface temperature (°C) values in different land use does not have standard normal distribution

Variable	Obs	Pr (Skewness)	Pr (Kurtosis)	chi2 (2)	Prob>chi2
City centre	936	0.000	0.5265	65.31	0.000
Sabkha	936	0.000	0.0772	63.03	0.000
Park	936	0.084	0.0000	40.92	0.000
Farm	936	0.000	0.0225	19.58	0.000
Factory	936	0.000	0.0216	33.19	0.000

Decision: Fail to accept null hypothesis at $P<0.05$ level. So, surface temperature (°C) values in different land use have lack of normal distribution.

Kruskal–Wallis test for median comparison of surface temperature (°C) among different land use types during winter (21/01/2011 to 28/02/2011) at $P\geq0.05$ level.

H_0 = Median values of surface temperature (°C) in different land use are equal i.e. median (city centre) = median (sabkha) = median (park) = median (farm) = median (factory) = median (airport)

H_1 = Median values of surface temperature (°C) in different land use are not equal or identical i.e. median (city centre) ≠ median (sabkha) ≠ median (park) ≠ median (farm) ≠ median (factory) ≠ median (airport)

Location	Observations	Rank sum
City centre	936	2.64e+06
Sabkha	936	2.13e+06
Park	936	1.57e+06
Farm	936	1.52e+06
Factory	936	3.10e+06

λ^2= 1100.003 with (4) *d.f.* P=0.0001
λ^2 with ties = 1100.008 with (4) *d.f.* P=0.0001

Decision: Fail to accept H_0 at $P\geq0.05$ level. So, significant difference exists in surface temperature (°C) median values of at least one pair of land use types. To identify significant difference between groups from possible pairs, need to perform further post-hoc test on median comparison between different land use groups.

Results of Kruskal–Wallis test of surface temperature during winter season between each two land use.

H_0 = between different land uses within a pair have identical distributions i.e. median values surface temperature (°C) in different land use are equal or identical. For example, median surface temperature (°C) of city centre = median surface temperature (°C) of sabkha with respect to adjusted P' value less than (<) 0.005

H_1 = between different land uses within a pair have different distributions i.e. median values surface temperature (°C) in different land use are not equal. For example, median surface temperature (°C) of city centre ≠ median surface temperature (°C) of sabkha with respect to adjusted P' value greater than (>) 0.005

Land use	**City centre**	**Sabkha**	**Park**	**Farm**	**Factory**
City centre					
Sabkha	≠ (0.000)				
Park	≠ (0.000)	≠ (0.000)			
Farm	≠ (0.000)	≠ (0.000)	= **(0.360)**		
Factory	≠ (0.000)	≠ (0.000)	≠ (0.000)	≠ (0.000)	

Note: '≠' indicates significant difference (fail to reject - H_1), '=' indicates insignificant difference (fail to reject – H_0) and values in paransethesis indicates calculated P values.

Adjusted probability (P'):

$$P' = \frac{P}{K(K-1)/2}$$

where, P =0.05 and K is the number of groups in sample. So, P' = 0.005 @ K = 5 (no. of land use = 5)

Results of Skewness/Kurtosis tests for normality (Surface temperature (°C) during summer season) (26/07/2011 to 31/08/2011)

H_0 = Surface temperature (°C) values in different land use have standard normal distribution

H_1 = Surface temperature (°C) values in different land use does not have standard normal distribution

Variable	Obs	Pr (Skewness)	Pr (Kurtosis)	chi2 (2)	Prob>chi2
City centre	888	0.002	0.000	268.44	0.000
Sabkha	888	0.046	0.000	4346.91	0.000
Park	888	0.002	0.000	397.29	0.000
Farm	888	0.408	0.000	91.55	0.000
factory	888	0.000	0.469	52.03	0.000

Decision: Fail to accept null hypothesis at $P<0.05$ level. So, surface temperature (°C) values in different land use have lack of normal distribution.

Kruskal–Wallis test for median comparison of surface temperature (°C) among different land use types during summer (26/07/2011 to 31/08/2011) at $P\geq0.05$ level.

H_0 = Median values of surface temperature (°C) in different land use are equal i.e. median (city centre) = median (sabkha) = median (park) = median (farm) = median (factory) = median (airport)

H_1 = Median values of surface temperature (°C) in different land use are not equal or identical i.e. median (city centre) ≠ median (sabkha) ≠ median (park) ≠ median (farm) ≠ median (factory) ≠ median (airport)

Location	Observations	Rank sum
City centre	888	2.82e+06
Sabkha	888	2.05e+06
Park	888	1.78e+06
Farm	888	733627.00
Factory	888	2.47e+06

λ^2= 1743.199 with (4) *d.f.* P=0.0001
λ^2 with ties = 1743.204 with (4) *d.f.* P=0.0001

Decision: Fail to accept H_0 at $P\geq0.05$ level. So, significant difference exists in surface temperature (°C) median values of at least one pair of land use types. To identify significant difference between groups from possible pairs, need to perform further post-hoc test on median comparison between different land use groups.

Results of Kruskal–Wallis test of surface temperature during summer season between each two land use.

H_0 = between different land uses within a pair have identical distributions i.e. median values surface temperature (°C) in different land use are equal or identical. For example, median surface temperature (°C) of city centre = median surface temperature (°C) of sabkha with respect to adjusted P' value less than (<) 0.005

H_1 = between different land uses within a pair have different distributions i.e. median values surface temperature (°C) in different land use are not equal. For example, median surface temperature (°C) of city centre ≠ median surface temperature (°C) of sabkha with respect to adjusted P' value greater than (>) 0.005

Land use	**City centre**	**Sabkha**	**Park**	**Farm**	**Factory**
City centre					
Sabkha	≠ (0.000)				
Park	≠ (0.000)	≠ (0.000)			
Farm	≠ (0.000)	≠ (0.000)	≠ (0.000)		
Factory	≠ (0.000)	≠ (0.000)	≠ (0.000)	≠ (0.000)	

Note: '≠' indicates significant difference (fail to reject - H_1), '=' indicates insignificant difference (fail to reject – H_0) and values in paransethesis indicates calculated P values.

Adjusted probability (P'):

$$P' = \frac{P}{K(K-1)/2}$$

where, P =0.05 and K is the number of groups in sample. So, P' = 0.005 @ K = 5 (no. of land use = 5)

Results of Skewness/Kurtosis tests for normality (relative humidity (%) during winter season) (21/01/2011 to 28/02/2011)

H_0 = relative humidity (%) values in different land use have standard normal distribution

H_1 = relative humidity (%) values in different land use does not have standard normal distribution

Variable	Obs	Pr (Skewness)	Pr (Kurtosis)	chi2 (2)	Prob>chi2
City centre	936	0.000	0.000	84.86	0.000
Sabkha	936	0.838	0.000	366.01	0.000
Park	936	0.000	0.000	118.74	0.000
Farm	936	0.087	0.000	946.43	0.000
Factory	936	0.000	0.022	33.19	0.000
Airport	936	0.001	0.000	186.13	0.000

Decision: Fail to accept null hypothesis at $P<0.05$ level. So, relative humidity (%) values in different land use have lack of normal distribution.

Kruskal–Wallis test for median comparison of relative humidity (%) among different land use types during winter (21/01/2011 to 28/02/2011) at $P\geq0.05$ level.

H_0 = Median values of relative humidity (%) in different land use are equal i.e. median (city centre) = median (sabkha) = median (park) = median (farm) = median (factory) = median (airport)

H_1 = Median values of relative humidity (%) in different land use are not equal or identical i.e. median (city centre) ≠ median (sabkha) ≠ median (park) ≠ median (farm) ≠ median (factory) ≠ median (airport)

Location	Observations	Rank sum
City centre	936	2.58e+06
Sabkha	936	3.10e+06
Park	936	2.92e+06
Farm	936	3.62e+06
Factory	936	703541.00
Airport	936	2.85e+06

λ^2= 2052.331 with (5) *d.f.* P=0.0001
λ^2 with ties = 2052.340 with (5) *d.f.* P<0.0001

Decision: Fail to accept H_0 at $P\geq0.05$ level. So, significant difference exists in relative humidity (%) median values of at least one pair of land use types. To identify significant difference between groups from possible pairs, need to perform further post-hoc test on median comparison between different land use groups.

Results of Kruskal–Wallis test of relative humidity during winter season between each two land use.

H_0 = between different land uses within a pair have identical distributions i.e. median values relative humidity (%) in different land use are equal or identical. For example, median relative humidity of city centre = median relative humidity (%) of sabkha with respect to adjusted P' value less than (<) 0.0033

H_1 = between different land uses within a pair have different distributions i.e. median values relative humidity (%) in different land use are not equal. For example, median relative humidity of city centre ≠ median relative humidity of sabkha with respect to adjusted P' value greater than (>) 0.0033

Land use	**City centre**	**Sabkha**	**Park**	**Farm**	**Factory**	**Airport**
City centre						
Sabkha	≠ (0.000)					
Park	≠ (0.000)	≠ (0.000)				
Farm	≠ (0.000)	≠ (0.000)	≠ (0.000)			
Factory	≠ (0.000)	≠ (0.000)	≠ (0.000)	≠ (0.000)		
Airport	≠ (0.000)	≠ (0.000)	= **(0.371)**	≠ (0.000)	≠ (0.000)	

Note: '≠' indicates significant difference (fail to reject - H_1), '=' indicates insignificant difference (fail to reject – H_0) and values in paransethesis indicates calculated P values.

Adjusted probability (P'):

$$P' = \frac{P}{K(K-1)/2}$$

where, P =0.05 and K is the number of groups in sample. So, P' = 0.0033 @ K = 6 (no. of land use = 6)

Results of Skewness/Kurtosis tests for normality (relative humidity (%) during summer season) (26/07/2011 to 31/08/2011)

H_0 = relative humidity (%) values in different land use have standard normal distribution

H_1 = relative humidity (%) values in different land use does not have standard normal distribution

Variable	Obs	Pr (Skewness)	Pr (Kurtosis)	chi2 (2)	Prob>chi2
City centre	888	0.000	0.000	278.52	0.000
Sabkha	888	0.000	0.269	99.31	0.000
Park	888	0.000	0.000	236.13	0.000
Farm	888	0.001	0.000	226.07	0.000
Factory	888	0.000	0.000	257.42	0.000
Airport	888	0.000	0.000	276.38	0.000

Decision: Fail to accept null hypothesis at $P<0.05$ level. So, relative humidity (%) values in different land use have lack of normal distribution.

Kruskal–Wallis test for median comparison of relative humidity (%) among different land use types during summer (26/07/2011 to 31/08/2011) at $P\geq0.05$ level.

H_0 = Median values of relative humidity (%) in different land use are equal i.e. median (city centre) = median (sabkha) = median (park) = median (farm) = median (factory) = median (airport)

H_1 = Median values of relative humidity (%) in different land use are not equal or identical i.e. median (city centre) ≠ median (sabkha) ≠ median (park) ≠ median (farm) ≠ median (factory) ≠ median (airport)

Location	Observations	Rank sum
City centre	888	2.09e+06
Sabkha	888	2.59e+06
Park	888	2.15e+06
Farm	888	3.44e+06
Factory	888	2.04e+06
Airport	888	1.89e+06

λ^2= 793.541 with (5) *d.f.* P=0.0001
λ^2 with ties = 793.559 with (5) *d.f.* P=0.0001

Decision: Fail to accept H_0 at $P\geq0.05$ level. So, significant difference exists in relative humidity (%) median values of at least one pair of land use types. To identify significant difference between groups from possible pairs, need to perform further post-hoc test on median comparison between different land use groups.

Results of Kruskal–Wallis test of relative humidity during summer season between each two land use

H_0 = between different land uses within a pair have identical distributions i.e. median values relative humidity (%) in different land use are equal or identical. For example, median relative humidity (%) of city centre = median relative humidity (%) of sabkha with respect to adjusted P' value less than (<) 0.0033

H_1 = between different land uses within a pair have different distributions i.e. median values relative humidity (%) in different land use are not equal. For example, median relative humidity of city centre ≠ median relative humidity of sabkha with respect to adjusted P' value greater than (>) 0.0033

Land use	**City centre**	**Sabkha**	**Park**	**Farm**	**Factory**	**Airport**
City centre						
Sabkha	≠ (0.000)					
Park	= **(0.483)**	≠ (0.000)				
Farm	≠ (0.000)	≠ (0.000)	≠ (0.000)			
Factory	= **(0.278)**	≠ (0.000)	= **(0.085)**	≠ (0.000)		
Airport	≠ (0.000)	≠ (0.000)	≠ (0.000)	≠ (0.000)	≠ (0.000)	

Note: '≠' indicates significant difference (fail to reject - H_1), '=' indicates insignificant difference (fail to reject – H_0) and values in paransethesis indicates calculated P values.

Adjusted probability (P'):

$$P' = \frac{P}{K(K-1)/2}$$

where, P =0.05 and K is the number of groups in sample. So, P' = 0.0033 @ K = 6 (no. of land use = 6)

Appendix 5.1:

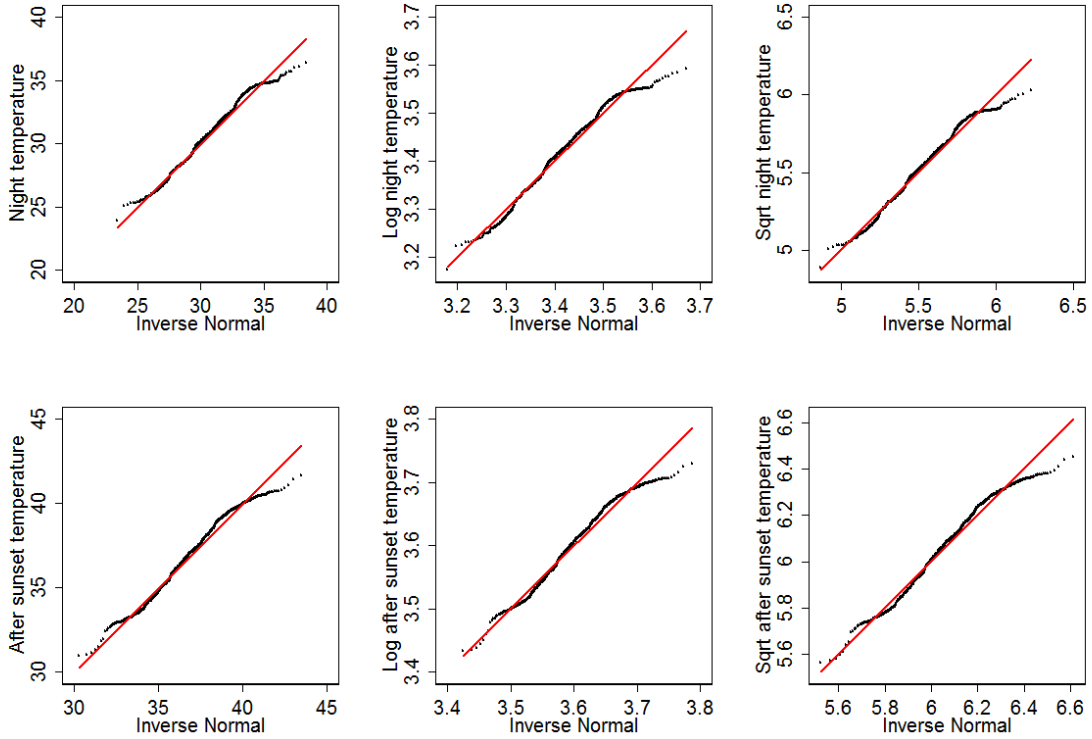

Quantile distribution plots of air temperature (°C) during winter traverses at night and after sunset. Original data left, log temperature in the middle, and square root transformation of air temperature right.

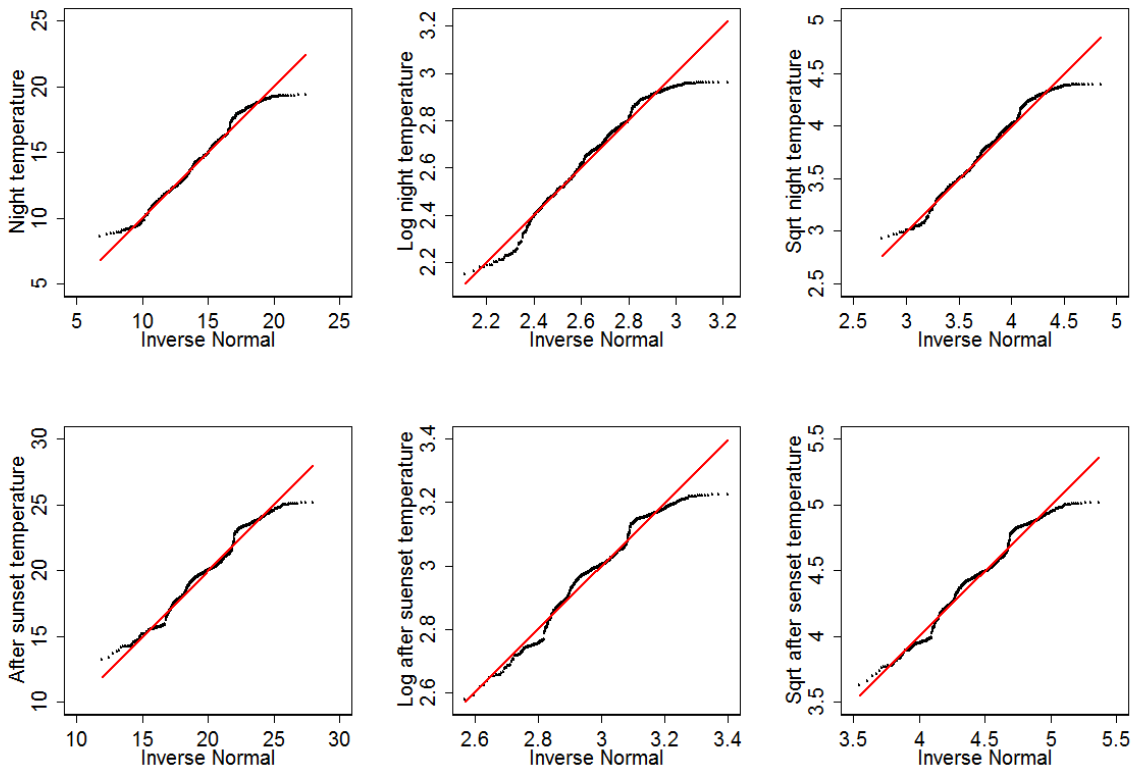

Quantile distribution plots of air temperature (°C) during summer traverses at night and after sunset. Original data left, log temperature in the middle, and square root transformation of air temperature right.

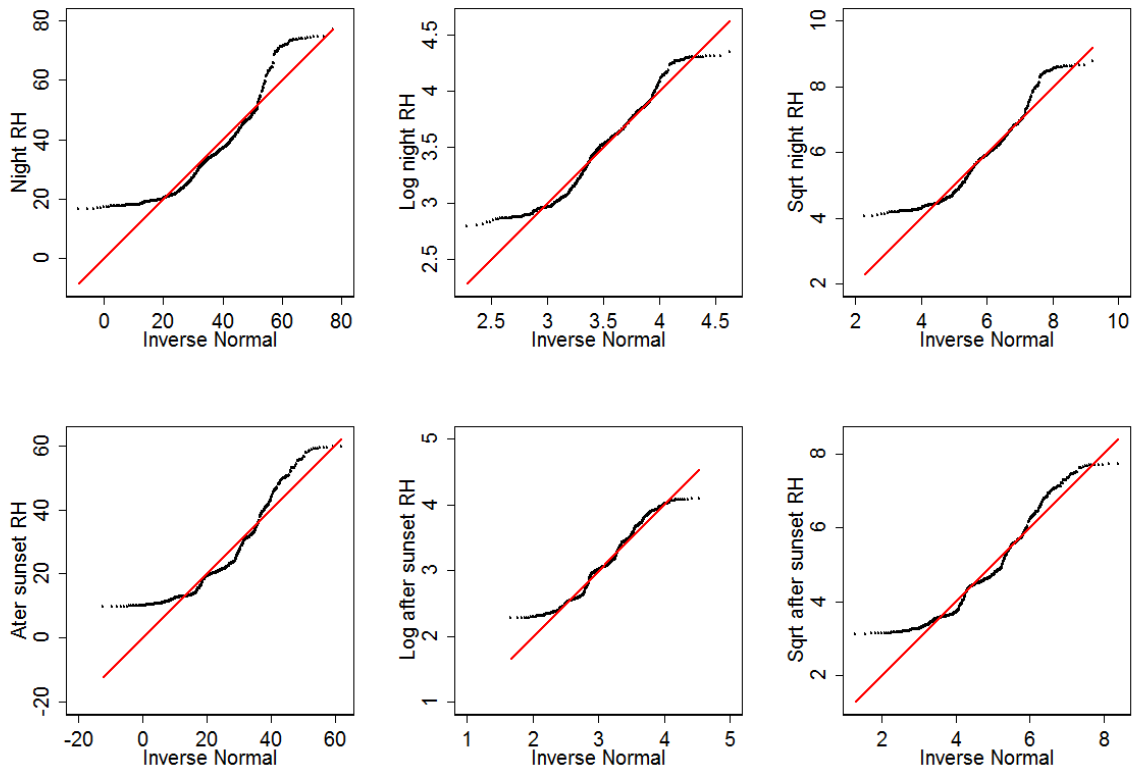

Quantile distribution plots of relative humidity (%) during winter traverses at night and after sunset. Original data left, log temperature in the middle, and square root transformation of air temperature right.

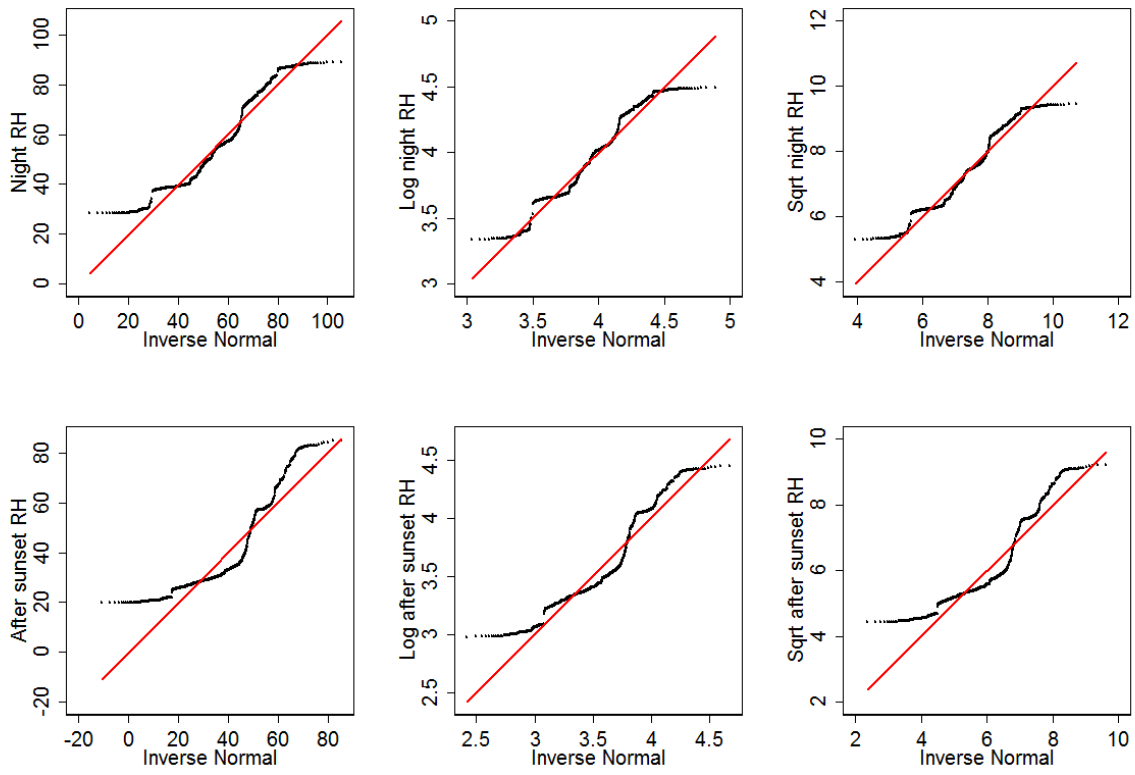

Quantile distribution plots of Relative humidity (%) during summer traverses at night and after sunset. Original data left, log temperature in the middle, and square root transformation of air temperature right.

Appendix 5.2:

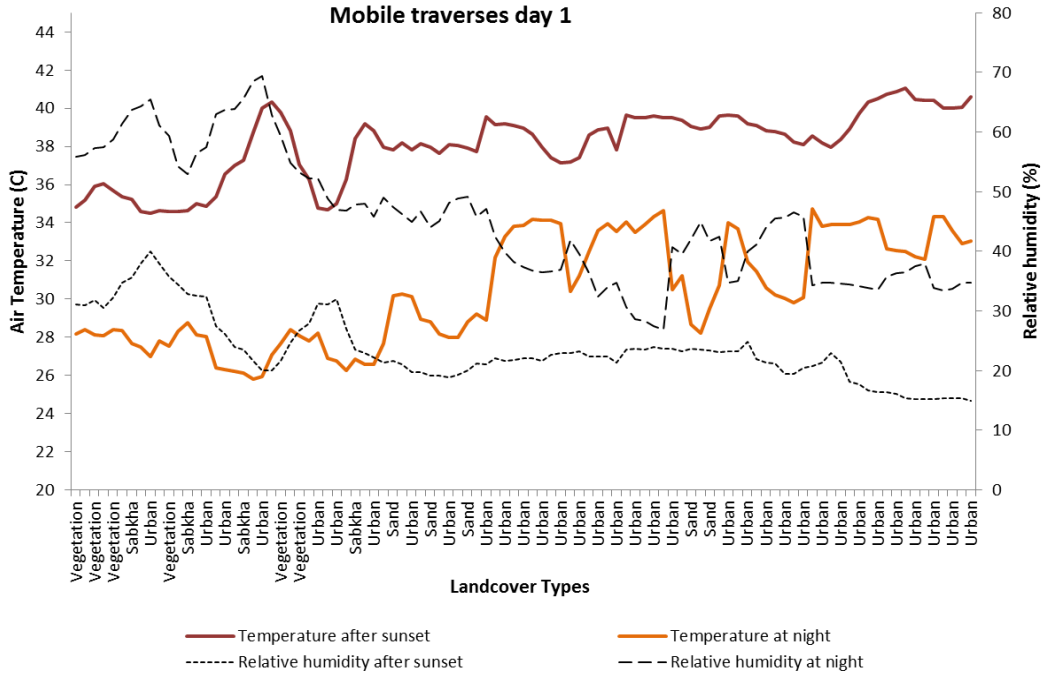

The relation between air temperature, relative humidity, and land cover types during summer season August 2011 (Mobile traverses day 1).

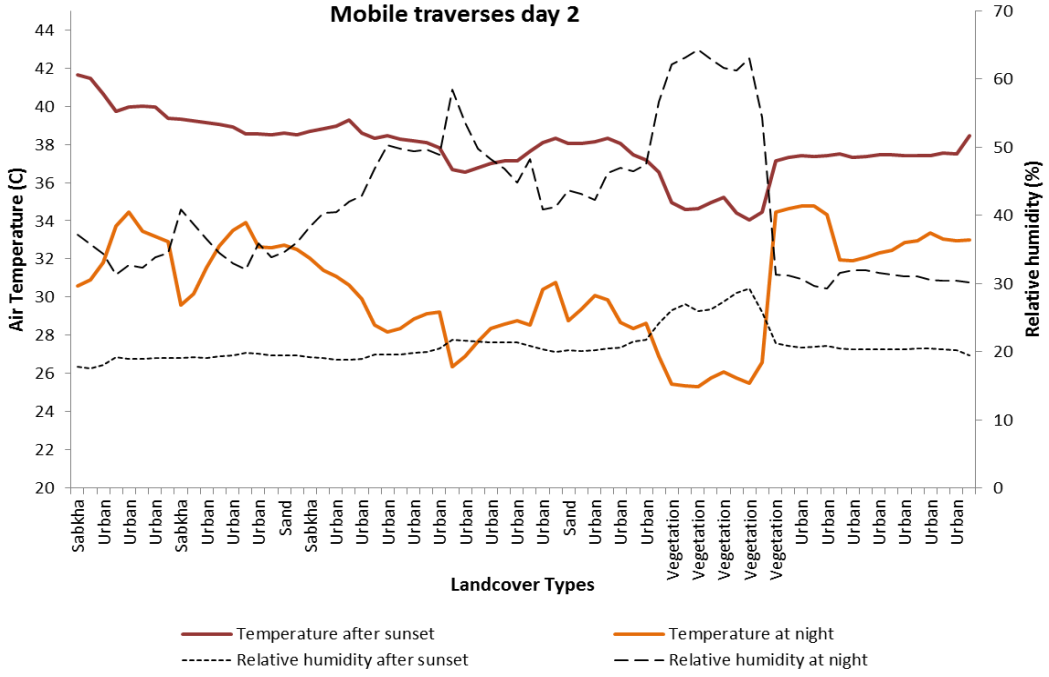

The relation between air temperature, relative humidity, and land cover types during summer season August 2011 (Mobile traverses day 2).

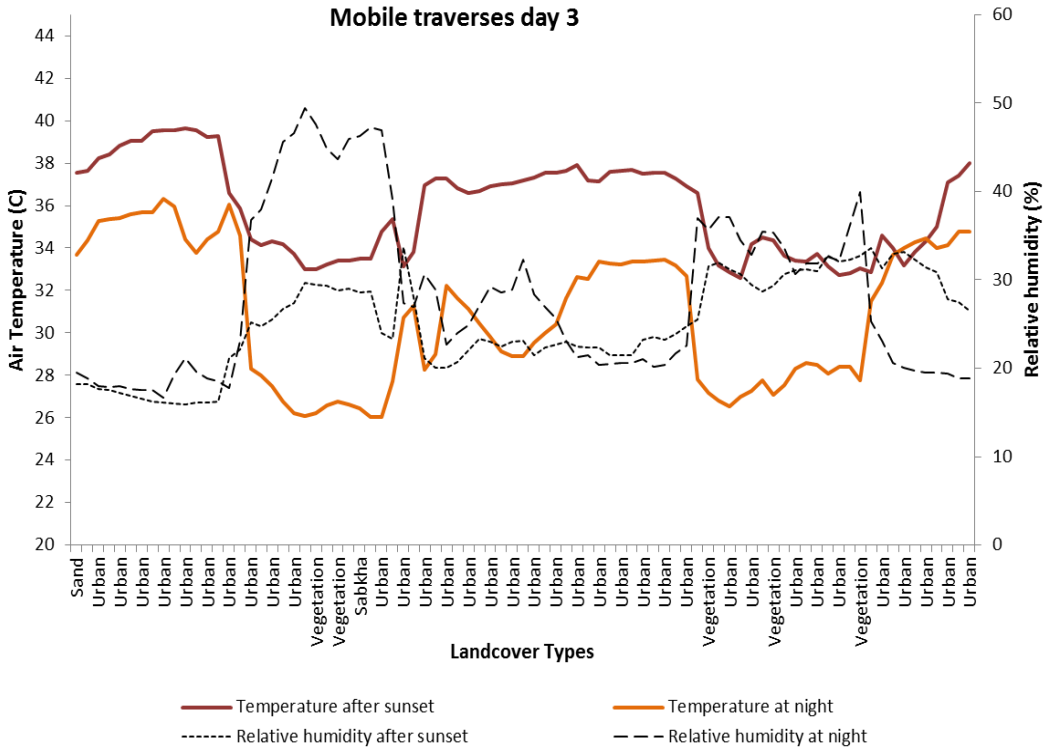

The relation between air temperature, relative humidity, and land cover types during summer season August 2011 (Mobile traverses day 3).

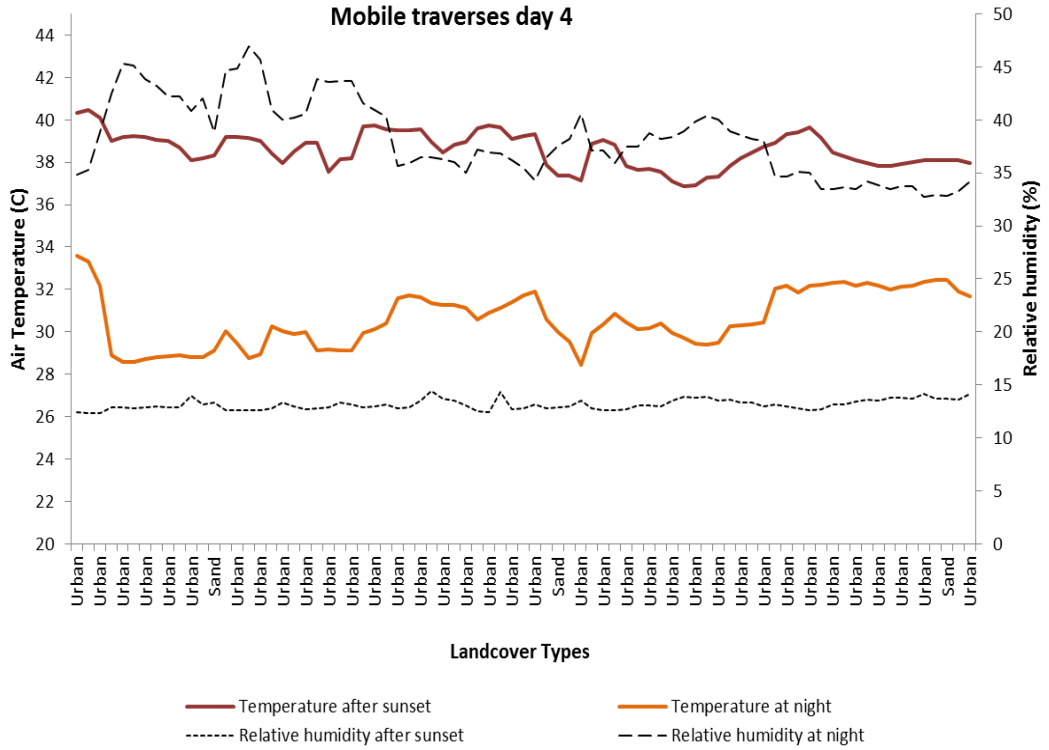

The relation between air temperature, relative humidity, and land cover types during summer season August 2011 (Mobile traverses day 4).

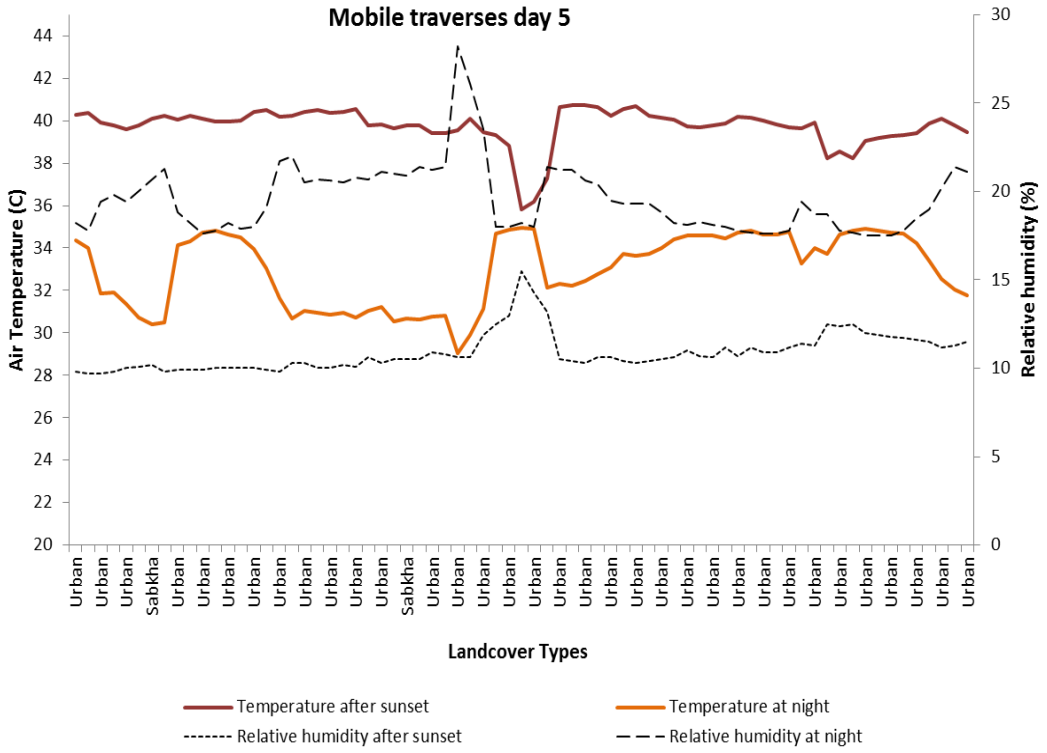

The relation between air temperature, relative humidity, and land cover types during summer season August 2011 (Mobile traverses day 5).

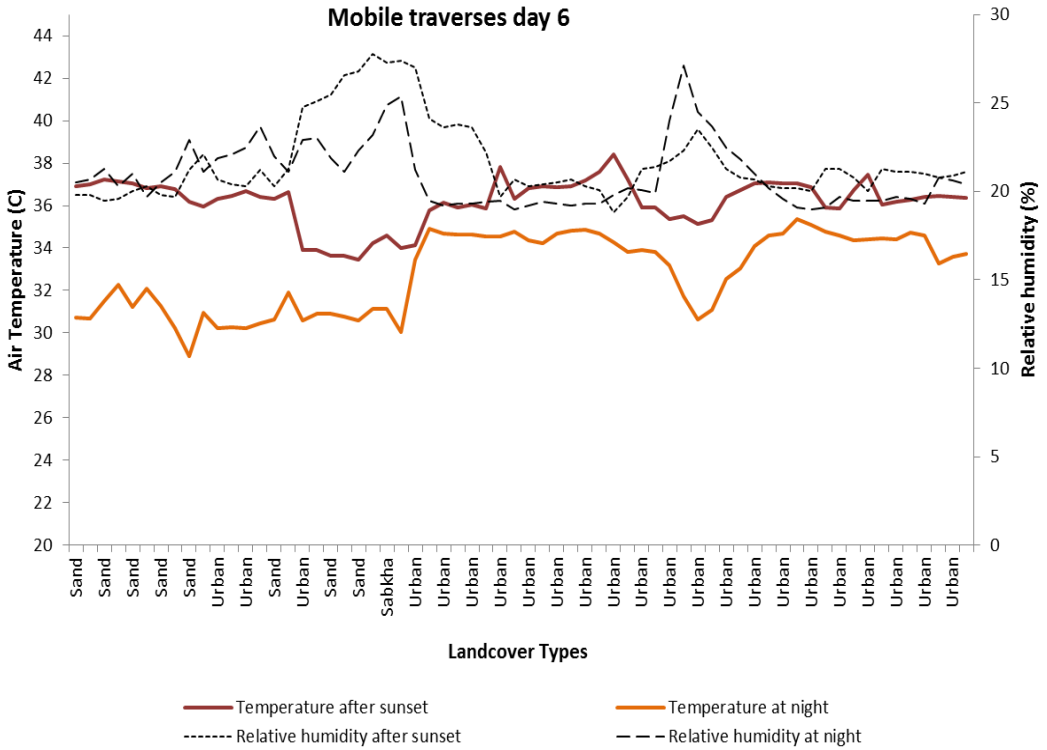

The relation between air temperature, relative humidity, and land cover types during summer season August 2011 (Mobile traverses day 6).

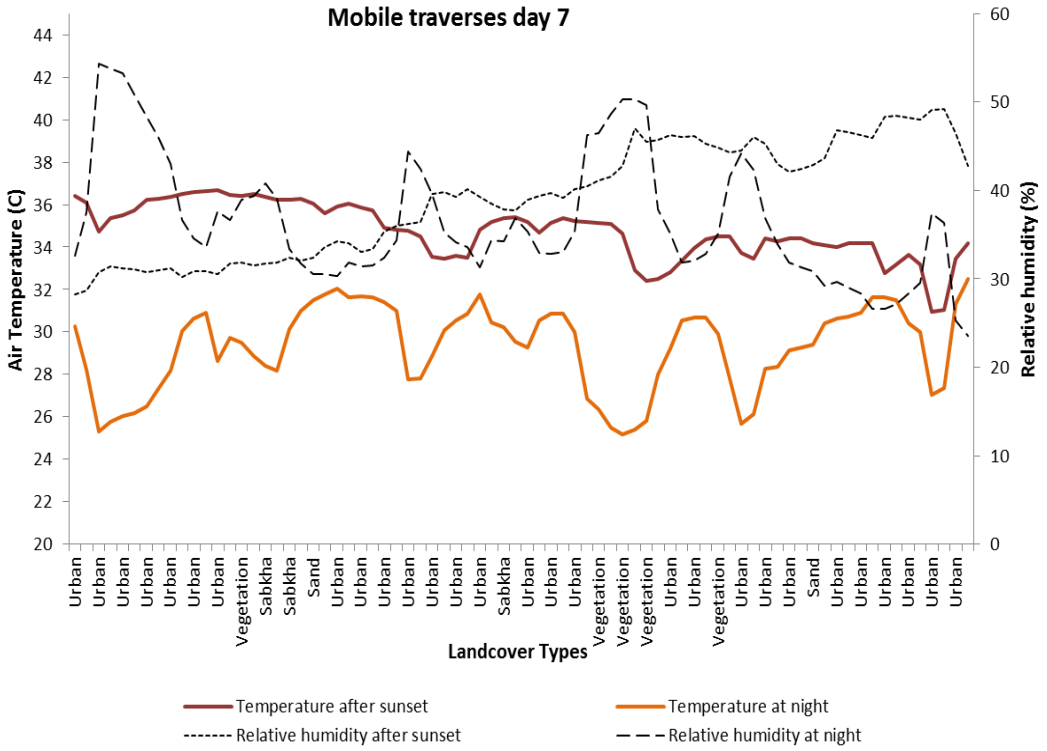

The relation between air temperature, relative humidity, and land cover types during summer season August 2011 (Mobile traverses day 7).

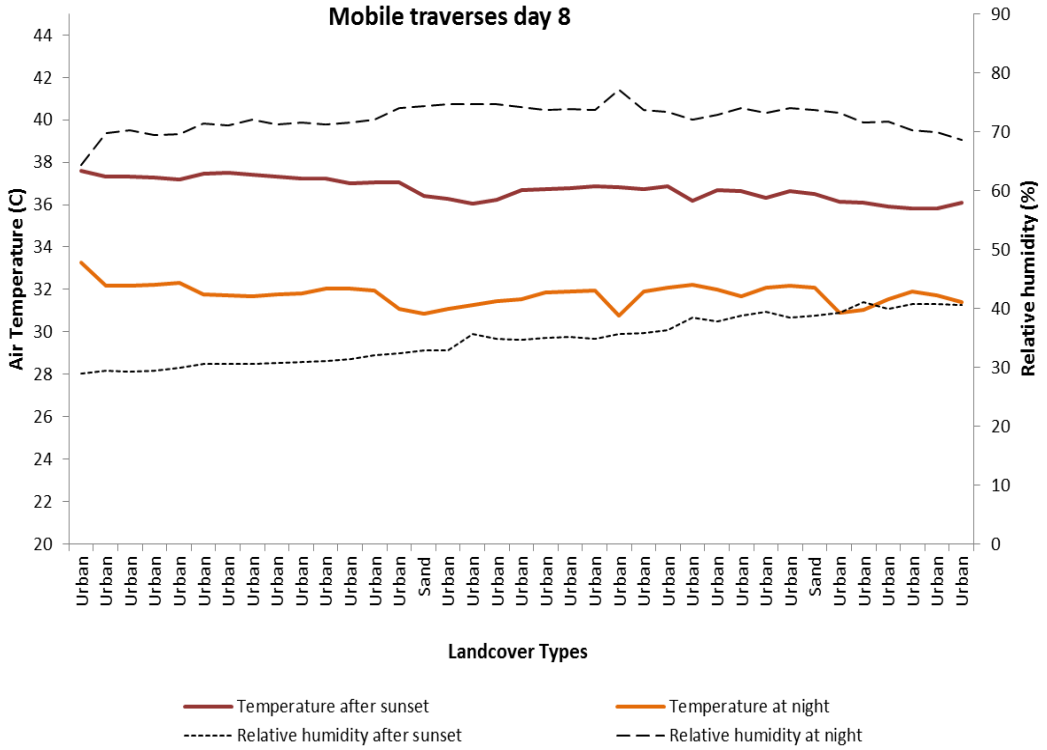

The relation between air temperature, relative humidity, and land cover types during summer season August 2011 (Mobile traverses day 8).

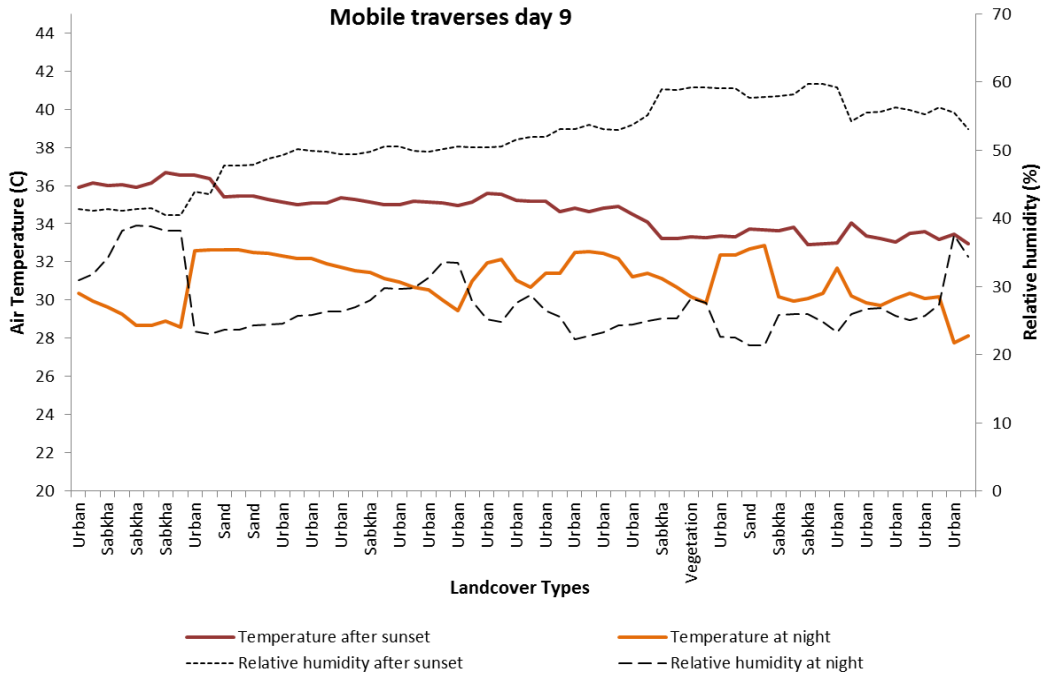

The relation between air temperature, relative humidity, and land cover types during summer season August 2011 (Mobile traverses day 9).

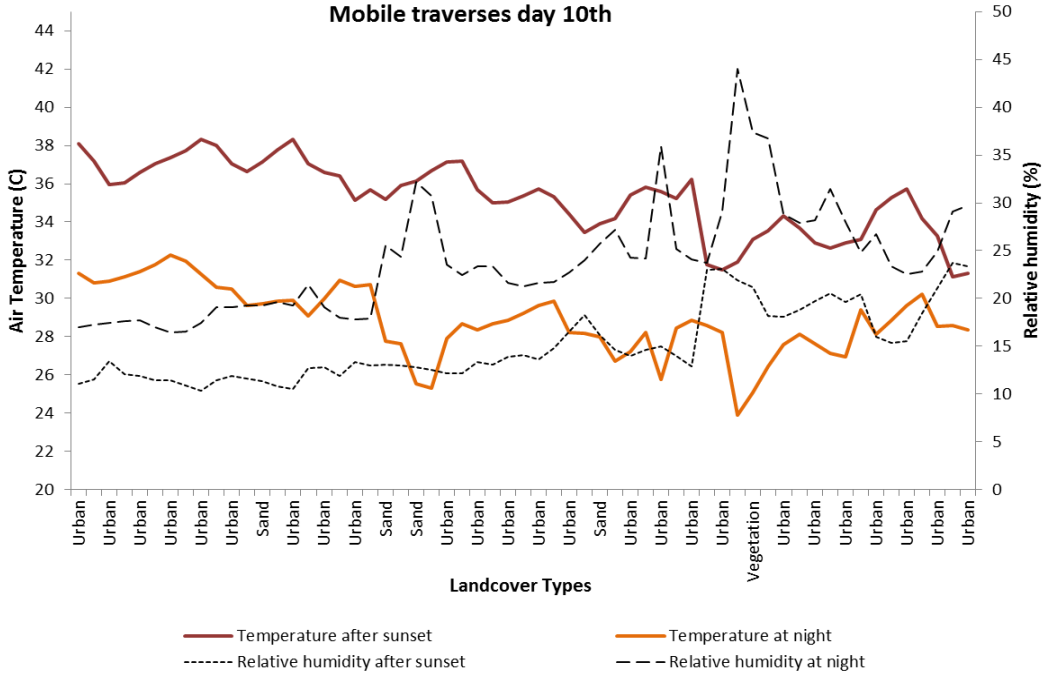

The relation between air temperature, relative humidity, and land cover types during summer season August 2011 (Mobile traverses day 10).

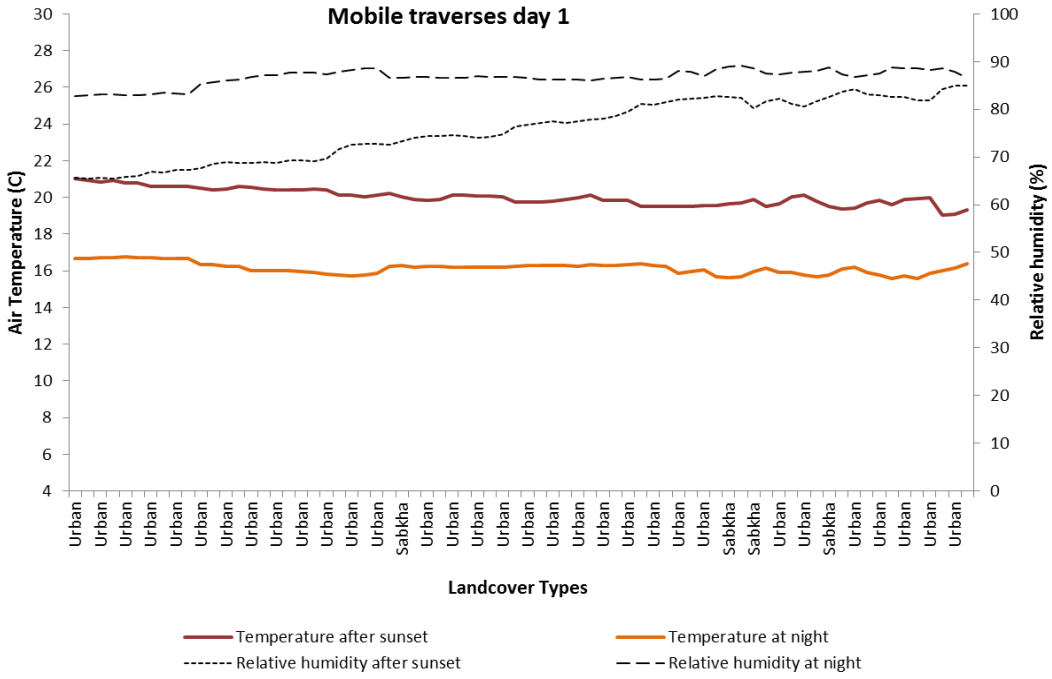

The relation between air temperature, relative humidity, and land cover types during winter season February 2011 (Mobile traverses day 1).

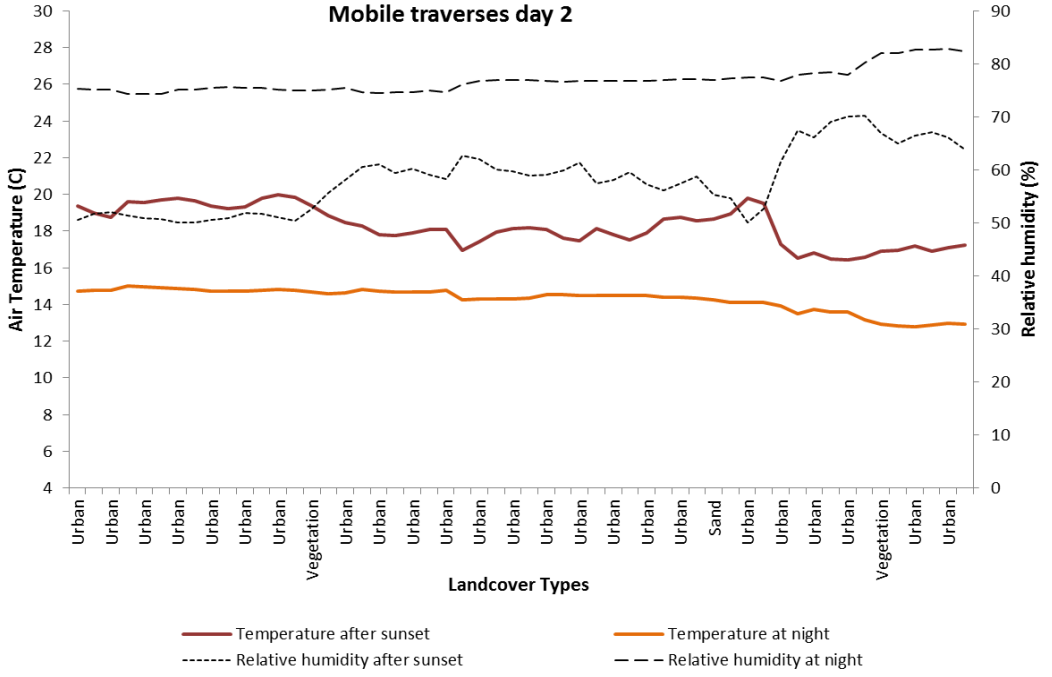

The relation between air temperature, relative humidity, and land cover types during winter season February 2011 (Mobile traverses day 2).

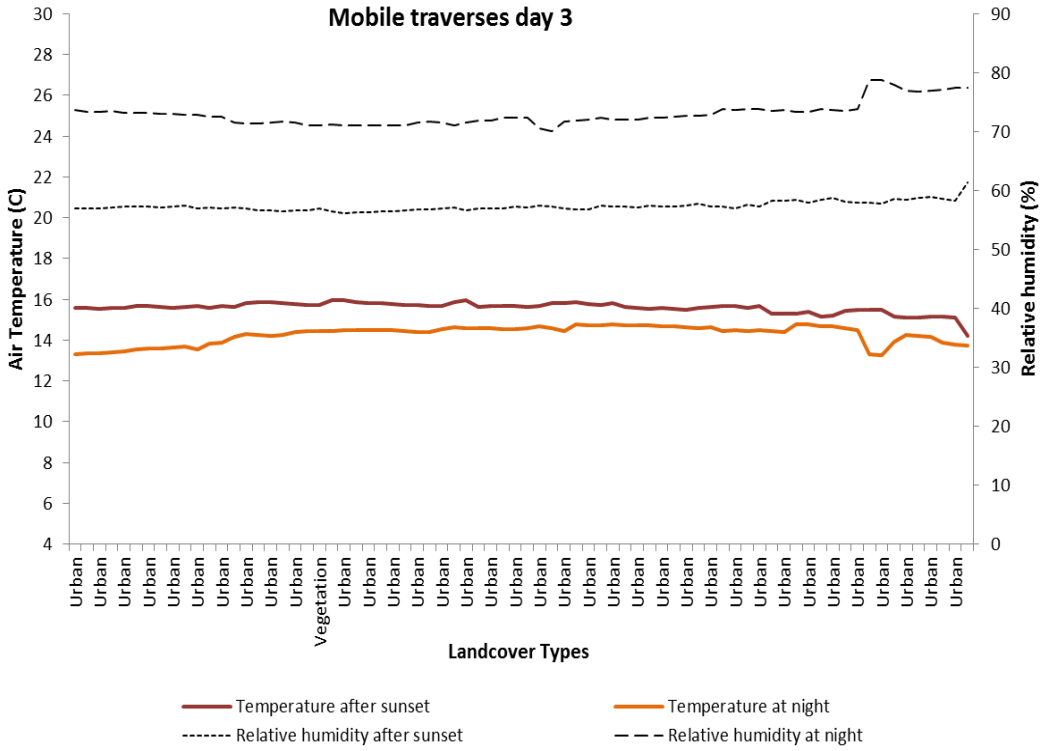

The relation between air temperature, relative humidity, and land cover types during winter season February 2011 (Mobile traverses day 3).

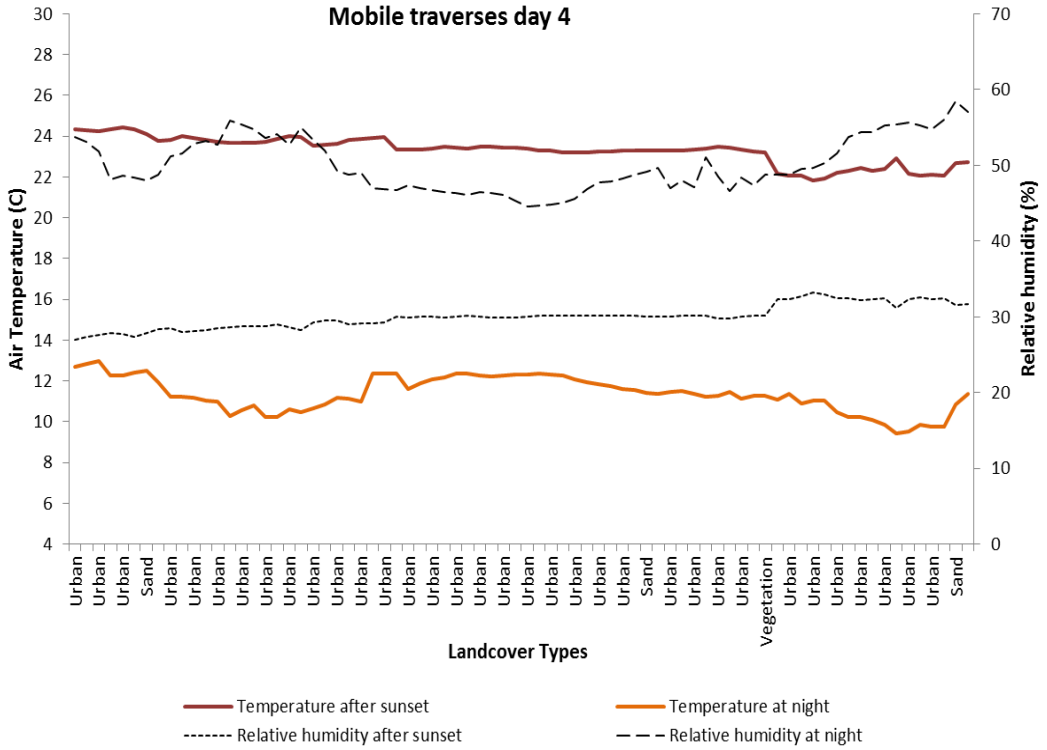

The relation between air temperature, relative humidity, and land cover types during winter season February 2011 (Mobile traverses day 4).

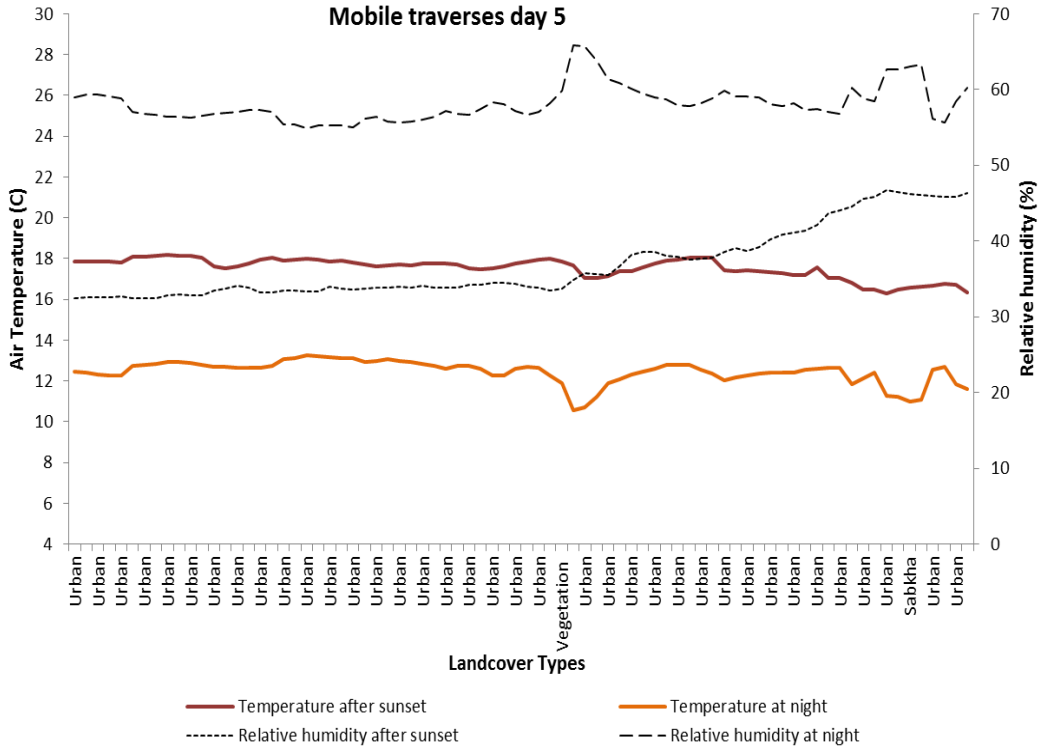

The relation between air temperature, relative humidity, and land cover types during winter season February 2011 (Mobile traverses day 5).

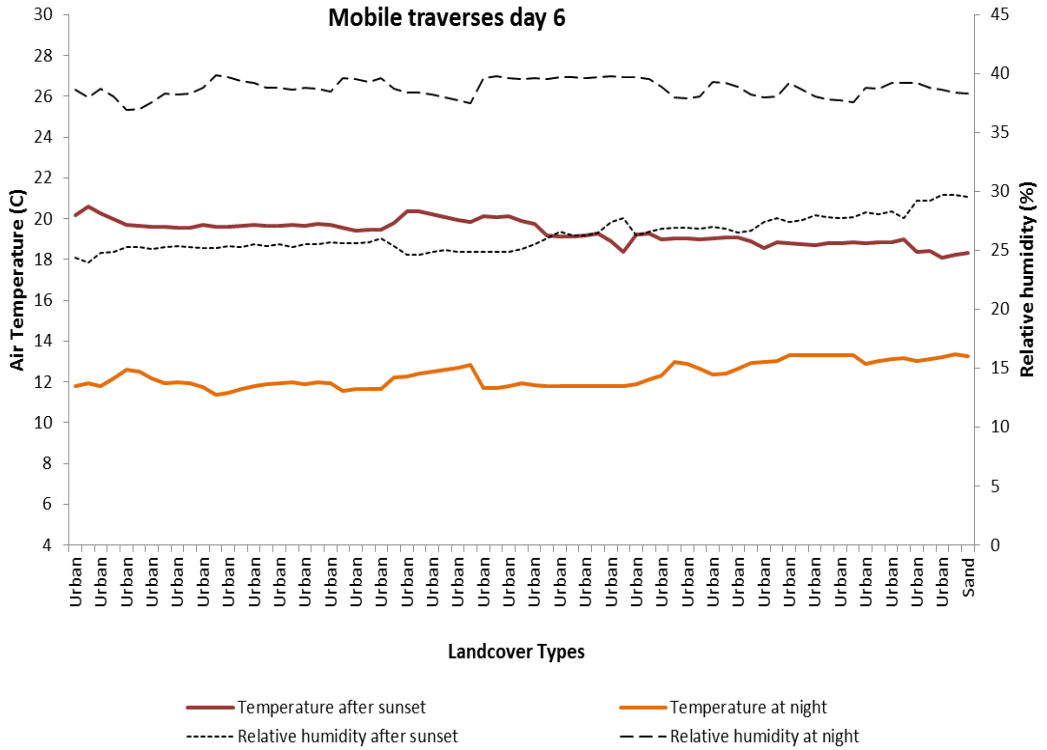

The relation between air temperature, relative humidity, and land cover types during winter season February 2011 (Mobile traverses day 6).

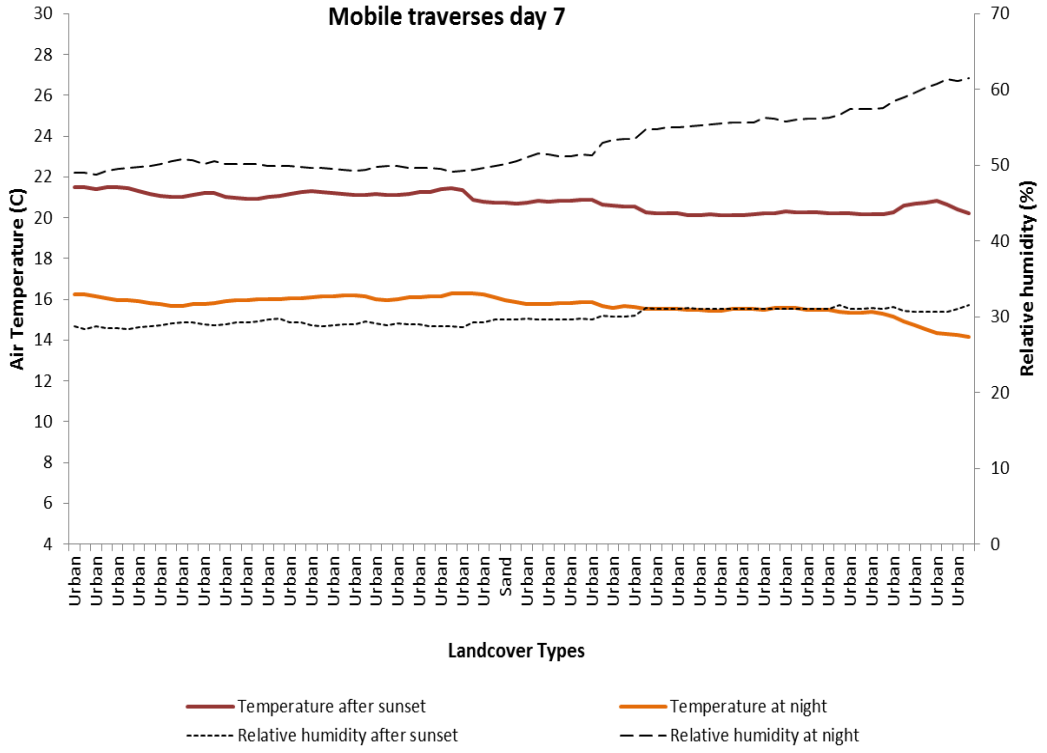

The relation between air temperature, relative humidity, and land cover types during winter season February 2011 (Mobile traverses day 7).

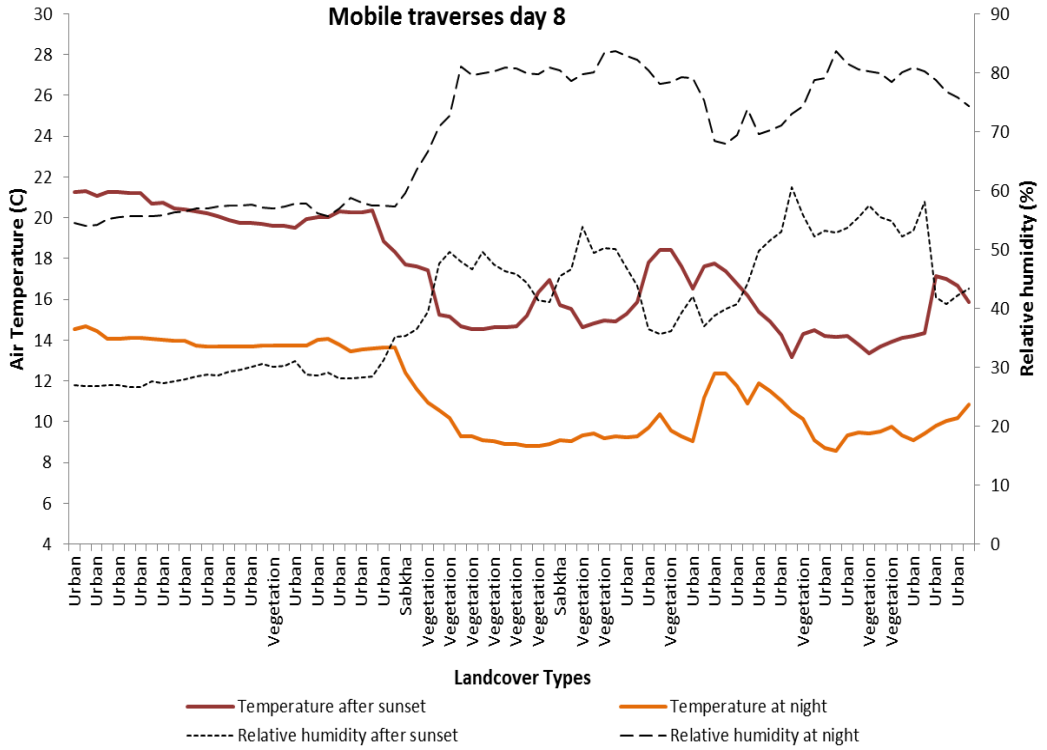

The relation between air temperature, relative humidity, and land cover types during winter season February 2011 (Mobile traverses day 8).

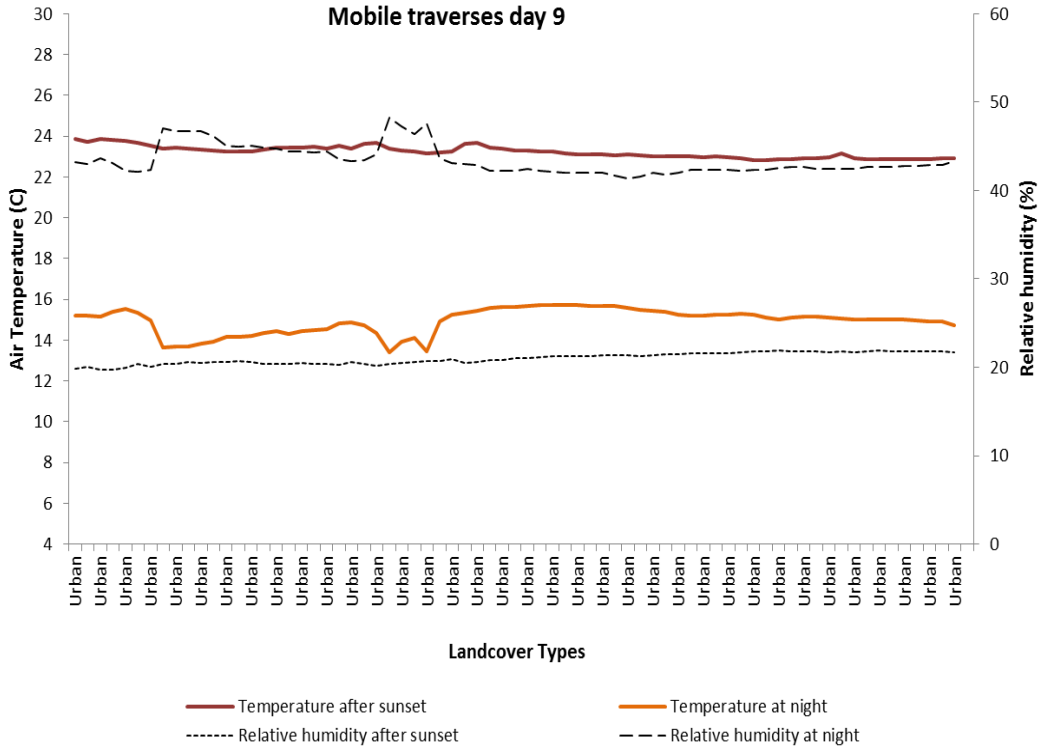

The relation between air temperature, relative humidity, and land cover types during winter season February 2011 (Mobile traverses day 9).

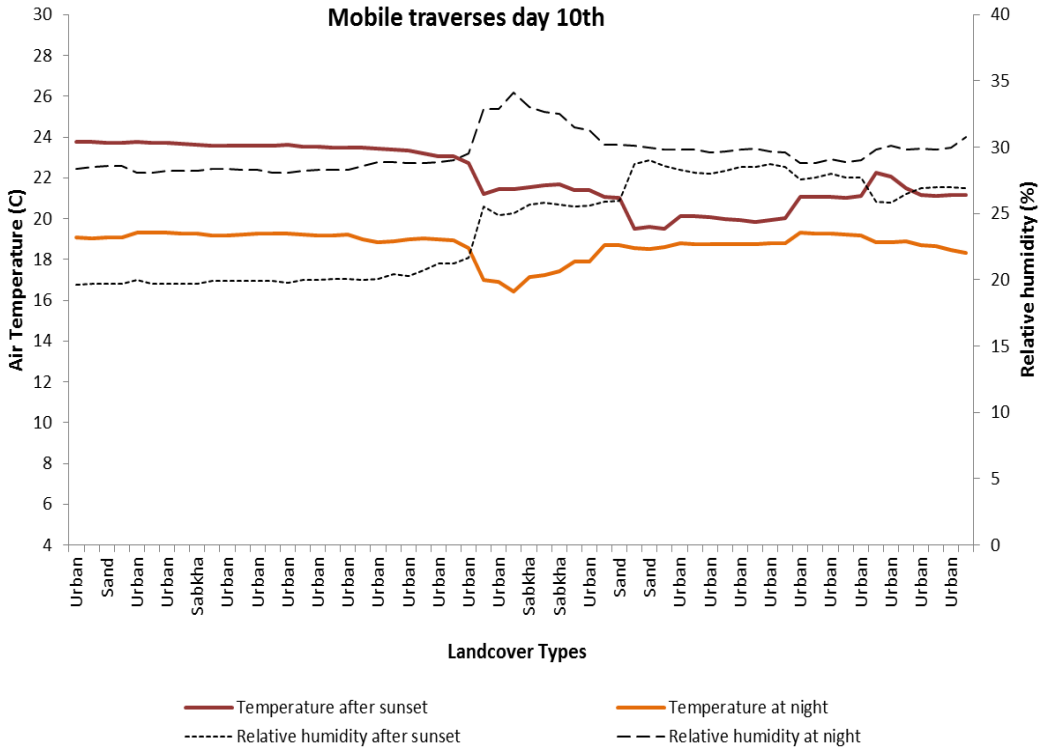

The relation between air temperature, relative humidity, and land cover types during winter season February 2011 (Mobile traverses day 10).

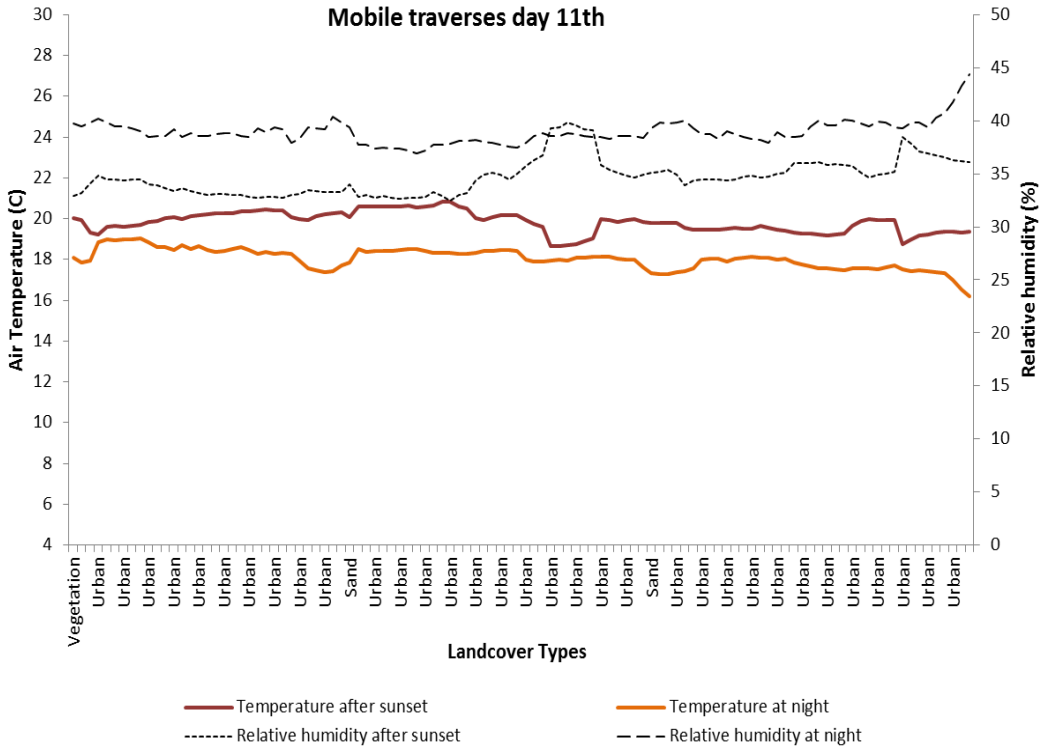

The relation between air temperature, relative humidity, and land cover types during winter season February 2011 (Mobile traverses day 11).

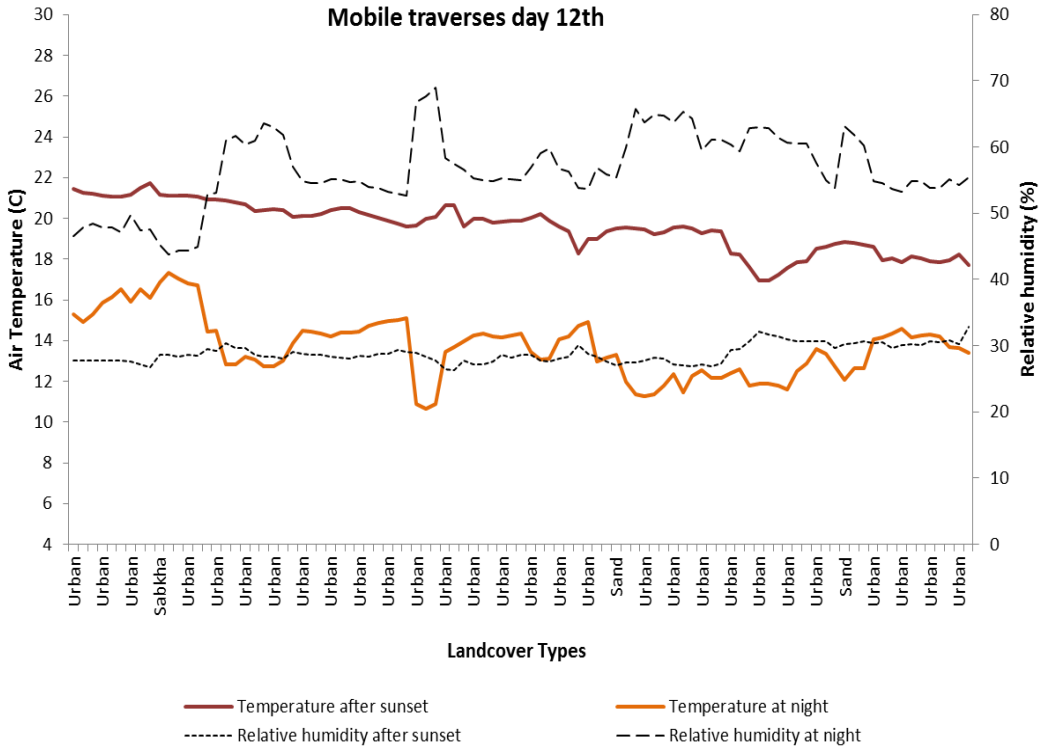

The relation between air temperature, relative humidity, and land cover types during winter season February 2011 (Mobile traverses day 12).

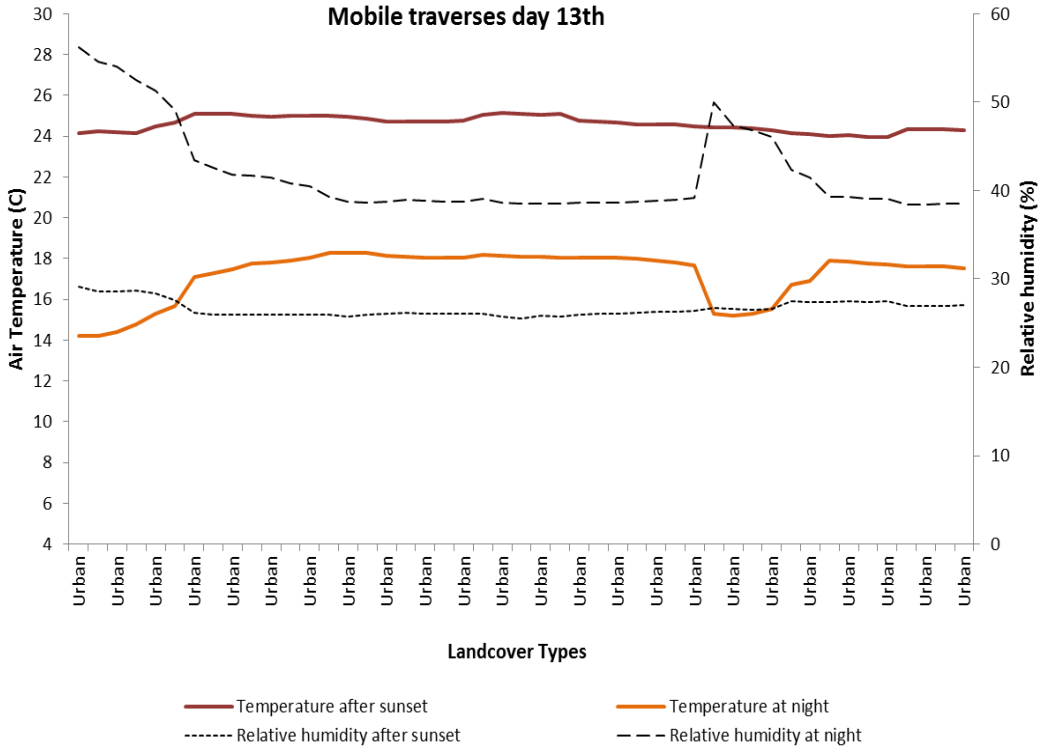

The relation between air temperature, relative humidity, and land cover types during winter season February 2011 (Mobile traverses day 13).